Acknowledgments

I wish to thank Dr. E. R. Wooding for providing the initial motiviation for this work and for his continual encouragement during the time that it was carried out. I also gratefully acknowledge the assistance given to me by Mr. B. Day of the Royal Aircraft Establishment, Farnborough, through whom the project was also financed. Much gratitude is expressed to Mr. J. Henley, Mr. L. P. Ellison, Mr. G. Waters, Mr. R. Mason and other technical staff of Royal Holloway College, for their assistance in various aspects of the experimental work, and lastly, but by no means least, I thank my wife for her help and tolerance during this time.

A STUDY OF AN ABLATION-DERIVED PLASMA IN AN ACCELERATION DEVICE

B.A.NORTON

UNIVERSITY OF LONDON

(ROYAL HOLLOWAY COLLEGE)

1975

Abstract

The results of a study of non-thermal Carbon and Fluorine plasmas in an electromagnetic acceleration device are presented, the plasmas being created by ablation from the surface of a solid dielectric. The dielectric is close to a steady discharge through which ablated material, on entry, is heated and accelerated, and it is concluded that the high level of radiative power loss, which consists mainly of optically thick resonance line radiation, is in part responsible for the uniformity and stability of the plasma plume. Plasma velocities around $1 - 2 \times 10^6$ cm/s. are attained.

In addition to conventional electrical and spectroscopic diagnostic methods, several new spectroscopic techniques are described, providing greater accuracy in the measurement of particle temperatures and densities in non-thermal, non-hydrogenic plasmas. In order to make these methods possible, as well as allowing estimates of the radiation losses, a model describing the population distibution among the bound ionic states was constructed and solved for a wide range of plasma conditions. From these results new values of collisional-radiative ionization and recombination coefficients are obtained, which are in broad agreement with experimental values.

A model was developed which described the rate of ablation from the solid and which formed part of a larger numerical scheme for calculating the temperature, density and velocity of the plasma plume. This model gives results which are in good agreement with the observations and is used to predict the plasma behaviour under different operating conditions and with different dielectric materials.

The extension of certain parts of this work to other situations is also discussed, in particular, laser heating of plasmas, problems of ablation in high-temperature plasma containment devices, and as a source for selective excitation spectroscopy. The possibility of using the device as a soft X-ray laser is also investigated.

CONTENTS

Chapter One

The purposes and results of a study of a compact ablation-derived plasma acceleration device

In this thesis the results of a study of an ablation-derived plasma source are presented and discussed. The source basically operates as a hydromagnetic plasma accelerator but, in the course of this work, new knowledge was gained not only in respect of the accelerator performance, but also in the ablation process itself and in the use of the plasma as a source for selective excitation spectroscopy[1].

Surface ablation is a process of removal of material from the surface of a solid following its decomposition as a result of receiving an energy flux. If the decomposition is thermal in nature, the ablation mechanism is one of pyrolysis followed by surface evaporation. Plasmas created by ablation have found increasing use in magnetic propulsion devices[2,3] and as light sources, where they have been used for spectro-chemical analysis[4,5]. The use of solid fuels eliminates the need for complex storage and fuel-feed equipment, and is thus of advantage in space propulsion where low weight is important.

The ablation is often initiated by means of a small pre-ionizing spark and then sustained by an electric discharge[6], or it may be triggered by irradiating a solid target with a focussed laser beam[7]. Laser induced ablation has also recently aroused interest in the quest for a laboratory thermonuclear source[8,9,10].

In previous investigations of ablation devices[11,12,13], relations have been established between electric current, plasma temperature and the amount of material ablated from surrounding walls, but without investigating in detail the ablation, acceleration or radiative loss mechanisms. Ogurtsova et.al.[11] assumed in their enclosed-channel discharge source that radiative losses and magnetic effects were small and considered the steady temperature situation in which all the Joule energy supplied to the plasma was expended in forming new plasma from the ablated material and gas-

dynamically expelling it out of the channel. The present study however, includes an investigation of the important interacting processes and the results are incorporated into a simple numerical model. The predictions of this model are in good agreement with experimental results obtained under different operating conditions and with different propellants[14].

Plasmas produced by ablation from organic materials are generally complex, containing many different ion species and, as is the case with many laboratory plasmas, are likely to exhibit departures from complete thermal equilibrium. Often the ionic and electronic temperatures are not equal[15], the Saha equations for the ions are not applicable and bound atomic states may not be populated in accordance with a Boltzmann distribution[16]. The importance of such deviations depends upon the particular application. For example, deviations from a Boltzmann population distribution may be unimportant in aerodynamic investigations, but may be very important if a spectroscopic diagnosis were being carried out and radiative energy losses were to be calculated.

For the range of parameters generally encountered in ablation plasma guns i.e. temperatures between about 1 eV. and 20 eV. and electron densities between about 10^{14} and 10^{18} cm^{-3}, some bound ionic levels will show a thermal distribution whilst others may not. This points to the need for reliable atomic data for non-thermal plasmas. In the course of this study, much of this data, previously absent from the literature, was calculated for Beryllium-like, Boron-like, Lithium-like and Oxygen-like ions namely ; eigenstate population parameters[17] and collisional-radiative ionization and recombination coefficients[18] for optically thick and thin plasmas, in a range of conditions just outside those for which a complete thermodynamic equilibrium could be assumed. It is worth noting that these ions represent most of the commonly encountered impurities in modern plasma devices, e.g. in the field of thermonuclear research, and in Astronomy they are observed from studies of hot dwarf stars[19] and Wolf-Rayet early emission stars[20]. Those parts of the numerical model which relate to the radiative energy loss could be used to describe the behaviour of other plasma devices[10,21].

The radiative losses from plasmas containing high-Z ions can be severe[10,22,23] and one of the aims of the experiment was to utilise these losses as much as possible,to produce an intense continuous ablation and thereby also a high accelerator thrust level. The stability of the accelerated plasma is thought to be due, in a large part, to the dominance of the radiative transport to the dielectric. The measured radiative loss was indeed large and the plasma enthalpy remained approximately constant even though the input power varied during the discharge. In the normal mode of operation, electrode ablation was negligible, as it would be if photo-emission from them was important.

Several new diagnostic techniques were developed[14,24] for making the accurate measurements of temperature and density and these are described. Using the source in its capacity as a plasma accelerator, a novel means of producing population inversion in ions by the velocity separation of excited levels is also described[25], which could lead to the operation of a soft X-ray laser and perhaps explain some observations of visible lasing in Z-pinch tubes[26,27]. Solid propellant mixtures can easily be made which would allow a multitude of different plasmas to be created.

References

1. B.A.Norton, Z.Naturf., 29a, p.1937, 1974

2. R.Vondra, K.Thomassen, A.Solbes, AIAA paper no. 70-179, 1970

3. A.P.Bruckner, R.G.Jahn, AIAA paper no. 72-499, 1972

4. J.Romand, J.Physique et.le radium, 16, p.489, 1955

5. J.Romand, J.Physique et.le radium, 18, p.641, 1957

6. A.G.Kalygin,N.P.Kozlov,N.A.Koreschenko,L.B.Leskov,V.B.Saenko, Sov. Phys. Tech. Phys. 15, p.928, 1970

7. H.Opower, W.Press, Z. Naturf. 21a, p.344, 1966

8. J.Knuckolls, L.Wood, A.Thiessen, G.Zimmerman, Nature, 239,p.139,1972

9. N.G.Basov, V.A.Boiko, V.A.Dement'ev, O.N.Krokhin, G.V.Sklivkov, Sov. Phys. J.E.T.P. , 24, p.659, 1967

10. M.Galanti, N.J.Peacock, B.A.Norton, J.Puric, Proc. IAEA 5th Conf. on Plasma Physics and Controlled Nuclear Fusion,Tokyo,November,1974

11. N.N.Ogurtsova, I.V.Podmoshenskii, P.N.Rogovtsev, High Temperature, 9 , p.468, 1971

12. Y.A.Valkov, N.L.Zbrailolova, Y.V.Skvortsov, Sov.Phys.Tech.Phys., 15 ,p.599, 1970

13. P.M.Kolesnikov, Sov.Phys.Tech.Phys., 14, p.1316, 1970

14. B.A.Norton,E.R.Wooding, Proc. 11th Int. Conf. Phenom. Ionized Gases, Prague, September, 1973

15. M.J.Forrest,B.A.Norton,N.J.Peacock, Proc. 6th European Conf. Contr. Fusion and Plasma Phys.,Part I, Moscow, July, 1973

16. S.Leonard, J.Quant.Spectr.Rad.Transf. 12, p.619, 1972

17. B.A.Norton,E.R.Wooding,to be published in J.Phys.B , 1975

18. B.A.Norton, to be published

19. S.Sahal-Bréchot,E.R.A.Segre,Astron.Astroph., 13, p.161, 1971

20. L.H.Aller, Ap. J., 97, p.135, 1943

21. V.I.Kogan, Sov.Phys. Doklady, 4, p.1057, 1959

22. G.Knorr, Z.Naturf. 13a, p.941, 1958

23. B.A.Norton, Z.Naturf., 30a, p.263, 1975

24. B.A.Norton,E.R.Wooding, Proc. 3rd Int.Conf. Gas Discharges, Inst. Electr.Eng., London, September, 1974

25. B.A.Norton,E.R.Wooding,to be published in Phys.Rev.A ,March, 1975

26. S.G.Kulagin,V.M.Likhachev,E.V.Markvson,M.S.Rabinovich,V.M.Sutovskii, J.E.T.P. Pis. 3, p.6, 1966

27. Y.Hashino,Y.Katsuyama,K.Fukuda, Jap.J.Appl.Phys., 13, p.1134, 1974

Chapter Two

Plasma production and electromagnetic acceleration

2.1 Review of plasma accelerators

Plasma accelerators and injectors are devices which impart large velocities to ionized gases which, unlike those used in thermal expansion systems, do not need to be heated substantially. Plasma acceleration is therefore efficient and useful in that the final velocity of the gas is not limited by the maximum temperature that the walls of the device can withstand.

There are several ways of transferring energy to a gas[1] i.e.

(i) Magnetohydrodynamic engines

(ii) Ion engines

(iii) Chemical rockets

(iv) Nuclear rockets

(v) Arcjets and resistojets

(vi) Ablation devices

In the case of MHD. or plasma engines, use is made of the high electrical conductivity of a plasma. An electric current ($\underline{J}$) is made to interact with a suitably orientated magnetic field ($\underline{B}$), producing a $\underline{J} \times \underline{B}$ body force on the plasma. With rapidly pulsed plasma guns, very large currents are obtained and the resulting self-induced magnetic fields can be utilised to provide the thrust. The plasma may be produced in the accelerator by the electrical breakdown of a gas introduced via a fast-acting valve[2,3], it can be derived from an exploding wire or evaporating electrode[1,4] or it can be obtained by the ablation of a solid insulator surface, such as polytetrafluoroethylene[5,6,7]. In an ion engine, ions are accelerated by the direct application of an electric field. However, although capable of high specific impulse, these devices are limited in thrust level by space-charge accumulations which occur between the source and accelerating grids. Conventional chemical rockets, on the other hand, are capable of producing high thrust but not high specific impulse since the directed energy per unit mass is limited by the convertible chemical energy that is available in the fuel, whilst nuclear rockets, arcjets and resistojets

are also limited in specific impulse by the mechanical strength and thermal resistance of the surrounding walls.

Typical examples of plasma accelerators are the coaxial gun, the rail gun and the induction pinch. In these devices momentum is transferred by a rapidly moving magnetic shock to a non-ionized propellant gas, initially at typically 0.1 Torr pressure. Due to the skin effect, a transient current flow is set up in a thin layer of gas which interacts with the self-magnetic field and causes the current sheet to travel along electrodes, which usually extend along the direction of motion and keep the plasma in the circuit for a long time. The inductance per unit length of the accelerator defines, for a given current, the amount of magnetic field energy that is available for thrust, and this parameter can be optimised with regard to various other parameters such as circuit capacitance, gas ionization potential, etc.

It is useful if the ionization state of the gas is known, as it may affect the nature of the interaction between the magnetic shock and the plasma just ahead of it. For example photo-ionization and photo-excitation processes within the gas could affect the thrust efficiency. The gas may be accelerated like a piston to a velocity approaching that of the current sheet, or it may become trapped within the sheet (the 'snow-plow' effect) in which case some of the energy of the encounter is converted into translational energy and some is converted into internal energy of the gas. If the propellant is fully ionized and collisionless however, total reflection from the sheet can occur and all the work done by the magnetic field is converted into plasma directed energy.

In the Marshall coaxial gun[2] acceleration is due to axial $\underline{J} \times \underline{B}$ forces acting on a radial current sheet. The current sheet velocity in such devices however, does not generally agree with the theoretical value obtained using measured values of the parameters. The maximum velocity attainable for a magnetically propelled plasma in crossed $\underline{E}$ and $\underline{B}$ fields is E/B , at which point the back emf. would cancel the applied electric field. This value is possibly not reached for a variety of reasons. For example , wrong mass-loading (mis-matching of the plasma inertia to that of the power source), or frictional drag at the walls or electrodes[8,9] can limit the efficiency of a plasma gun

as can also any unwanted ablation by increasing the radiation losses or diverting the current. However,the importance of each of these processes depends upon the overall operating conditions. For a comprehensive study it is evident that the properties of the propellant must be considered as well as those of the environmental electromagnetic fields.

In the case of solid fuel thrusters, the propellant is generally a dielectric located at the back wall of a rail gun or coaxial gun. These devices operate into a vacuum and a fast trigger pulse generally acts as pre-ionizer. The complete process of ablation, ionization and acceleration develops in a few microseconds or less, and some of the performance characteristics of these devices have been adequately described assuming simple field configurations and without resorting to a complete analysis of the thermodynamic state of the plasma[10]. In addition to the accelerated current sheet, secondary discharges have often been observed near the gun breach and the current profile may also be skewed[11,12,13,14]. This skewing may be due to the field geometry or ablation products from the electrodes[14].

Studies by Kolesnikov et.al.[15,16] have dealt with the effects on efficiency in coaxial guns of various mass-transfer processes namely,(i)plasma ionization and recombination,(ii) ambipolar diffusion,(iii) charge exchange,(iv) erosion of electrodes and (v) viscous drag. By solving the macroscopic equations of continuity,the relative influence of the mechanisms (i) to (v) upon the efficiency of particular coaxial systems was formulated.

In the work described in this report,a plasma source is discussed in which an electric discharge across the surface of a solid dielectric produces a fast-travelling plasma column. The uniformity,stability and velocity of this column were measured together with the plasma current and self magnetic field and possible loss and instability mechanisms assessed.Time and space-resolved spectroscopic measurements allowed determination of constituent particle temperatures and densities.

References

1. 'Plasma Acceleration', S.Kash (Ed.),Stanford Univ. Press, 1960
2. J. Marshall, Phys. Fluids, 3, p.134 , 1960
3. L.C.Burkhardt, R.H.Lovberg, Phys. Fluids, 5 ,p.341 , 1962
4. W.H.Bostick, Phys.Rev. 105 , p.46 , 1957
5. Y.Suzuki et.al., J.Phys.Soc.Japan, 19 , p.779 , 1964
6. A.G.Kalygin,N.P.Kozlov,N.A.Koreschenko,L.V.Leskov,V.B.Saenko, Sov.Phys.Tech.Phys. 15 , p.928 , 1970
7. K.I.Thomassen,R.J.Vondra, AIAA paper no. 71-194 , 1971
8. K.Thom,J.Norwood,N.Jalufka, Phys. Fluids , 7 , p.S67 , 1964
9. J.Norwood, NASA TN, D-3796 , 1967
10. R.Vondra,K.Thomassen,A.Solbes, AIAA paper no. 70-179, 1970
11. L.Lindberg,C.T.Jacobsen, Phys.Fluids, 7 , p.S44 , 1964
12. A.P.Bruckner,R.G.Jahn, AIAA paper no. 72-499 , 1972
13. J.B.Workman, Phys.Fluids,12 ,p.2162 , 1965
14. Y.A.Valkov,N.L.Zbrailolova,Y.V.Skvortsov, Sov.Phys.Tech.Phys. 15 , p.599 , 1970
15. P.M.Kolesnikov, Sov.Phys.Tech.Phys. 14 , p.1316 , 1970
16. P.M.Kolesnikov, N.N.Stolovich, Sov.Phy.Tech.Phys. 15, p.922, 1971

2.2 The acceleration and loss mechanisms in the plasma gun

In order to understand fully the behaviour of the accelerator and predict its performance, a comprehensive set of equations is required. In this section the equations of continuity of mass, momentum and energy are derived for a collisional plasma fluid which contains several ion species and in which there is a continual injection and expulsion of matter. The equations are derived from Boltzmann equations for the electrons and ions. Isotropy, equal electron and ion temperatures and unidirectional magnetic thrust are assumed for the plasma, which is located between two plane electrodes. Expressions for the radiative and collisional ionization and excitation power loss densities are derived and compared with other energy loss mechanisms. Simplifications made on the basis of these comparisons, assist in the prediction of the accelerator performance.

During the operation of this device the average values of current, self-magnetic field and particle temperatures and densities are such that, the ratio of the kinetic and magnetic pressures (β) at the dielectric surface is much less than 0.1 where,

$$\beta = 2\mu_0 n\, kT/B^2 \quad .$$

The accelerator is powered by a ringing electrical discharge across a dielectric surface and the plasma obtained contains several ion species. Spectroscopic measurements of T_e and n_e in the plasma showed that T_e was between 2 and 5 eV. and n_e was $\geq 10^{16} cm^{-3}$ during most of the first half-cycle of the discharge, which was $\simeq 8\mu$sec.

The relaxation time (t_{ee}) for electrons to thermalize to an isotropic Maxwellian distribution by random binary elastic collisions is given by Spitzer[1] as,

$$t_{ee} = 3.4 \times 10^5 \; kT_e^{3/2} \Big/ n_e \ln.\Lambda$$

where t_{ee} is in seconds if n_e is in cm^{-3} and kT_e is in eV. $\ln.\Lambda$ is the Debye parameter[1] and is generally of the order 10 in magnitude.

Under these experimental conditions t_{ee} is much less than 10^{-10}sec. which in turn is much less than the plasma lifetime. The equipartition time between the heavy particles and the electrons (t_{ei}) scales as $m_i\, t_{ee}/2m_e$, and a similarly instantaneous thermalization is assumed.

The velocity distribution for particles j is then a Maxwellian

$$f_j = n_j \left(\frac{m_j}{2\pi T_j}\right)^{3/2} \exp\left(-m_j v_{rj}^2/2T_j\right)$$

where v_{rj} is the random velocity = $v_j - U_j$, and U_j is the average velocity.

$$U_j = \frac{1}{n_j}\int v_j f_j \, d^3v$$

In this plasma the particle Larmor radii (r_{Lj}) are greater than or equal to the collision mean free paths (λ_{mj}), the latter being themselves much less than the characteristic dimensions of the accelerator, which are of the order 5 - 10 mm. Thus the plasma is collisional and can be described by the first few moments of the distribution functions, i.e. by density, velocity and temperature. These parameters are coupled via the MHD conservation equations for particles, momentum and energy, obtained from the Boltzmann kinetic equations.

The Boltzmann equation for particles of type j is[1]

$$\frac{\partial f_j}{\partial t} + v_j \nabla_r f_j + F_j \nabla_v f_j = \left(\frac{\delta f_j}{\partial t}\right)_c \qquad (2.2.1)$$

where $\left(\frac{\delta f_j}{\partial t}\right)_c$ is a collisional source term representing the influence of elastic or inelastic processes on changes in f_j , and F_j is the force per unit mass acting on the particles.

Under the influence of electric and magnetic fields, and neglecting the effects of gravitation and viscous drag,

$$F_j = \frac{eZ_j}{m_j}\left(E + v_j \times B\right) = \frac{1}{n_j m_j}\nabla_r \tilde{T}_j \qquad (2.2.2)$$

where $\tilde{T}_j$ is the Maxwell stress tensor.

Viscous drag has been discussed by Thom et.al.[2] in order to explain the exhaust velocity limitation in a coaxial plasma gun. This friction force is caused by ion impacts on the cathode, which were associated with the electric current in the gun, and relates to their subsequent loss of axial momentum. It is shown in chapter 6 that negligible ion current flows in the strongly radiating plasmas produced in the present device, thereby justifying the neglect of drag effects. Turbulent friction is also not considered as experimental correlation between the spectroscopically derived temperature and the classical conductivity temperature[1] shows that it is not important.

The Boltzmann transport equations are obtained by averaging the velocity moments[3] of equation (2.2.1),

$$\int Q_j(r,v,t)\frac{\partial f_j(r,v,t)}{\partial t}\,d^3v + \int Q_j(r,v,t)\nabla_r v_j f_j(r,v,t)\,d^3v$$

$$+\int Q_j(r,v,t)\nabla_v F_j f_j(r,v,t)\,d^3v = \int Q_j(r,v,t)\left(\frac{\delta f_j(r,v,t)}{\partial t}\right)_c d^3v \qquad (2.2.3)$$

and putting Q_j equal to unity, m_j, $m_j v_j$ or $m_j v_j^2/2$.

The particle continuity equations become, in the case of the i^{th} ion stage of an ion species k, and assuming that most of the ions are in their ground states,

$$\frac{\partial n(k,i)}{\partial t} + \nabla_r\left(n(k,i)\,u(k,i)\right) = \left(\frac{\delta n(k,i)}{\partial t}\right)_c \qquad (2.2.4)$$

A similar equation exists for electrons and metastable levels.

As electron and ion energies do not exceed the ionization energies of the ion species, and certainly not by orders of magnitude, ionization is assumed to be accomplished solely by means of electron encounters. If σ_{ie} is the cross-section for ionization by electron impact then the ionization

coefficient $S_j = \langle \sigma_{je} v_e \rangle$

$$\therefore S_j = \int \sigma_{je}(v_e) f_e(v_e) v_e \, d^3v \qquad (2.2.5)$$

The various coefficients and their evaluation are discussed in section 4.3 . As a result of the ablation process neutral atoms are injected into the plasma. If the injection rates are $G_j^*(t)$ particles per second per cm^3, equation (2.2.4) becomes, for neutrals,

$$\frac{\partial n_n}{\partial t} - q_j^* = \left(\frac{\delta n_n}{\partial t}\right)_c \qquad (2.2.6)$$

It is shown in chapter 6 however, that at the densities and temperature prevailing in the plasma, the neutrals can be assumed to be ionized instantly on entering the plasma. Thus, for the region between the electrodes, $\frac{\partial n_n}{\partial t} = 0$ and

$$\left(\frac{\delta n_n}{\partial t}\right)_c = - q_j^* \qquad (2.2.7)$$

The total mass conservation equation from equation (2.2.3) becomes, after summing over all species,

$$\frac{\partial \rho}{\partial t} + \nabla_r(\rho u) = \sum_j m_j q_j^* \qquad (2.2.8)$$

The particle momentum transport equations also follow from equation (2.2.3) with $Q_j = m_j v_j$, and following some algebraic reduction,

$$\frac{\partial (n_j m_j u_j)}{\partial t} + \nabla_r (n_j m_j \langle v_{j\alpha} v_{j\beta} \rangle) = e n_j Z_j (E + u_j \times B) + \int m_j v_j \left(\frac{\delta f_j}{\partial t}\right)_c d^3v \qquad (2.2.9)$$

With $\langle v_{rj} \rangle = 0$ and $\langle v_{j\alpha} v_{j\beta} \rangle = u_{j\alpha} u_{j\beta} + \langle v_{rj\alpha} v_{rj\beta} \rangle$, the second term in equation (2.2.9) becomes

$$\nabla_r (n_j m_j u_{j\alpha} u_{j\beta}) + \nabla \cdot \tilde{P}_{j\alpha\beta}$$

where $\tilde{P}_{j\alpha\beta} = n_j m_j \langle v_{rj\alpha} v_{rj\beta} \rangle$ is the kinetic stress tensor.

As the random velocity distributions are isotropic Maxwellians in the present situation, $\tilde{P}_{j\alpha\beta}$ is a scalar pressure P_j where,

$$P_j = \frac{n_j m_j \langle v_{rj}^2 \rangle}{3} = n_j KT_j \qquad (2.2.10)$$

Further simplifications can be made because $m_e \ll m_i$ and also, because the Debye length is much smaller than the plasma dimensions, charge neutrality is assumed locally whence $n_e = \sum_i n_i Z_i$.

From equations (2.2.9) for ions and electrons, one obtains

$$\frac{\partial(\rho u)}{\partial t} = J \times B + \nabla_r \left(\tilde{T} + P \right) \qquad (2.2.11)$$

By subtracting the ion and electron terms Ohm's law for the plasma results,

$$\frac{m_e}{n_e e^2} \frac{\partial J}{\partial t} = E + u \times B - \frac{J \times B}{e n_e} + \frac{\nabla_r P_e}{e n_e} - \eta J \qquad (2.2.12)$$

η is the resistivity and represents the momentum exchange between the ions and electrons during Coulomb collisions.

$\eta = m_e \nu / e^2 n_e$ where ν is the collision frequency for the electrons.

Putting $Q_j = m_j v_j^2/2$ in equation (2.2.3) and summing the equations for the electrons and ions, again assuming an isotropic velocity distribution for each, the energy equation results i.e.,

$$\frac{\partial}{\partial t}\left[\left(\frac{n_e m_e u_e^2}{2} \right) + \sum_i \frac{n_i m_i u_i^2}{2} + \frac{3}{2}\left(n_e KT_e + \sum_i n_i KT_i \right) \right]$$

$$+ \nabla_r \left[\left(\frac{n_e m_e u_e^2 u_e}{2} \right) + \sum_i \frac{n_i m_i u_i^2 u_i}{2} + \frac{5}{2}\left(n_e KT_e u_e + \sum_i n_i KT_i u_i \right) \right] \qquad (2.2.13)$$

$$= JE + \sum_i \int \left(\frac{m_e u_e^2 + m_i u_i^2}{2} \right) \left(\frac{\delta f}{\partial t} \right)_c d^3 v$$

As electrons alone effect ionizing and exciting collisions, the collision integral in equation (2.2.13) becomes,(see chapter 4)

$$Y_{pc} = \sum_{k}\sum_{i>1}\Big\{ n_e n(k,i-1,g) S_{c+}(k,i-1,g) \chi(k,i-1,g)$$

$$- n_e n(k,i,g)\alpha_{c+}(k,i,g)\chi(k,i,g) + n_e n(k,i,g)\alpha(k,i,g)\chi(k,i,g)$$

$$+ \sum_{p}\sum_{q} n(k,i-1,p) A(k,i-1,p,q) F(\tau) E(k,i-1,p,q)\Big\} \qquad (2.2.14)$$

where g refers to the ground state of an ion .

In this device, it is assumed that within the electrode gap, magnetic and kinetic pressure influence the axial velocity U_x of the electrons and ions , whilst kinetic pressure alone influences the velocity components U_y and U_z which are less than U_x . As it can be established that the ion contribution to the conduction current is negligible, $U_{ey} > U_{iy}$. Equation (2.2.13) then reduces to

$$\frac{3}{2}\frac{\partial}{\partial t}\Big(n_e K T_e + \sum_i n_i K T_i\Big) = JE - \frac{1}{2}\frac{\partial}{\partial t}(\rho u^2) - Y_{pc}$$

$$- \frac{5}{2}\frac{KT_e}{e}\frac{\partial J}{\partial x} - \nabla_r\Big(\frac{5}{2}KT_e + \frac{\rho u^2}{2}\Big)u_e \qquad (2.2.15)$$

By integrating over volume,

$$\frac{3}{2}V\frac{d}{dt}\Big(n_e K T_e + \sum_i n_i K T_i\Big) = R_p I_q^2 - \frac{1}{2}\frac{d M u^2}{dt} - Y_{pc} V$$

$$- \frac{5KT_e}{2e} I_q - \Big(\frac{5}{2}KT_e + \frac{Mu^2}{2}\Big)\sqrt{n_e} \qquad (2.2.16)$$

where $\sqrt{n_e}$ accounts for conduction and convection losses at the plasma edge. In chapter 6 it is shown that these losses are negligible compared to the radiative and ionization term Y_{pc} .

References

1. L.Spitzer,Jr.,'Physics of fully ionized gases',Interscience Pub,N.York 1956
2. K.Thom,J.Norwood,N.Jalufka, Physics Fluids, 7 , p.S67 , 1964
3. Montgomery D.C.,Tidman D.A. , 'Plasma Kinetic Theory', McGraw Hill, N.York, 1964

2.3 Ablation and surface discharge mechanisms

The general mechanism for the formation of a plasma by ablation from a solid involves the thermal degradation of a thin surface region after it has been subjected to an energy flux, and its subsequent removal by evaporation. The degree of dissociation depends upon the thermal stability and conductive properties of the solid as well as the magnitude of the surface energy flux.

Ablation-derived plasmas may be specially created (e.g. laser-produced plasmas for fusion research[1,2], or solid fuel thrustors[3,4]) or they may be an undesirable occurence (e.g. impurity injection in plasma confinement machines[5,6,7], high-voltage breakdown over an insulator[8,9]). The energy transfer to the solid can be by irradiation from an intense light source such as a laser or a high-power gas discharge[10,11]. In many plasma confinement systems however, thermal transport to surrounding walls is important as well as losses in the form of high-energy runaway electrons[12], which become relativistic and able to leak through the confining magnetic fields. In arc discharges, high energy ion impacts[13,14] may be responsible for electrode decomposition, and in high energy plasmas produced by laser-irradiation of solid targets[2], radiation from the plasma itself may cause further target ablation. In the latter case, such a mechanism may explain observations of plasma densities higher than the critical density when the laser beam is reflected. The absorption of energy may be complex in the case of photo-irradiation, depending upon the power and the thermal conductivity of the solid. If power levels are large, as in most laser produced plasma systems[1,2], the degradation is intense and shock waves can propagate in the solid, which could lead to compression[15]. Sufficient energy can be deposited at the target surface to completely dissociate, ionize and heat the material, at which stage non-linear absorption processes may also become important[2,16].

Existing descriptions of the development of low-power ablation generally only consider the time necessary for the surface of a material to reach its melting or boiling point when subjected to a constant energy flux from its

surroundings[13,17,18]. Details of the ablation mechanism can be ignored if all that is required is the time at which pyrolised material from outer walls or immersed objects is likely to contaminate a plasma. Recently however, surface ablation has been investigated in more detail as part of a wider study of the ignition and burning rates of solid fuels used in rocket propulsion[19]. Heat evolution within the surface as a result of exothermic processes, surface recession, optical transparency and the effects of residue formation have also been discussed , but only for constant surface flux.[20,21]

In the present device, after initiation with a small pre-ionization discharge, the plasma is supplied entirely by ablation products from the front surface of the dielectric in the region between the electrodes. The time-evolution of material from this surface can be described only after a relationship is found between the energy flux and the plasma parameters and if further, the ablation mechanism can be quantified.

A simple model is presented for the case in which a short pulse of energy from the plasma, incident on the polymer surface causes it to heat, dissociate and evaporate. In this model use is made of published experimental data. Ablation occurs at the interface between the dielectric and the plasma and the following assumptions were also made ;

1) Heat conduction in the dielectric is described adequately using a one-dimensional semi-infinite slab model .
2) The propellant remains isotropic at all times.
3) Thermodynamic and transport properties are temperature independant and thermal expansion of the dielectric is neglected.
4) Propellant decomposition occurs within an incremental layer at the surface, restricting heat convection to the interface with the plasma.
5) Ablation is a process of partial de-polymerization, in the case of an organic polymer dielectric, followed by evaporation and with the bulk of the solid remaining intact.

6) De-polymerization is a volume process, quantifiable as a first order chemical reaction, the rate of which can be expressed by an Arrhenius - type function.

7) Surface recession is uniform and occurs to a depth equivalent to the volume of material ablated in a previous time interval, with a shift of the surface temperature to satisfy the boundary conditions at the new subsurface layer.

8) Ablation is complete, i.e. no surface residue is formed.

9) The incident energy flux is uniform over the propellant surface.

Assumptions 2, 3, 5, 6, and 8 are based on published experimental studies of the pyrolysis of those materials used in the present case.[22-27] During the discharge lifetime (less than 10μseconds) the conduction depth is very small (less than 10^{-3} cm), so justifying assumptions 1 and 4.

For organic polymer dielectrics such as PTFE, polyethylene and polypropylene, thermal scission of the main polymer chain is the initiation mechanism for pyrolytic dissociation[28,29]. This can occur either randomly along the chain or at one end, resulting in the formation of free radical groups, where a free radical is a sub-chain with a spare valence site (see fig. 2.3.1). The subsequent dissociation depends upon the relative stability of the chain structure towards transfer or propagation. Transfer is a process in which a Hydrogen atom joins onto a free radical (abstraction) from another polymer chain, thereby saturating the free radical, but breaking the donor into two parts. One part becomes a free radical and a double bond is formed at the end of the other. Propagation is a mechanism by which a free radical breaks up on its own into a monomer fragment and another free radical. Termination occurs when two free radicals mutually saturate with the exchange of a Hydrogen atom. Defining a 'zip' length as,

$$\left(\frac{\text{The probability of propagation}}{\text{The probability of transfer plus termination}} \right)$$

Fig. 2.3.1

Pyrolytic degradation processes in Carbon Polymers

Initiation :

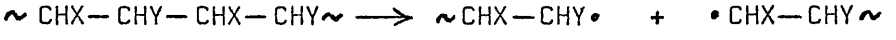

Transfer :

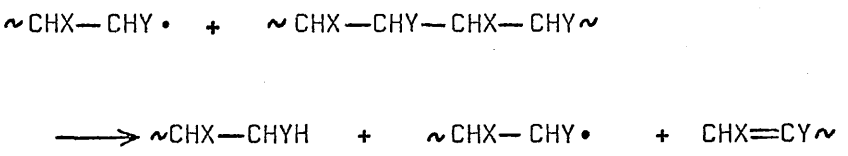

Propagation :

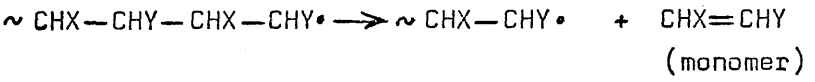

Termination :

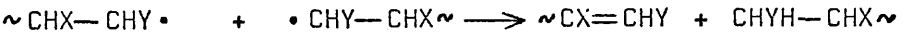

then clearly a large 'zip' length means that a large monomer yield is obtained from decomposition. Wall and Florin[30] discussed the general characteristics of the thermal degradation of polymers in terms of the mechanisms outlined above. From their plots of rate of volatilization (weight percent per second) against conversion (weight percent), and by comparison with experimental observations[22-26], it is seen that the thermal decomposition of these polymers can be described by a first-order reaction. In the case of Polyethylene and Polypropylene, a break occurs in the curves after some degree of initial conversion, but after that a first-order reaction still describes the decomposition. In accordance with its chain structure (i.e. strong tightly arranged C-F bonds and secondary carbon atoms), chain propagation is the dominant pyrolytic mechanism in PTFE, with observed monomer yields greater than 95%. The chain structures of Polyethylene and Polypropylene contain many C-H bonds and some tertiary Carbon sites, which favours intermolecular transfer[25]. For these polymers the volatilization characteristics do not suggest an appreciable transfer mechanism, although experimentally observed monomer yields are low (less than 20%)[27]. However, as a result of the tendency in their chain structure towards Hydrogen abstraction, intermolecular transfer can occur simultaneously with random scission[31,32], thereby leading to the formation of large saturated groups. Thus, due to these competing mechanisms, the rate of monomer formation is not dominant.

Some modification of the published values of the heats of depolymerization was necessary for this model, as they are given in terms of monomer concentrations, This is because they are evaluated from the polymerization reaction. In the case of PTFE the use of published data is straightforward as the zip-length is large and monomer formation is almost 100% . In order however, to represent the decomposition of Polyethylene and Polypropylene as a single depolymerization to monomer, the assumption is made that the total change in enthalpy involved in breaking a chemical bond and saturating the free radical is independant of the mechanism.

The total degradation products are equated to an equivalent monomer yield with a gram -molecular weight M' where

$$M' = 100 \sum_i M_i^* / p_i$$

and P_i is the weight percent composition of each degradation product of gram -molecular weight M_i^* .

Using published values[22-25], the decomposition rates for all three polymers can be expreesed by an Arrhenius equation of the form

$$\text{Rate } (T) = G \exp(-E_a/RT)$$

where E_a is the activation energy (kcal./mole) and G is a pre-exponential factor, in units of sec^{-1} for a first order reaction .

The published values refer to bulk isothermal degradation and some justification must be sought if they are to be used to describe transient decomposition. Equipartition rates for the 'activation' process , that is when the molecules have sufficient internal energy to commence dissociation, must be greater than the decomposition rates. This should be the case in view of the fact that 'activation' is a second order process and the associated energy exchanges are smaller. Variations in the incident energy flux should also be small during the activation equilibrium times, so that a succession of quasi-isothermal states are passed through. In the present experiment $\sim 10^{19}$ molecules per second are dissociated at the dielectric surface,and so equipartition times will be much less than the time over which the discharge current varies.

Assuming that the energy is transferred by thermal conduction within the propellant, a first order mechanism is only valid if the total energy required to ablate a volume bounded by the conduction depth in a given time interval is greater than the total incident energy during that time. If this were not the case, a zero-order reaction would be more applicable. Literature values of the thermal constants for the three materials used in the present study are shown in table 2.3.1.

Table 2.3.1

PHYSICAL AND CHEMICAL DATA FOR PROPELLANT MATERIALS [1]

Sample:			P.T.F.E.	Polypropylene	Polyethylene
			'Fluon' sintered sheet supplied by I.C.I. *	Isotactic extruded sheet supplied by G.H.Bloore **	Low-density extruded sheet supplied by G.H.Bloore **
ρ	density	gm./cm	2.1	0.92	0.93
c_p	specific heat	cal/gm.^{o}K	0.25	0.45	0.55
K_c	thermal conductivity	cal/sec.cm.^{o}K	6.0×10^{-4}	3.3×10^{-4}	8.0×10^{-4}
α_c	thermal diffusivity	cm^2/sec.	1.24×10^{-3}	8.0×10^{-4}	1.56×10^{-3}
M	gram monomer weight	gm.	100	42	28
M*	equivalent monomer weight	gm.	100	70 ($< 700^{o}$K) [2] 42 ($> 700^{o}$K)	34 ($< 800^{o}$K) [3] 25 ($> 800^{o}$K)
ΔH_p	heat of polymerization to solid polymer at 298.15 ^{o}K	Kcal/mole of monomer	-41.12	-25	-25.6
G	pyrolytic pre-exponential factor	sec^{-1}	4.0×10^{18}	6.6×10^{16}	6.1×10^{18}
E_a	pyrolytic activation energy	Kcal/mole	80.0	61.0	70.0

* Imperial Chemical Industries Ltd., Plastics Div., Welwyn Garden City, Herts, England

** G.H.Bloore Ltd., Stanmore, Middlesex, England.

1. [Representative selection from: Fortschr.Hochpolymer Forsch. 2 , p.465, 1961, Brandrup J. et.al. Polymer Handbook, Interscience, New York, 1966, 'JANAF Thermochemical Tables', The Dow Chemical Co., Michigan, 1965 'Fluon', Technical Service Note F 12., I.C.I. Ltd., England, 1968]

2. Calculated from decomposition products observed by Bailey W.J. et.al. Abstracts of 134th Meeting of Am.Chem.Soc. Chicago, p.83, 1958, and Tsuchiya Y. et.al. J.Polym.Sci. (A-1), 7 , p.1599, 1969.

3. Calculated from decomposition products observed by Oakes W.G. et.al.J.Chem.Soc. p.2929, 1949.

References

1. H.Opower,W.Press, Z.Naturf., 21a, p.344, 1966

2. M.Galanti,N.J.Peacock,B.A.Norton,J.Puric, Proc. 5th IAEA Conf. on Plasma Phys.,Contr.Nucl.Fus.Res. , Tokyo, 1974

3. A.G.Kalygin,N.P.Kozlov,N.A.Koreschenko,L.B.Leskov,V.B.Saenko, Sov.Phys.Tech.Phys., 15, p.928, 1970

4. K.I.Thomassen,R.J.Vondra, AIAA paper no.71-194, AIAA New York, 1971

5. W.M.Burton,R.Wilson,Proc.Phys.Soc., 78, p.1416, 1961

6. D.C.Hagerman,J.E.Osher, Nature, 181, p.226, 1958

7. F.C.Jahoda,E.M.Little,W.E.Quin,G.A.Sawyer,T.F.Stratton, Phys.Rev., 119, p.843, 1960

8. M.J.Kofoid, AIEE Trans., 79, p.991, 1960

9. R.Hawley, Vacuum, 18, p.383, 1968

10. N.G.Basov, Sov.Phys.JETP, 24, p.659, 1967

11. B.A.Norton,E.R.Wooding,11th Int.Conf.Phenom.Ionized Gases,Prague,1973

12. C.W.Gowers,J.W.Long,A.A.Newton,B.A.Norton,D.C.Robinson,A.J.Verhage, H.A.B.Bodin,6th European Conf.on Contr.Fus.,Plasma Phys.,Moscow,1973

13. A.Sharah,G.D.Cormack, Can.J.Phys., 49, p.2962, 1971

14. P.R.Smy, Proc.Phys.Soc., 82, p.231, 1963

15. J.Knuckolls,L.Wood,A.Thiessen,G.Zimmerman, Nature, 239, p.139, 1972

16. A.V.Vinogradov,V.V.Pustelov,J.E.T.P.Pis.Rev., 13, p.317, 1971

17. D.E.T.F.Ashby, J.Nucl.En.(Part C), 5, p.83, 1963

18. R.H.Lovberg,'Plasma diagnostic techniques',Academic Press,N.York,1965

19. G.Lengelie, AIAA J., 8, p.1989, 1970

20. H.G.Landau, Quart.Appl.Math., 8, p.81, 1950

21. E.W.Price,H.H.Bradley,J.Dehority,D.Ibiricu,AIAA J., 4, p.1154, 1966

22. S.L.Madorsky,V.E.Hart,S.Strauss,V.A.Sedlak,J.Res.Nat.Bur.Stand., 51, p.327, 1951

23. S.L.Madorsky, J.Polymer Sci., 9, p.133, 1952

24. S.L.Madorsky, J.Polymer Sci., 11, p. 491, 1953

25. S.L.Madorsky,S.Strauss,J.Res.Nat.Bur.Stand., 53, p.361, 1954

26. J.M.Cox, J.Appl.Polymer Sci., 8, p.2935, 1964

27. Y.Tsuchiya, J.Polymer Sci., Part A-1, 7, p.1599, 1969

28. R.Simha, L.A.Wall, J.Polymer Sci., 6, p.39, 1951

29. N.Grassie,H.W.Melville, Proc.Roy.Soc., A199, p.1,14,24,39, 1949

30. L.A.Wall, R.E.Florin, J.Res.Nat.Bur.Stand., 60,p.451, 1958

31. H.Staudinger, A.Steinhofer, Ann.Chem. Justus Liebigs, 517, p.35, 1935

32. S.L.Madorsky, S.Strauss, J.Res.Nat.Bur.Stand., 55, p.223, 1955

2.4 Spectroscopy and radiative transfer from dense plasmas

The spectral emission from a plasma is important both because of the loss of plasma energy that it represents and because it provides some information on the conditions within the plasma. As the plasma in this experiment is only of the order 1 cm^3 in size, with a power input of the order 1 MWatt, spectroscopy is the only feasible non-perturbing diagnostic method. In order to describe the observed spectral emission, as well as the internal distribution of energy amongst the excited ions present, the total ion and electron densities and the particle temperatures must be known. The present study relates to plasmas containing Carbon or Fluorine in various stages of ionization and for which no simple equilibrium description previously existed. A general treatment would require the solution of a set of differential equations describing the population of each ionic energy level, involving collisional and radiative transitions between the levels and successive ionization stages, together with a set of radiative transfer equations and including processes such as particle loss or gain or MHD-compression. In most cases however, conditions allow for simplifications to be made when describing the plasma state. Any assumptions involved must be checked before a particular model is set up and generally concern;

1) The relative importance between collisional and radiative decay rates in establishing equilibrium population densities among quantum levels.
2) The equilibration times for relaxation of the population densities of the various quantum states, compared to times over which the plasma parameters vary (e.g. variations in T_e).
3) The effect of local radiation densities upon the establishment of equilibrium distributions.
4) The importance of metastable levels and multiply-excited states on the total population density of an ion.

From measurements of spectral line intensities, the instantaneous populations of the upper levels of the transitions which they represent can be determined. If these levels have reached a state of quasi-equilibrium with the instantaneous populations of the other excited levels and the populations of the ground state and continuum of free electrons, then the latter can be deduced provided that the nature of the equilibrium is known. When the electron density is high, the system tends towards complete Local Thermodynamic Equilibrium (LTE). In this situation, collision induced transitions are dominant in the establishment of all the excited level populations which are then related by Boltzmann factors to the population densities of all the other levels. When the electron density is low, the radiative transitions compete with, or overwhelm, the corresponding collisional transitions and interfere with the statistical-mechanical equipartition between quantum states as represented by the LTE model. In the limit of very low electron density, de-population of most of the excited levels is accomplished solely by radiative decay and the plasma is said to be in a 'Coronal' regime. Very often however, as is the case in the present experiment, plasmas are non-thermal and lie somewhere between the LTE and Coronal extremes.

These models are described in detail in Chapter 4. Densities of the lower atomic states are required in order to estimate the resonance line radiation losses, which are the most important, and also to check the absorption of the plasma to these wavelengths. The latter effect is found to be important as it effectively shields the plasma from very rapid radiation cooling. A large number of basic atomic parameters such as collisional - radiative ionization and recombination coefficients, spontaneous transition probabilities and electron impact line-broadening parameters were required and these were calculated when they could not be found in the literature.

Chapter Three

The Operating Characteristics of the Plasma Accelerator

3.1 Introduction

In this chapter the plasma source and its mode of operation are described. The dynamic stability of the accelerated plasma is investigated and related to the gun geometry, the power input and the chemical and physical properties of the propellant. The results of electrical and photographic measurements on the plasma are in good agreement with theoretical predictions, which are outlined in chapter 6 .

Expressions are derived for the relative stability and overall acceleration efficiency, which are compared with experimental results obtained under a variety of operating conditions. The accelerator is basically a 'static-arc' device from which a continuous, high velocity plasma plume developes. This plume exhibits a high degree of stability and uniformity during the greater part of each discharge half-cycle, but becomes distorted at the end of each half-cycle. This is thought to be due to some slight instability or non-uniformity which is allowed to grow when the discharge current is low.

3.2 The plasma source

The plasma source is produced from a capacitor-driven electrical discharge between two flat electrodes across a PTFE surface, in the first instance, although some results have also been obtained using polypropylene and polyethylene. Fig. 3.2.1 shows the source and the operating system that was developed. Values of the resistance and inductance of the circuit elements are also shown. Fig. 3.2.2 is a simplified sketch of the plasma current sheet, depicting the ideal current and magnetic field configuration. The Molybdenum electrodes were housed in Copper clamps whilst, throughout the rest of the circuit, screwed brass connections were used.

From measurements of the mass lost per shot, and from an analysis of spectrograms taken around the dielectric surface, it was found that Molybdenum electrodes were eroded considerably less than electrodes made from Copper, invar or stainless steel. The corners of the Copper clamps were rounded and polished in order to avoid forming any preferential breakdown sites. D.C. breakdown tests with clean smooth electrodes gave breakdown fields of approx. 50 kV/cm across PTFE in a vacuum less than 10^{-5} Torr, dropping to approx. 30 kV/cm after 50 discharges.(Photographs of these breakdowns showed that a set of minor discharges was formed, originating from several regions spread across the electrodes). The air spark-gap was a double hemisphere incorporating a single concentric trigger electrode. With the gap set at between 2 mm and 6 mm, current and voltage measurements showed that the resistance of the switching circuit was constant to within 2 milliohms at 34 milliohms over the first full cycle of the discharge, and constant to within 4 milliohms at 43 milliohms over the second cycle.

In normal operation the device was evacuated to less than 2×10^{-6} Torr and a 7.5 kV - 50 mAmp. pulse of less than 100 nsec. duration was used as the trigger. During the discharge, the current interacts with the self-induced magnetic field to provide the axial thrust and a plane electrode

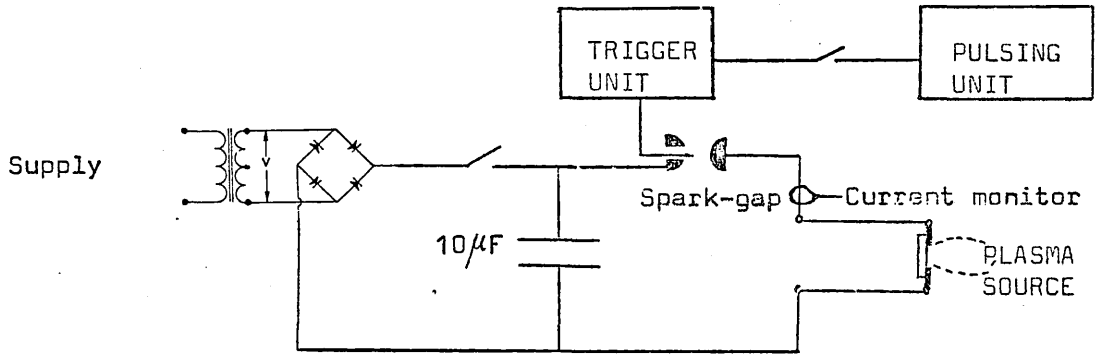

Fig. 3.2.1

Plasma inductance	20nH	Gun inductance	265nH	Total inductance	610nH ± 20nH
Plasma resistance	~ 8mΩ	Spark-gap resistance	~ 35mΩ	Total resistance	~ 45mΩ
Charging voltage	6kV	Peak current	18kA		

Fig. 3.2.2

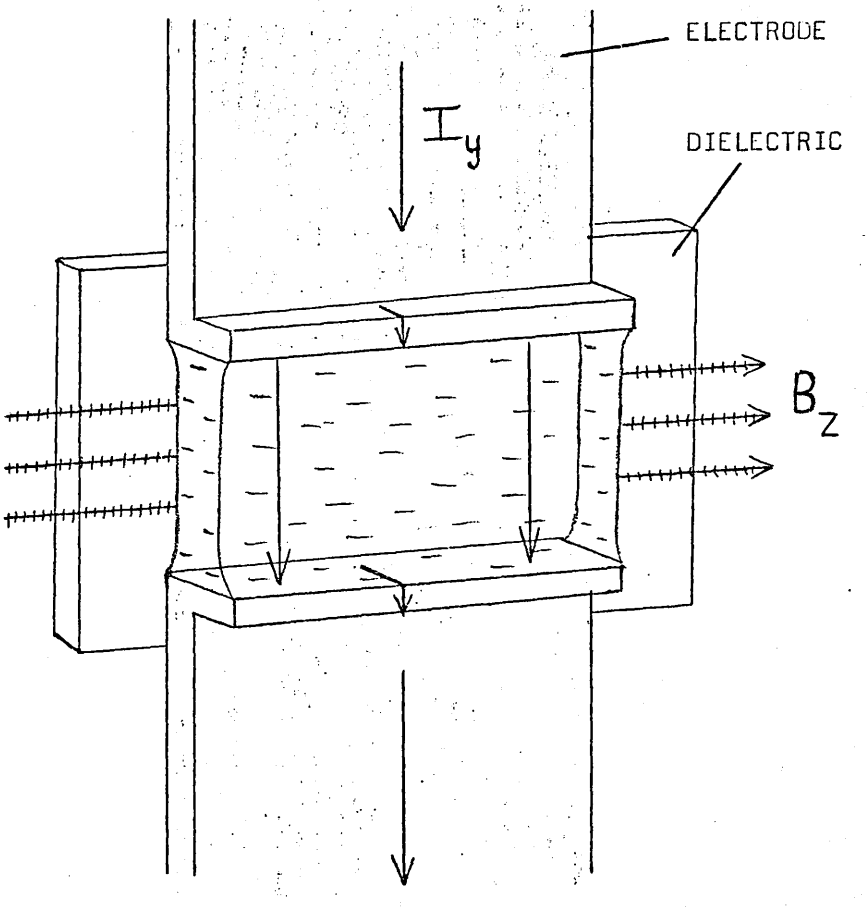
ELECTRODE
DIELECTRIC
I_y
B_z
DISCHARGE CURRENT
INDUCED MAGNETIC FIELD

geometry was chosen in order to obtain a quasi-planar current sheet. This simplifies the task of making spectroscopic measurements and the subsequent analysis. The electrode width b was made much larger than the separation d. This minimizes field-fringing effects over the greater part of the current sheet, allowing for a representation of the magnetic field lines as in fig. 3.2.2 . Unlike more conventional ablation-derived plasma accelerators, it will be noticed that the electrodes in this device do not extend in the direction of acceleration. Provided that variations in conductivity of the plasma are not too great across the electrode dimensions, and if the ablation in the gap region is uniform, a standing arc discharge is maintained with negligible distortion in the axial direction, and through which ionized propellant material is continuously accelerated. This mode of operation resembles that of a gas-fed magnetoplasmadynamic arc[1]. If the current sheet remains approximately planar, large Hall currents cannot flow and the axial thrust should be maintained.

The current waveform is governed mainly by the total circuit resistance and inductance. Variations of 100% in the plasma resistance and inductance have little effect on the current magnitude and no distortion of the sinusoidal waveform was observed during the total duration of the discharge. From measurements on this waveform, no overall variation of plasma inductance greater than the experimental uncertainty of $\pm$ 20 nH could be detected. This fact gives an indication of the overall current sheet stability, as the inductance per unit length (L') along the axis is approx. 30 nH/mm for an electrode separation of 3 mm . High-speed photographs of the discharge with an electrode gap of 3 mm (figs. 3.2.3 and 3.2.4) also show a high degree of axial thrust during most of the first half-cycle, the gas-dynamic expansion velocity being much smaller. Towards the end of the first half-cycle however, as with successive half-cycles, a deflection away from the anode was seen.

Steady uniform discharges were obtained with electrode gaps of between 2 mm and 12 mm and capacitor bank voltages between 5 kV and 7 kV . The anode suffered a slight loss in weight over several hundred shots (approximately

Fig. 3.2.3

P.T.F.E. PLASMA : HIGH SPEED PHOTOGRAPHS

VIEWING DIRECTION :

RESOLUTION---10nSEC.

DELAYS---μSEC.

SCALE----

0 3 9cm.

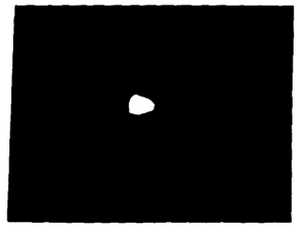

2μs.

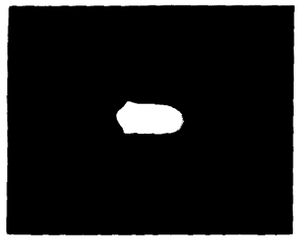

4.2μs.

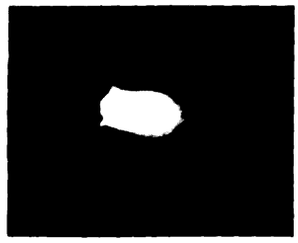

5.1μs.

6μs.

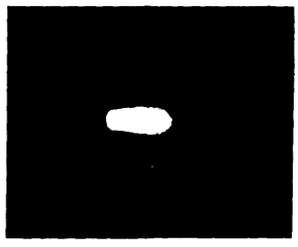

8.1μs.

Fig. 3.2.4

PTFE. PLASMA : HIGH SPEED PHOTOGRAPHS

VIEWING DIRECTION :

RESOLUTION---10nSEC.

DELAYS---μSEC.

SCALE----

0 3 9cm.

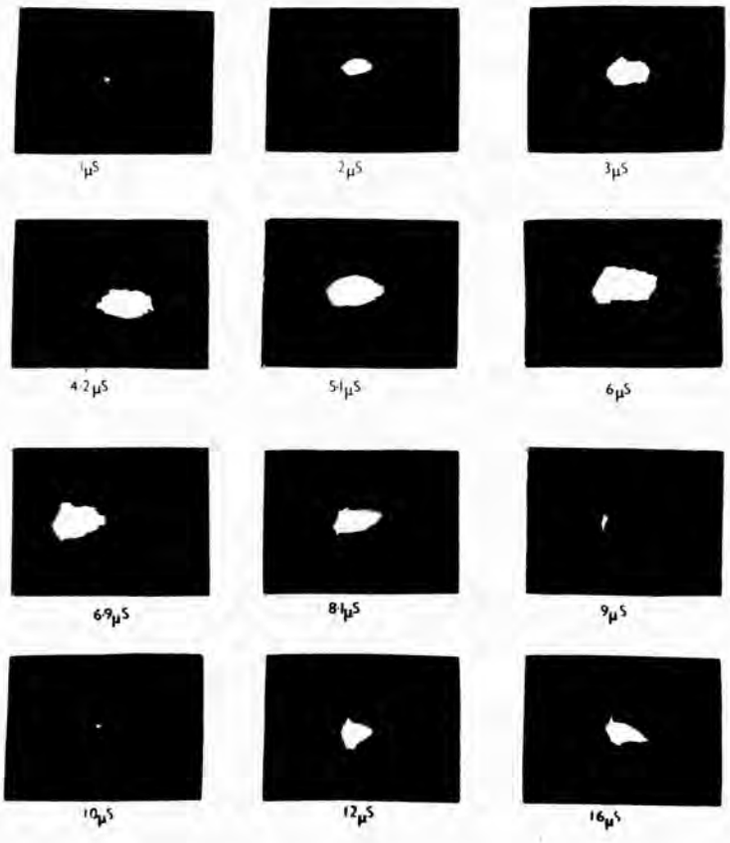

0.03% of the total plasma mass), whilst the cathode suffered hardly at all (less than 0.002% of the total plasma mass). This suggests a small ion current. When the system was operated with higher voltages and smaller electrode gaps, much more electrode material entered the plasma, and small luminous particles were observed being accelerated downstream of the device, having been sputtered from the cathode. With gaps greater than approx. 15 mm the operation became erratic and unpredictable.

Reference

1. Zh.D.Genchev, Proc. 3rd Int. Conf. Gas Discharges, IEE, London, 1974

3.3 The magnetic field and the uniformity of the current sheet

From the assumptions of section 3.2 the magnetic field can be considered linear in the z-direction behind the current sheet. Integrating Maxwell's $\nabla \times B$ equation with respect to distance x and neglecting the displacement current and the effects of any inhomogeneities in temperature or density in the arc,

$$B_z(0,t) = \mu_0 I(t)/b \qquad (3.3.1)$$

In this experiment $B_z(0)$ reached a peak value of approximately 1.7 Tesla, and is assumed to fall to zero across the thickness of the current sheet. The half-period of the discharge was $\sim 8\,\mu$sec.

Assuming a uniform plasma conductivity and provided that currents cannot flow beyond the front faces of the electrodes, the geometry of the system will constrain the driving field in the plasma to a depth of ~ 1 mm. If there is a sufficient flow of ablated material to maintain the uniformity in the conductivity, then a continuous steady current sheet will be set-up, provided that also the skin depth for penetration of the current is greater than the acceleration length l_a. l_a is equal to the thickness of the electrodes, i.e. 1 mm.

In the present geometry, from Maxwell equations,

$$\frac{\partial B_z}{\partial t} = -\frac{\partial E_y}{\partial x} \qquad (3.3.2)$$

$$J_y = \frac{-1}{\mu_0}\frac{\partial B_z}{\partial x} \qquad (3.3.3)$$

From the Ohm's law (equation (2.2.12), neglecting terms in $\frac{\partial J}{\partial t}$ and $\nabla_r P$ as these can be shown to be small, and assuming no Hall current flow,

$$J_y = \sigma (E_y - U_x B_z) \qquad (3.3.4)$$

From equations (3.3.2), (3.3.3) and (3.3.4),

$$\frac{\partial J}{\partial t} = (\mu_o \sigma)^{-1} \frac{\partial^2 J}{\partial x^2} - \frac{\partial (UJ)}{\partial x} \qquad (3.3.5)$$

Assuming that the current can be described by a function of the form $J = J_o \exp(i\omega t - x/\delta)$, the skin depth for the current in a stationary plasma is $\delta_o = (\mu_o \omega \sigma)^{-1/2}$. When the plasma has a velocity U_x, then if $4\omega/\mu_o \sigma U_x^2 < 1$ (which is the case here), $\delta = (\mu_o \sigma U_x)^{-1}$. R_m, the magnetic Reynolds number, is defined as the ratio of convective to diffusive transport, i.e. δ/δ_o, and is > 1 if $U_x > (\omega/\mu_o \sigma)^{1/2}$

In the present set of experiments $\omega \simeq 6.3 \times 10^4$ sec^{-1}, $\sigma(T_e = 3$ eV$) \simeq 2 \times 10^4$ mho m^{-1} and $\delta_o \simeq 25$ mm. At the time of peak current, when $U_x \simeq 10^6$cm sec^{-1}, $\delta \simeq 4$ mm.

Expanding equation (2.2.12) in Cartesian coordinates, and neglecting the $\partial J/\partial t$ terms,

$$E_y = U_x B_z + \eta J_y + J_x B_z/n_e e - \frac{1}{n_e e}\frac{\partial P_e}{\partial y}$$

$$E_x = U_y B_z + \eta J_x + J_y B_z/n_e e - \frac{1}{n_e e}\frac{\partial P_e}{\partial x}$$

$$E_z = \eta J_z - \frac{1}{n_e e}\frac{\partial P_e}{\partial z} \qquad (3.3.6)$$

The Hall parameter ψ will be found useful in the following discussion. For electrons or ions, ψ is defined as the ratio of the collision mean free times to the cyclotron orbit times, i.e. $\omega_e \tau_e$ and $\omega_i \tau_i$.

$$\omega_e = eB/m_e$$

$$\tau_e = m_e T_e^{3/2} \times 3.2 \times 10^4 / n_e e^2 \ln\Lambda = m_e \sigma / n_e e^2$$

with T_e in eV.

$$\psi_e = \psi = B\sigma/n_e e \quad \text{and} \quad \psi_i = \psi_e (m_e/m_i)^{1/2}$$

In these experiments $\psi \simeq 1$ and the conductivity is a tensor. However, $J_x = J_z = 0$ before the onset of any sheet instability and so, neglecting U_y and $\frac{\partial P_e}{\partial y}$, equations (3.3.6) become,

$$\begin{aligned} E_y &= \eta J_y + U_x B_z \\ E_x &= J_y B_z/n_e e - \frac{1}{n_e e}\frac{\partial P_e}{\partial x} \\ E_z &= -\frac{1}{n_e e}\frac{\partial P_e}{\partial z} \end{aligned} \qquad (3.3.7)$$

E_x is responsible for accelerating the ions and is established as a result of the J x B force acting on the electrons which separates them from the ions. Integrating equation (3.3.2) over x and using equation (3.3.7),

$$E_o = \frac{\partial}{\partial t}\int_0^x B\,dx + \eta J_y + U_x B_z$$

where E_o is the electric field at the gun terminals (x = 0). Across the electrode gap $V_o = E_o d$, and,

$$V_o(t) = L_p \frac{dI(t)}{dt} + R_p(t) I(t) + U_x B_z d \qquad (3.3.8)$$

During the discharge V_o was measured simultaneously with the current. The resistance of the electrodes was 10^{-3} Ohm. By analysing the waveforms, the total external circuit inductance was found and equation (3.3.8) was solved numerically for $R_p(t)$ using a fourth degree interpolation for the current derivative and assuming that the plasma inductance was constant.

Reference

1. L.Spitzer,'Physics of Fully Ionized Gases',Intersc.Pub.,N.York,1962

3.4 Acceleration Performance

From electrical and spectroscopic measurements of the temperature and density around the dielectric surface it was observed that the current sheet was free from large scale (~ 1 mm) instabilities during most of the first two discharge half-cycles. Effects due to spatially non-uniform ablation from the dielectric wall, evaporation of electrode material, or the growth of magnetohydrodynamic instabilities were therefore not important. Variations in density, temperature and conductivity, however, can substantially affect the growth of any non-uniformities and hence the efficiency of the acceleration. This problem will now be discussed.

From equations (2.2.11) and (2.2.12), neglecting the terms in $\partial J/\partial t$ and $\nabla_r P_e$ in comparison to the others,

$$J = \sigma E - \frac{\psi}{B}(J \times B) + \frac{\psi\psi_i}{B^2}(J \times B) \times B \qquad (3.4.1)$$

where $\psi_e \psi_i \simeq \psi_e^2 \sqrt{m_e/m_i}$

With Carbon or Fluorine ions the last term in equation (3.4.1) is small for $\psi \lesssim 10^2$. Such high values of ψ only occur when the magnetic field is high and the electron density is low, a combination unlikely in self-field devices. In the present case, for example, $\psi \sim 1$.

In the rectangular geometry, assuming a homogeneous plasma with an applied electric field E_y , equation (3.4.1) can be written as

$$J_y = \sigma E_y + \psi J_x \qquad (3.4.2)$$

$$J_x = \sigma E_x - \psi J_y \qquad (3.4.3)$$

σ is the electrical conductivity in the absence of a magnetic field. If an x-directional Hall current is allowed to flow, ψ defines its magnitude. If there is no closure for such a current however (as is the case for an ideal current sheet in this accelerator), the accelerating space charge field $E_x = \psi E_y$.

In the present set of experiments j_y is approximately constant from shot to shot as the external circuit components dominate the discharge. Variations in average conductivity therefore result only in changes in E_y and thus also the power input, without affecting the thrust force.

From equations (3.4.2) and (3.4.3),

$$J_y = \frac{\sigma}{1+\psi^2}\left(E_y + \psi E_x\right) \qquad (3.4.4)$$

$$J_x = \frac{\sigma}{1+\psi^2}\left(E_x - \psi E_y\right) \qquad (3.4.5)$$

These show that if a Hall current flows there is a reduction in the conductivity in the normal current direction with a corresponding decrease in efficiency.

Through a simple model the effect of non-uniformities in n_e or T_e can be assessed. A situation similar to that described by Rosa[1] is prescribed in which equal-thickness planes of alternately varying temperature or density exist either perpendicular or parallel to the normal current direction viz:

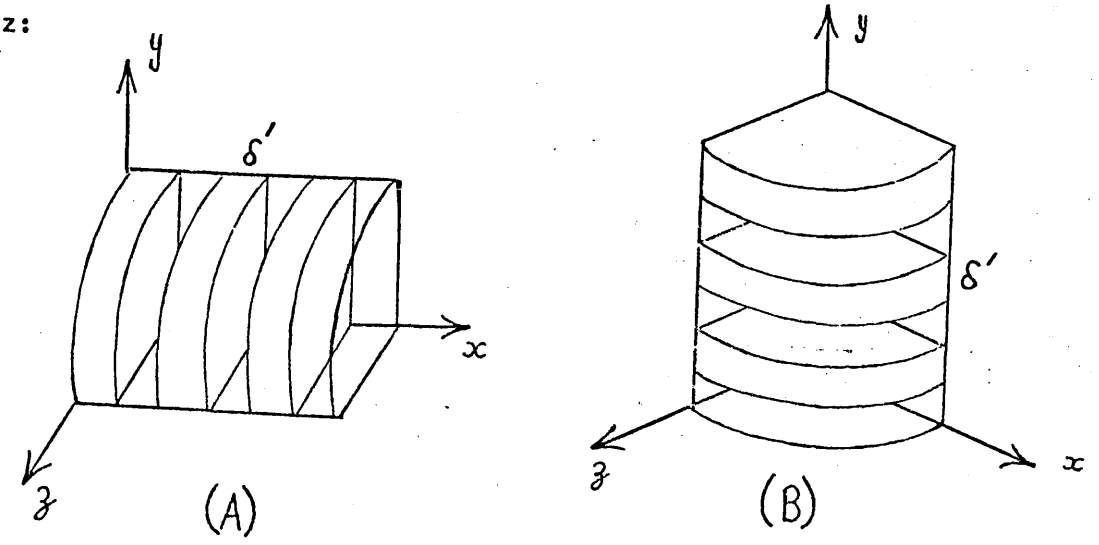

In case (A) J_y and E_x are functions of x whilst E_y and J_x are constant. Averaging Equations (3.4.2) and (3.4.3) over x,

$$\langle J_y \rangle_x = \langle \sigma \rangle_x E_y + \langle \psi \rangle_x J_x \tag{3.4.6}$$

$$J_x = \langle \sigma E_x \rangle_x - \langle \psi J_y \rangle_x \tag{3.4.7}$$

Re-arranging Equations (3.4.7), (3.4.2) and (3.4.3),

$$J_x = \frac{\langle \sigma \rangle_x \langle E_x \rangle_x}{C_x} - \frac{\langle \psi \rangle_x \langle J_y \rangle_x}{C_x} \tag{3.4.8}$$

where C_x is a homogeneity factor and = $\langle \sigma \rangle_x \left\langle \frac{1+\psi^2}{\sigma} \right\rangle_x - \langle \psi \rangle_x^2$

If the plasma is homogeneous $C_x = 1$.

In case (B) J_x and E_y are functions of y whilst J_y and E_x are constant. Averaging over y one obtains,

$$\langle J_x \rangle_y = \langle \sigma \rangle_y E_x - \langle \psi \rangle_y J_y \tag{3.4.9}$$

$$J_y = \frac{\langle \sigma \rangle_y \langle E_y \rangle_y}{C_y} + \frac{\langle \psi \rangle_y \langle J_x \rangle_y}{C_y} \tag{3.4.10}$$

where C_y is identical to C_x except that averages are made with respect to y.

For a highly ionized plasma with a classical electrical conductivity, σ is $\propto T_e^{3/2}$ and ψ is $\propto T_e^{3/2}/n_e$. The non-uniform distributions in cases (A) and (B) can be described by infinite Fourier series of the form,

(A) $$\left(\frac{Q_1+Q_2}{2}\right) + \frac{2}{\pi}(Q_1-Q_2) \sum_{n\ odd} \frac{1}{n} \sin \frac{n\pi}{\delta'} x$$

(B) $$\left(\frac{Q_1+Q_2}{2}\right) + \frac{2}{\pi}(Q_1-Q_2) \sum_{n\ odd} \frac{1}{n} \sin \frac{n\pi}{\delta'} y$$

where δ', the width of each channel, is less than the plasma dimension

and Q is some property of the plasma such as T_e , n_e , σ or ψ .
If only T_e varies such that $\sigma_1/\sigma_2 = k = \psi_1/\psi_2$ (i.e. $T_{e1}/T_{e2} = k^{2/3}$ with $k > 1$) then,

$$\langle\sigma\rangle = \sigma_1 (k+1)/2$$
$$\langle\psi\rangle = \psi_1 (k+1)/2$$
$$C = (k+1)^2/4k$$

If only n_e varies such that $\sigma_1/\sigma_2 = 1$ and $\psi_1/\psi_2 = k$ (i.e. $n_{e1}/n_{e2} = 1/k$),

$$\langle\sigma\rangle = \sigma_1$$
$$\langle\psi\rangle = \psi_1 (k+1)/2$$
$$C = 1 + (\psi(k-1)/2)^2$$

Curves of C for various values of ψ and k for these two situations are shown in fig. 3.4.1.

In case (A) if no Hall current can flow ($J_x = 0$), $\langle J_y\rangle_x$ is governed by the average conductivity $\langle\sigma\rangle_x$ which changes little with fluctuations in temperature, unless they are greater than $\sim 100\%$, and which does not vary with density. Therefore,

$$\langle J_y\rangle_x = \langle\sigma\rangle_x E_y$$

and the Joule power input per unit volume (P^*) is given by,

$$P_y^* = \langle J_y\rangle_x^2 / \langle\sigma\rangle_x$$

If a Hall current can flow across the whole normal current sheet, $\langle E_x\rangle_x = 0$ to a good approximation . Then $\langle J_y\rangle_x = C_x \langle\sigma\rangle_x E_y / (C_x + \langle\psi\rangle_x^2)$

and $P_y^* = \langle J_y\rangle_x^2 (C_x + \langle\psi\rangle_x^2) / \langle\sigma\rangle_x C_x$

In this latter situation there would be no space-charge field and hence no acceleration of the plasma. Normally, however, Hall currents which may flow as a result of distortion of the current sheet, would not necessarily reduce $\langle E_x\rangle_x$ to zero over the whole of the sheet.

Fig. 3.4.1

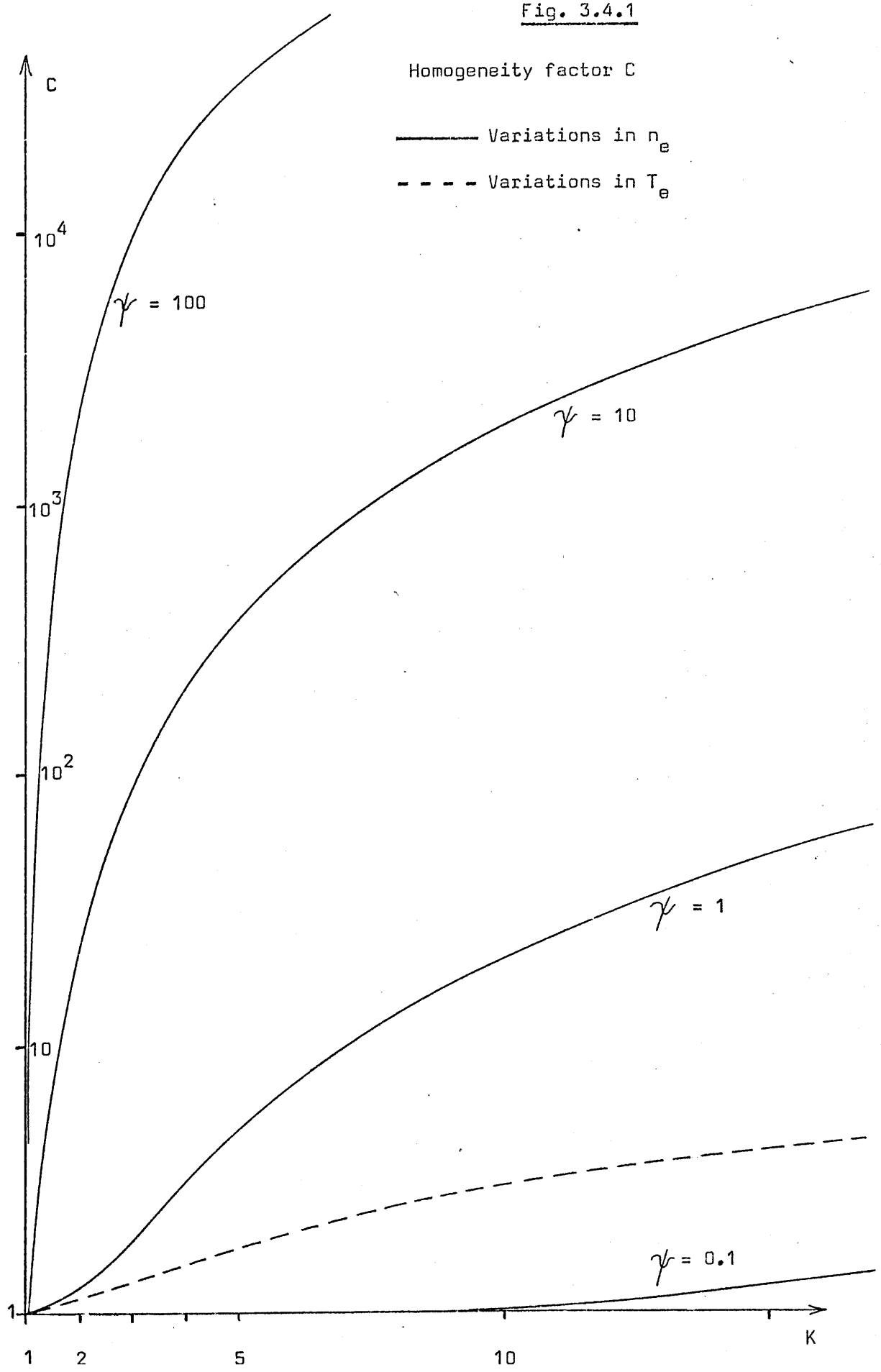
Homogeneity factor C
Variations in n_e
Variations in T_e
C
10^4
10^3
10^2
10
1
ψ = 100
ψ = 10
ψ = 1
ψ = 0.1
1
2
5
10
K

$\langle E_x \rangle_x$ can be put = $\frac{\langle \psi \rangle_x E_y}{\beta}$ where β = 1 signifies no Hall current flow across the sheet and $\beta = \infty$ signifies complete Hall current flow.

Then, $$\langle J_y \rangle_x = \frac{\langle \sigma \rangle_x E_y}{C_x + \langle \psi \rangle_x^2} \left(C_x + \frac{\langle \psi \rangle_x^2}{\beta} \right)$$

and $$P_y^* = \frac{\langle J_y \rangle_x^2}{\langle \sigma \rangle_x} \cdot \left(\frac{C_x + \langle \psi \rangle_x^2}{C_x + \langle \psi \rangle_x^2 / \beta} \right) = A^* \frac{\langle J_y \rangle_x^2}{\langle \sigma \rangle_x}$$

If $\beta \gg 1$, $$P_x^* \simeq \frac{\langle J_y \rangle_x^2 \langle \psi \rangle_x^2}{\langle \sigma \rangle_x \beta}$$

Acceleration of the plasma can take place whilst β is small. Curves of $A^*(T_e)$ and $A^*(n_e)$ are shown in fig. 3.4.2

In case (B) in the absence of a Hall current,

$$J_y = \frac{\langle \sigma \rangle_y \langle E_y \rangle_y}{C_y} \quad , \quad P_y^* = J_y^2 C_y / \langle \sigma \rangle_y$$

thus inhomogeneities increase the power input above that governed by the average conductivity by the factor C_y . If only T_e varies inhomogeneities must be greater than 100% if the power input is to increase by more than 25% . If only n_e varies it is desirable that ψ be as low as possible (i.e. $\ll 10$) as otherwise even inhomogeneities $\sim$ 20% could more than double the power input without increasing the resultant thrust.

In the case that some Hall current can flow, i.e. $E_x = \frac{\langle \psi \rangle_y \langle E_y \rangle_y}{C_y \beta}$,

$$J_y = \langle \sigma \rangle_y \langle E_y \rangle_y \left(\frac{1 + \langle \psi \rangle_y^2 / C_y \beta}{C_y + \langle \psi \rangle_y^2} \right)$$

and $$P_y^* = \frac{J_y^2}{\langle \sigma \rangle_y} \cdot \left(\frac{C_y + \langle \psi \rangle_y^2}{1 + \langle \psi \rangle_y^2 / C_y \beta} \right) = B^* \frac{J_y^2}{\langle \sigma \rangle_y}$$

$B^*(T_e)$ and $B^*(n_e)$ are shown in figs. 3.4.3 and 3.4.4.

In the present experiments $\psi \sim 1$ and inhomogeneities are unlikely to significantly affect efficiency. However, variations of n_e along y when there is a uniform pressure profile would give rise to sheet distortion which in turn could cause a Hall current to flow.

Fig. 3.4.2

The plasma inhomogeneity factor A^* as a function of K and ψ .

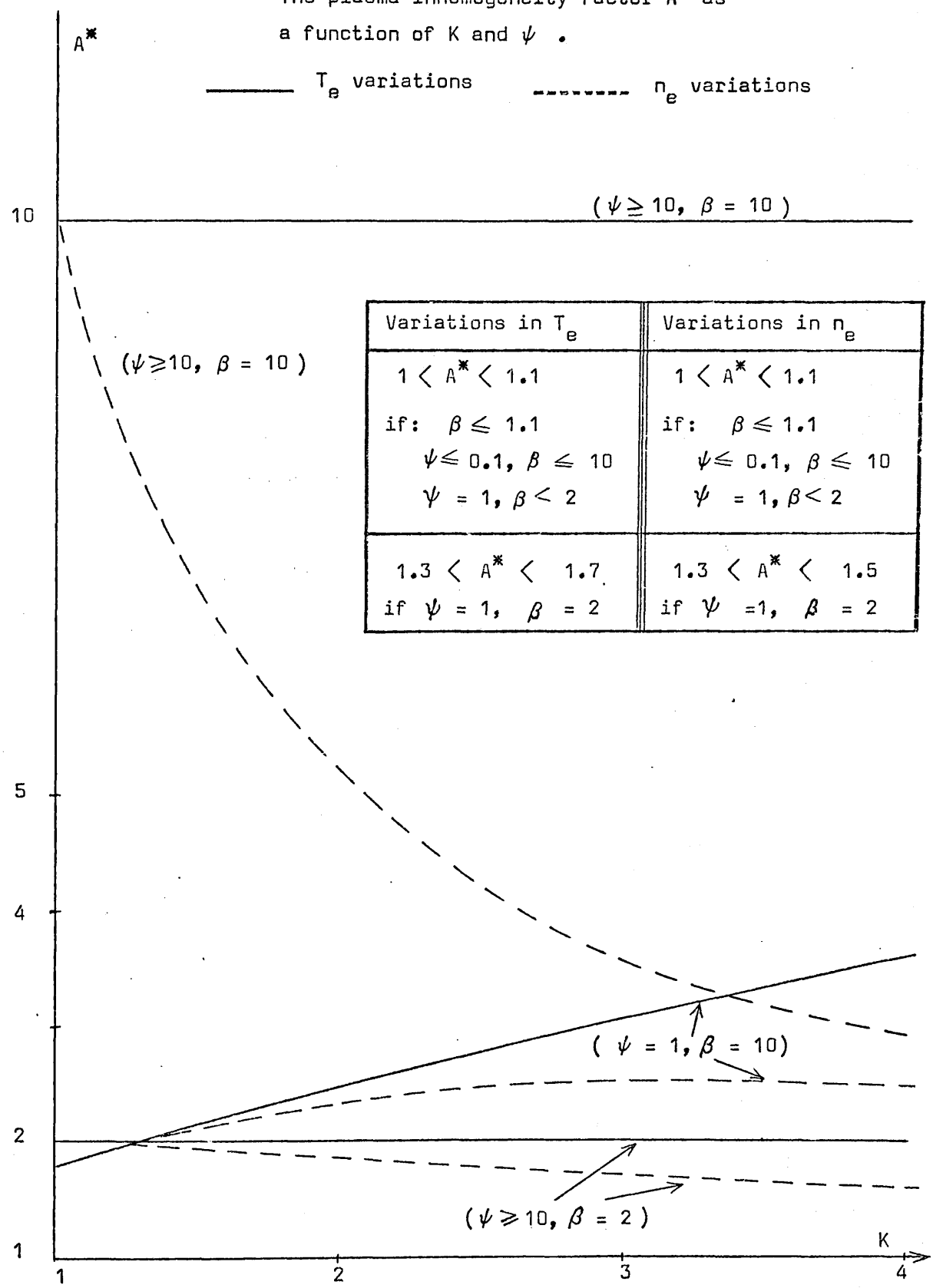

Variations in T_e	Variations in n_e
$1 < A^* < 1.1$ if: $\beta \leq 1.1$ $\psi \leq 0.1$, $\beta \leq 10$ $\psi = 1$, $\beta < 2$	$1 < A^* < 1.1$ if: $\beta \leq 1.1$ $\psi \leq 0.1$, $\beta \leq 10$ $\psi = 1$, $\beta < 2$
$1.3 < A^* < 1.7$ if $\psi = 1$, $\beta = 2$	$1.3 < A^* < 1.5$ if $\psi = 1$, $\beta = 2$

Fig. 3.4.3

B^* as a function of ψ and K , for variations in T_e

$1 < B^* < 1.5$ if ; $\psi \leq 0.1$, $\beta \leq 10$
$\psi = 1$, $\beta < 2$
$\beta \leq 1.1$

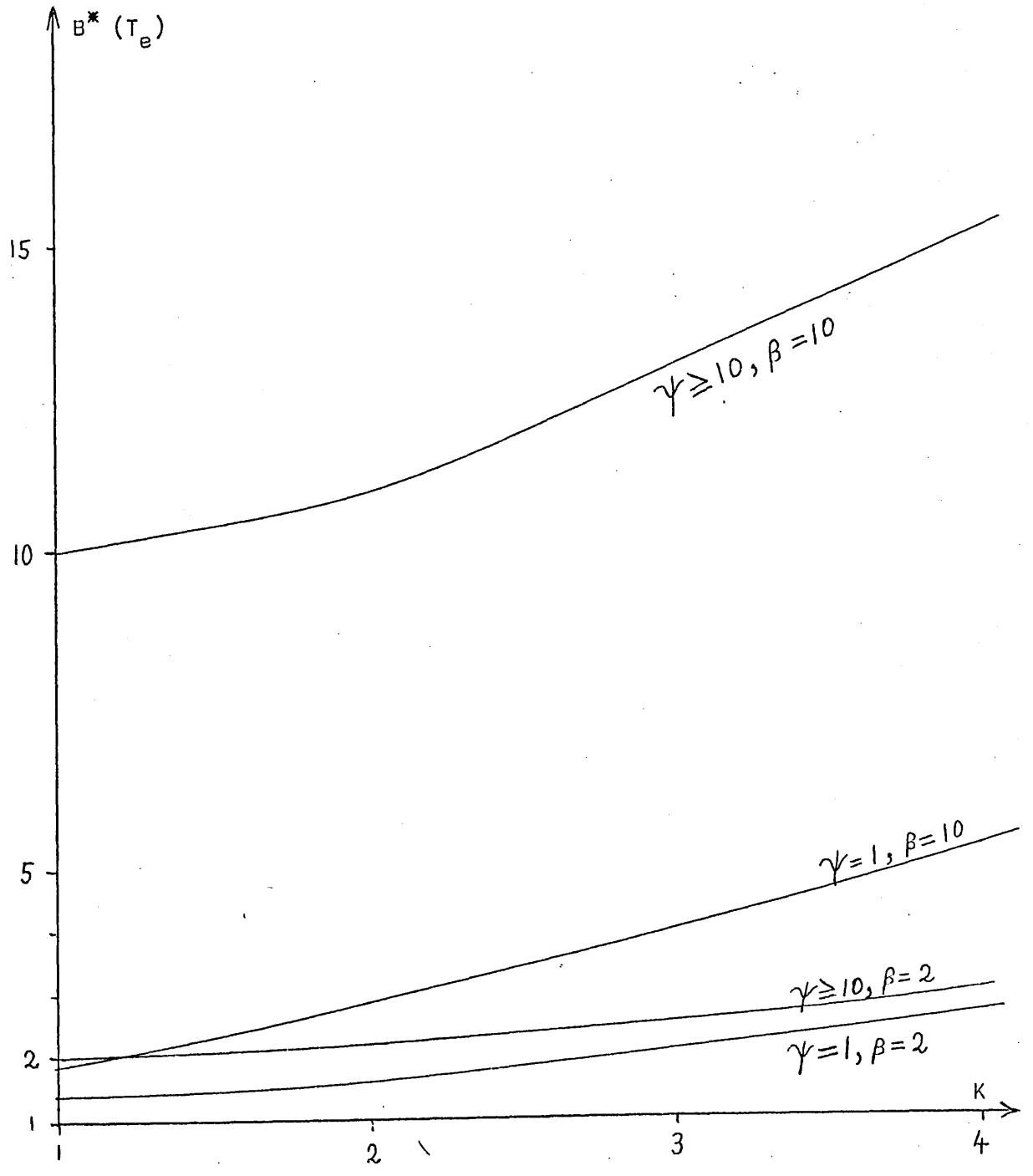

Fig. 3.4.4

B^* as a function of ψ and K , for variations in n_e

$1 < B^* < 1.1$ if $\psi \leq 0.1$, $\beta \leq 10$

$B^* = \beta C$ if $\psi > 10$

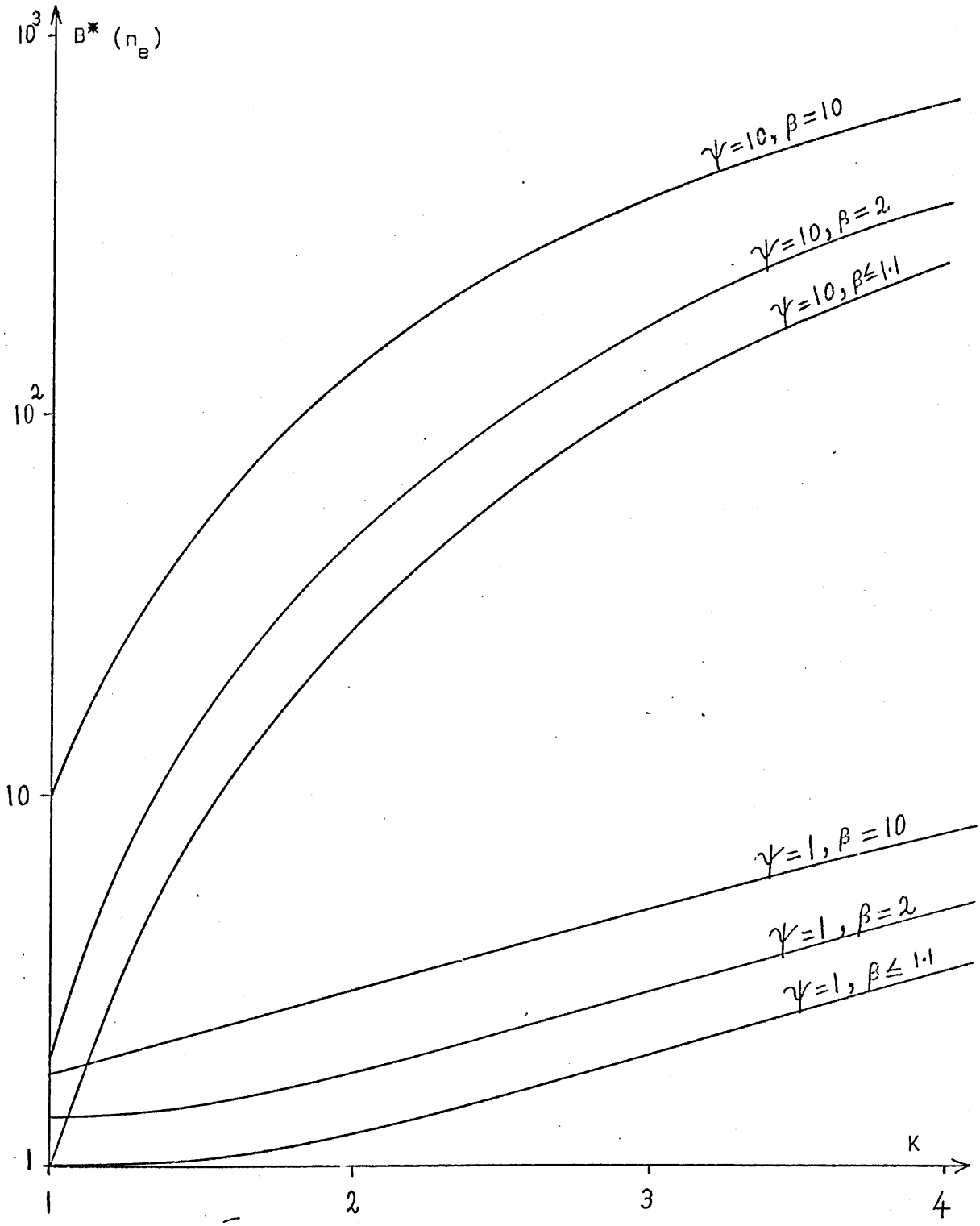

Although affecting the efficiency of the device, inhomogeneities as in case (A) do not directly lead to sheet distortion and Hall currents. These therefore become more important in the presence of effects caused by MHD instabilities and density variations of the type described in situation (B).

Efficiency

An efficiency $\mathcal{E}$ can be defined as the ratio of thrust power to applied power i.e.

$$\mathcal{E} = j_y u_x B / j_y E_{app}$$

where $E_{app} = j_y/\langle\sigma\rangle + u_x B$

If the current sheet is uniform,

$$\mathcal{E} = \mathcal{E}_0 = \left(1 + \frac{j_y}{\langle\sigma\rangle u_x B}\right)^{-1}$$

When the temperature is high $j_y/\langle\sigma\rangle \to 0$ and $\mathcal{E}_0 \to 1$

If the temperature is low,

$$\mathcal{E}_0 \to \sim \frac{\langle\sigma\rangle u_x B}{j_y} \ll 1$$

If the current sheet is not uniform,

$$\mathcal{E} = \mathcal{E}_0\left(1 + \frac{\mathcal{E}_0 j_y (A^*-1)}{\langle\sigma\rangle u_x B}\right)^{-1} \text{ or } \mathcal{E}_0\left(1 + \frac{\mathcal{E}_0 j_y (B^*-1)}{\langle\sigma\rangle u_x B}\right)^{-1}$$

depending upon the type of inhomogeneity. At high temperatures $j_y/\langle\sigma\rangle \to 0$ and $\mathcal{E} \to 1$ unless A^* or B^* are very high. If the temperature is low ,

$$\mathcal{E} \to \mathcal{E}_0/A^* \text{ or } \mathcal{E}_0/B^*$$

In this device, at the time of peak current with PTFE as the dielectric, $\mathcal{E}_0 \simeq 0.17$. If $A^* = 2$, $\mathcal{E} = 0.089$. Thus for a homogeneous plasma current front, 17% of the input power is converted to thrust energy. A plot of $\mathcal{E}$ as a function of A^* or B^* for various values of $\mathcal{E}_0$ is shown in fig. 3.4.5.

Reference

1. R.J.Rosa, Phys.Fluids, 5 , p.1081 , 1962

Fig. 3.4.5

Values of $\mathcal{E}$ for various values of $\mathcal{E}_o$ and A^*

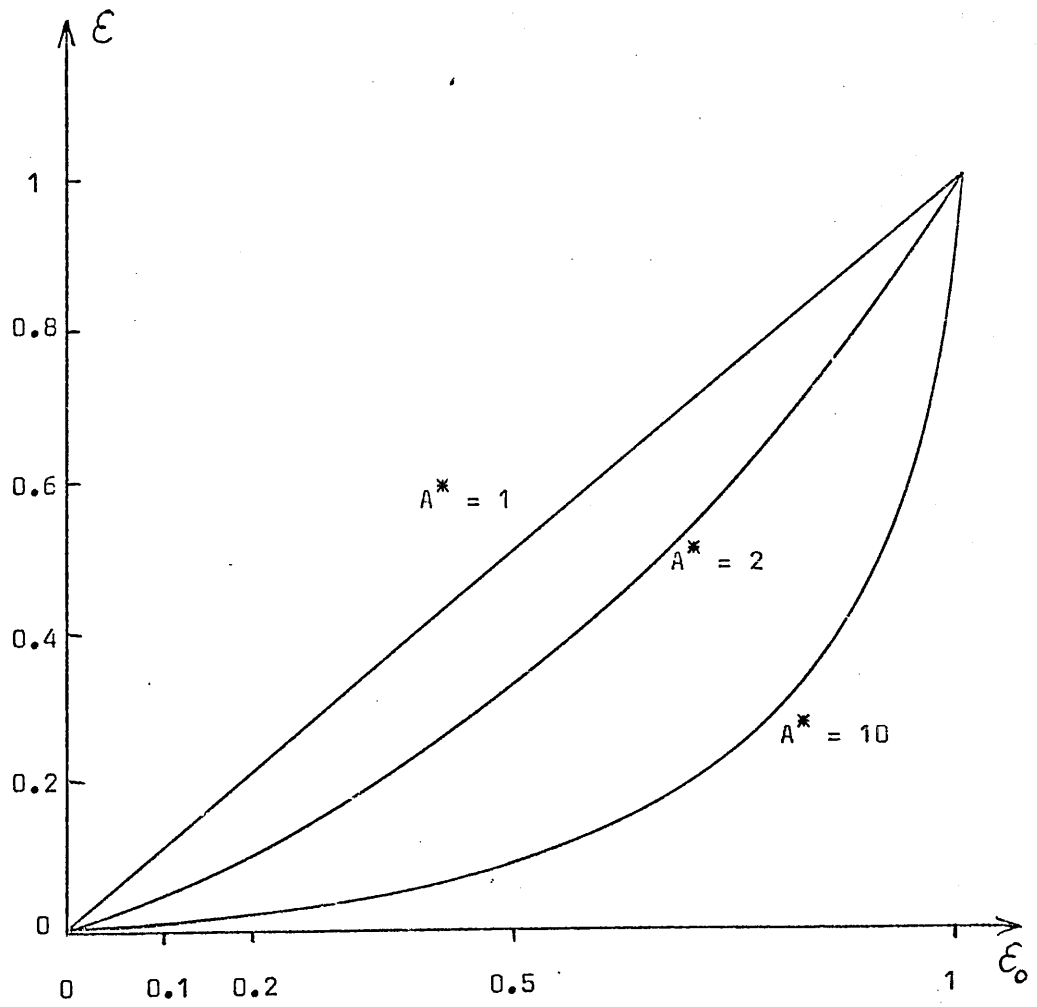

3.5 Current sheet stability

Within the current sheet, if there is any shear in the Hall field as a result of deformations or variations in conductivity, then Hall currents can flow, forming eddies on closure[1]. The vector addition of these Hall currents with the normal current component defines the resultant sheet structure at each point. This effect depends upon the magnitude of ψ and any resultant thrust depends upon the extent to which there is no closure for currents in the direction perpendicular to the magnetic field. Averaging over a finite portion of the current sheet it is only those eddies which close within the electrodes which will define a Hall current that adds to the normal current component. Defining R_o as the ratio of $\left|\langle J_x\rangle/\langle J_y\rangle\right|$ at a point then if $R_o \simeq 1$ the presence of Hall currents can serve to accentuate or reduce local deformations, depending upon the direction of the shear. If $R_o \gg 1$ disruption of the sheet can occur as the sideways thrust would be large whilst, if $R_o \ll 1$, deformations will not alter during the acceleration. Values of R_o calculated using the results of section 3.4 are shown in figs. 3.5.1 and 3.5.2 for various types of inhomogeneity. These show that in order to easily maintain $R_o \lesssim 1$, ψ should be $\lesssim 1$.

Some simple types of sheet deformation are shown below:

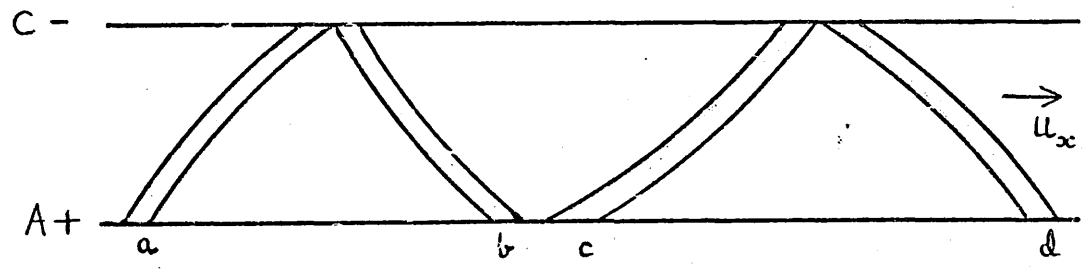

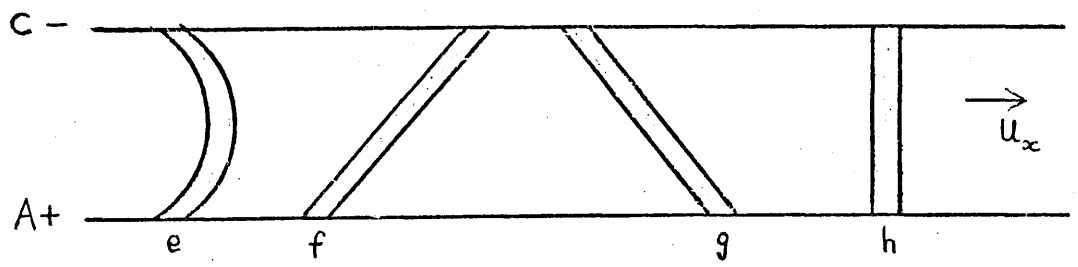

Fig. 3.5.1

Values of R_o for variation in temperature

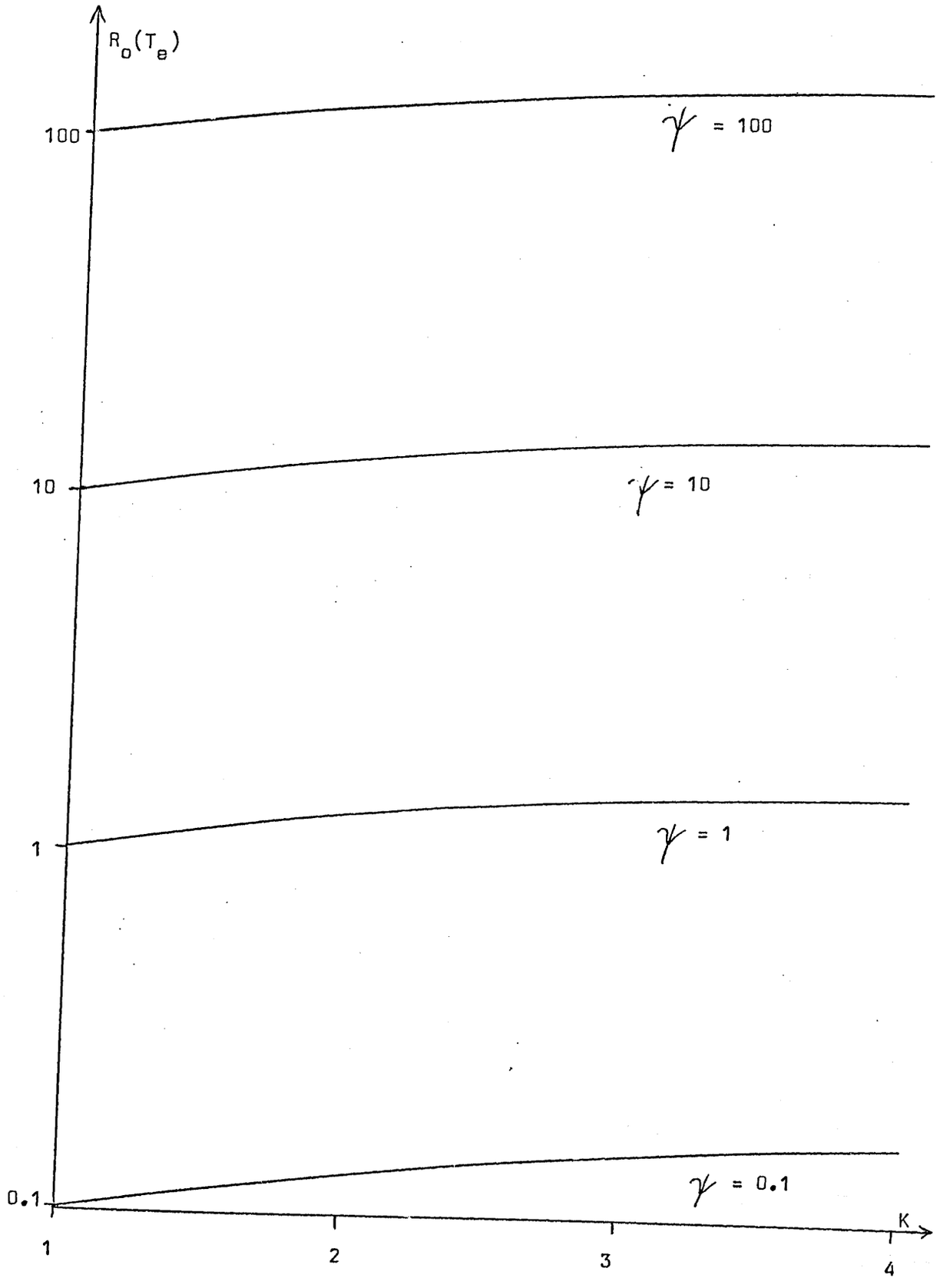

Fig. 3.5.2

Values of R_o for variations in density

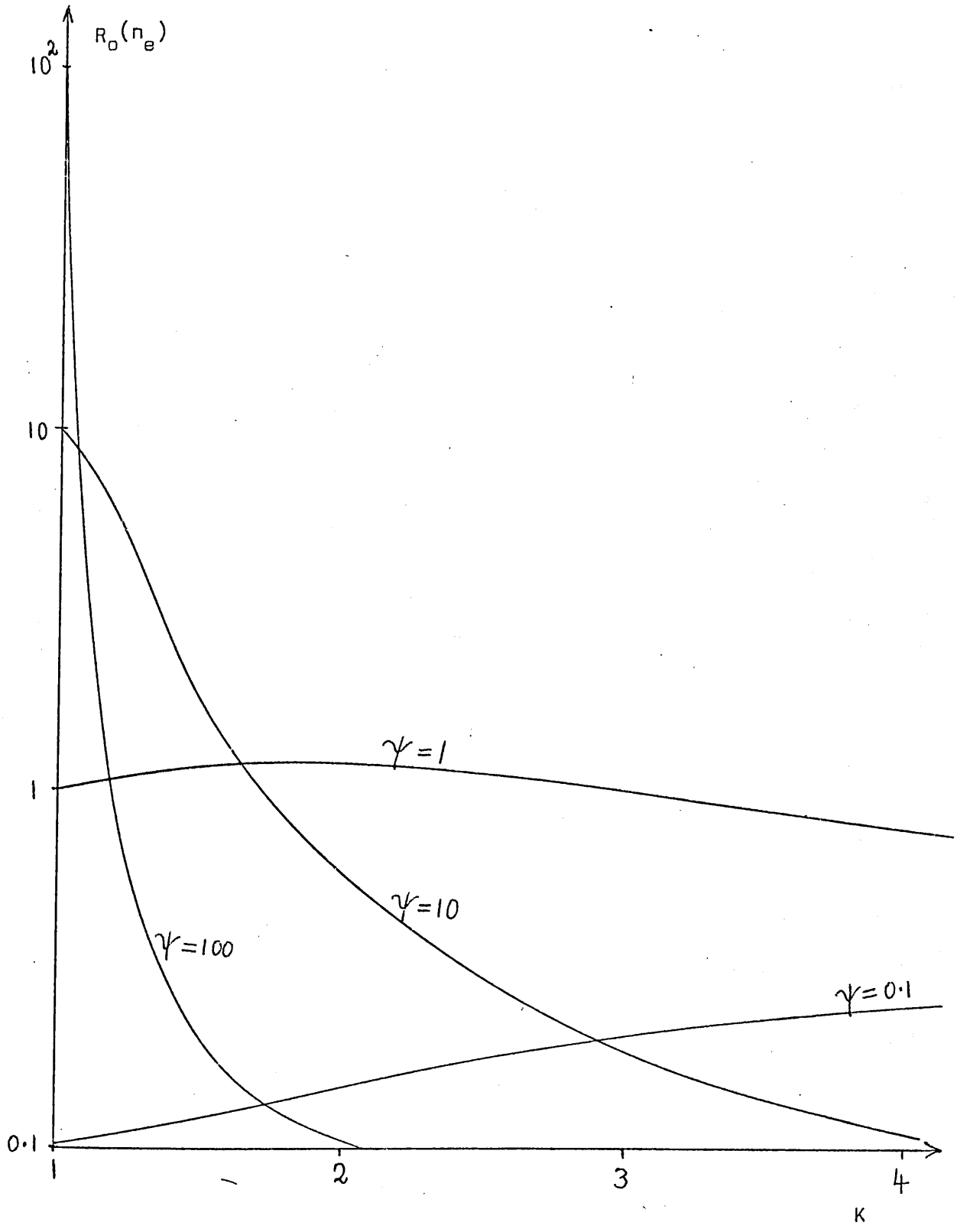

When $R_o \simeq 1$, forward sloping sheets such as a), c) and e) will be further distorted. Backward sloping structures such as b), d) and e) will tend to be straightened whilst, for profiles f), g) and h), there is no shear in the Hall field, except perhaps near the ends, and so no Hall current flows. Sputtering from the cathode would introduce heavy ions into the plasma which would slow down the current sheet locally. The slope formed in this case is forward and a sizeable Hall current would amplify the distortion. There would be a component of non-axial thrust arising from the Hall flow. Experimentally, lateral displacements have been observed, but only at the end of each half-cycle. This observation can be explained by the fact that sputtering was negligible during the greater part of the discharge and that ψ was > 1 only at the end of each half-cycle.

The high-speed photographs of the plasma (Figs. 3.2.3 and 3.2.4) showed that the current sheet and plasma velocity structure remained stable for the greater part of the first few discharge cycles. In chapter 6 the results of a detailed spectral analysis also show that the temperature and density vary little across the current carrying region. As, however, inhomogeneities in this region could produce a non-axial thrust, some mechanisms which could lead to variations within the current sheet are considered.

MHD Rayleigh-Taylor Instabilities

These can occur at a plasma surface when the magnetic acceleration acts in the direction normal to that surface. This situation is similar to the hydrodynamic instability described by Taylor[2] and has been observed in plasmas[3,4].

Assuming that there is an initial displacement of the plasma surface in the x-direction of the form $A_o \sin(2\pi x/\lambda)$, and an acceleration $\underline{a}$ acts across the boundary of that surface where the density on either side is ρ_1 or ρ_2, the displacement will develop in time according to[2],

$$A = A_o \, e^{-\left(\left\{\frac{\rho_2-\rho_1}{\rho_2+\rho_1}\right\} \underline{a}\, 2\pi/\lambda\right)^{1/2} t} \qquad (3.5.1)$$

When the density gradient across the surface of interaction is negative in the direction of acceleration, where ρ_2 is the density of the current carrying plasma region, the disturbances will be attenuated. This situation is analogous to that of a light fluid supported against gravity by a heavy fluid. This will be the case in this device up to the time of the peak ablation rate. After this time the density gradient becomes positive and the disturbances will grow. To have any effect, however, in view of the fact that the source operates as a steady arc, the growth time t_g must be much less than the acceleration time along the electrodes. It is evident from equation (3.5.1) that the smaller the wavelength of the disturbance the faster it grows. Resistive diffusion and viscosity will damp out the smaller wavelength disturbances so that the most serious growth mode is the smallest wavelength wave which can still exist (wavelength λ_{min}).

In this experiment it can be shown that resistive diffusion is the most important damping mechanism. The fastest growth rate permissible is that for a disturbance for which t_g is just equal to the diffusion time t_d across a distance equal to its wavelength. In the most serious case ($\rho_1 = 0$), from equation (3.5.1),

$$t_g = \left(\lambda_{min}/2\pi\underline{a}\right)^{1/2} \qquad (3.5.2)$$

From equation (3.3.5), assuming $B = B_o \exp(i\omega t - x/\lambda)$,

$$\lambda^2 = \frac{1}{\mu_o \omega \sigma} = \frac{t_d}{\mu_o \sigma} \qquad (3.5.3)$$

and therefore,

$$\lambda_{min} = \left(2\mu_o^2 \sigma^2 \pi \underline{a}\right)^{-1/3} \qquad (3.5.6)$$

Relating $\underline{a}$ to the current and the mass of the plasma between the electrodes, and using the measured value for σ of $\sim 2\times10^4$ mho/m ,

$$\lambda_{min} \simeq 10^{5} \left(M/I^{2}\right)^{1/3} \text{ mm.}$$

λ_{min} is $\lesssim$ 1mm and the growth times are $\gg 10^{-7}$ sec., the acceleration time. Thus, in view of the fact that $\rho_1 \neq 0$, Rayleigh-Taylor instabilities will not be important unless the temperature or acceleration are much larger.

Non-uniform Ablation

If there are inhomogeneities in the plasma in front of the solid, the resulting ablation may be affected. Consider first, variations in T_e or n_e in the direction perpendicular to the current.

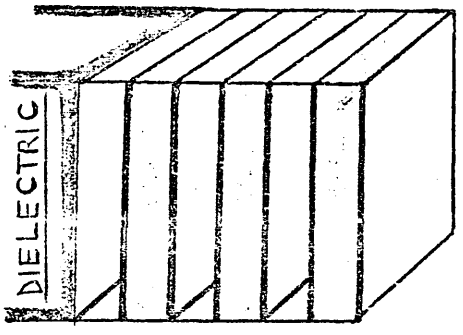

It will be shown in chapter 4 that the main radiant energy flux to the solid is from optically thick resonance lines of Carbon and Fluorine ions. Of the layers nearest to the solid, that which has the greatest emissivity will absorb radiation from layers further away, so shielding the solid from the effects of inhomogeneities further out. Because the line widths depend upon density and may therefor vary between successive layers, the uniform surface irradiation may come from more than one layer, but the overall flux should not depend on the detailed nature of the variations such as would be the case if the emission were optically thin.
This type of non-uniformity in the plasma is very likely to occur as the current varies in time and mixing within the arc may take place as the driving force varies.

Now consider inhomogeneities that are parallel to the dielectric surface :

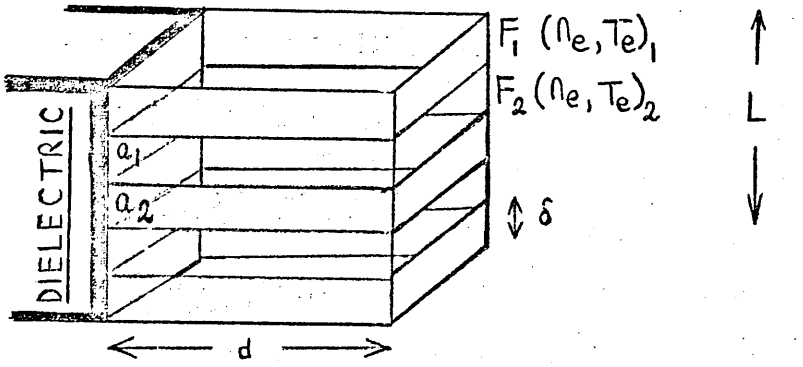

This type of variation could be caused by local hot spots on the solid surface. If the variations are in n_e only, the wings of the resonance lines will be different in each region. If $F_1 > F_2$ then, approximately, all points a_1 lying underneath an unshaded portion receive flux over solid angle from the extra increment of flux from the sides of the shaded portions in the same way that all points a_2 underneath the shaded regions do. Inhomogeneities in this case must not be geometrically severe, i.e. - as d is of the order 1 cm and L is $\sim$ 3 mm, δ /L must be no less than 1/2 If the variations are in T_e only, some regions will greatly dominate in intensity. If $F_1 > F_2$ the unshaded region will absorb the radiation from the shaded region and points a_1 and a_2 will receive different fluxes. If this difference is not too severe (20% variation in T_e can cause a 100% change in the emissivity), more propellant will be ablated locally where the flux is highest which will tend to cause a reduction in that flux. In this way a variable flux profile will be smoothed out. It is unlikely that inhomogeneities could be severe even in the first instance because, if the temperature variation were large, there would be a large difference between the line profiles and virtually no absorption of them between the layers. Thus again it is seen that the ablation and thrust are likely to be uniform when the plasmas are collision dominated, like those produced here, and when saturated radiant emission is the dominant energy loss mechanism.

Micro-instabilities

The development of current driven microscopic oscillations in a plane current sheet with a transverse magnetic field has been discussed by Aref'ev[5] and Sagdeev[6]. Turbulent oscillations of the electrons or ions can be excited by a fraction of the electron distribution if the current drift velocity v_d is greater than the threshold velocity for the particular type of instability. These authors derive the dispersion equations for the oscillations and show that the fastest growth rate γ_m occurs for the smallest wavelength disturbance. For cases where $T_e \gtrsim T_i$ ion-acoustic oscillations develope with the unstable wavelengths in the range r_{Le} to c/ω_{ce} and are excited if $v_d/v_{Te} > (m_e/m_i)^{1/2}$. The fastest growth rate occurs when $\lambda = r_{Le}$ and is equal to $(\omega_{ce}\omega_{ci})^{1/2}$.
If $T_i > T_e$, electron-acoustic oscillations develope if also v_d/v_{Ti} is $> (m_e/m_i)^{1/4}$ and γ_m is also $(\omega_{ce}\omega_{ci})^{1/2}$.

If two ion species in the plasma have different velocities (equivalent temperatures T_{i1} and T_{i2}), then ion-ion instabilities[7] will grow if v_{i1}/v_{i2} is greater than $(n_{i1}/n_{i2})^{1/2}$, where v_{i1} is the velocity of the light ions. These velocities are given to the ions through the polarization sheath in the current sheet and the turbulent friction acts on the light ions, slowing them down and speeding the heavy ions up.

As a result of scattering on the noise fluctuations, electrons experience a turbulent frictional force in addition to the Coulomb friction. The effect of this is to cause a decrease in the electrical conductivity and an increase in the plasma thermal energy. For an accelerator this would mean a loss of efficiency. As a result of this friction there is some equipartition of ion and electron temperatures until the electron temperature is reached when the instabilities are no longer excited.
Rewriting equation (2.2.12),

$$\frac{m_e}{n_e e^2}\frac{\partial \underline{j}}{\partial t} = \underline{E} + \underline{u}\times\underline{B} - \frac{\underline{j}\times\underline{B}}{n_e e} + \frac{\nabla_r P_e}{n_e e} - j(\gamma+\gamma^*)$$

where $\eta^* \simeq m_e \gamma_m / n_e e^2$

The ratio of turbulent to classical resistivity is approximately γ_m / ν_{ei} or $\sim (\omega_{ce}\omega_{ci})^{1/2}\tau_{ei}$ which, in the present case, is $\simeq 10^{-4}$.

As would be expected therefore, the value of η derived from the current and voltage waveforms agreed with the classical value using the temperature derived spectroscopically.

η^*/η is proportional to $\frac{B\, T_e^{3/2}}{n_e}$ and thus conditions would have to alter considerably before η^* was important.

References

1. W.H.Bostick, Phys.Fluids, 6, p.1598, 1963

2. G.I.Taylor, Proc.Roy.Soc., A201, p.192, 1950

3. D.J.Albares,N.A.Krall,C.L.Oxley, Phys.Fluids, 4, p.1031, 1961

4. T.S.Green,G.B.F.Niblett, Nucl.Fusion, 1, p.42, 1960

5. V.I.Aref'ev, Sov.Phys.Tech.Phys., 14, p.1487, 1970

6. R.Z.Sagdeev, Sov.Phys.Tech.Phys., 6 , p.867 , 1962

7. V.I.Aref'ev, Sov.Phys.Tech.Phys., 17, p.1829, 1973

Chapter Four

The spectroscopy of dense non-hydrogenic plasmas

4.1 Introduction

In this chapter the steady state equilibrium distributions in the population of bound states of ions present in dense non-thermal Carbon and Fluorine plasmas are derived. Each type of ion has a fundamentally unique electronic structure and thus no single equilibrium model will be applicable for them all. From a knowledge of these distributions, radiation intensities can be calculated together with the total populations of each ion within a plasma. Ionization and recombination coefficients for a wide range of plasma parameters are also derived.

Consider the mechanisms controlling the population of a level p of an ion stage i of an ion species k in a plasma, neglecting at this stage any re-absorption of radiation. At some temperature T_e let X(k,i,p,q) and X(k,i,q,p) represent the rate coefficients for collisional excitation and de-excitation, i.e. the process ;

$$\text{ion}(k,i,p) + e \underset{X}{\overset{X}{\rightleftharpoons}} \text{ion}(k,i,q) + e$$

As was shown in chapter 2, in most plasmas, due to the short electron self-collision times, a Maxwellian velocity distribution for the free electrons can be assumed. As soon as the degree of ionization becomes greater than a few percent, inelastic collisions can be assumed to be caused predominantly by electrons impacting with ions.

Letting S(k,i,p) and β(k,i+1,p) represent the rate coefficients for collisional ionization and three-body recombination respectively, the transitions to and from the ground states of the higher ion stage are the most significant[1], e.g.,

$$\text{ion}(k,i,p) + e \underset{\beta}{\overset{S}{\rightleftharpoons}} \text{ion}(k,i+1,g) + e + e$$

α (k,i+1,p) represents the rate coefficient for radiative recombination into level p of an ion i where,

$$\text{ion}(k,i+1,g) + e \xrightarrow{\alpha} \text{ion}(k,i,p) + h\gamma$$

and A(k,i,p,q) represents spontaneous radiative decay i.e. ;

$$\text{ion}(k,i,p) \xrightarrow{A} \text{ion}(k,i,q) + h\gamma$$

Neglecting photo-excitation and photo-ionization, the rate of change of the population of level p can be written as,

$$\frac{d\,n(k,i,p)}{dt} = -n(k,i,p)\left[n_e S(k,i,p) + n_e \sum_{q \neq p} X(k,i,p,q) + \sum_{q<p} A(k,i,p,q)\right]$$

$$+ n_e \sum_{q \neq p} n(k,i,q)X(k,i,q,p) + \sum_{q>p} n(k,i,q)A(k,i,q,p)$$

$$+ n_e n(k,i+1,g)\left[n_e \beta(k,i+1,p) + \alpha(k,i+1,p)\right] \quad \ldots\ldots(4.1.1)$$

It can be readily shown that the relaxation times for excited levels to reach a quasi-steady state are much smaller (less than or equal to the inverse radiative decay rates) than those for ground states. Thus excited states can be regarded as relaxing instantaneously compared to the ground states, often even during the transient stages of an ionizing or decaying process. Thus in equation (4.1.1),

$$\sum_{p>1} \frac{d\,n(k,i,p)}{dt} = 0 \qquad (4.1.2)$$

The resulting infinite set of simultaneous equations can be solved to give n(p) in terms of n(g), n_e and T_e. Bates et.al.[2] and McWhirter and Hearn[3] found solutions for the first twenty levels of hydrogenic ions by suitably truncating the set, after noting that, as the principal quantum number p increases, n(p) approaches the Saha-Boltzmann value. The effect of upper levels upon the population density of lower levels is then easily accounted for.

The equations defined by (4.1.1) and (4.1.2) are linear in n(g) and their solutions can be expressed in the form[2],

$$\frac{n(k,i,p)}{n_E(k,i,p)} = r_o(k,i,p) + r_1(k,i,p)\,\frac{n(k,i,g)}{n_E(k,i,g)} \qquad (4.1.3)$$

$$\frac{d\,n(k,i,g)}{dt} = \alpha_{cr}(k,i+1)n_e n(k,i+1,g) - S_{cr}(k,i)n_e n(k,i,g) \qquad (4.1.4)$$

where n_E is the Saha-Boltzmann population density and α_{cr} and S_{cr} are collisional-radiative recombination and ionization coefficients[2].

References

1. R.W.P.McWhirter,'Plasma Diagnostic Techniques', p.201, Academic Press, New York, 1965

2. D.R.Bates,A.E.Kingston,R.W.P.McWhirter, Proc.Roy.Soc.,A257,p.297, 1962

3. R.W.P.McWhirter,A.G.Hearn,Proc.Phys.Soc.,82,p.641, 1963

4.2 Equilibrium relations

Distinguishing between the two extremes of an LTE or Coronal distibution between ionic energy levels, a thermal limit p_T can be defined as that quantum level at which the probability for collisional transitions out of it will approximately equal the probability for radiative decay. Above p_T a Boltzmann distribution is likely to hold whilst sufficiently below, levels are likely to exhibit a Coronal distribution. Criteria given by McWhirter[1] and Griem[2] for complete or partial LTE embody the requirement that, between any two relevant levels, collision rates should exceed radiative rates by at least a factor of ten.

In the atomic equilibrium models described by Bates et.al.[3] and McWhirter and Hearn[4], levels up to p=20 were considered, with a thermal distribution assumed for higher levels. In the case of non-hydrogenic systems, the procedure is more complex as, due to the removal of the degeneracy of the lower levels as the nuclear charge Z increases, no simple formulae are available for the level separations and oscillator strengths. Various simplified methods for the treatment of non-hydrogenic ions have been developed. Drawin[5] solved the set of equations describing the population of levels up to p=27 in He I, with the assumption that levels greater than p=2 were degenerate and by using both tabulated Helium data and Hydrogen-like values. Elwert[6] discussed the extreme cases in which all levels of an ion have a coronal distribution. Oertel and Griem[7] adopted a coronal model for levels below p_T and used Boltzmann factors to relate the populations of levels above p_T. The latter approach would be unsatisfactory, for the purposes of diagnostics, if the thermal limit is not greatly removed from those levels out of which most spectroscopically observed transitions originate. Suckewer[8] has outlined a method whereby approximations for the excited level populations of Hydrogen and Carbon II are obtained, without solving for all upper levels under certain conditions, but taking collisional and radiative processes into account for each level.

Rewriting the equation governing the population of level p from equation (4.1.2) one obtains,

$$n(k,i,p) = \frac{n_e \sum_{q<p} n(k,i,q)X(k,i,q,p)}{\sum_{q<p}\left(A(k,i,p,q) + n_e X(k,i,p,q)\right)}$$

$$+ \frac{\left[\begin{array}{l} n_e \sum_{q>p} n(k,i,q)X(k,i,q,p) \;-\; n_e n(k,i,p) \sum_{q>p} X(k,i,p,q) \\ + \sum_{q>p} n(k,i,q)A(k,i,q,p) \;+\; n_e n(k,i+1,g)\{\alpha(k,i+1,p) \\ + n_e \beta(k,i+1,p)\} - n_e n(k,i,p)S(k,i,p) \end{array}\right]}{\sum_{q<p}\left(A(k,i,p,q) + n_e X(k,i,p,q)\right)}$$

..... (4.2.1)

The term in square brackets can be neglected when n_e is large as the first and second and the fourth and fifth terms within it tend to zero. Generally, the third expression is also small. With this approximation one can write

$$\frac{n(k,i,p)}{n(k,i,g)} = B_p \frac{g_p}{g_g} \cdot e^{-(E_p - E_g)/kT_e} \qquad (4.2.2)$$

$$\text{where } B_p = \frac{\sum_{q<p} B_q \tau^*_{p\,q}}{1 + \sum_{q<p} \tau^*_{p\,q}} \qquad \text{and } B_g = 1$$

$$\tau^*_{p\,q} = \frac{n_e X(k,i,p,q)}{\sum_{q<p} A(k,i,p,q)} \qquad \text{.....(4.2.2A)}$$

Bates and Kingston[3] and McWhirter and Hearn[4] have considered isolated Hydrogen plasmas at electron temperatures up to ~ 25 eV, at which temperature the ground level populations are vanishingly small. Normally in such cases the last two terms in the bracket in equation (4.2.1) are important in determining the balance of population of level p, the latter tending towards the Saha-Boltzmann values at high values of n_e. If there is a large source of cold atoms or ions entering the plasma however, the ground level population can be maintained higher than the normal ionization equilibrium value by several orders of magnitude so that, even if the temperature is much greater than the ionization energy, excited state populations can be mainly supplied from the ground state. This situation has been considered by Abromov et.al.[9] for Hydrogen in plasmas of electron temperature up to 1.5 keV. The nearer level p is to the ionization limit, the more accurate is the approximation of (4.2.2A).

When n_e is so low that the term in square brackets in equation (4.2.1) is not negligible and B_p must be modified. The main contribution to this term comes from the third spontaneous radiative decay expression, especially if level p is populated mainly by means of forbidden transitions from the ground level, when other low lying levels are less populated.

B_p in equation (4.2.2) is then replaced by $B_p^* + \Delta B_p$ with

$$\Delta B_p = \sum_{q>p} \frac{B_q A(q,p)\, g_q\, e^{-(E_q - E_p)/kT_e}}{g_p \sum_{r<p} A(p,r) \left(1 + \sum_{r<p} \tau^*_{p\,r}\right)} \qquad (4.2.3)$$

where subscripts k and i are dropped when only one ion species is considered.

B_p^* is obtained from equation (4.2.2) but with forbidden transitions included in the evaluation of $\tau^*_{p\,q}$. The justification for neglecting the correction of equation (4.2.3) can be checked in aby situation once a value for B_p has been obtained. If cascade transitions into levels from above are unimportant (and likewise forbidden transitions from below), then from equation (4.2.1),

$$n_e \sum_{q<p} n(q)X(q,p) \gg \sum_{r>p} n(r)A(r,p) \qquad (4.2.4)$$

Expressing A(r,p) in terms of the absorption oscillator strength f(p,r) and using an expression for collisional excitation derived by Seaton[10] which covers a large range of temperatures, the criterion above can be written as,

$$\frac{7.3\, n_e \sum_{q<p} (g_q B_q f(q,p))/(E_p - E_q)}{10^{14}\, kT_e^{1/2} g_p \sum_{r>p} B_r f(p,r) (E_r - E_p)^2\, e^{-(E_r - E_p)/kT_e}} \gg 1 \qquad .....(4.2.5)$$

with E, kT_e in eV.

The results obtained using this approximation for Hydrogen[8] are in good agreement (within 20%) with those obtained by McWhirter and Hearn[4] for electron densities 10^8 to 10^{18} cm^{-3} and temperatures 0.34 to 5.5 eV. Suckewer has also tabulated the coefficients B_p for Carbon II for electron densities 10^{10} to 10^{18} cm^{-3} and temperatures 2.8 to 22 eV.

In the high density limit the collision terms dominate in equation (4.2.1) and $B_p \longrightarrow 1$, the LTE solution. In the limit of low density, without significant reabsorption, radiative decay dominates and the main contribution to excitation comes from the ground level, there being very few ions in other excited levels. The coronal excitation equation results for which,

$$n(p) = \frac{n_e n(g) X(g,p)}{\sum_{q<p} A(p,q)} \qquad (4.2.6)$$

Expressing the population densities in this case as a modified Boltzmann distribution,

$$B_p = \frac{n_e X(g,p)\, g_g\, e^{E_p/kT_e}}{g_p \sum_{q<p} A(p,q)} \qquad (4.2.7)$$

A deviation parameter θ_p similar to B_p can be defined such that $\theta_p = B_p/B_\infty$ and signifies the degree to which radiative processes interfere with the collision-coupling between levels higher than p . In practice, B_∞ can be replaced by B_m where m is a higher level at which $B_m/B_{m-1} \sim 1$.

The significance of the thermal level p_T can be appreciated when it is realised, that collisions involving the transition of electrons from levels lower than p_T into any level higher than it are effectively ionization processes, because these electrons are more likely to become free than cascade downwards. Similarly, following a transition of an electron into a

level below p_T from a higher level, the latter will be filled rapidly from the continuum, thereby maintaining its previous relative thermal population. This is equivalent to a recombination process. The rate coefficients in equation (4.1.4) represent the rates of entering and leaving the ground level by electrons which also pass through the continuum of states above the ionization limit. As p_T represents the level at which radiative and collisional excitation and ionization mechanisms are approximately equal in influence, radiative recombination into levels $< p_T$ is important. Three-body recombination is the dominant process for recombination into levels above p_T. The total recombination coefficient can be expressed as an effective two-body collisional process namely,

$$n_e n(k,i+1,g)\,\alpha_{cr}(k,i+1,g) = \sum_{p<p_T} n_e n(k,i+1,g)\,\alpha(k,i+1,g) + \sum_{p\geqslant p_T}\sum_{q<p_T} n(k,i,p)\left(A(k,i,p,q) + n_e X(k,i,p,q)\right) \quad \ldots\ldots(4.2.8)$$

As transitions are faster between close lying levels, equation (4.2.8) can be simplified by summing over $p \gtrsim p_T$ and $q \lesssim p_T$. Above the thermal limit levels are effectively collision-coupled to the next ion-stage and $\theta_{p>p_T} \longrightarrow 1$. Using the Saha equation and putting $\theta_{p>p_T} = 1$ in equation (4.2.8) therefore,

$$\alpha_{cr}(k,i+1,g) = \frac{n_e kT_e^{-3/2}}{2.9\times10^{21}} \sum_{p\gtrsim p_T}\sum_{q\lesssim p_T} \frac{g(k,i,p)}{g(k,i+1,g)}\, e^{\chi_p/kT_e} \left\{ X(k,i,p,q) + \frac{A(k,i,p,q)}{n_e} \right\} + \sum_{p<p_T} \alpha(k,i+1,p) \quad \ldots\ldots(4.2.9)$$

Byron et.al.[10] have obtained good agreement with the values of Bates and Kingston[3] for the collisional radiative rate in Hydrogen for electron densities 10^9 to 10^{19} cm^{-3} at a temperature of 16,000 ^oK using a simple form of equation (4.2.9) namely,

$$n_e n(k,i+1,g)\,\alpha_{cr}(k,i+1,g) = n(k,i,p_T)\sum_{q<p_T} A(k,i,p_T,q) + n_e n(k,i,p_T)X(k,i,p_T,p_T-1) + n_e n(k,i+1,g)\,\alpha(k,i+1,g) \quad .....(4.2.10)$$

The other terms are negligible if the temperature is low (i.e. $kT_e < E_{p_T-1}$).

The collisional-radiative ionization coefficient S_{cr} can be similarly obtained i.e.,

$$n_e n(k,i,g)\,S_{cr}(k,i,g) = n_e n(k,i,g)\left(S(k,i,g) + \sum_{p\geq p_T} X(k,i,g,p)\right) + n_e \sum_{q=2}^{p_T-1}\sum_{p\geq p_T} n(k,i,q)X(k,i,q,p) \quad .....(4.2.11)$$

In the low density limit $S_{cr}(k,i,g) \longrightarrow S(k,i,g)$. As n_e increases, the thermal limit drops towards the ground level and S_{cr} and α_{cr} tend towards the collisional rate coefficients to and fro between the ground level and the first few resonance levels. This sets the lower limit to the relaxation time associated with that ion.

For all levels a modified Saha equation can be used, incorporating the deviation parameters, to describe the populations in terms of those of the electrons and the ground state of the next ion stage. i.e.,

$$\frac{n(k,i+1,g)n_e}{n(k,i,p)} = \frac{2g(k,i+1,g)}{g(k,i,p)\Theta_p} 2\pi m_e kT_e^{3/2} e^{-\chi(k,i,p)/kT_e} \quad .....(4.2.12)$$

The expressions obtained so far relate to an isolated optically thin, homogeneous, steady-state plasma. Their applicability to situations in which there is a time varying energy input, injection and loss of plasma and possibly large self-absorption of line radiation must now be examined. Regarding the excited level populations, their ionization and excitation relaxation times $t^o(p)$ are generally less than or equal to their natural radiative lifetimes. These times can be compared to times over which changes in the plasma may occur. For a range of parameters relevant to the present experiment, checks have shown that most excited levels of the ions , if not the ground states, relax instantaneously compared to overall ' plasma times'. At any instant therefore, the populations of excited levels can be related to the ground state populations and metastable populations using the steady state LTE deviation-parameters already discussed.
It is also required that, during the relaxation time, an atom or ion, in travelling a mean diffusion length in the plasma, will not experience a significant variation in conditions. If this were not so, the excitation and ionization equilibrium would not reflect a purely local set of parameters. The mean diffusion length $r_d = \lambda' (t^o/\tau')^{1/2}$ where λ' is the collision mean free path and τ' is the collision mean free time. Spatial variations can be neglected, for temperature say, if

$$\left| \frac{kT_e(r) - kT_e(r + r_d)}{kT_e(r)} \right| \ll 1$$

Apart from the sheath region at the solid surface, experimentally measured variations in temperature within this plasma were found to be negligible. The plasma has so far been considered optically thin for all wavelengths. With re-absorption taking place there will be a corresponding reduction in the radiative transition rates. In equation (4.1.1) additional terms

$$\sum_{q<p} \int I(\gamma)\, \hat{\chi}(\gamma_{p,q})\, d\gamma$$ representing absorption, where $\hat{\chi}$ is

the absorption coefficient in units of cm^{-1}, should be included for line and continuum emission processes. These terms can most easily be incorporated into equation (4.1.1) by means of escape factors F such that, for example, A(p,q) is replaced by F(p,q)A(p,q) in the case of line emission, where

$$F(p,q) = 1 - \frac{n(q)B(q,p)4\pi}{n(p)A(p,q)c} \int \langle I(\gamma)\rangle L(\gamma)\, d\gamma$$

For self-absorption it is assumed* that, $\langle I(\gamma)\rangle = \frac{\hat{\mathcal{E}}(\gamma,x)}{4\pi\hat{\chi}(\gamma,x)}\left(1-e^{-\int\hat{\chi}\,dx}\right)$

then, neglecting stimulated emission,

$$F(p,q) = 1 - \frac{1}{4\pi}\int\left(1 - e^{-\gamma}\right)L(\gamma)\, d\gamma \qquad (4.2.13)$$

$\hat{\mathcal{E}}(\gamma,x)$ is the emission coefficient and $\gamma = \int\hat{\chi}\, dx$ is the optical depth. Some knowledge of the line shape is required in this expression. For non-hydrogenic ions with $Z > 1$, the assumption of Doppler broadening only should not prove too inaccurate for densities below those normally necessary for LTE and allows a simple analytical expression for F(p,q) to be derived[11], i.e.,

*See section 5.3

$$F(p,q) = 1 - \frac{1}{\sqrt{\pi}} \int_{-\infty}^{\infty} e^{-\left(\frac{\nu-\nu_0}{\Delta\nu_D}\right)^2} \left(1 - e^{-\tau_0 e^{-\left(\frac{\nu-\nu_0}{\Delta\nu_D}\right)^2}}\right) d\frac{(\nu-\nu_0)}{\Delta\nu_D}$$

$$= 1 - \sum_{n} \left((-1)^n \, \tau_0^{\,n} / n! \sqrt{n+1} \right)$$

In the case of a homogeneous plasma of depth δ,

$$\tau(\nu) = \frac{n(q)\, g_p A(p,q)\, c^2 h \nu_0\, L(\nu)\, \delta}{8\pi g_q\, h\nu_0^3} \qquad (4.2.14)$$

For a Doppler profile,

$$L(\nu) = \frac{1}{\sqrt{\pi}\,\Delta\nu_D}\, e^{-\left(\frac{\nu-\nu_0}{\Delta\nu_D}\right)^2}$$

For a Stark or dispersion profile,

$$L(\nu) = \frac{1}{\pi \Delta\nu_S} \left(1 + \left(\frac{\nu-\nu_0}{\Delta\nu_S}\right)^2\right)^{-1}$$

Rewriting equation (4.2.14) for a Doppler profile in wavelength terms,

$$\tau_0(\lambda_0) = 1.61\times10^{-32} n(q) A(p,q) \frac{g_p}{g_q}\, \delta \lambda_0^3 \sqrt{\mu/T} \qquad (4.2.15)$$

where μ is in atomic units, T in eV, λ_0 in Angstrom and δ in cm.

Rewriting in terms of the ground state density,

$$\tau_0 = 1.61\times10^{-32} n(g) A(p,q) \frac{g_p}{g_g} \sqrt{\mu/T}\, \lambda_0^3 \delta\, B_q^{**}\, e^{-E(q)/kT_e} \qquad (4.2.16)$$

B_q^{**} is the wholly or partially optically-thick LTE-deviation parameter.

If the line has a dispersion profile, equation (4.2.14) becomes

$$\tau_o = 4.17\times10^{-37} \frac{g_p A(p,q) n(q)}{g_q} \lambda_o^4 \qquad (4.2.17)$$

From equation (4.2.16) the optical transparency of spectral lines from levels high up in the term schemes can be checked. The deviation parameters B_q^{**} for the lower levels must be found and these depend upon the populations of all the neighbouring levels i.e. the partition function for all levels below p must be known. In most laboratory plasmas only the main resonance levels are likely to be affected by self-absorption although, in the case of Hydrogenic ions, the first members of the Balmer sequence may also be optically thick[12,13].

In most non-hydrogenic ions there are many discrete levels with differing multiplicities. Levels within a particular multiplicity scheme for which transitions to the lowest state are allowed by the selection rules for electric dipole radiation (excluding intercombination transitions for low -Z ions) can be termed 'normal', and all others can be called 'irregular'. The correction of equation (4.2.3) is generally unnecessary for normal levels, as the populations of levels higher up in the term scheme are smaller and the transition probabilities tend to decrease also. For ease of calculation it can be assumed that the B-values for the metastable levels are unity. In a steady state this is reasonable as only collisional transitions between them and the ground state are effective, at other than very low densities. The cross-section for collisional excitation of the $2s2p\ ^3P^o$ metastable level in C III has been obtained by Osterbrock[14] and those for excitation of the $2s^22p^4\ ^1S$ and $2s^22p^4\ ^1D$ metastable levels in F II by Seaton[15]. The relaxation times for these levels in the present range of temperatures is $\sim 10^{-9}$ sec. at an electron density of 10^{17} cm^{-3}, and $\sim 10^{-7}$ sec. if $n_e = 10^{15}$ cm^{-3}.

The excitation of the metastable $2s2p^2\ ^4P$ level from the $2s^22p\ ^2P^o$ ground state in C II can be considered as a quasi-Beryllium-like process with an extra 2p electron present. As the cross-sections for the transitions $2s^2\ ^1S$ — $2s2p\ ^3P^o$ and $2s2p\ ^1P^o$ — $2p^2\ ^3P$ in Beryllium are almost the same in value[14], it is reasonable to assume that the C II cross-section is of the same order of magnitude with the additional 2p electron partly compensating the increased nuclear charge, in which case B_p for all the metastable levels can be put equal to unity in this experiment.

Neglect of the correction of equation (4.2.3) was assessed using equation (4.2.5). If cascade transitions into irregular levels from above are unimportant (and, likewise, forbidden transitions from below) then, from equation (4.2.1)

$$n_e \sum_{q<p} n(q)X(q,p) \gg \sum_{r>p} n(r)A(r,p) \qquad (4.2.18)$$

Expressing A(r,p) in terms of the oscillator strength and with the help of equation (4.3.3), the criterion for this neglect is ;

$$\frac{7.3\ n_e \sum_{q<p} (B_q f(q,p) g_q)/(E_p - E_q)}{10^{14}\ kT_e^{1/2}\ g_p \sum_{r>p} B_r f(p,r)(E_r - E_p)^2\ e^{-(E_r-E_p)/kT_e}} \gg 1 \qquad .....(4.2.19)$$

with E and kT_e in eV.

This criterion is satisfied for C II, C III, C IV and F II ions for electron densities $\gtrsim 10^{15}\ cm^{-3}$.

For irregular levels, at very low densities in an optically thin plasma, a coronal balance exists between them and the ground state. At intermediate densities, such levels will be populated by stepwise transitions from below and radiative cascades from above.

At higher intermediate densities, stepwise excitation of the irregular levels dominates and the B-parameters become proportional to n_e^2 . As the density decreases, with the correction $B_p^* + \Delta B_p$, the B-values will become proportional to n_e, as the populations of higher levels which cascade down also become proportional to n_e. With increase of density the B-values tend to unity for all levels. It is evident therefore, that for irregular levels, the value of n_e/B_p passes through a minimum when the electron density falls just below the value necessary for the establishment of complete LTE. This behaviour is utilised in a diagnostic method outlined in chapter 5.

At low densities the transition in the values of the deviation parameters to those given by equation (4.2.7) should be quite smooth for normal levels. These values can be inserted into equation (4.2.3) in order to find the B-values for irregular levels at low density.

References

1. R.W.P.McWhirter,'Plasma Diagnostic Techniques',Academic Press, New York,R.H.Huddlestone & S.L.Leonard Eds., 1965

2. H.R.Griem,'Plasma Spectroscopy',McGraw-Hill,New York, 1964

3. D.R.Bates,A.E.Kingston,R.W.P.McWhirter,Proc.Roy.Soc.,A267,p.297,1962

4. R.W.P.McWhirter,A.G.Hearn,Proc.Phys.Soc., 82, p.641,1963

5. H.W.Drawin,Z.Naturf.,19a,p.1451,1964

6. G.Elwert,Z.Naturf.7a,p.432,1952

7. G.K.Oertel,H.R.Griem, Phys.Fluids, 8, p.186, 1965

8. S.Suckewer, J.Phys.B.,3, p.380, 1970

9. V.A.Abramov,E.I.Kuznetsov,V.I.Kogan,Atomniya Energiya,26,p.516,1969

10. M.J.Seaton,'Atomic and Molecular Processes',D.R.Bates Ed, Academic Press, New York, 1962

11. M.W.Zemansky,Phys.Rev. 36, p.219, 1930

12. M.Galanti,N.J.Peacock,B.A,Norton,J.Puric, Proc. 5th IAEA Conf. on Plasma Phys. and Contr. Nucl. Fus. Res., Tokyo,November,1974

13. A.G.Hearn, Proc.Phys.Soc.,88, p.171,1966

14. D.E.Osterbrock, J.Phys.B, 3, p.149, 1970

15. M.J.Seaton, Rev.Mod.Phys.,30, p.979, 1958

4.3 Atomic Parameters

The energy levels, ionization potentials, oscillator strengths and transition rate coefficients for all the ions present in this source are required in order to completely describe the spectral emission and calculate the total radiation loss. From such information, parameters describing the state of internal equilibrium and general coefficients for ionization and recombination are obtained for each ion. The term schemes of the ions C II, C III, C IV, and F II are shown in figs. 4.3.1 to 4.3.4 and depict the first twenty or more terms. The classification is taken from Moore[1].

C IV is isoelectronic with Lithium and has no metastable levels. Though the second level is near to the ground state and may be in thermal equilibrium with it, the equilibrium may not extend to higher levels.

C III belongs to the Beryllium isoelectronic sequence. Here the triplet $2s2p\ ^3P^o$ levels are metastable and, at sufficiently low densities, through intercombination transitions, influence the populations of higher levels. The population densities of these triplet levels can approach the thermal equilibrium values with respect to the ground level so that, for example, the $2s2p\ ^1P^o$ levels may be populated significantly from the metastable term as well as from the ground state. If the spontaneous decay rate of this singlet term is much greater than the exit collisional rates, then levels such as $2p^2\ ^1D$ and $2p^2\ ^1S$ may be similarly populated. At higher densities, or higher up in the term scheme, the effect of the metastable levels diminishes as all levels approach a thermal equilibrium population density.

C II is Boron-like and has one metastable $2s2p^2\ ^4P$ term which is near the ground state. This term should generally be in thermal equilibrium with the ground as the only likely radiative route for its depopulation is via excitation to the third, fourth or fifth $2s2p^2$ doublet levels. These transitions are forbidden for electric dipole radiation, whereas the transition $2s2p^2\ ^4P - 2s^22p\ ^2P^o$ is not and should have a larger cross-section.

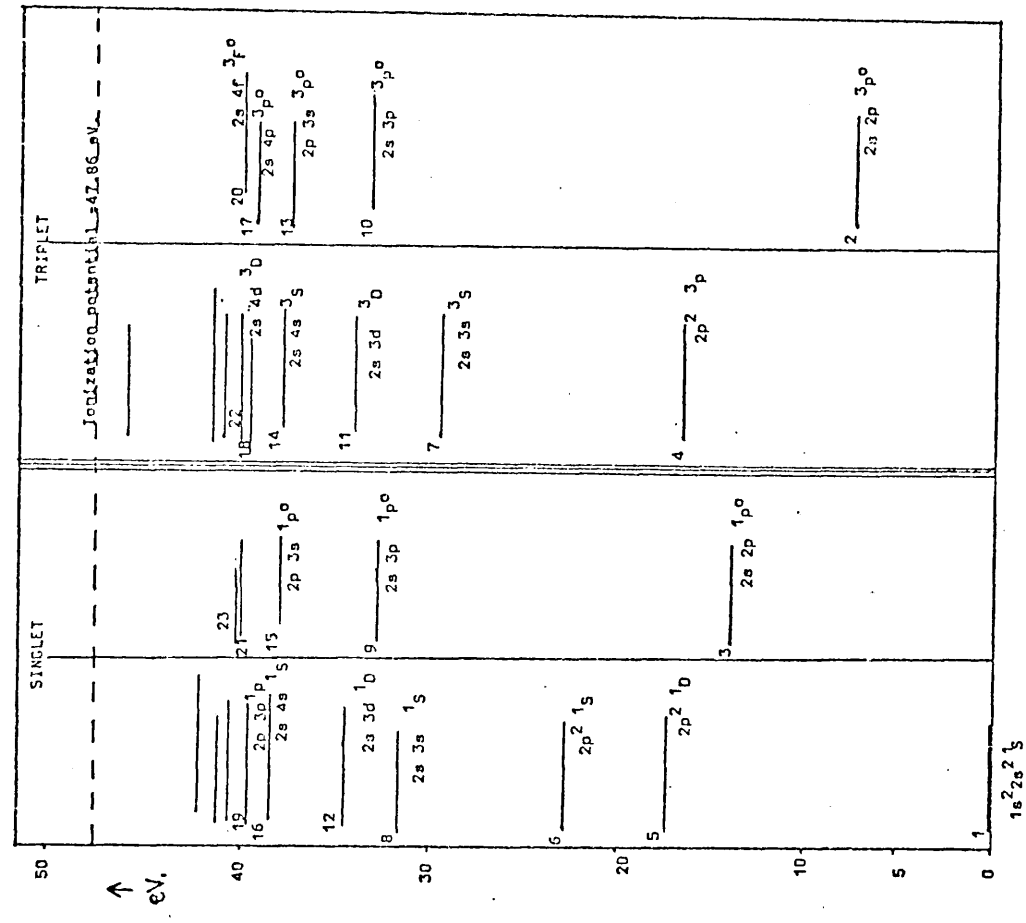

Fig. 4.3.2 Energy levels of C III

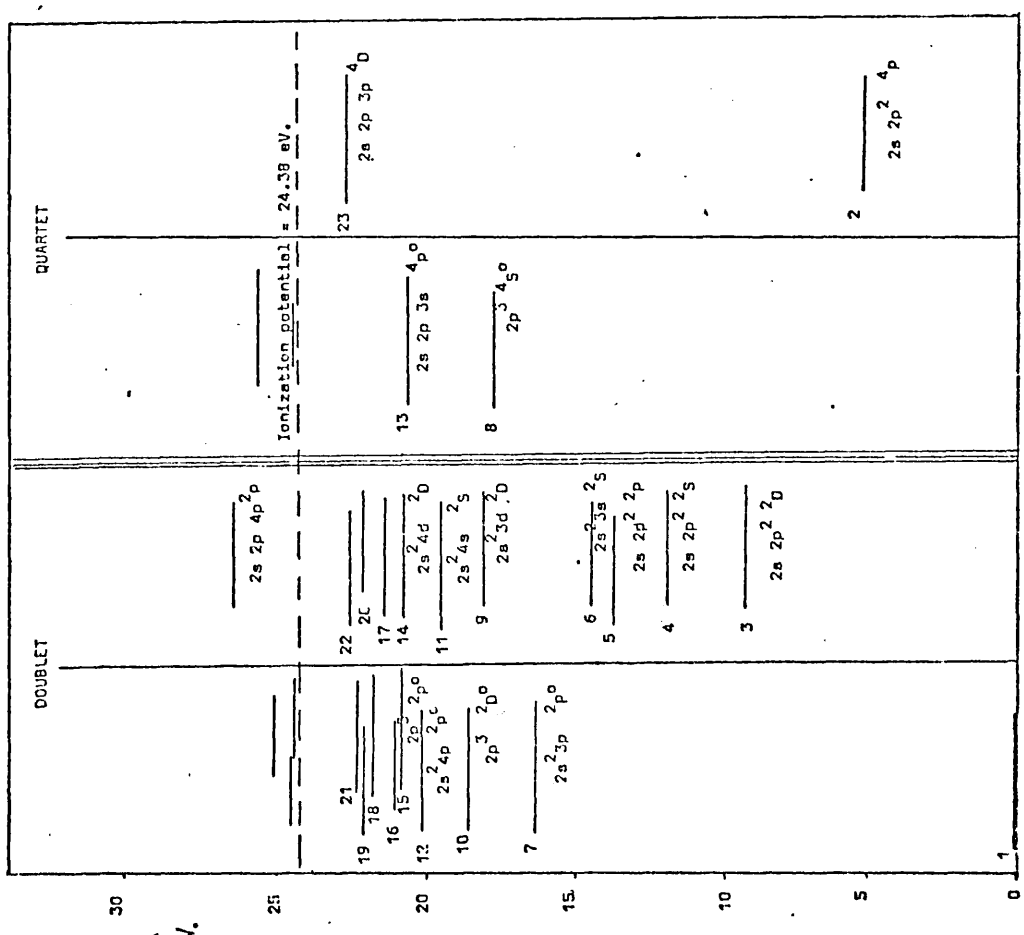

Fig. 4.3.1 Energy levels of C II

Fig. 4.3.3 Energy levels of C IV

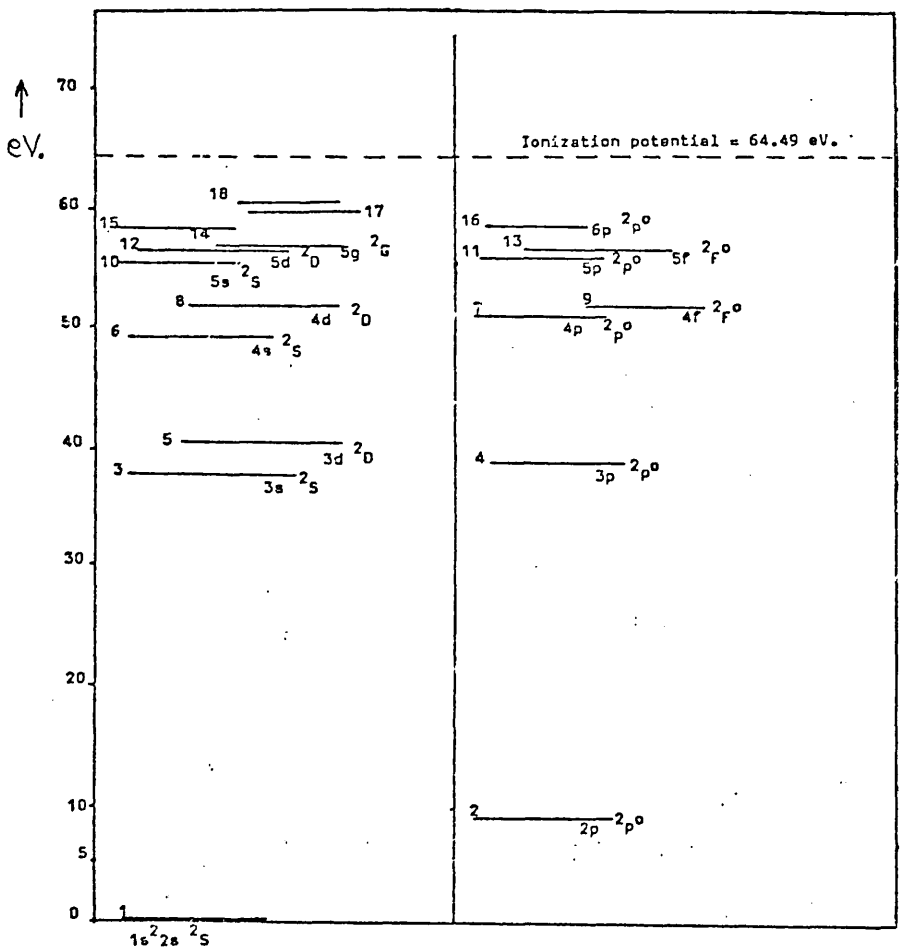

Fig. 4.3.4 Energy levels of F II

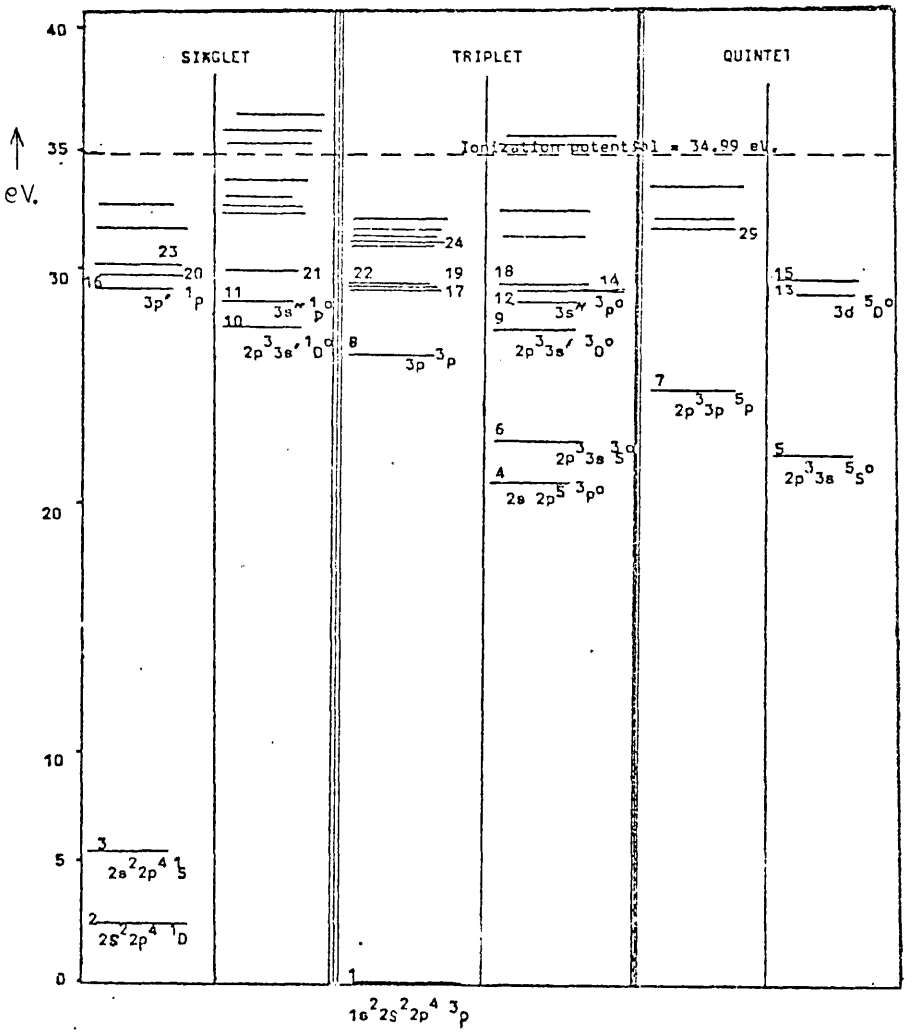

F II and F III each have many terms representing states in which two or more electrons are excited or in which the total spin of the core is varied. Thus each has several metastable levels but, some of these are close enough to the ground state to generally be in thermal equilibrium with it. Other metastables may be in thermal equilibrium with the higher states and with the continuum of free electrons.

It is assumed here that, at all times, the population of a level is statistically distributed amongst its degenerate states as a result of collisions. Even if the plasma were not dense enough to ensure this, the subsequent errors in the ionization and recombination coefficients would be small[2].

Spontaneous Radiative Transition Probabilities

Under the present experimental conditions, only transitions allowed by the selection rules for electric-dipole radiation are important. Intercombination transitions ($\Delta S \neq 0$) are forbidden in pure L-S coupling although allowed by the electric dipole rules. All important transition probabilities were taken from the tables of Wiese et.al.[3], where available, or were calculated using the Coulomb approximation method of Bates and Damgaard[4]. This method is only applicable for transitions between levels with the same parent term. Where necessary, account was taken of double excitation in determining an effective principal quantum number n^*, but the depression of the ionization potential by the plasma was not included in the calculation as the effect of this upon n^* is small. The multiplet strengths required for this method were taken from the tables of Goldberg[5,6]. The errors associated with the use of the Coulomb method have been estimated[3] after comparison with other theoretical and experimental values. For He, Li, Be and B - like ions, the method should be accurate to better than 25% and, for N, O and F - like ions, the accuracy should be better than 50%.

A few remaining transition probabilities, innaccessible by the Coulomb method, were calculated from tabulated literature values of spectral line intensities[7,8], using a branching ratios technique. The errors in the intensities were $\sim \pm 100\%$. Transition probabilities were found for the first twenty levels of each ion. Above this value collisions were assumed to be dominant.

Collisional excitation and de-excitation

Collisional electron excitation rate coefficients are related to the excitation cross-section by the expression

$$X(p,q) = \langle \sigma_e(p,q)\, v_e \rangle = \int_{E_o}^{\infty} \sigma_e(p,q)\, v_e\, f_e(E)\, dE \qquad \ldots\ldots(4.3.1)$$

where E_o is the threshold excitation energy, equal to $E_q - E_p$.

An approximate formula developed by Seaton[9] and van Regemorter[10] for electric dipole transitions, using a Coulomb-Born method, is adopted as it is particularly useful for systematic tabulation. For electron energies at and above threshold, the cross-sections can be written,

$$\sigma_e(p,q) = \frac{8\pi^2 a_o^2 f(p,q) \bar{g}}{3^{1/2} E (E_q - E_p)} \qquad (4.3.2)$$

where a_o is the Bohr radius, $\bar{g}$ is the Kramers-Gaunt factor and E is the electron energy. σ_e is in units of cm^{-2} if a_o is in cm. and energies are in Rydbergs. From equation (4.3.1), assuming a Maxwellian electron energy distribution and with E_o and kT_e in eV,

$$X(p,q) = 1.58\times10^{-5} f(p,q)\bar{g}\, kT_e^{-1/2} (E_q - E_p)^{-1} e^{-(E_q - E_p)/kT_e} \qquad \ldots\ldots(4.3.3)$$

Van Regemorter[10] has tabulated values of $\bar{g}$ for neutral atoms and positive ions. For the latter, $\bar{g}$ takes on the constant value 0.2 for E_o/kT_e between $\sim$ 1 and 100. $\bar{g} \simeq$ 0.6 when $E_o/kT_e = 0.1$. Seaton[9] has estimated that equation (4.3.3) will be accurate to within a factor of 2, over this temperature range. From the principle of detailed balancing in thermal equilibrium, the inverse rate coefficients are given by,

$$X(q,p) = (g_p/g_q)\, X(p,q)\, e^{(E_q - E_p)/kT_e} \qquad (4.3.4)$$

Radiative recombination

The photo-ionization rate from level p of an ion due to absorption of radiation of intensity $I(\nu)$ is[11],

$$n(k,i,p) \int_{\nu_o}^{\infty} \frac{I(\nu)}{h\nu}\, \sigma(k,i,p,\nu)\, d\nu \qquad (4.3.5)$$

with ν_o the threshold frequency.

From the principle of detailed balancing, the radiative recombination rate coefficient to level p of an ion from the higher ion stage is,

$$\alpha(k,i+1,p) = \frac{g(k,i,p)\, 2^{1/2}\, e^{\chi_p/kT_e}}{g(k,i+1,g)\, c^2\, \pi^{1/2}\, (m_e kT_e)^{3/2}} \times \int_{\chi_p}^{\infty} (h\nu)^2\, \sigma(k,i,p,\nu)\, e^{-h\nu/kT_e}\, d(h\nu) \qquad \ldots.(4.3.6)$$

Generally, when radiative recombination is most important, kT_e is $\ll \chi_p$ and $(h\nu)^2 \sigma(\nu)$ is $\simeq (h\nu_0)^2 \sigma(\nu_0)$ around threshold. Beyond this range $\sigma(\nu)$ tends to zero and so,

$$\alpha(k,i+1,p) = \frac{7.03\, \chi_p^2\, g(k,i,p)\, \sigma(k,i,p,\nu_0)}{kT_e^{1/2}\, g(k,i+1,g)} \qquad (4.3.7)$$

α is in $cm^3 sec^{-1}$ if χ_p, kT_e are in eV and σ in cm^2.

For recombination into the ground states and lower levels of C I, CII, F I and F II ions, values of $\sigma(\nu_0)$ obtained by a quantum defect method are used[12]. For recombination into higher levels of these ions, and into all levels of higher ion stages, Hydrogen-like values for $\sigma(\nu_0)$ are used. Seaton[11] has adapted the expression for $\sigma(\nu)$ of Menzel and Pekeris[13] from which a simple numerical expression for α is obtained,

$$\alpha(k,i+1,p) = \frac{1.9\ \chi(k,i,p)}{10^{14}\, kT_e^{1/2}} \qquad (4.3.8)$$

The estimated accuracy of this formula is $\sim \pm 30\%$.

Collisional Ionization

The numerical expression for the electron collision ionization rate coefficient derived by Kolb and Lupton[14] was adopted because of its simplicity and range of applicability.

$$S(k,i,p) = \frac{1.1\times10^{-5}\, kT_e^{1/2}\, A'\, e^{-\chi_p/kT_e}}{\chi_p^2\, (6 + kT_e/\chi_p)} \qquad (4.3.9)$$

where A' is the number of optical electrons. Values obtained when kT_e/χ_p varies from 0.02 to 100 agree to within 20% with experimental data.

References

1. C.E.Moore,'Atomic Energy Levels',Nat.Bur.Stand., Washington, 1945

2. D.R.Bates,A.E.Kingston,Planet.Space Sci.,11, p.1, 1963

3. W.L.Wiese et.al.,Nat.Bur.Stand.Rept.No. NSRDS'NBS-4,Volume 1, Washington, 1966

4. D.R.Bates,A.Damgaard,Phil.Trans.Roy.Soc.,Series A, 243,p.101, 1949

5. L.Goldberg, Ap.Journ., 82, p.1, 1935

6. L.Goldberg, Ap.Journ., 84, p.11, 1936

7. A.Striganov,N.Sventitskii, 'Tables of Spectral Lines of Neutral and Ionized Atoms', Plenum Pub. Corp., New York, 1968

8. W.F.Meggers,C.H.Corliss,B.F.Scribner,'Tables of Spectral Line Intensities',Parts I,II,Nat.Bur.Stand., Washington, 1961

9. M.J.Seaton, 'Atomic and Molecular Processes', D.R.Bates Ed., Academic Press, New York, 1962

10. H.vanRegemorter,Astrophys.Journ., 136, p.906, 1962

11. M.J.Seaton, Mon.Not.R.A.S., 119, p.81, 1959

12. D.R.Bates, Mon.Not.R.A.S., 106, p.423, 1946

13. D.H.Menzel,C.L.Pekeris,Mon.Not.R.A.S., 96, p.77, 1936

14. A.C.Kolb,W.H.Lupton, private communication in 'Plasma Diagnostic Techniques',R.H.Huddlestone,S.L.Leonard Eds., p.222, Academic Press, New York, 1965

4.4 Radiative Losses

The main radiative transitions originate from the low-lying levels of each ion present, as for these, the populations and radiative transition probabilities are highest. The contribution from higher levels can be neglected when their contribution becomes less than a few percent of the total. The following transitions accounted for more than ~ 90% of the total radiation loss.

C II

$2p\ ^2P^o - 2p^2\ ^2D$ (1335 Å)
$2p\ ^2P^o - 2p^2\ ^2S$ (1037 Å)
$2p\ ^2P^o - 2p^2\ ^2P$ (904 Å)
$2p\ ^2P^o - 3s\ ^2S$ (858 Å)
$2p\ ^2P^o - 3d\ ^2D$ (687 Å)
$2p^2\ ^2S - 3p\ ^2P^o$ (2837 Å)
$2p^2\ ^4P - 2p^3\ ^4S^o$ (1010 Å)

C IV

$2s\ ^2S - 2p\ ^2P^o$ (1549 Å)
$2s\ ^2S - 3p\ ^2P^o$ (312 Å)
$2p\ ^2P^o - 3s\ ^2S$ (420 Å)
$2p\ ^2P^o - 3d\ ^2D$ (384 Å)

F II

$2p^4\ ^3P - 2p^5\ ^3P^o$ (600 Å)
$2p^4\ ^3P - 3s\ ^3S^o$ (547 Å)
$2p^4\ ^3P - 3d\ ^3D^o$ (431 Å)

C III

$2s^2\ ^1S - 2s2p\ ^1P^o$ (977 Å)
$2s^2\ ^1S - 3p\ ^1P^o$ (386 Å)
$2p\ ^1P^o - 2p^2\ ^1D$ (2297 Å)
$2p\ ^1P^o - 2p^2\ ^1S$ (1247 Å)
$2p\ ^1P^o - 3s\ ^1S$ (690 Å)
$2p\ ^1P^o - 3d\ ^1D$ (574 Å)
$2p\ ^3P^o - 2p^2\ ^3P$ (1176 Å)
$2p\ ^3P^o - 3s\ ^3S$ (538 Å)
$2p\ ^3P^o - 3d\ ^3D$ (459 Å)

F III

$2p^3\ ^4S^o - 2p^4\ ^4P$ (657 Å)
$2p^3\ ^2D^o - 2p^4\ ^2D$ (568 Å)
$2p^3\ ^2P^o - 2p^4\ ^2D$ (630 Å)

Most are multiplet transitions.

The optical depth was checked for each line using equations (4.2.16) and (4.2.17), with lower level densities expressed in terms of the ground level population. In all the above transitions there was strong self-absorption. The total loss for each line was calculated using the approximation of a band of black-body continuum centred around the line, with a width equal to that of the points on the otherwise undistorted line profile at which the intensity would have dropped to the black-body value. From equations (5.3.18) and (5.3.1), the total loss for a single line, I^*, is given by, assuming the emission is uniform over a length δ ,

$$I^*(p,q) \simeq 4\pi\Delta\lambda_S \left(\frac{I_{b.b.}(\lambda_c)\, n_g\, g_p\, A(p,q)(E_p-E_q)\, B_p\, e^{-E_p/KT_e}\, 1.6\,\delta}{\Delta\lambda_D\, g_g\, 4\pi \times 10^{19}} \right)^{1/2} \qquad (4.4.1)$$

$$I^*(p,q) \simeq \left(\frac{1.44\,\Delta\lambda_S}{10^9} \right) n_g^{1/2} \left(\frac{I_{b.b.}(\lambda_o)\, g_p\, A(p,q)(E_p-E_q)\, B_p\, e^{-E_p/KT_e}\, \delta}{\Delta\lambda_D\, g_g} \right)^{1/2} \qquad (4.4.2)$$

I^* is in W/cm^2 if δ is in cm, $I_{b.b.}$ is in W/cm^2 Å st. , E in eV, and if $\Delta\lambda_D$, $\Delta\lambda_S$ are in Å. Under the present experimental conditions, the main resonance lines are strongly absorbed when the ground state densities are greater than $\sim 10^{13}$ cm^{-3}. The deviation parameters are ~ 1 for lower levels as LTE conditions are imposed when F(p,q) tends to zero. In the case of the optically thick multiplets, account was taken of overlapping lines.

For a wide range of values $\Delta\lambda_S$ is proportional to the electron density and relatively insensitive to temperature. Thus the total radiative power loss is proportional to $n_e\, n_i^{1/2}$. Temperature changes affect I^* through the term $I_{b.b.}\exp(-E_p/kT_e)$, the temperature dependence associated with the Doppler width being negligible by comparison.

Expressing the total loss for a single ion species in the form,

$$I_T^*(k,i,kT_e) = \sum_p I^*(k,i,p,q,kT_e) = n(k,i,g)^{1/2}\,\phi(k,i,n_e,kT_e) \qquad \text{.....(4.4.3)}$$

then the temperature dependence of the ratio of the densities ofsuccessive ion species must be evaluated. For Carbon (k=1) or Fluorine (k=2), if doubly-charged ions (i=3) are taken to represent the average ion stage,

$$I_T^*(k,n_e,kT_e) = \sum_i I_T^*(k,i,kT_e)$$

$$= n(k,3,g)^{1/2}\left[\phi(k,3,n_e,kT_e) + \left(\frac{\alpha_{cr}(k,2,n_e,kT_e)}{S_{cr}(k,2,n_e,kT_e)}\right)^{1/2}\phi(k,2,n_e,kT_e)\right.$$

$$\left. + \left(\frac{S_{cr}(k,4,n_e,kT_e)}{\alpha_{cr}(k,4,n_e,kT_e)}\right)^{1/2}\phi(k,4,n_e,kT_e)\right] \qquad \text{.....(4.4.4)}$$

Total Continuum-Radiation Loss from the Plasma

Recombination radiation represents a loss of ion potential energy at a total rate,

$$L_C^* = \sum_k \sum_i \sum_n n_e n(k,i+1,g)\,\alpha(k,i,p)\,\chi(k,i,p) \qquad (4.4.5)$$

Seaton[1] has derived an expression for the kinetic energy lost by recombining electrons, i.e.,

$$\sum_K \sum_i \sum_n n_e n(k,i+1,g)\,\alpha^*(k,i,p)\,kT_e$$

$$\text{where } \frac{\alpha^*}{\alpha} = \frac{0.51\ln(\chi_p/kT_e) + 0.64(\chi_p/kT_e)^{-1/3} - 0.0713}{0.51\ln(\chi_p/kT_e) + 0.469(\chi_p/kT_e)^{-1/3} + 0.4288}$$

$\alpha^* \simeq \alpha$ when $\chi_p \gg kT_e$, in which case, the total energy loss is obtained by replacing χ_p by $\chi_p + kT_e$ in equation (4.4.5)

The total Bremsstrahlung loss is approximated by the expression[2],

$$\sum_k \sum_i 1.42\times10^{-32}\, Z^2\, n_e n(k,i,g)\, kT_e^{1/2}$$

The loss is in W/cm^3 if kT_e is in eV. When $(\chi_g/kT_e) \gtrsim 3$, the total Bremsstrahlung loss is small compared to the recombination loss.

The plasma is transparent to the recombination radiation if $\tau(\nu) \lesssim 0.1$.

$$\tau(\nu) = \hat{\chi}\,\delta \simeq n(k,i,p)\ \sigma(k,i,p,\nu)\ \delta$$

Using the value of $\sigma(k,i,p,\nu)$ in equation (4.3.7) at the absorption head, where it is largest, the criterion for transparency becomes,

$$n(k,i,p) \lesssim \frac{4\times10^{14}\ g(k,i,p)\ \chi(k,i,p)}{g(k,i+1,g)\quad \delta}$$

This criterion was satisfied for all the ions in the plasma, which will then also be transparent to the Bremsstrahlung[3], using the free-free absorption coefficient[4].

References

1. M.J.Seaton, Mon.Not.R.A.S., 119, p.81, 1959

2. G.Elwert, Z.Naturf., 9a, p.637, 1954

3.R.Wilson, J.Qu.Sp.Rad.Tr.,2, p.477, 1962

4. L.Spitzer Jr.,'Physics of fully ionized gases',Interscience,N.Y.,1956

Chapter Five

Experimental Study of the Plasma Source

5.1 Introduction

A description is given of the electrical and optical apparatus used for diagnosing the plasma and the means by which the operating characteristics of the source were determined. Most of the work involved spectroscopic measurements, and some new diagnostic methods had to be developed to deal with the non-thermal plasmas produced.

The electrical parameters namely, the current and voltage distributed around the circuit, were measured using a Rogowski coil and high-voltage probes. From these measurements, and assuming a uniform current sheet structure, the power delivered to the plasma, the plasma resistance and inductance and the driving magnetic field were deduced. The value of the electron temperature derived from the plasma resistivity is compared with the value determined spectroscopically as a basis for assessing some of the assumptions made.

Quantitative Spectroscopic measurements were made using a monochromator and a spectrometer in the visible and ultra-violet regions. Particle densities and temperatures were determined from spectral line intensity measurements, as were the total radiative losses and, by isolating certain ion lines, the energy and velocity structure within the expanding plasma plume was also examined.

High speed photographs were taken which traced the developement of the discharge, the shape and uniformity of the plasma plume and its expansion velocity.

5.2 Instrumentation

Electrical Measurements

The current through the discharge was measured with the aid of a Rogowski coil which consisted of a few hundred turns of thin gauge wire wound onto a toroidal former of minor diameter ~ 2 cm and major diameter ~ 6 cm. The coil inductance (L_o) was 87.9 μ Henries and the resistance 4.73 Ohms. The output from the coil, being proportional to the rate of change of the current enclosed by it, was fed to a symmetrical double R-C integrator and from there to an oscilloscope via a differential amplifier. The integrator consisted of a 47 kOhm resistance (R_o) shunted by a capacitor of 5000 pF, having a time constant of $\sim$ 235 μ sec. The output is, in this case, proportional to the current for times less than $\sim 100\ \mu$ sec. and frequencies less than R_o/L_o, i.e. 50 MHz, greater than the band-width of the oscilloscope. The coil was calibrated by using a flat copper 'shorting strip' in place of the plasma, and measuring the voltage peaks of the periodic discharge. The spread in the logarithmic decrement, which was mainly due to variations in the spark-gap resistance, was less than 5% in this case. Voltages around the circuit were measured using Tektronix P6013A high voltage probes. These had an attenuation of 1000 : 1, a rise-time of 14 nsec. and a maximum rating of 12 kVolts at frequencies up to 100 kHz, falling to 5.5 kVolts at 1 MHz.

Optical Measurements

The optical system was designed to allow accurate scanning in any direction in the plasma plume, using the spectrograph and monochromator for simultaneous spatial and time-resolved line intensity measurements. The lay-out and scanning arrangement are shown in figs. 5.2.1 and 5.2.2 respectively.

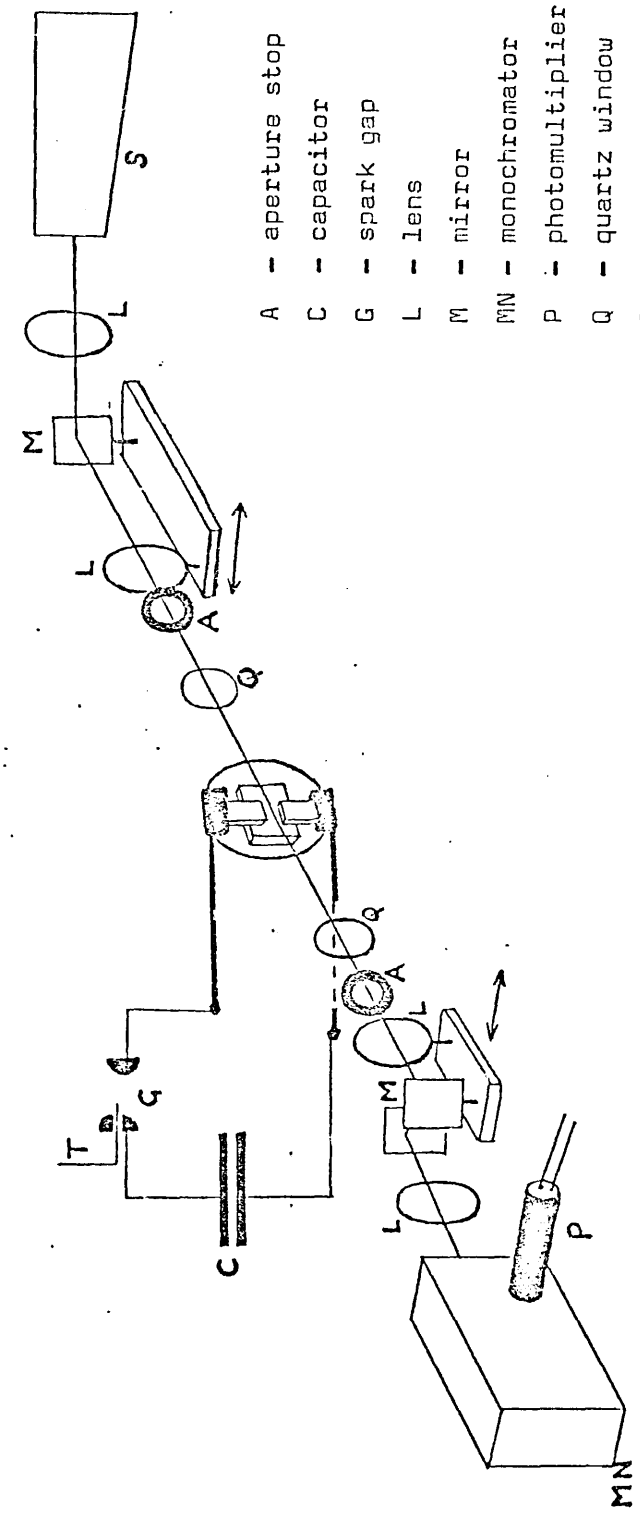
A - aperture stop
C - capacitor
G - spark gap
L - lens
M - mirror
MN - monochromator
P - photomultiplier
Q - quartz window
S - spectrograph
T - triggering electrode
S
L
M
L
A
Q
Q
A
L
M
L
P
MN
C
T
G

Fig. 5.2.1

FIG. 5.2.2

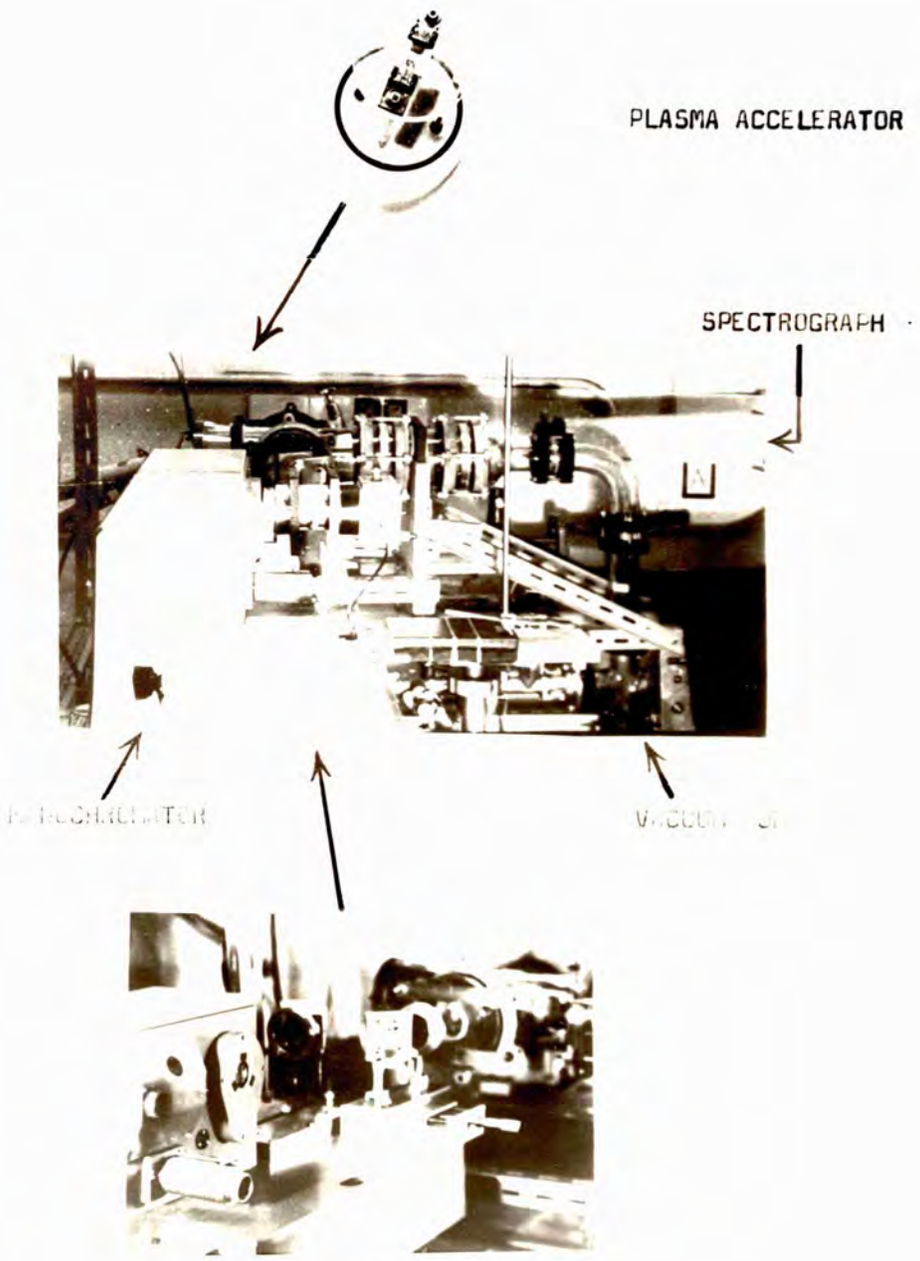

SCANNING SYSTEM

Double-mirror double-lens systems were used in order to ensure that the central part of the plasma remained in focus on the entrance slits during a scan. The plasma was focussed with the centre of the electrode gap coincident with the central optic axis of each instrument. For time - resolved measurements, a photomultiplier tube rigidly held to the exit slit of the monochromator was used, with its photocathode 2.5 cm. from the slit. In this way the phototube window was illuminated with a diffuse cone of light, thereby avoiding any errors arising from non-uniformities in the photocathode response. The accelerator mount was rotateable through 90^{o} so that scans could be made in the axial direction.

The monochromator was a Hilger and Watts D-275 Littrow dispersion device, having interchangeable glass and silica prisms and with a relative aperture of f/16 . This instrument is stigmatic, covering a wavelength range from 1600 Å to 18000 Å. A calibrated wavelength drum provided an accuracy of $\pm$ 2 Å at 2000 Å and $\pm$ 5 Å at 6000 Å . The input slit jaws were straight whilst the output jaws were curved to account for image curvature. Both sets of jaws operated symmetrically and synchronously by means of a single cam and lever mechanism, with a scale provided for slit width settings between 0.001 mm. and 2.0 mm.

The spectrograph was a Hilger and Watts medium quartz instrument with a relative aperture of f/22 and a minimum slit width of 0.002 mm. It covered a wavelength range of 2000 Å to 10000 Å . Ilford HP3 photographic plates were used to record the time- integrated spectra. For the time-resolved studies, an E.M.I. 9592B 11-stage photomultiplier was used. It had a time response of 20 nsec. and an S-10 spectral response which, with its quartz window gave it a range of 1800 Å to 8000 Å .

The mirrors used in the scanning assemblies were Al - MgF coated optical flats supplied by Rank Precision Industries Ltd. with a measured reflectivity of between 82% and 90% in the visible - Ultra-violet region.

Quartz lenses were used throughout, and the viewing windows on the vacuum system were 2 mm. thick quartz discs. The anode current of the photo - multiplier was passed through a load resistor of either 1 kOhm or 5 kOhm and the voltage across it measured with a Tektronix 556 oscilloscope, which had a bandwidth of 50 MHz.

The relative aperture of the imaging system was made less than that of each dispersing instrument, thereby enabling the collimator and prism in each case to be equally filled from all points on the entrance slit to a height of 1 cm. A stop placed in front of the first imaging lens enabled a cone of light of half angle $\tan^{-1} 1/25$ to be recieved. By means of another movable, variable stop positioned in front of the monochromator entrance slit, different portions of the source were observed. For stability all the optical components were mounted on a spring-tensioned, micrometer-driven base, and the complete accelerator assembly was securely bolted to the floor so that no displacement occured during each shot which would alter the portion of plasma being viewed.

The high speed photographs were made with a Beckman and Whitley model 500A biplanar image converter camera having a spatial resolution of 12 line pairs per mm. and fitted with an 85 mm. f/1.4 objective lens. The spectral response ranged from 3500 Å to 6500 Å, and a range of exposure times greater than 5 nsec. were available which could be delayed in time steps of 100 nsec. The inherent camera delay was 300 nsec. Because of the high-voltage gradient in the biplanar tube (120 kV/cm.), the linearity of the object to image conversion is maintained even in the presence of large external electromagnetic fields.

A relative calibration of the HP3 plates was carried out both by superimposing many shots and by varying the aperture stop. The spectrograph was not shuttered so that the time resolution for each shot was governed by the length of the plasma plume and its velocity, being typically about 2 μsec.

The line profiles on the plates were measured using a Joyce Loebl Mk. IIIc automatic recording micro-densitometer with a calibrated linear optical attenuating wedge for reference. The effective scanning aperture of this instrument was adjustable upwards from $\sim 1\,\mu$m. and could be matched to the slit width of the spectrograph, producing a scanning behaviour equivalent to a monochromator system.

Absolute calibration of the recording system in the visible region (3000 Å to 7000 Å) was carried out using a secondary standard tungsten strip lamp, which was calibrated by the General Electric Company against a National Physical Laboratory primary standard. The calibration was extended to below 3000 Å by relating the intensities of the C II multiplets at 2510 Å and 2747 Å and the C III 2163 Å line to the intensities of various lines in the visible region (see Appendix). The spectral intensity of the lamp was determined from the theoretical black-body emission together with the known spectral emissivity of the tungsten ribbon[1] at the true temperature of the lamp, which was 2798 ^{o}K .

Reference

1. J.C.deVos, Physica, 20, p.690, 1954

5.3 Spectroscopic diagnostic methods

Total line intensities of C II, C III, C IV and F II lines from the plasma were measured using the monochromator and from these n_e , kT_e and n_i determined. The total intensity of a spectral line representing an ionic transition between states p and q is,

$$I(p,q) = \frac{n(p)A(p,q)h\nu(p,q)\,\delta}{4\pi} \qquad (5.3.1)$$

where δ is the geometrical depth of the emission, assumed uniform. Equation (5.3.1) is a particular solution of the more general equation of radiative transfer[1] in which the plasma was assumed to be homogeneous, and optically transparent to this line, and stimulated and scattered radiation was neglected. Often, however, and especially in the case of resonance line radiation, absorption must be accounted for. The radiant intensity per unit solid angle per unit frequency from the plasma in the general case is given by,

$$\frac{dI(\nu)}{dx} = \hat{\mathcal{E}}(\nu,x) - I_\nu(x)\,\hat{\chi}(\nu,x) \qquad (5.3.2)$$

where $\hat{\mathcal{E}}(\nu,x)$ is the spectral emissivity defined as,

$$\hat{\mathcal{E}}(\nu,x) = n(p)L_1(\nu)\,\frac{h\nu}{4\pi}\,(A(p,q) + I_\nu B(p,q)) \qquad (5.3.3)$$

and $\hat{\chi}(\nu,x)$ is the absorption coefficient defined by,

$$\hat{\chi}(\nu,x) = n(q,x)L_2(\nu)\,\frac{h\nu}{4\pi}\,B(q,p) \qquad (5.3.4)$$

$L_1(\nu)$ and $L_2(\nu)$ are the emission and absorption line profile functions.

For any line L_1 can be put equal to L_2 provided that the radiative lifetime is much longer than the ion collision times[2], in which case the two processes of emission and absorption can be assumed independant. It has been shown[3] that the neglect of a variable source term in finding solutions to equation (5.3.2) will generally result in an error of less than 10%. To account for the resonance lines, it is assumed here that scattering and stimulated emission are negligible, that the density of emitters and absorbers is constant over the plasma thickness δ , but that absorption is not negligible. The solution of equation (5.3.2) then becomes,

$$I(\gamma,x) = \frac{\hat{\varepsilon}(\gamma,x)}{\hat{\chi}(\gamma,x)}\left(1-e^{-\hat{\chi}\delta}\right) \qquad (5.3.5)$$

S_γ , the source function $= \hat{\varepsilon}/\hat{\chi}$ and $\hat{\chi}\delta$ is the optical depth τ . Integrating over the line shape, equation (5.3.5) reduces to equation (5.3.1) when τ is small. The use of the latter is therefore justified provided that deviations using this simplification are less than 10%, i.e. if

$$\left|\frac{I(\gamma,0) - S_\gamma\tau_\gamma}{S_\gamma\tau_\gamma}\right| \ll 0.1$$

Expanding equation (5.3.5) this criterion becomes,

$$\tau_\gamma \ll 0.2 \qquad (5.3.6)$$

Knowledge of the line shape is required in order to check the above criterion. Cooper[4] has considered the case of Doppler (Gaussian) and Stark (Lorentzian) profiles for which respectively, the criteria become,

$$n(q,x) \leq 8\times10^{18}\,\Delta\lambda_D/\lambda_o^2\,\delta\,f(P,q) \qquad (5.3.7)$$

$$n(q,x) \leq 1.2\times10^{19}\,\Delta\lambda_S/\lambda_o^2\,\delta\,f(P,q) \qquad (5.3.8)$$

When the inequality of equation (5.3.6) is not fulfilled, (5.3.5) becomes,

$$I(p,q,\gamma) = \frac{B_p^{**}\, 2h\gamma^3 \left(1-e^{-\tau_\gamma}\right)}{B_q^{**} c^2 \left(e^{\frac{(E_p-E_q)}{KT_e}} - \frac{B_p^{**}}{B_q^{**}}\left(1-e^{-\tau_\gamma}\right)\right)} \qquad (5.3.9)$$

where B_p^{**} is the wholly or partially optically thick deviation parameter described in chapter four. These approach unity as τ_γ becomes large and the intensity at frequency γ approaches the black-body value.

From absolute measurements of total line intensities, the population densities of the upper levels of an ion from which the transitions originate can be determined. To obtain the more general parameters n_e, n_i and kT_e, a relationship between these upper levels and the free electrons or ground state ions is required. For all the levels of an ion, using equations (5.3.1) and (4.2.12) one obtains,

$$I(p,q) = \left(\frac{h^2}{2\pi m_e KT_e}\right)^{3/2} \frac{A(p,q)\, g_p\, h\gamma(p,q)\, \theta_p\, n_e\, n'(g)\, \delta}{8\pi\, g'_g\, e^{-\chi_p/KT_e}} \qquad (5.3.10)$$

($'$ refers to the next highest ion stage.)

more conveniently this becomes,

$$I(p,q) = \frac{2\cdot 618\times 10^{-38}\, A(p,q)\, g_p\, n_e\, n'(g)\, \theta_p\, \delta}{(KT_e)^{3/2}\, \lambda(p,q)\, g'_g\, e^{-\chi_p/KT_e}} \qquad (5.3.11)$$

I is in W/cm^2 st. if λ is in Å, kT_e and χ are in eV., n_e and n_i are in cm^{-3} and δ in cm.

From the intensity ratios of pairs of lines whose upper levels both lie above the thermal limit in the case of a partial LTE plasma, and thus for which the deviation parameters θ are ~ 1, the following simplification

results,

$$\frac{I(p,q)}{I(r,s)} = \frac{g_p\, A(p,q)\, e^{(\chi_p - \chi_r)/kT_e}}{g_r\, A(r,s)} \qquad (5.3.12)$$

this method is not ideal, as two lines from the same ion stage must be chosen whose upper levels are widely separated in energy in order that the exponential term be sufficiently temperature- sensitive to overcome the inherent errors associated with both the intensity measurements and the values of the transition probabilities. If the partial LTE conditions are such that the thermal limit is high up in the level scheme, the choice of lines as well as the level separations becomes reduced. From the analysis of section 4.2 it would seem that an alternative approach would be to relate the level populations of widely separated terms to the ground state density using the B-parameters. However,in non-thermal plasmas these parameters depend upon a large number of other rate coefficients which could introduce more uncertainty than does the assumption that the θ parameters are ~ 1, especially as, in the case of non-hydrogenic ions, one cannot expect a general trend in B-values with increasing principal quantum number.

The use of equation (5.3.12) does not require knowledge of the electron or ion densities, but if I is measured absolutely, then the product of $n_e\, n(k,i+1,g)$ can be determined once kT_e is known, using equation (5.3.11), and n_e can be inferred. As already outlined, the fine structure levels of each term are assumed to be in thermodynamic equilibrium amongst themselves. When transitions between such multiple states occurs (i.e. multiplet emission) average rate coefficients and transition probabilities can be used, which enables the terms to be treated as though they were single levels. Total multiplet intensities must then be measured but, as the multiplet spread is often less than the Stark or Doppler widths of each component, this is generally unavoidable . The average coefficients are defined by,

$$\overline{A(p,q)} = \frac{\sum_p \sum_q g_p A(p,q)}{\sum_p g_p} \qquad (5.3.13)$$

In order to overcome the low temperature sensitivity when line ratios from the same ion stage are used, those from successive stages can be employed, with a substantial enhancement of the exponential term. Careful choice of the lines can result in very accurate measurements of kT_e and hence n_e. Using the Saha-Boltzmann equation for the lower ion stage, the ratio is,

$$\frac{I(p,q)}{I'(r,s)} = \frac{1.66\, g_p\, n_e\, \theta_p\, A(p,q)\, \lambda'(r,s)}{10^{22}\, g'_r\, kT_e^{3/2}\, A'(r,s)\, \lambda(p,q)\, B'_r}\, e^{\left(\frac{\chi_p + E'_r}{kT_e}\right)} \qquad (5.3.14)$$

where primes refer to the higher ion stage and kT_e is in eV.

It was found in section 4.2 that for the lower ion stage, if the upper level of the transition is above the thermal limit, which it should be easy to arrange, $\theta_p \simeq 1$. For the upper ion stage, it was also shown that for irregular levels below the thermal limit, n_e/B'_r could be taken as constant in value over a wide density range. Consideration of these facts for the C II line at 4267 Å and the C III line at 5696 Å shows[5] that over a density range 10^{15}cm^{-3} to 10^{18}cm^{-3}, n_e/B'_r does not vary a great deal and so n_e need not be known in order to accurately determine the temperature. The ratio of the intensities of these lines is shown in fig. 5.3.1 for both optically thin plasma, and a plasma optically thick to resonance radiation. The intensity of two lines from the same ion is given by equation (5.3.12) multiplied by the factor B_p/B_r. If lines are observed which originate from irregular levels suitably separated, this

Fig. 5.3.1

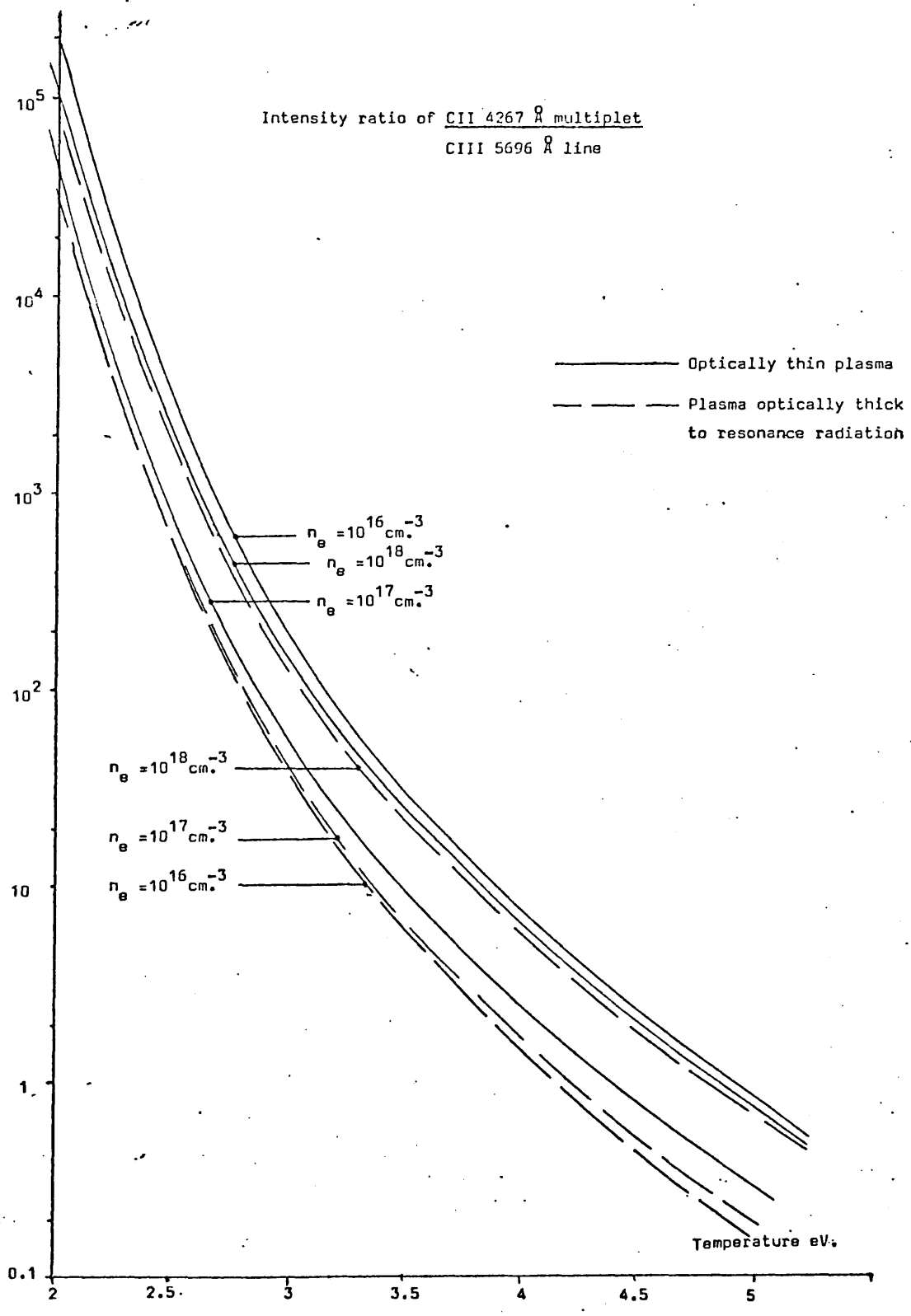
Intensity ratio of CII 4267 Å multiplet
CIII 5696 Å line
Optically thin plasma
Plasma optically thick to resonance radiation
$n_e = 10^{16}$ cm.$^{-3}$
$n_e = 10^{18}$ cm.$^{-3}$
$n_e = 10^{17}$ cm.$^{-3}$
$n_e = 10^{18}$ cm.$^{-3}$
$n_e = 10^{17}$ cm.$^{-3}$
$n_e = 10^{16}$ cm.$^{-3}$
10^5
10^4
10^3
10^2
10
1
0.1
2
2.5
3
3.5
4
4.5
5
Temperature eV.

factor is density dependant in the non-thermal case, enabling n_e to be determined if kT_e is known[5]. The ratios of the intensities of the C III lines at 2297 Å and 5697 Å for plasmas optically thin or thick to resonance radiation are shown in fig. 5.3.2. These curves relate to plasmas optically thin to both of these lines, such as would be the case if C III were an impurity. If self-absorption is important the curves could be modified or, more conveniently, the local values of the line intensities had reabsorption been unimportant could be deduced.

From a comparison between the Stark and Doppler widths it is generally the case that the latter dominates near the line centre whereas a Stark profile alone describes the wings (Griem [6]). When the line is strongly self-absorbed, equation (5.3.5) shows that the intensity around the peak reaches the black-body value. The total observed line intensity I^* can then be approximated as a band of black-body radiation centred around the line peak and with a bandwidth equal to the separation on the profile of those points at which the otherwise non-absorbed line would have fallen to the black-body value. At these points, distance $\Delta\lambda$ from the line centre λ_o, $\tau(\lambda_c \pm \Delta\lambda)$ will be of the order unity and the contribution from further out in the wings will be small. Thus,

$$I^* = \int_{\lambda_o-\Delta\lambda}^{\lambda_o+\Delta\lambda} I_{b.b.}(\lambda_o)\,d\lambda \sim I_{b.b.}\,2\Delta\lambda \qquad (5.3.15)$$

For lines strongly absorbed, $\Delta\lambda$ will be sufficiently far out on the profile that Stark broadening dominates and, for the unperturbed line, this approximation leads to

$$I(\Delta\lambda) = I(\lambda_c)\left(1+\left(\frac{\Delta\lambda}{\Delta\lambda_S}\right)^2\right)^{-1} = I_{b.b.}(\lambda_c)$$

As $\Delta\lambda$ is greater than $\Delta\lambda_S$,

$$\Delta\lambda^2 \simeq \frac{I(\lambda_o)\Delta\lambda_S^2}{I_{b.b.}(\lambda_o)} \qquad (5.3.16)$$

Fig. 5.3.2

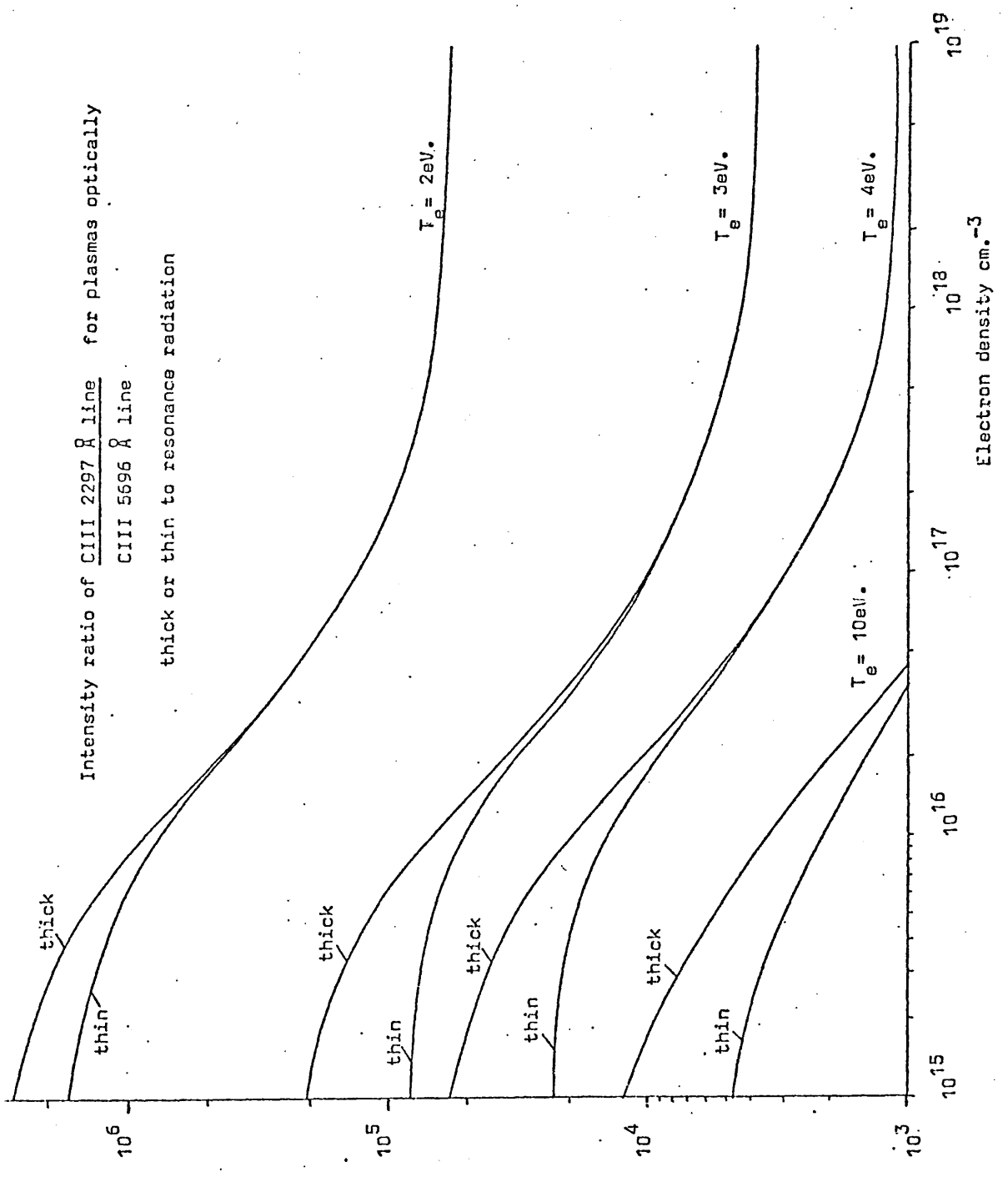
Intensity ratio of CIII 2297 Å line / CIII 5696 Å line for plasmas optically thick or thin to resonance radiation
T_e = 2eV.
T_e = 3eV.
T_e = 4eV.
T_e = 10eV.
thick
thin
10^6
10^5
10^4
10^3
10^{15}
10^{16}
10^{17}
10^{18}
10^{19}
Electron density cm.$^{-3}$

As a Doppler profile is appropriate near the line centre,

$$I_{total}\ (\text{unperturbed}) \simeq I(\lambda_o)\Delta\lambda_b \left(\frac{\pi}{1.67}\right)^{1/2} \simeq I(\lambda_o)\Delta\lambda_b \qquad (5.3.17)$$

Thus, with equation (5.3.15),

$$I_{total}(\text{unperturbed}) \simeq \frac{\Delta\lambda_b I^{*2}}{4\Delta\lambda_s^2 I_{b.b.}(\lambda_c)} \qquad (5.3.18)$$

The relaxation times for reaching a steady state equilibrium between ionic levels is, in most cases, less than the inverse collisional excitation or de-excitation rates from the ground states to the first few resonance levels, being less than $\sim 10^{-8}$ sec. under the present conditions. These times are at least an order of magnitude smaller than times in which plasma conditions vary significantly as a result either of variations in the current or mixing with the ablated plasma coming from the dielectric. A similar situation exists for the ionization balance between the ion stages C I to C III and F I to F III so that a time independant model may be used for this plasma. Even for the C III - C IV balance at $kT_e \sim 3$ eV, $\tau_{relax.}$ is $\sim 10^{-6}$sec. As temperature variations are not large and the temperature is sufficiently low that ionization into C IV and C V (relatively 'stable' Li-like and He-like ions) is not pronounced, errors involved in using a time independant model for this balance should be small.

The spectral intensity of recombination radiation into level p of an ion i is given by,

$$I(\nu)_{rec.} = \int n_e\, n(k,i+1,g)\, \alpha(k,i,p,\nu)\, h\nu\, dx \qquad (5.3.19)$$

From equation (4.3.6),

$$I(\nu)_{rec.} = \int \frac{g(i,p)\, 2^{1/2} h^4 \nu^3 n_e n(i+1,g)\, \sigma(\nu)\, e^{\left(\frac{\chi_p - h\nu}{kT_e}\right)}}{g(i+1,g)\, \pi^{1/2} c^2 (kT_e m_e)^{3/2}} dx \qquad (5.3.19A)$$

The intensity per unit wavelength interval becomes, assuming spatial uniformity over a path length δ,

$$I(\lambda)_{rec.} = \frac{g(i,p) \left(\frac{2}{\pi}\right)^{1/2} h^4 c^2\, n_e n(i+1,g)\, \sigma(\lambda)\, \delta\, e^{\left(\frac{\chi_p - hc/\lambda}{kT_e}\right)}}{g(i+1,g)\, (m_e kT_e)^{3/2}\, \lambda^5} \qquad (5.3.20)$$

which, for Hydrogenlike ions becomes, from equation (4.3.7) using the expression for the cross-section derived by Seaton[7],

$$I(\lambda)_{rec.} = \frac{h^4 2^3 \hat{n}_p\, \chi_p^3\, g(i,p)\, n_e n(i+1,g)\, \delta\, e^{\left(\frac{\chi_p - hc/\lambda}{kT_e}\right)}}{(c Z \pi e m_e)^2\, 3^{3/2}\, Z^2 g(i+1,g)\, \lambda^2 (m_e kT_e)^{3/2}} \qquad (5.3.21)$$

$\hat{n}_p$ is the principal quantum number of level p .

The spectral intensity of the Bremsstrahlung resulting from the interaction of free electrons having a Maxwellian velocity distribution, with ions of charge Z_i has been given by Elwert[8],

$$I_{Br}(\lambda) = \frac{1.9 \times 10^{-28} n_e n(i+1,g)\, Z^2\, g_I\, e^{\left(\frac{-hc}{\lambda kT_e}\right)}}{\lambda^2 (kT_e)^{1/2}} \qquad (5.3.22)$$

g_I is the free-free Gaunt factor and is of order unity. I_{Br} is in units of W/cm^2 Å st. if kT_e is in eV and λ in Angstroms. The total continuum intensity is

$$\left(\frac{n_e\, n(k,3,g)\,\delta}{\lambda^2\,(kT_e)^{1/2}}\right)\times\left[\frac{n(k,2,g)}{n(k,3,g)}\left(\sum_p \frac{K_1\, e^{\left(\frac{\chi_p-h\nu}{kT_e}\right)}\chi_p^3\,\hat{n}_p}{kT_e} + K_2\, e^{\frac{-h\nu}{kT_e}}\right)\right.$$

$$\left.+\left(\sum_p \frac{K_1\, e^{\left(\frac{\chi_p-h\nu}{kT_e}\right)}\chi_p^3\,\hat{n}_p}{4kT_e} + 4K_2\, e^{\frac{-h\nu}{kT_e}}\right)+\frac{n(k,4,g)}{n(k,3,g)}\left(\sum_p \frac{K_1\, e^{\left(\frac{\chi_p-h\nu}{kT_e}\right)}\chi_p^3\,\hat{n}_p}{9kT_e} + 9K_2\, e^{\frac{-h\nu}{kT_e}}\right)\right] \quad \ldots\ldots(5.3.23)$$

where k_1 and k_2 are constants. The doubly ionized species is separated here because, at temperatures around 3 eV, the first and third terms in the previous equation are much smaller than the second term. The ratios of the ion stages are much less than unity, at any particular wavelength for Carbon or Fluorine, under the plasma conditions here. Thus, as the total density of doubly ionized ions is 1/2 n_e, measurement of the continuum intensity in a line-free spectral region should give a value proportional to n_e^2 if the temperature remains approximately constant.

Line broadening measurements

The elctron density can also be obtained from measurements of the Stark widths and shifts of isolated spectral lines, provided that these can be distinguished from other broadening mechanisms, which in plasmas are predominantly due to thermal motion of the emitting ions or self-absorptiom. The Stark broadening theory relevant to lines from neutral and ionized atoms has been developed extensively by Griem[6,9,10] and Baranger[11,12]. From their results parameters for determining shifts and widths have been obtained which agree with experimental results to within a factor of two for a large number of atoms including those species present in this experiment.
The classical path approximation is generally used in which ions or electrons, considered as point charge perturbers, follow straight paths near neutral atoms, or hyperbolic paths[13,14] in the case of ions. For perturbation methods to be valid using this assumption, the impact parameter b must be less than

$h/m_e v$, in which case the average interaction is 'weak' or long-range. This condition can be shown to be satisfied for a wide range of plasma conditions. It is found[11] that most of the broadening comes from these long-range interactions mainly because there is a cut-off in the broadening that a close collision can cause. Thus occaisonal strong collisions can be neglected. Adiabaticity is also generally assumed, which means that energy exchanges between the perturber and the atom or ion are small compared to the perturber energy, having no effect therefore on its trajectory. When the collision duration τ_c is $\gg \frac{1}{\Delta\omega}$ where $\Delta\omega$ is the angular frequency separation of the emission from the line centre, the atom or ion will experience a static perturbing field, which is the basis of the quasi-static approximation method. The broadening in this case is calculated from the splitting due to an arrangement of static charged perturbers, averaged over all possible field distributions and including the effect of Debye shielding. If τ_c is $\ll \frac{1}{\Delta\omega}$, perturber motions must be considered. This treatment is known as the impact approximation and is appropriate for weak interactions as several impacts take place during the temporal bandwidth of the line. An optical radius $\tilde{r}$ can be defined by[9]

$$\pi \tilde{r}^2 n_e v = \omega \qquad \text{with} \quad \tau_c = \tilde{r}/v$$

thus, for a thermal distribution of particles,

$$\frac{1}{\Delta\omega} = \left(\frac{\omega}{\pi n_e}\right)^{1/2} KT_e^{-3/4} m^{3/4} \qquad (5.3.24)$$

defines the boundary point on the profile between the two limiting approximations. The impact approximation will be valid for both electrons and ions very close to the line centre but, as $m_i \gg m_e$, it will be valid for electrons much further out in the wings than for the ions. Baranger[12] has derived an expression for electron impact broadening where the full half-width w_s for a dispersion profile, due to inelastic and elastic collisions in non-hydrogenic ions namely, is

$$\omega_s = \frac{n_e}{2}\left\langle v\left[\sum_{i'}\sigma_{ii'} + \sum_{f'}\sigma_{ff'} + \left(\int|\phi_i(\theta,\psi) - \phi_f(\theta,\psi)|^2 d\Omega\right)\right]\right\rangle \qquad (5.3.25)$$

where $\sigma_{ii'}$ is the inelastic cross-section for a collisional transition from initial level i to a perturbing level i' and similarly for final levels f,f'. $\phi_i(\theta,\psi)$, $\phi_f(\theta,\psi)$ are the elastic scattering amplitudes of the initial and final states. Most broadening collisions are inelastic if the energy separation ΔE to the nearest or strongest perturbing level is $< kT_e$ when the adiabatic assumption is also valid. This is not so if ΔE is $> kT_e$, such as may be the case with low lying ionic levels, where the acceleration of an electron in the Coulomb field of an ion leads to large cross-sections around threshold. At low values of kT_e the inelastic collision cross - section becomes small and elastic and superelastic collisions become the main broadening interactions. Griem[10] has extrapolated the inelastic cross-section in the limit of zero perturber energy to account for broadening in this situation, without directly calculating the elastic contribution. Using Van Regemorters semi-empirical Gaunt factor, agreement to within 50% was obtained with experimental values for many lines with values of $KT_e/\Delta E$ ranging from 0.5 to 50.

Further simplifications in the calculations of ion line widths and shifts are often made. For example, in many plasmas, splitting of energy levels by ionic fields can be neglected during the duration of an electron collision[10] and often, because the polarizability of the atom increases with increasing principal quantum number, interaction in the lower state of a transition can be neglected. Griem has calculated parameters for determining widths and shifts of lines from neutral and singly ionized ions, including Carbon and Fluorine, using the adiabatic and classical path approximations. Parameters $\underline{\omega}$, $\underline{\alpha}$ and $\underline{d}$ are tabulated from which half-widths and shifts are derived using the following expressions,

$$\Delta\lambda_S = \frac{2}{10^{16}}\left[1 + 1{\cdot}75\times10^{-4} n_e^{1/4}\,\underline{\alpha}\left(1 - 0{\cdot}068\, n_e^{1/6} T_i^{-1/2}\right)\right] n_e \underline{\omega} \qquad (5.3.26)$$

$$\Delta\lambda_{SHIFT} = \frac{1}{10^{16}}\left[\frac{\underline{d}}{\underline{\omega}} \pm 2\times10^{-4} n_e^{1/4}\,\underline{\alpha}\left(1 - 0{\cdot}068\, n_e^{1/6} T_i^{-1/2}\right)\right] n_e \underline{\omega} \qquad (5.3.27)$$

In the temperature range covering the steady-state appearance of neutral or singly ionized ions, these parameters are weakly temperature dependant. Generally the second terms in equations (5.3.26) and (5.3.27), representing the ion influence is small, and measurement of Stark widths and shifts gives a direct measurement of n_e, independant of any specified distribution among bound energy states.

Quantitative spectral measurements

With the photorecording system the integral $\int_{\lambda}^{\lambda+\Delta\lambda} I(\lambda)\, d\lambda$ is recorded, where $\Delta\lambda$ is the total bandwidth. The entrant flux to the monochromator is

$$F_{in}(\lambda)\,d\lambda = G\, s_1\, I(\lambda)\, d\lambda \qquad (5.3.28)$$

G is a geometrical factor for the imaging system, assumed independant of wavelength, which incorporates the aperture stops, etc. s_1 is the input slit width. At a wavelength setting λ_o, the emergent radiant flux is proportional to that entering and can be expressed through,

$$F_{out}(\lambda)\,d\lambda = F_{in}(\lambda)\,\gamma(\lambda)\,\underline{\delta}(\lambda-\lambda_o)\,d\lambda \qquad (5.3.29)$$

where γ is the overall efficiency representing reflection, transmission, diffraction losses, astigmatism, spurious reflections, non-focus etc. $\underline{\delta}(\lambda-\lambda_o)$ is a slit function, being the relative transmission of the instrument for a particular combination of slit widths and representing

the extent to which the image of the input slit overlaps the exit slit. When one slit is wider than the other, uniform transmission results for a bandwidth equal to $(s' - s'')/D$, falling linearly to zero at either side of this region and presenting a total bandwidth of $(s' + s'')/D$. s' is the larger of the two slits and $1/D$ is the inverse dispersion of the instrument.

$\underline{\delta}$ -functions for the three basic combinations of rectangular slits are shown below.

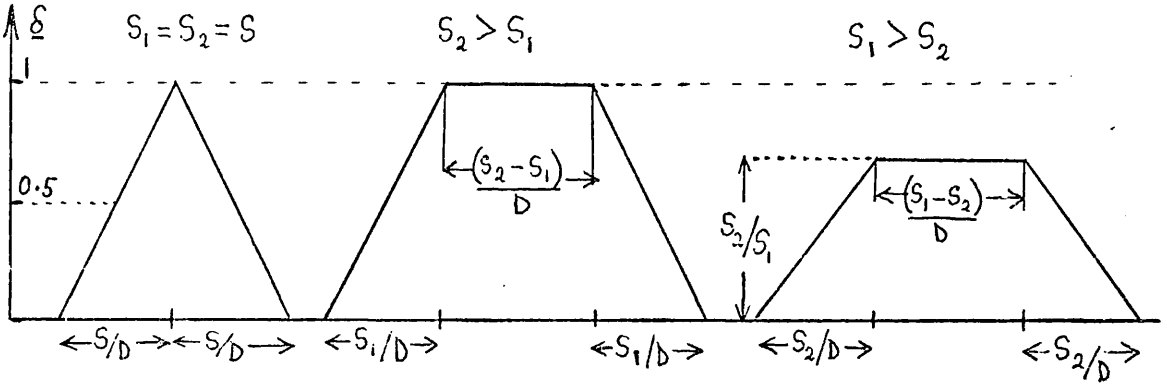

Any deviations due to imperfect alignment of the slits or diffraction effects are accounted for in $\gamma(\lambda)$

The total emergent flux is $F'_{out}(\lambda_o) = \int F_{out}(\lambda)\, d\lambda$

$$\text{i.e. } F'_{out}(\lambda_o) = G\, s_1\, \gamma(\lambda_o) \int_{\lambda}^{\lambda+\Delta\lambda} I(\lambda)\, \underline{\delta}(\lambda - \lambda_o)\, d\lambda \qquad (5.3.30)$$

assuming that γ is constant over the bandwidth.

When viewing a spectral line, the total flux entering the monochromator is

$$F_{line} = G\, s_1 \int_{\lambda}^{\lambda+\delta\lambda} I(\lambda)\, d\lambda = G\, s_1\, I_{line} \qquad (5.3.31)$$

$\delta\lambda$ is the linewidth.

From equation (5.3.30), as $I(\lambda)$ is not constant, F'_{out} can only be related to the total line intensity if either $\underline{\delta}(\lambda - \lambda_o)$ is constant over the linewidth (i.e. $\Delta\lambda > \delta\lambda$) or both $\underline{\delta}(\lambda - \lambda_o)$ and the line shape are known. As line shapes are uncertain, it was the practise here to have one slit wider than the other. The line is scanned by shifting the centre of the

passband in increments of s_1/D so that the sloping regions of the δ - profile overlap completely to restore uniformity. In the case where $S_1 > S_2$, the voltage output V_{line} is given as

$$V_{line} = G\, s_2\, I_{line}\, \gamma(\lambda_c)\, \gamma^*(\lambda_c) = Q(\lambda_c)\, s_2 I_{line} \qquad (5.3.32)$$

$\gamma^*(\lambda_c)$ is the detector sensitivity and includes geometrical factors as well as the photocathode quantum efficiency and the overall gain of the photomultiplier etc.

In the case of a continuum intensity, constant over the bandwidth $\Delta\lambda$, the integral term in equation (5.3.30) is simply the area under the δ - profile, which is s_2/D .

The voltage output is thus,

$$V_{cont} = \frac{G\, s_1 s_2}{D(\lambda_0)}\, \gamma(\lambda_c)\, \gamma^*(\lambda_c)\, I(\lambda_c) \qquad (5.3.33)$$

As the monochromator and spectrograph are both prism instruments, the inverse dispersion and bandwidth vary with wavelength, although they can be assumed constant within the set passbands. Certain conditions must be satisfied if accurate measurements of total emission are to be made ;

i) The bandwidth should be sufficiently broad to transmit the major part of a line or multiplet, thereby reducing the number of overlap shots required and minimizing shot-to-shot uncertainties.

ii) The bandwidth should be sufficiently narrow to permit scanning close to a line for determining the amount of background continuum without interference from neighbouring lines.

iii) The flat portion of the δ -profile should be sufficiently broad that overlap regions lie near the line wings, thereby reducing errors arising from an incomplete overlap.

iv) It must be possible to calibrate the slit widths accurately to within about 5%.

The normalised sensitivity $Q(\lambda_0)$ for a fixed set of experimental conditions (see Appendix) is shown in fig. A2 for both silica and glass prisms. The errors shown are due both to the spread in the readings taken during the calibration and the uncertainty in the lamp emission arising from its calibrated temperature variation ($\pm$ 7 ^{o}K).

References

1. V.A.Ambartsumyan (Ed.)'Theoretical Astrophysics',Pergamon Press,1958
2. R.W.P.McWhirter,'Plasma Diagnostic Techniques',Academic Press,N.Y.1965
3. A.G.Hearn, Proc.Phys.Soc.,88, p.171, 1966
4. J.Cooper,Repts.on Progr.in Phys.,29, p.35, 1966
5. B.A.Norton,E.R.Wooding, Proc.3rd Int. IEE conf. Gas Discharges, London,September,1974
6. H.R.Griem,'Plasma Spectroscopy',McGraw Hill,N.York, 1964
7. M.J.Seaton, Mon.Not.Roy.Astr.Soc.,119, p.81, 1959
8. G.Elwert,Z.Naturf.,7a, p.432, 1952
9. H.R.Griem et.al., Phys.Rev., 125, p.177, 1962
10. H.R.Griem, Phys.Rev., 165, p.258, 1968
11. M.Baranger,'Atomic and Molecular Processes',Academic Press,N.Y.,1962
12. M.Baranger, Phys.Rev.,112, p.855, 1958
13. H.R.Griem,Phys.Rev.Lett., 17 , p.509, 1966
14. J.Cooper,G.K.Oertel, Phys.Rev.Lett.,18, p.958, 1967
15. H.Van Regemorter, Astrophys.Journ., 136, p.906, 1962

5.4 Experimental Accuracy

Values of plasma parameters derived from spectral intensity measurements are affected both by experimental errors and uncertainties in the atomic parameters and other related plasma parameters. Calibration errors were less than 10% in the visible region and less than 20% in the ultraviolet. Uncertainties due to shot-to-shot variations were less than 5% and the assumption of a constant emission profile along the length of view was found to be in error by at most $\sim$ 10%. It was found in practise that s_1 = 0.1 mm. and s_2 = 0.02 mm. provided adequate transmission and resolution for all of the lines observed.Close to the gun face, two or three wavelength settings were generally needed to cover each line fully.

The most accurate measurements of electron temperature are obtained from the line ratios method of equation (5.3.14) utilizing adjacent ion species. The temperature can be obtained accurate to within 5% over a wide range even if the total error in the ratio approaches 100%. Some of the oscillator strengths used in the analysis are known from published theoretical and experimental results to be accurate to within about 20%, whilst some others are only accurate to $\pm$ 50% . Measurements of ion and electron densities from line intensities depend upon the combined errors in atomic parameters, measurement and the electron temperature. The latter should be below about 5% if errors in density are not to be much higher than 50%, because of the exponential terms involved.

The deviation parameters for the first twenty levels of each ion which were calculated, are accurate to within $\sim$ 20%. This was deduced by repeating the calculations with the transition rates varying by up to a factor of two to account for the maximum possible uncertainties in the oscillator strengths and excitation cross-sections. The accuracy of the electron density obtained from Stark broadening and shift measurements is greatly dependant upon that of the parameters used.

The lines chosen for measurement were the C II lines at 2747 Å, 2837 Å and 3920 Å and the C III 4187 Å line. For the C II lines, Griem[1] has calculated parameters applicable to the temperature range encountered in this experiment. The width parameter for the C III line was calculated using the semi-approximate formula developed from equation (5.3.25) i.e.,

$$\omega_{\frac{1}{2}\frac{1}{2}} = 8\left(\frac{\pi}{3}\right)^{3/2} n_e \left(\frac{\hbar}{m_e a_o}\right)\left(\frac{E_H}{kT_e}\right)^{1/2}\left[\langle i|r^2|i\rangle g^*(i) + \langle f|r^2|f\rangle g^*(f)\right] \qquad (5.4.1)$$

where g^* is the semi-empirical Gaunt factor which has the limiting value of 0.2 when ΔE, the energy separation to the nearest perturbing level, is greater than kT_e.[2] $\langle i|r^2|i\rangle$ is the square of the matrix elements of the position vector[3]. At temperatures around 3 eV, as the nearest perturbing level lies within 1 eV of the upper level, the adiabatic condition is satisfied and, as the upper level is high up in the term scheme, hydrogen-like values for the matrix elements can be used[2]. Bogen has found agreement with experiment to within 10% for the 4187 Å line at an electron temperature of 5.2 eV.[4] For the 2747 Å and 3920 Å lines, the nearest perturbing levels in each case are within 0.5 eV, so that the broadening parameters should be within the estimated accuracy of ~ 20%. For the 2837 Å line however, is between 3 and 6 eV, and the straight path approximation may be in error. Deviations as much as a factor of 2 - 10 have been observed[2] with this approximation.

The high-voltage probes used for the electrical measurements were accurate to ± 5%. All measurements on the oscilloscope were accurate to ±2%. The inductance of the plasma source was measured on a bridge to within 10% whilst the accuracies of the plasma resistance and current were each estimated to be less than 10%.

References

1. H.R.Griem, U.S. Naval Res.Lab.Rept. no. NRL 6084 , 1964, Washington

2. H.R.Griem, Phys.Rev., 165, p.258, 1968

3. D.R.Bates,A.Damgaard, Phil.Trans., A242, p.101, 1949

4. P.Bogen, Z.Naturf.,27a, p.210, 1972

Chapter Six

Experimental and Computational Results.

6.1 Introduction

In this chapter the experimental and computational results are presented in detail and compared. In particular, they are used as a basis for predicting the behaviour of this and similar devices under different operating conditions. In sections 6.2 and 6.3 the electrical and spectroscopic results are detailed, whilst section 6.4 deals with the ablation from the dielectric, In sections 6.5 to 6.7, the computational models describing the properties of the plasma and its interaction with the electromagnetic field are dealt with, together with the calculations of atomic coefficients for Carbon and Fluorine ions in plasmas. These coefficients have been calculated for a wide range of plasma conditions and could, therefore, be of use in other plasma systems.

Reasonable agreement was observed between values of electron and ion temperatures and densities obtained from the intensities and widths of various spectral lines and from the electrical conductivity, both near to the dielectric surface and far out in the accelerated plasma plume.

6.2 Accelerator Performance

The high speed photographs of the discharge (figs. 3.2.3 and 3.2.4) provide confirmation that the plasma plume produced is both symmetric and stable and that edge effects are not important. The sideways expansion of the plume is seen to be much smaller than the axial displacement during the first current cycle, which indicates a large unidirectional component of magnetic thrust as a purely adiabatic thermal expansion from the solid surface would be three-dimensional. No intensification of any of the spectral lines was detected beyond the electrode region, supporting the assumption made initially, that the current and associated magnetic field do not extend out into the plume.

Examples of the visible spectra obtained near to the dielectric surface are shown in figs. 6.2.1 and 6.2.2. These time-integrated spectrograms show that, close to the surface, many of the lines are Stark broadened. If this were not the case, Doppler broadening alone being the mechanism, all of the lines would be similarly affected. The spectrogram in fig. 6.2.1 was taken through the electrodes and in fig. 6.2.2 , taken 4 mm. away from the surface, the bright central portion of each line is attributed to the narrowness of the accelerated plasma . This effect was detectable on the spectrograms even out as far as 2 cm. from the surface. By comparing spectrograms of PTFE and Polypropylene-derived plasmas, using Molybdenum and Copper electrodes, most of the intense lines in the region 2000 Å to 6000 Å were identified. By considering the behaviour of the Saha-Boltzmann equation with changes in temperature, the mere presence of intense lines of Carbon IV is sufficient to suggest an electron temperature of between 1 and 5 eV is reached. By restricting the entrance slit height of the monochromator, time-resolved vertical scans of several spectral lines were made in order to check the plasma uniformity. The results using the F II 4025 Å multiplet are shown in fig.6.2.3. Within the experimental uncertainty, the emission is uniform over y $\pm$ 1.5 mm and z $\pm$ 6.0 mm.

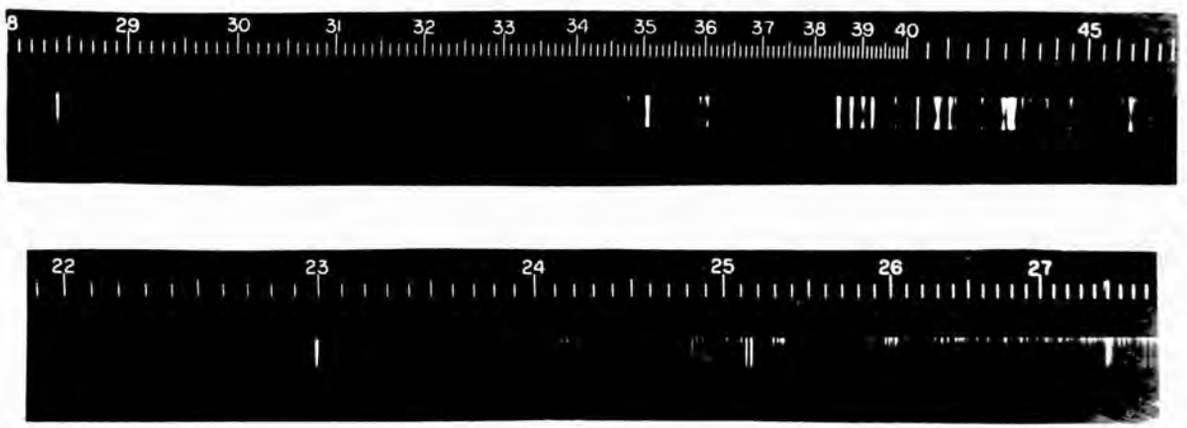

FIG. 6.2.1

PTFE PLASMA

2 SHOTS

LOCATION : PTFE SURFACE

INSTRUMENT SLIT WIDTH : 0.05 MM.

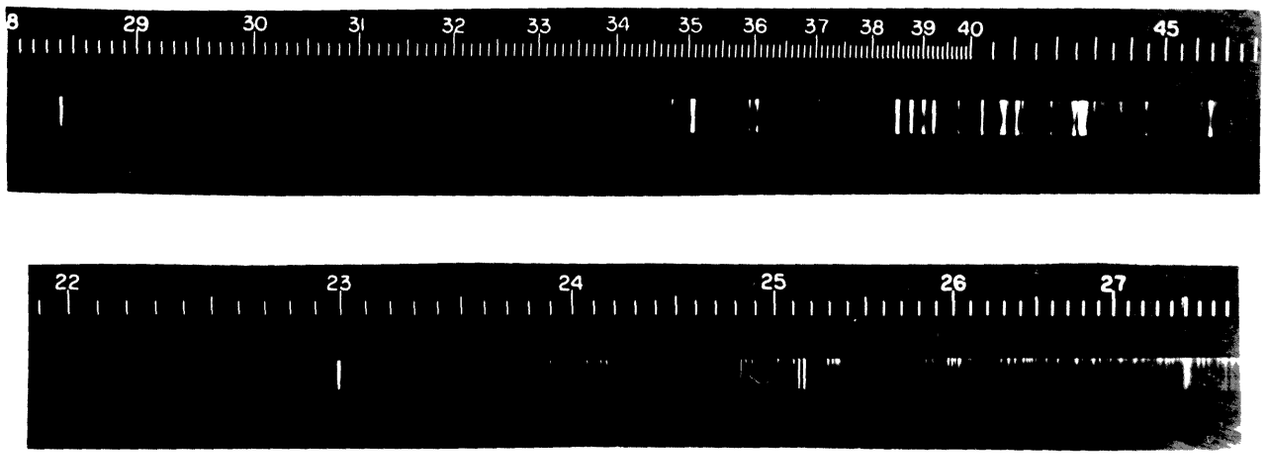

FIG. 6.2.1

PTFE PLASMA

2 SHOTS

LOCATION : PTFE SURFACE

INSTRUMENT SLIT WIDTH : 0.05 NM.

Fig. 6.2.3

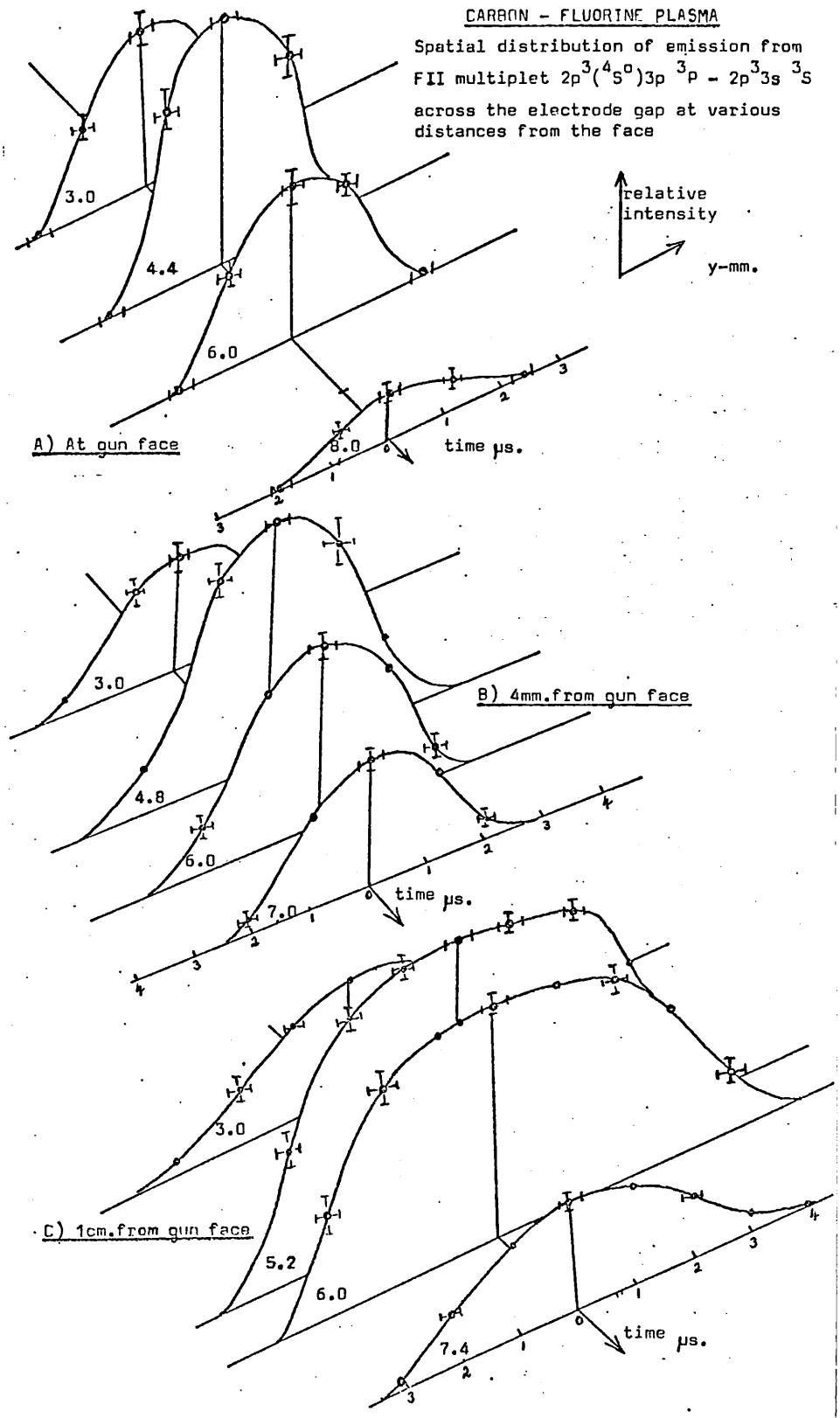
CARBON - FLUORINE PLASMA
Spatial distribution of emission from FII multiplet $2p^3(^4S^o)3p\ ^3P - 2p^3 3s\ ^3S$ across the electrode gap at various distances from the face
relative intensity
y-mm.
3.0
4.4
6.0
8.0
time μs.
A) At gun face
3.0
4.8
6.0
7.0
time μs.
B) 4mm.from gun face
3.0
5.2
6.0
7.4
time μs.
C) 1cm.from gun face

From measurements of line and continuum intensities and line widths, consistent time-resolved values of n_e, n_i and T_e were obtained. In the normal operating conditions, i.e. with a 3 mm gap between Molybdenum electrodes, some Molybdenum lines were observed, being strongest near the electrodes, but no lines of copper, which could come from the electrode clamps, were observed. At a few mm from the dielectric surface, weak Molybdenum lines were only observed after many shots were superimposed. In fig. 6.2.2 , with the line of sight along the z-direction, the Mo II line at 3292.3 Å for example, is brightest on either side of the region in which the Carbon and Fluorine lines are most intense. From the relative intensities of the F II 3202 Å and Mo II 3290 Å lines, the Molybdenum content of the plasma was estimated as being less than 1%.

The discharge current was affected mainly by the external circuit resistance and no changes were detected when the three dielectric materials were interchanged. The plasma resistance R_p , which includes the back-e.m.f term, was determined in each case from the current and voltage measurements and equation (3.3.8). Errors in the measurements result in an error in R_p of $\lesssim$ 5% , values of which are shown in fig. 6.2.4. The Joule power and total energy input to a PTFE plasma are shown in fig. 6.2.5. The power delivered in the case of polythene and polypropylene, is in proportion to the value of R_p .

The velocities of the plasma constituents were determined both from time of flight measurements and from the Doppler shift of spectral lines in the direction of motion. Figure 6.2.6 is a microdensitometer recording from a spectrogram taken in the direction of thrust, showing the blue shift of the C III 2297 Å line superimposed on the unshifted line in a PTFE - derived plasma. The velocity derived from this measurement is 1.95×10^6 cm/sec. ($\pm$ 0.6×10^6). Time of flight data obtained with the monochromator and scanning arrangement are presented in fig. 6.2.7.

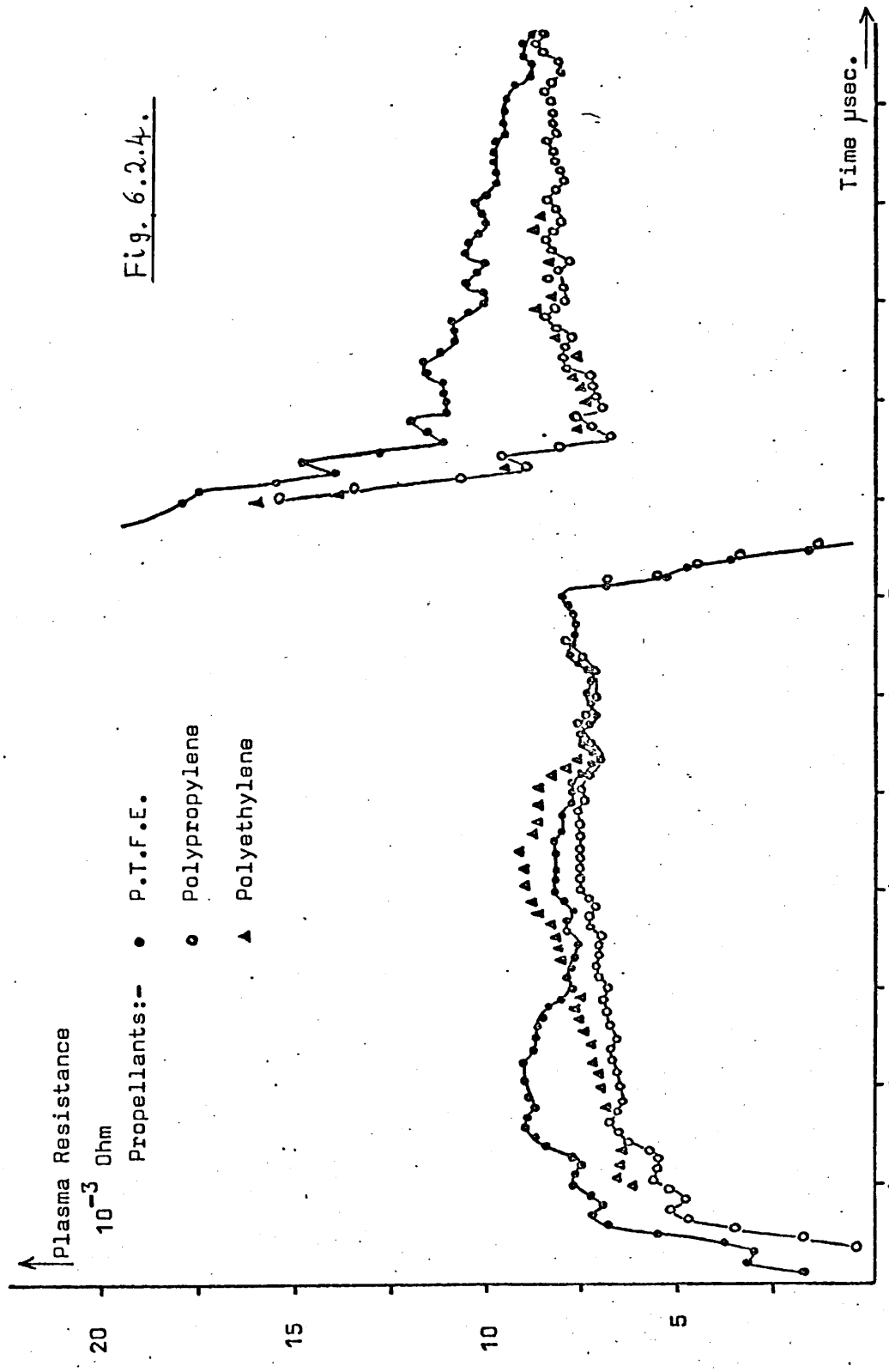
Plasma Resistance
10^{-3} Ohm
Propellants:-
• P.T.F.E.
o Polypropylene
▲ Polyethylene
20
15
10
5
1
2
3
4
5
6
7
8
9
10
11
12
Time μsec.

Fig. 6.2.4.

Fig. 6.2.5

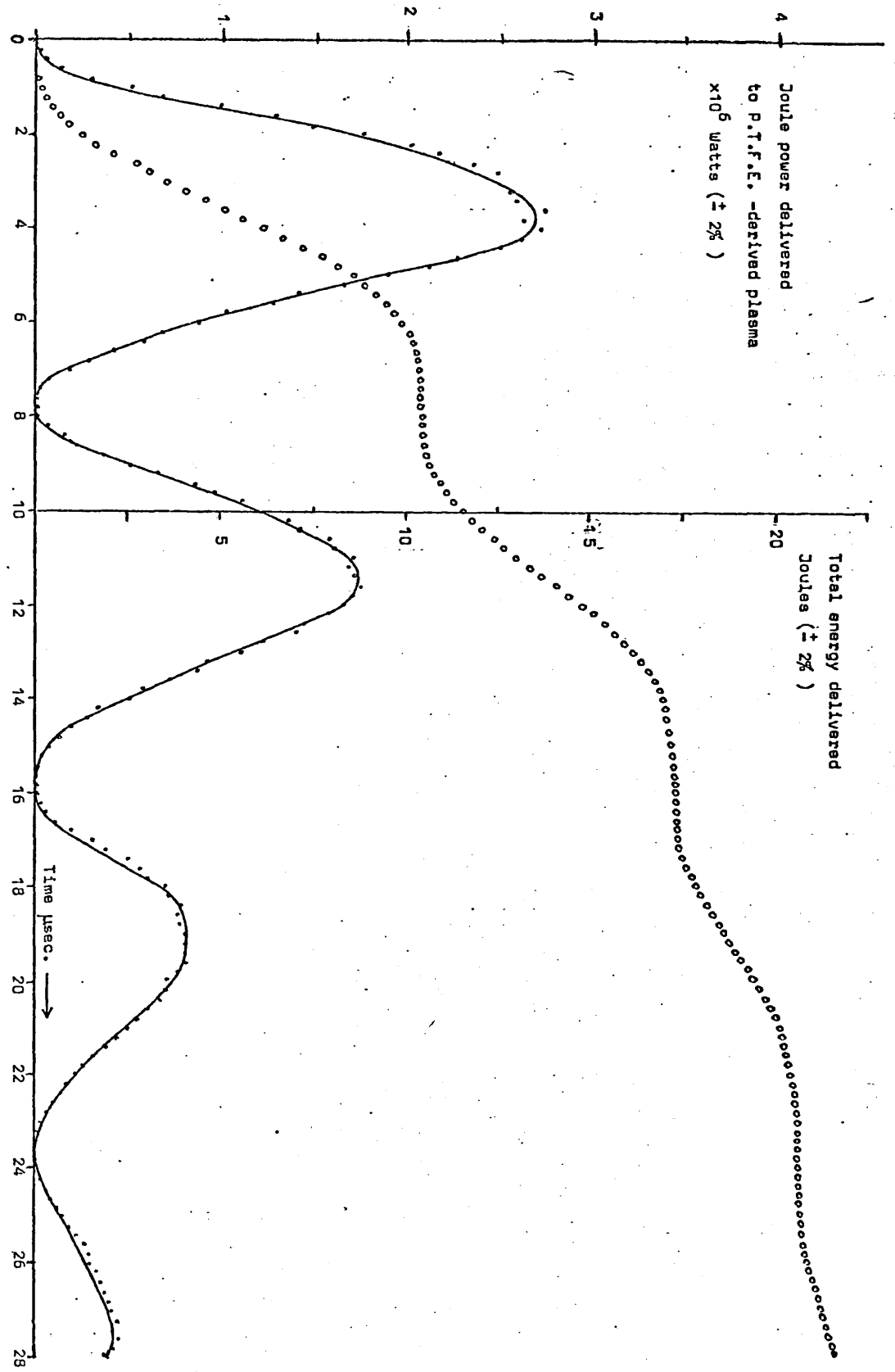
Joule power delivered
to P.T.F.E. -derived plasma
x10^6 Watts (± 2%)
Total energy delivered
Joules (± 2%)
Time μsec.

Fig. 6.2.6

Doppler shift of C III 2297 Å line

in a PTFE-derived plasma

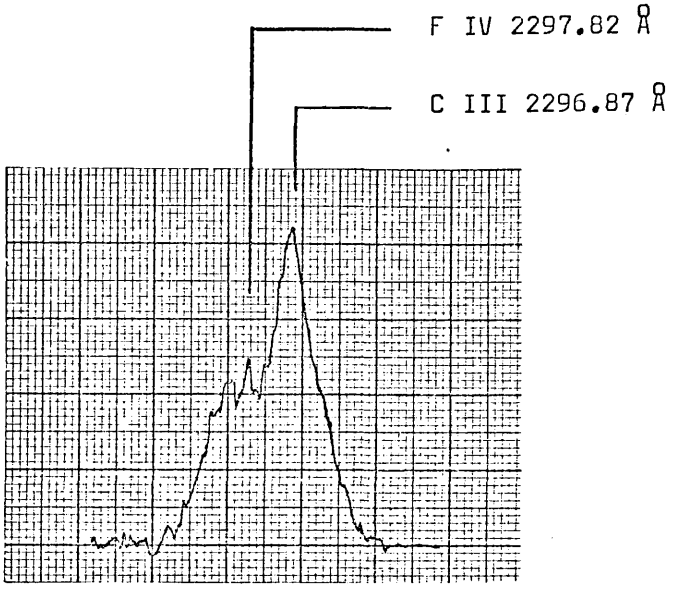

i) Plasma viewed perpendicular to direction of motion

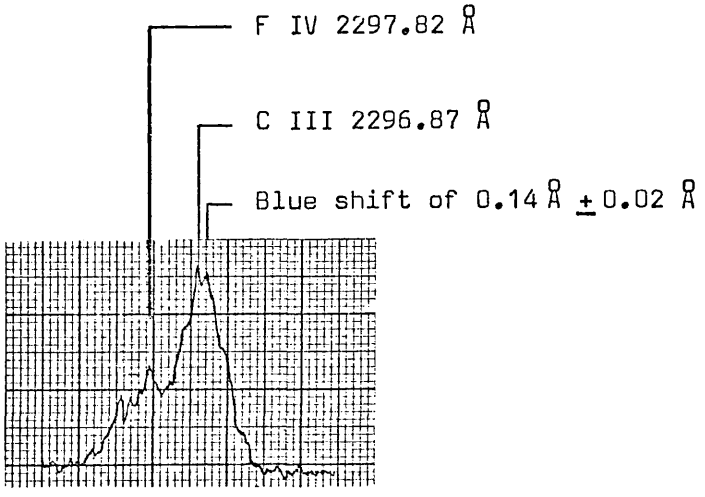

ii) Plasma viewed opposite to direction of motion

Blue shift equivalent to plasma velocity $\sim 2 \times 10^6$ cm/sec.

Fig. 6.2.7

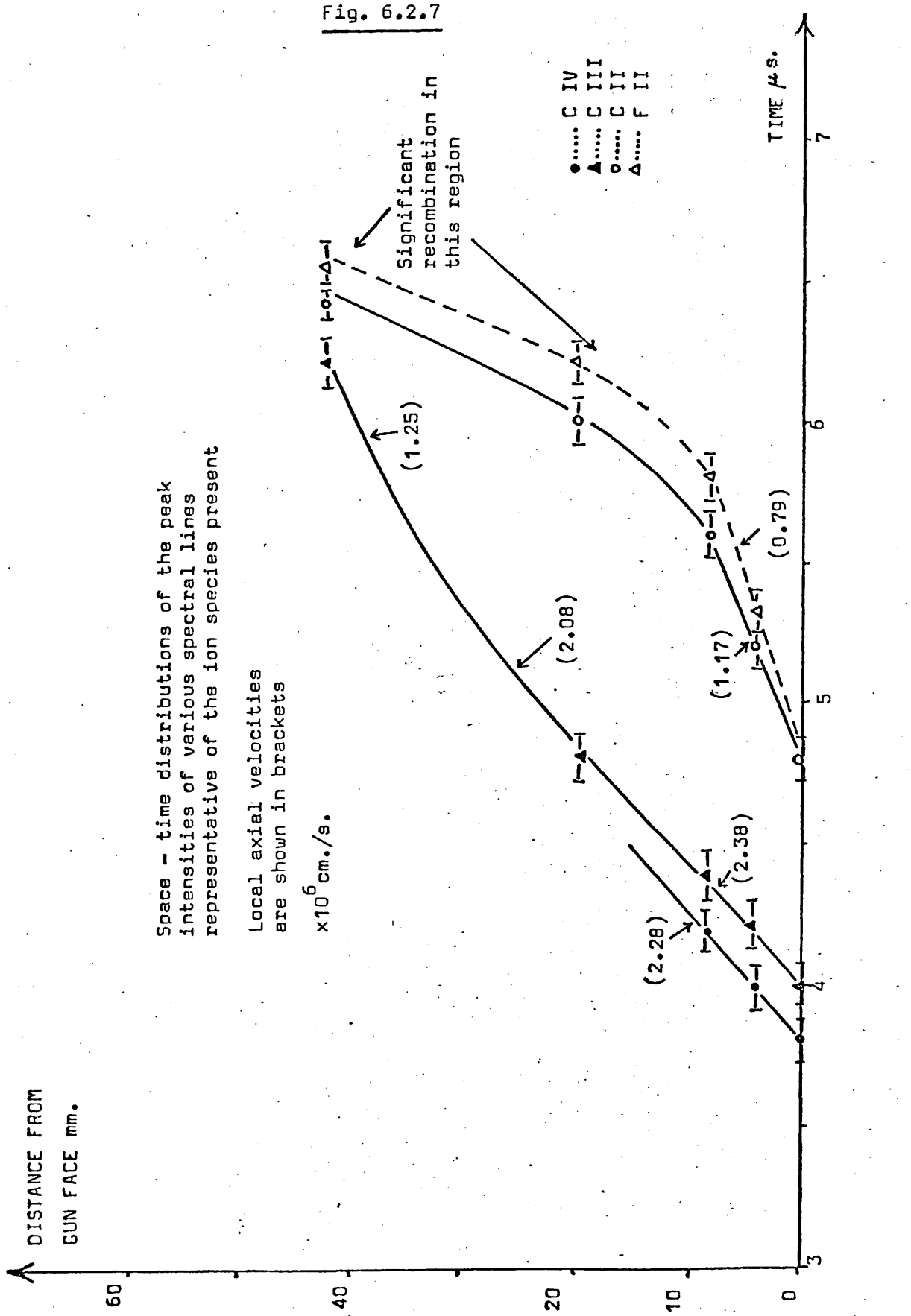
DISTANCE FROM GUN FACE mm.
60
40
20
10
0
TIME μs.
3
4
5
6
7
Space - time distributions of the peak intensities of various spectral lines representative of the ion species present
Local axial velocities are shown in brackets
x10^6 cm./s.
Significant recombination in this region
C IV
C III
C II
F II
(1.25)
(2.08)
(2.28)
(2.38)
(1.17)
(0.79)

It is evident from these results that each ion species has a different velocity up to the time when the effects of recombination are important. The velocities scale approximately as Z_i/m_i , which is to be expected from equation (3.3.6) if space charge is responsible for ion acceleration, and provides justification for the neglect of ion-ion friction.
From an analysis of the high-speed photographs in figs. 3.2.3 and 3.2.4 , an average plasma velocity of $\sim 1.2\times10^6$ cm/sec is obtained for a PTFE - derived plasma. This value is midway between the values for C II, F II and C III derived previously. The S-11 response of the camera photocathode peaks at between 3500 Å and 6500 Å , in which region most of the radiation comes from C II, C I, F II and F I ions, and to a much smaller extent from higher ions. Thus the non-spectrally resolved measurements monitor the lowest ion stages. In this plasma, Fluorine is the main constituent and the velocity of F III ions will be roughly the same as that of C II ions. Thus, the camera need not be operated with the use of narrow band filters if an average velocity is required.

Before interpreting the velocities as they relate to a particular ion stage it is necessary to show that the effects of recombination are not important during the time of observation. As can be seen in fig. 6.2.7 recombination of C III and F III can be neglected at distances up to $\sim$ 1 cm from the solid. The recombination rates of C II and F II are slower, so that time of flight measurements on these ions should be satisfactory at greater distances. After $\sim$ 1 cm , the balance between ionization and recombination processes is lost because of the radiation losses and, as no further energy is supplied, recombination takes over. Away from the solid surface, surface radiation losses from the plasma plume are severe and the cooling time is of the order NkT_e/γ_R . Under the present experimental conditions, the temperature will drop by about 20% in $\sim 1/\mu$ sec, during which time the plasma front will have travelled $\sim$ 1 cm.

Such a temperature drop would result in a rapid process of recombination, as was observed. At distances between 4 mm and 10 mm from the solid , whilst the temperature dropped by about 20% , the electron density dropped by a factor of two. For an adiabatic expansion, $kT_e n_e^{-2/3}$ is constant, and the temperature would have dropped by about 50% instead. Thus , further than $\sim$ 4 mm from the dielectric surface, the density and temperature of the fast-moving plume are not governed by adiabatic expansion. The sideways thermal expansion velocity, measured from fig. 6.2.3 was 2.0 ($\pm$ 0.4)x10^5 cm/sec.

By weighing the dielectric before and after several hundred discharges, the mass ablated per shot was found. For PTFE this was 57.6 ($\pm$ 2) μ gm. , for polypropylene it was 43.7 ($\pm$ 2) μ gm. and for polyethylene, 26.9($\pm$ 2) μ gm. was ablated per shot.

6.3 Spectroscopic Results

The methods outlined in chapter 5 have been used for the analysis. In order to maintain a uniform instrument slit function across the width of each spectral line when determining the total intensity, it was necessary to modify the D275 monochromator, in which both sets of slit jaws normally opened simultaneously. It was necessary to hold one set of jaws open independently of the other, and the entrance jaws were chosen as they were not curved. The jaws were kept apart at the top and bottom with small pieces of brass sheet fastened with a blob of modelling clay. Using the standard lamp and the calibrating system, the instrument slit settings were found to be accurate to within 5% in the range 0.5 mm to 0.05 mm. The exit slit was calibrated against the monochromator scale provided, with the entrance slit held at 0.1 mm. Deviation from the scale reading occurred below 0.05 mm with a minimum width of 0.021 mm. With repeated opening and closing, no changes in this behaviour were obtained and the slits had to be re-adjusted only twice in one period of six months. It was found that entrance and exit slit widths of 0.1 mm and 0.02 mm respectively provided adequate transmission and resolution for most of the lines observed. Close to the gun face, where the lines were broadest, only two or three wavelength settings were generally needed to cover the line profiles.

The photomultiplier response to large pulses was checked using the C II 4267 Å multiplet. Decoupling capacitors on the last few dynodes allow large pulses to flow without affecting the bias voltages, although space-charge effects can still occur with very large pulses. The photomultiplier used here had a 'box and grid' dynode arrangement and the maximum anode current allowable for less than 10% distortion was specified by the manufacturers to be around 0.5 mA. Using calibrated neutral density filters and averaging over several shots, it was found that the deviation from linearity in the response was less than 2% if the anode current was less than 0.25 mA. Care was taken always to

ensure that this value was not exceeded. The frequency response was checked by introducing an emitter-follower circuit between the photomultiplier and the leads to the oscilloscope. The input of the oscilloscope had an impedance of 1 MOhm in parallel with a capacitance of 33 pF, that of the signal leads being approximately 80 pF. No distortion of the signal should have occurred at frequencies below ~ 1 MHz with a 1 kOhm load, or below ~ 200 MHz with a 5 kOhm load, and no variation was in fact observed either with or without the emitter-follower. The time histories of some of the lines and multiplets at various distances from the dielectric surface are shown in figs. 6.3.1 to 6.3.6.

Spectrograms obtained with the medium quartz spectrograph provided a degree of time resolution due to the non-linear response of the photographic plates. Approximately 80% of the radiant emission at any axial position occurred during a time interval from ~ 2 - 4 μsec. after commencement of the discharge, during which also the intensity varied by a factor of about 2. From multiple-shot measurements it was found that the plate darkening from the remaining 20% was minimal. The emulsion was calibrated relatively , either on a multi-shot basis or, where possible, by utilising multiplet transitions in which the intensity of one component line was, to within a few percent, a known fraction of that of another component. The HP3 plates were developed for 5 minutes in a 1:4 solution of 'Ilford PQ Universal ' developer at a temperature of 25 ^{o}C . Some typical microdensitometer recordings from the plates are shown in figs. 6.3.7 to 6.3.12. With the spectrograph slit width set at 0.02 to 0.05 mm , representing a compromise between resolution and light gathering efficiency, the spectrograms were built up progressively over 12 shots, during which time the C II 4267 Å line was monitored on the oscilloscope as a check for reproducability. The half-widths and shifts of these 'partially time resolved' lines were measured at various axial positions. Fig. 6.3.13 is a list of the lines studied.

FIG. 6.3.1

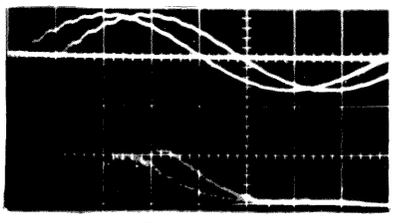

2830.2 Å 200mV/div.

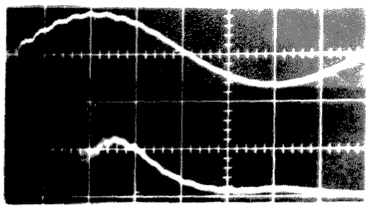

2832.7 Å 200mV/div.

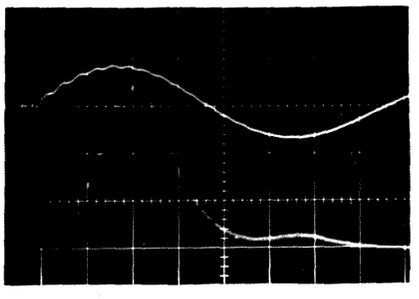

2835.2 Å 200mV/div.

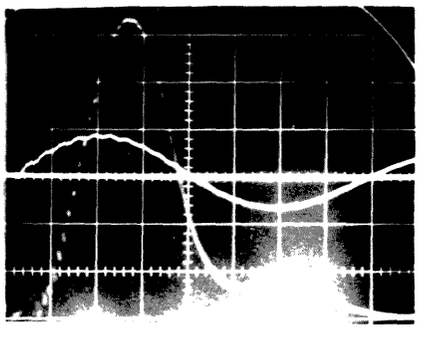

2837.7 Å 500mV/div.

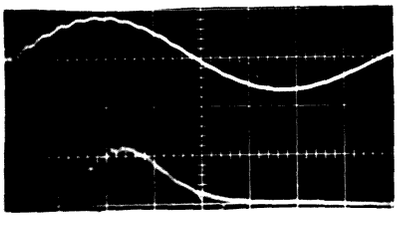

2845.2 Å 200mV/div.

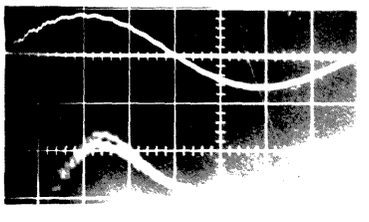

2840.2 Å 200mV/div.

PTFE UPPER TRACE : CURRENT

LOWER TRACE : C II $2s2p^2 - 2s^2 3p\ ^2P^o$ MULTIPLET

TIME BASE : 2 μSEC/DIV.

BANDWIDTH : 2.5 Å LOCATION : PTFE SURFACE

FIG. 6.3.2

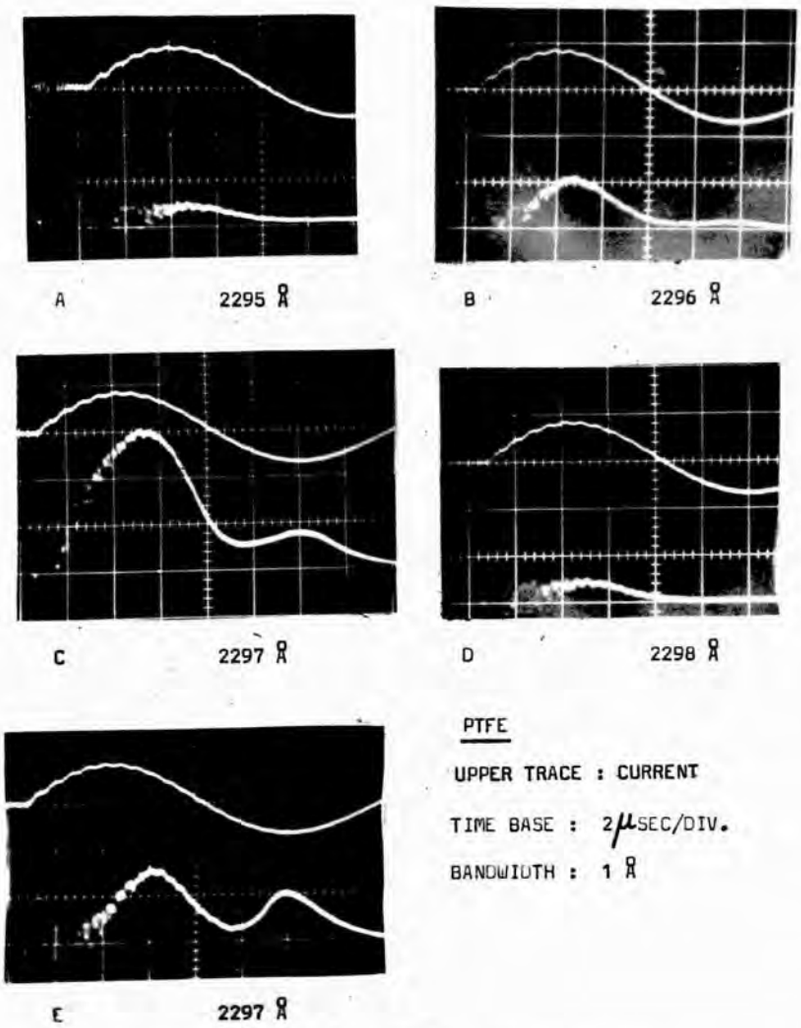

A 2295 Å

B 2296 Å

C 2297 Å

D 2298 Å

E 2297 Å

PTFE

UPPER TRACE : CURRENT

TIME BASE : 2μSEC/DIV.

BANDWIDTH : 1 Å

LOWER TRACE : $2s2p\ ^1P^o - 2p^2\ ^1D$ C III TRANSITION

LOCATION : A–D, PTFE SURFACE ; E, 2 CM FROM SURFACE

SENSITIVITY : A–D 500mV/div. ; E 50mV/div.

FIG. 6.3.3

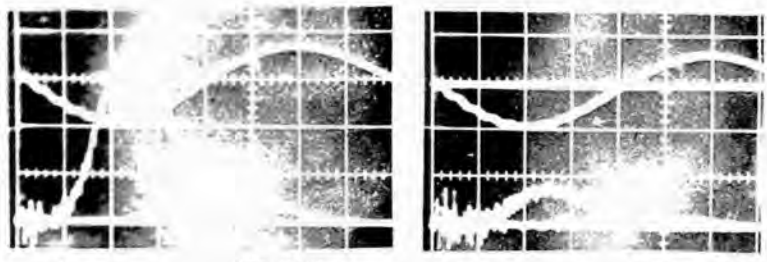

A 500mV/div. B 100mV/div.

PTFE LOWER TRACE : 4f $^1F^o$ – 5g ^1G C III TRANSITION

TIME BASE : 2μSEC/DIV.

LOCATION : A, PTFE SURFACE ; B, 1 CM FROM SURFACE

WAVELENGTH : 4187 Å BANDWIDTH : 8 Å

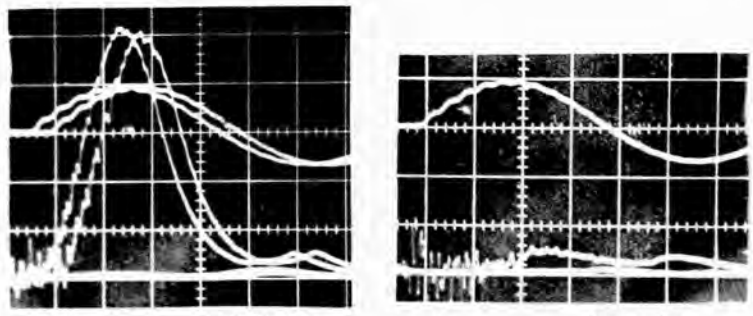

A 200mV/div. B 10mV/div.

PTFE LOWER TRACE : 3s ^2S – 3p $^2p^o$ C IV TRANSITION

TIME BASE : 2μSEC/DIV.

LOCATION : A, PTFE SURFACE; B, 2 CM FROM SURFACE

WAVELENGTH : 5801 Å BANDWIDTH : 10 Å

FIG. 6.3.4

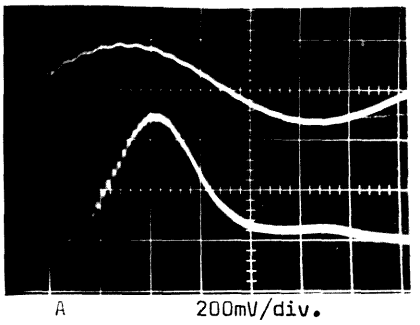

A 200mV/div.

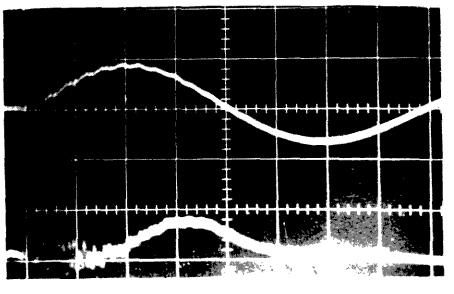

B 40mV/div.

PTFE UPPER TRACE : CURRENT

LOWER TRACE : F II 3s $^3S^o$ - 3p ^3P TRANSITION

WAVELENGTH : 4025 Å BANDWIDTH : 7.2 Å

LOCATION : A, PTFE SURFACE ; B, 2 CM. FROM SURFACE

TIME BASE : 2 μSEC/DIV.

FIG. 6.3.5

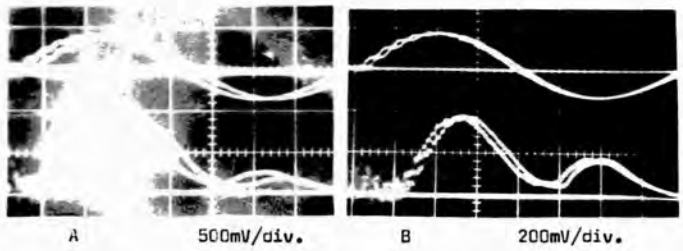

POLYPROPYLENE TIME BASE : 2μSEC/DIV.

LOWER TRACE : C III $2s2p\ ^1P^o - 2p^2\ ^1D$ TRANSITION

WAVELENGTH : 2297 Å BANDWIDTH : 1 Å

LOCATION : A, SOLID SURFACE ; B, 1 CM. FROM SURFACE

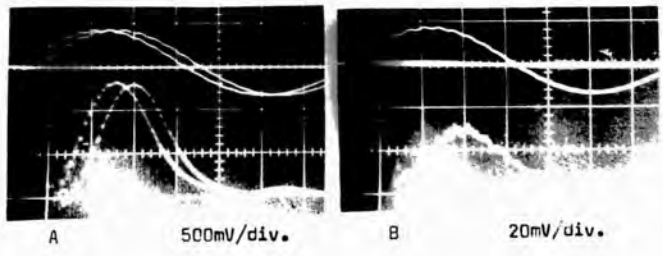

POLYPROPYLENE TIME BASE : 2μSEC/DIV.

LOWER TRACE : C II $3p\ ^2P^o - 4s\ ^2S$ TRANSITION

WAVELENGTH : 3920 Å BANDWIDTH : 6.6 Å

LOCATION : A, SOLID SURFACE ; B, 2 CM. FROM SURFACE

FIG. 6.3.6

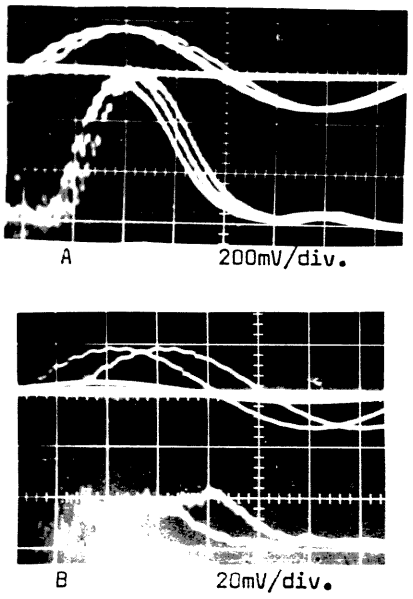

POLYPROPYLENE TIME BASE : 2μSEC/DIV.

LOWER TRACE : C IV 4d ^2D - 5f $^2F^o$ TRANSITION

WAVELENGTH : 2524 Å BANDWIDTH : 1.6 Å

LOCATION : A, SOLID SURFACE ; B, 2 CM. FROM SURFACE

Fig. 6.3.7

Recording from a spectrogram taken at the surface of the dielectric in a PTFE-derived plasma.

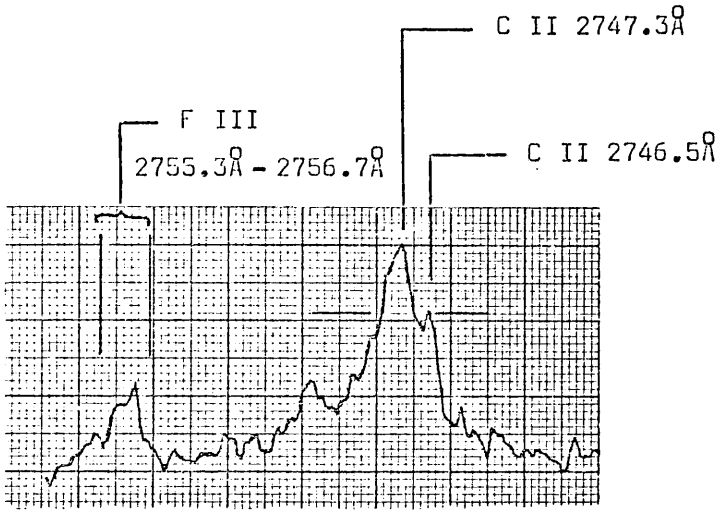

Fig. 6.3.8

Recording from a spectrogram taken at the surface of the dielectric in a PTFE-derived plasma.

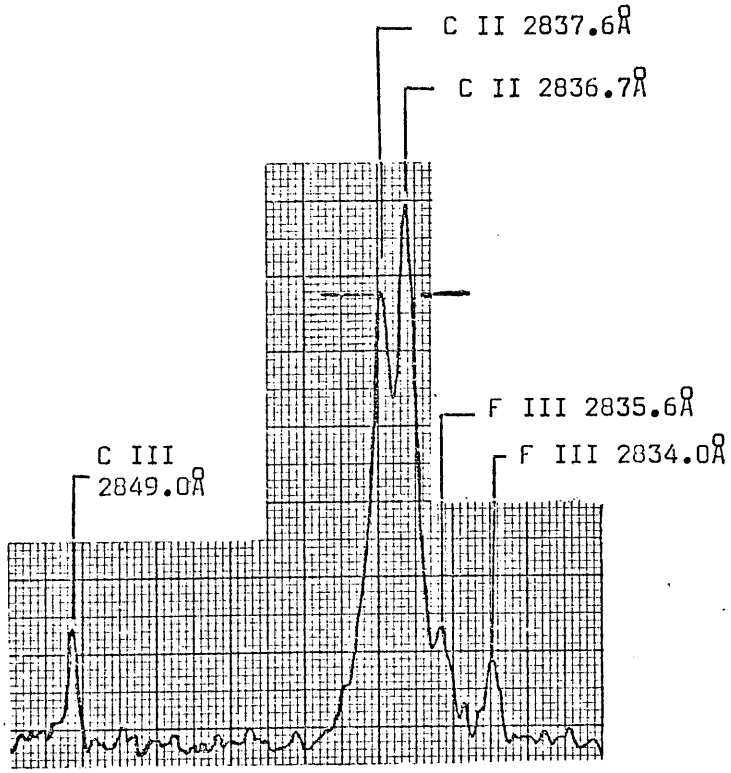

Fig. 6.3.9

Recording from a spectrogram taken at the surface of the dielectric in a PTFE-derived plasma.

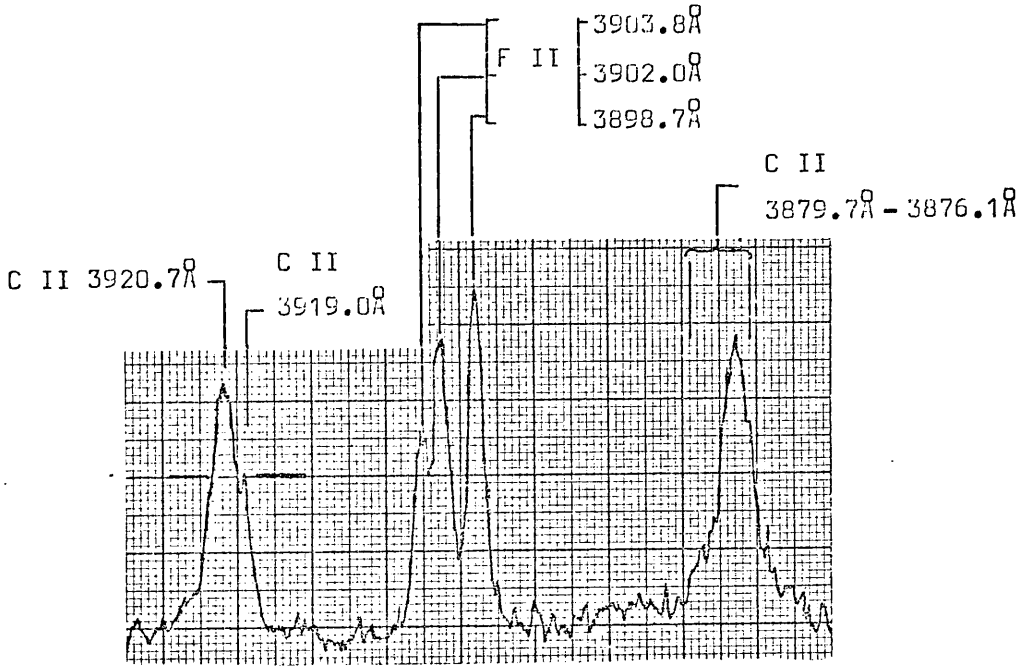

Fig. 6.3.10

Recording from a spectrogram taken at the surface of the dielectric in a PTFE-derived plasma.

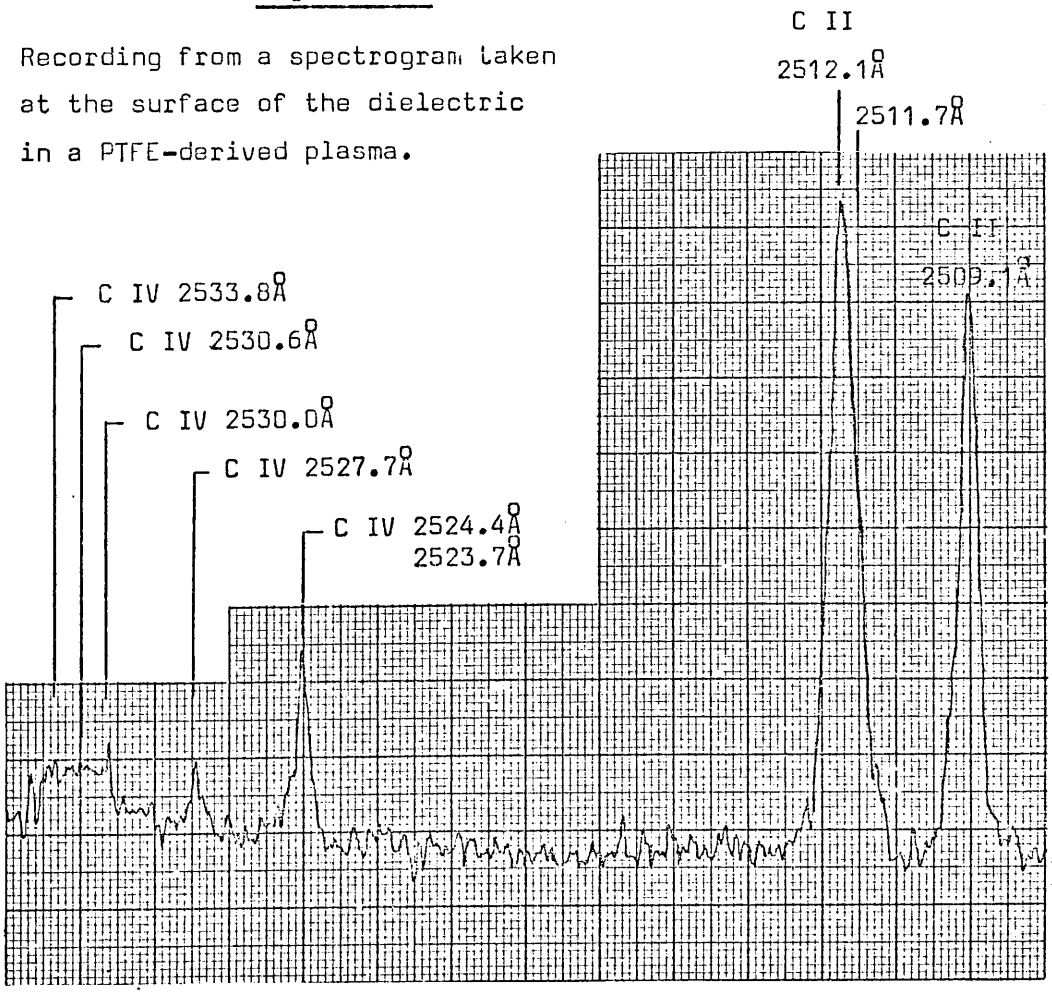

Fig. 6.3.11

Recording from a spectrogram taken 4 mm from the surface of the dielectric in a PTFE-derived plasma.

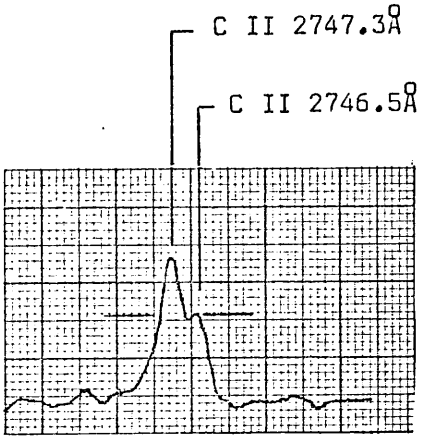

Fig. 6.3.12

Recording from a spectrogram taken 8 mm from the surface of the dielectric in a PTFE-derived plasma.

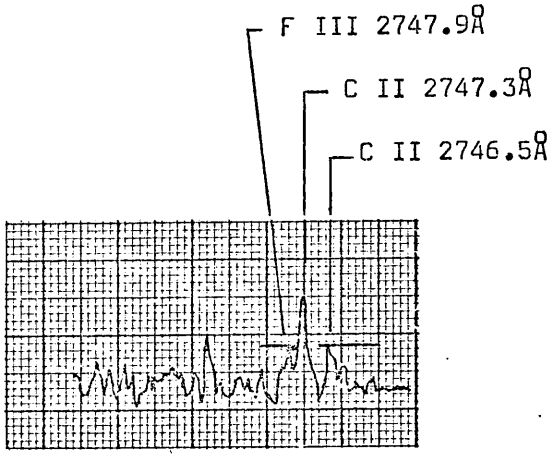

Fig. 6.3.13

Wavelength Å	Transition	Level number	E eV.	$\sum A \times 10^8$	g
	C II				
4267*	$3d\ ^2D - 4f\ ^2F^o$	16	20.95	2.46	14
3920*	$3p\ ^2P^o - 4s\ ^2S$	11	19.49	1.87	2
2512*	$2s2p^2\ ^2P - 2p^3\ ^2D^o$	10	18.65	0.97	10
2837*	$2s2p^2\ ^2S - 2s^23p\ ^2P^o$	7	16.33	0.35	6
	C III				
2163	$3d\ ^1D - 4f\ ^1F^o$	23	40.01	10.46	7
5696	$2s3p\ ^1P^o - 2s3d\ ^1D$	12	34.28	0.5	5
2297	$2s2p\ ^1P^o - 2p^2\ ^1D$	5	18.09	3.6	5
4187	$4f\ ^1F^o - 5g\ ^1G$	35	42.97	4.27	9
4516*	$4p\ ^3P^o - 5s\ ^3S$	28	42.14	1.66	3
	C IV				
2524	$4d\ ^2D - 5f\ ^2F^o$	13	55.78	7.44	14
5801	$3s\ ^2S - 3p\ ^2P^o$	4	39.68	0.318	6
2530	$4f\ ^2F^o - 5g\ ^2G$	14	55.78	7.05	18
	F II				
4246	$2p^33d\ ^5D^o - 2p^34f\ ^5F$	29	31.58	2.449	35
4025*	$2p^33s\ ^3S^o - 2p^33p\ ^3P$	8	25.75	1.24	9
3202	$2p^33s'\ ^1D^o - 2p^33p'\ ^1D$	23	30.53	1.4	5

* Multiplet

To obtain the line widths, the instrumental broadening factor had to be removed. The broadening introduced by the microdensitometer system was assumed to be equal to the width of the narrowest lines observed on the photographic plate, likely to be lines from the highly ionized species for which the Stark broadening is smallest. The profiles in these cases should be almost triangular, and in fact this was found to be so, within the experimental uncertainty. The half-width of this experimental profile was 0.02/D , where 1/D is the inverse dispersion of the spectrograph in Å/mm. Adopting the Stark broadening theory outlined in chapter five, a broadened dispersion profile was assumed for each measured line, with an intensity distribution of the form,

$$I(\Delta\lambda) \propto \left(1+\left(\frac{\Delta\lambda}{\lambda_s}\right)^2\right)^{-1}$$

A numerical computer program was written , which folded a succession of dispersion profiles of increasing half-width into the triangular instrumental profile until a resultant profile of half-width equal to that previously observed was obtained. Using existing tabulated Stark broadening parameters for these lines[1], mean values of electron density were found, together with the errors arising from uncertainties in the measurements. The accuracy of the folding routine depends upon the size of the wavelength increments. These were made less than one tenth of the instrument half-width, and the final results varied by less than 5% when the increments were halved. Doppler broadening was neglected to a first approximation, and a subsequent check showed that this was acceptable as the dispersion width was much greater than the thermal width. The results are summarized in detail in fig. 6.3.14. and fig. 6.3.14A.

A new method for obtaining the electron density using the Stark broadening theory was also devised during these experiments. When a multiplet consists of relatively few isolated lines, then the electron density can be

Wavelength	distance from gun face mm.	measured half-width	instrumental half-width	Doppler half-width	Dispersion half-width	Theoretical half-width $n_e = 10^{16} cm^{-3}$ T_e = 3eV.	$\langle n_e \rangle$ peak $\times 10^{17} cm^{-3}$	Reference
3920 Å	0	1.02 Å (± 10%)	0.3 Å	0.077 Å	0.92 Å	0.038 Å	2.4 ±25%	A
2747 Å	0	0.52 Å (± 10%)	0.11 Å	0.055 Å	0.505 Å	0.033 Å	1.54 ±20%	A
2837 Å	0	0.22 Å (± 5%)	0.11 Å	0.055 Å	0.16 Å	0.0039 Å	4.1 ±25%	A
4187 Å	0	1.60 Å (± 10%)	0.38 Å	0.082 Å	1.55 Å	0.045 Å	3.44 ±20%	B
2747 Å	5	0.34 Å (± 10%)	0.11 Å	0.055 Å	0.31 Å	0.033 Å	0.82 ±20%	A
4187 Å	5	0.81 Å (± 15%)	0.38 Å	0.082 Å	0.54 Å	0.045 Å	1.2 ±20%	B
2747 Å	8	0.19 Å (± 10%)	0.11 Å	0.055 Å	0.12 Å	0.033 Å	0.32 ±50%	A

Fig. 6.3.14.

Half-widths represent the wavelength separation between the peak intensity position and the point on the profile at which the intensity is one half of the maximum.

A. Griem,H.R.,'Plasma Spectroscopy',McGraw-Hill Pub. Co.,N.York,1964

B. Bogen,P., Z. Naturforschung,27a,p.210 ,1971

Fig. 6.3.14A

a) Spectrogram of CII multiplet
$2s2p^2\ {}^2S\text{-}2s^2 3p\ {}^2p^o$

Location:- Gun face

Instrument $\frac{1}{2}\frac{1}{2}$ width:- 0.115 Å

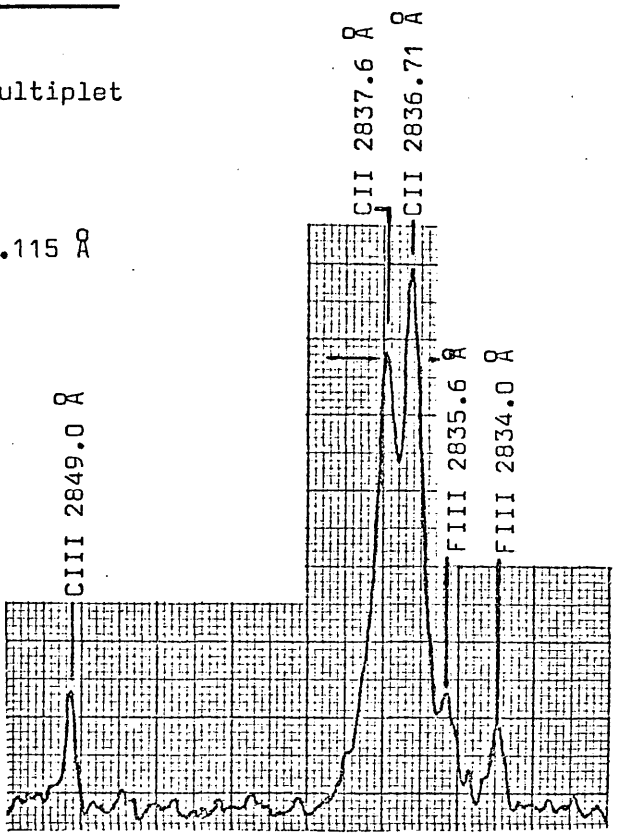

b) Comparison between experimental profile (x x x), and computed values for a dispersion profile (of $\frac{1}{2}\frac{1}{2}$ width = 0.16 Å) folded into a triangular instrument profile of $\frac{1}{2}\frac{1}{2}$ width = 0.115 Å (———)

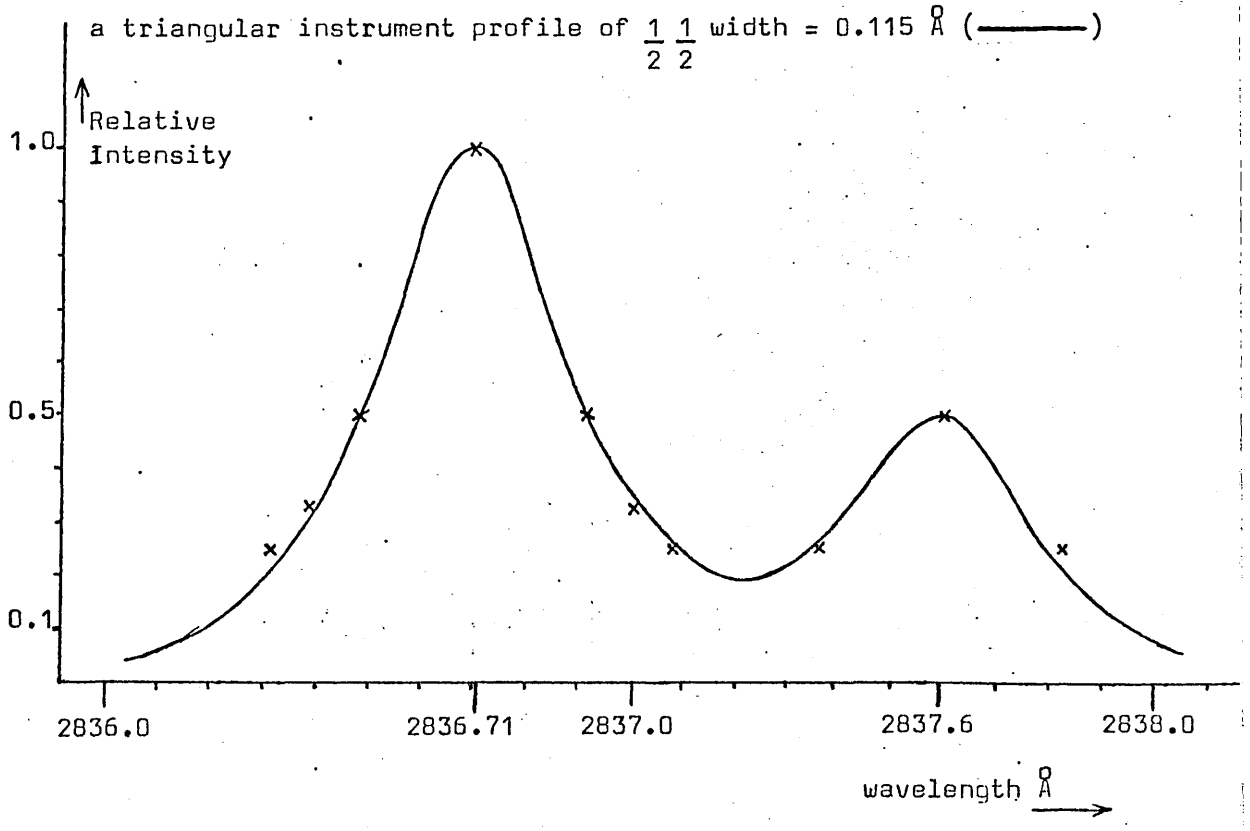

measured even when instrument resolving power is too poor for complete profile scanning, provided that the line shape is accurately known.

A determination of n_e is possible if: (i) the Stark broadening by electrons is at least comparable to Doppler or other broadening mechanisms, (ii) reliable Stark-broadening data is available for the range of conditions likely to be encountered (Generally this will restrict the method to lines of neutral or singly ionized atoms). Even when the instument bandwidth is several times larger than the half-width of a spectral line, a significant portion of the intensity residing on the wings may not be recorded, if the profile is of the dispersion type. By measuring the contribution to the total intensity outwards from some point on the wings, the half-width can be estimated. Consider the C II multiplet $2s2p^2\ {}^2S - 2s^2('s)\ 3p\ {}^2P^o$, with components at 2836.71 Å ($J = 3/2 \rightarrow J' = 1/2$) and 2837.6 Å ($J = 1/2 \rightarrow J' = 1/2$). The multiplet is shown schematically in fig. 6.3.15 and some actual recordings are shown in fig.6.3.1. Close to the multiplet the continuum was found to be free from any other spectral lines. The inverse dispersion of the monochromator at 2837 Å was 24.8 Å/mm ($\pm$ 1.0 Å/mm), so that with input and exit slits of 0.1 mm and 0.021 mm respectively, the instrument passband i.e. s_1/D , was $\sim$ 2.5 Å. The locating error on the wavelength drum of the monochromator was $\pm$ 0.05 Å. With a setting of 2837.71 Å, practically the whole of both lines is collected, excepting a portion of the red wing of the $J = 3/2 \rightarrow J' = 1/2$ transition, as is seen from fig. 6.3.15. The remaining portion of the multiplet was recorded with the passband centred at 2835.1 Å . Several readings were taken at each step and averaged, the main errors being due to uncertainties in locating the wavelength, the sloping edge of the slit-function profile and shot-to-shot variability.

By maximising the peak output over several shots, the wavelength 2836.7 Å was located to within about 0.1 Å. The wavelength setting was then displaced by 1.5 Å $\pm$ 0.05 Å , using a pointer and scale attachment which was made to

Fig. 6.3.15

Sectoral diagram of the combined Stark and Doppler profile of the C II 2837 Å doublet, showing the portions received by the monochromator at various settings.

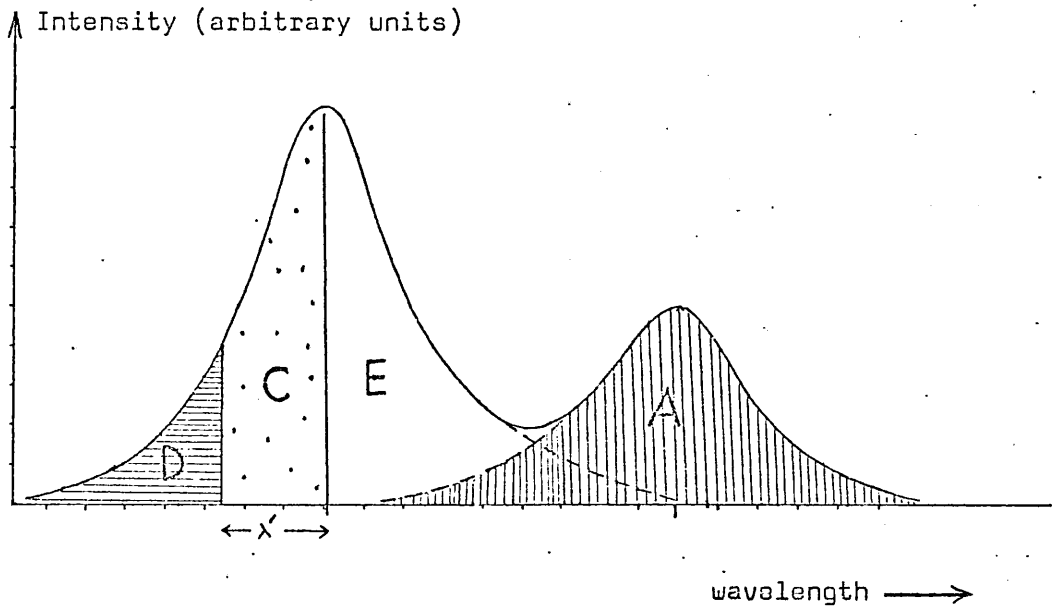

(For explanation see text)

fit onto the wavelength drum. A shift of 2.5 Å was taken to represent the required shift of 2.48 Å. After subtracting the background contribution, the portions of the total intensity represented by the sectors A + E + C in fig. 6.3.15 at the setting 2837.7 Å, and sector D at the setting 2835.2 Å were determined. The output signals are denoted by V_1 and V_2 respectively. Using tabulated transition probabilities for these lines[2] it is seen that the intensity of the strongest line is 2.057 times larger than that of the other.

Defining γ = C/E ,

$$\gamma = \int_0^{\lambda'} I(\lambda)\,d\lambda \Big/ \int_0^{\infty} I(\lambda)\,d\lambda \qquad (6.3.1)$$

where λ' is the cut-off separation from the line maximum and = 0.24 Å

$$\text{also } \frac{V_2}{V_1} = \frac{1-\gamma}{2+\gamma} \qquad (6.3.2)$$

The electron temperature had been previously estimated to be between 1 eV and 5 eV and, as the electrons were expected to be in thermal equilibrium with the ions, the Doppler half-half width for each of these lines would be between 0.04 Å and 0.066 Å. A simple check showed that Stark broadening was not negligible. If Doppler broadening alone had been important then,

$$\gamma = \text{erf}(\lambda'/\Delta\lambda_D) \qquad (6.3.3)$$

With λ' = 0.24 Å , both erf(0.24/0.04) and erf(0.24/0.066) are within 1% of unity in which cases V_2/V_1 would = 0 . Observed values of V_2/V_1 however, ranged from 0.05 to 0.2, indicating some other mechanism.

The total profile due to both Doppler and Stark effects is obtained from a convolution integral of the form,

$$I_T(\lambda^*) = 2\int_0^\infty I_b(\lambda) I_s(\lambda^* - \lambda)\, d\lambda \qquad (6.3.4)$$

The convolution of these two types of profile results in a Voigt profile, examples of which have been tabulated[3]. The compound profile resembles a dispersion profile if the Doppler width is not much greater than the dispersion width, which it is not here. An iterative numerical program can be written which folds successively adjusted Stark profiles into a given Doppler shape, terminating when the integrated wing fraction corresponds to the experimental result. In view of the large uncertainties in λ' , $\pm$ 0.1 Å due to errors in locating 2836.7 Å, the total profile was assumed here to be dispersion in shape, and the sectors were integrated analytically. Thus ,

$$\gamma_{Stark} = \frac{2}{\pi} \tan^{-1}(\lambda' / \Delta\lambda_{Tot}) \qquad (6.3.5)$$

The measured values of γ derived from equation (6.3.2) were used to find $\Delta\lambda_{Tot}$ from which a Doppler profile of half-half width = 0.055 Å was unfolded, using the tables of Voigt profiles[3], resulting in values for the Stark half-half-width. Using the parameters ω, α of Griem[1] together with his formula for Stark broadening, the electron density was calculated through;

$$\Delta\lambda_s \simeq 10^{-16}\, \omega\, n_e \left[1 + \frac{1.75 n_e^{1/4} \alpha \left(1 - 0.11 n_e^{1/6} T^{-1/2}\right)}{10^4} \right] \qquad (6.3.6)$$

being applicable to lines of singly ionized atoms. Errors are $\sim \pm 50\%$ here. Values of n_e at the surface of the dielectric are shown in fig.6.3.16 .

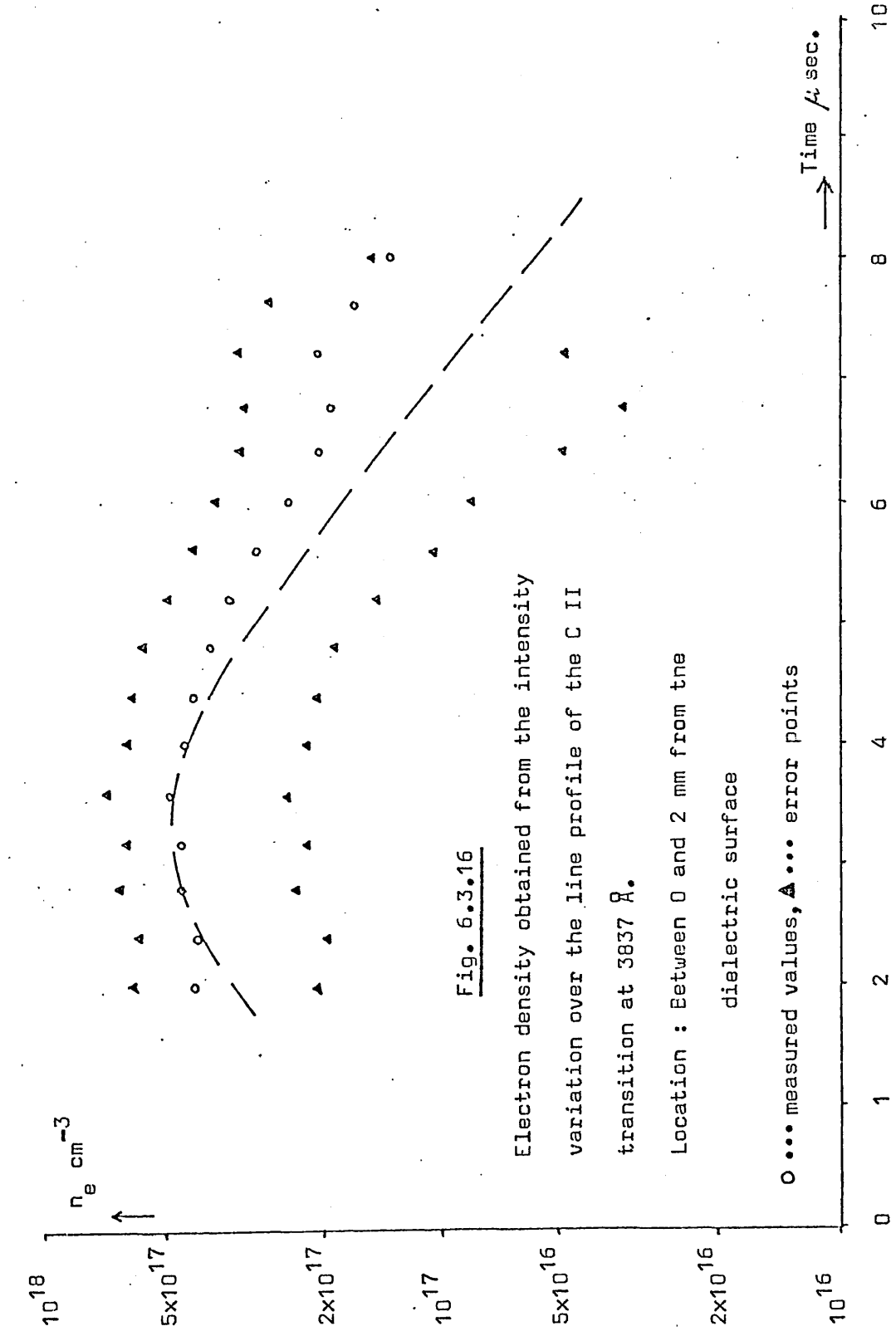

Fig. 6.3.16

Electron density obtained from the intensity variation over the line profile of the C II transition at 3837 Å.

Location : Between 0 and 2 mm from the dielectric surface

O ••• measured values, Δ ••• error points

The electron temperature was evaluated in several ways. The intensity ratios of the F II lines at 4246 Å, 4025 Å and 3202 Å were compared using equations (5.3.10) and (5.3.12). At the expected densities prevailing here, average values of the population deviation parameters can be assumed. Values of temperature for the first 10μ sec. of a PTFE-derived discharge are shown in fig. 6.3.17. The more accurate method of equation (5.3.14) was also used for the C II line at 4267 Å and the C III line at 5696 Å. The results are shown in fig.6.3.18 together with the others,for comparison. The electron density was assumed to lie between 10^{15} and 10^{18} cm^{-3}.

The electron density was also determined from the ratio of the intensities of the C III 2297 Å and 5696 Å lines, using the curves of fig. 5.3.2 , which relate to lines which are optically thin. In this experiment however, comparison of the measured intensities with the black-body values, shows this not to be the case for the 2297 Å line, at distances up to 20 mm away from the dielectric. If the local value of this intensity without self-absorption could be inferred, then the curves of fig. 5.3.2 could still be used, provided that the absorption of radiation between the levels $2s2p\ ^1P^o$ and $2p^2\ ^1D$ does not greatly affect the deviation parameters for the higher levels. The parameters B_3, B_5 and B_9 become equal to unity when absorption is strong, which is the case when the ground level population density n(g) is greater than $\sim 10^{14}$ cm^{-3}. The absorption of the 2297 Å radiation does not affect the ratio by more than 20% if n_e is greater than about $10^{16} cm^{-3}$. In the C III scheme the $2s3d\ ^1D$ state is mainly populated from the $2s2p\ ^1P^o$ and $2s3p\ ^1P^o$ levels. The most serious effect on the rates of these processes occurs when B_9 is also unity.From equation (4.3.3), the population rates to level 12 from levels 3 and 9 are compared for temperatures between 3 - 4eV. These rates are in the ratio $\sim$ 13:1 respectively, so that the assumption that absorption of the 2297 Å line does not perturb the population of level 12 is well justified.

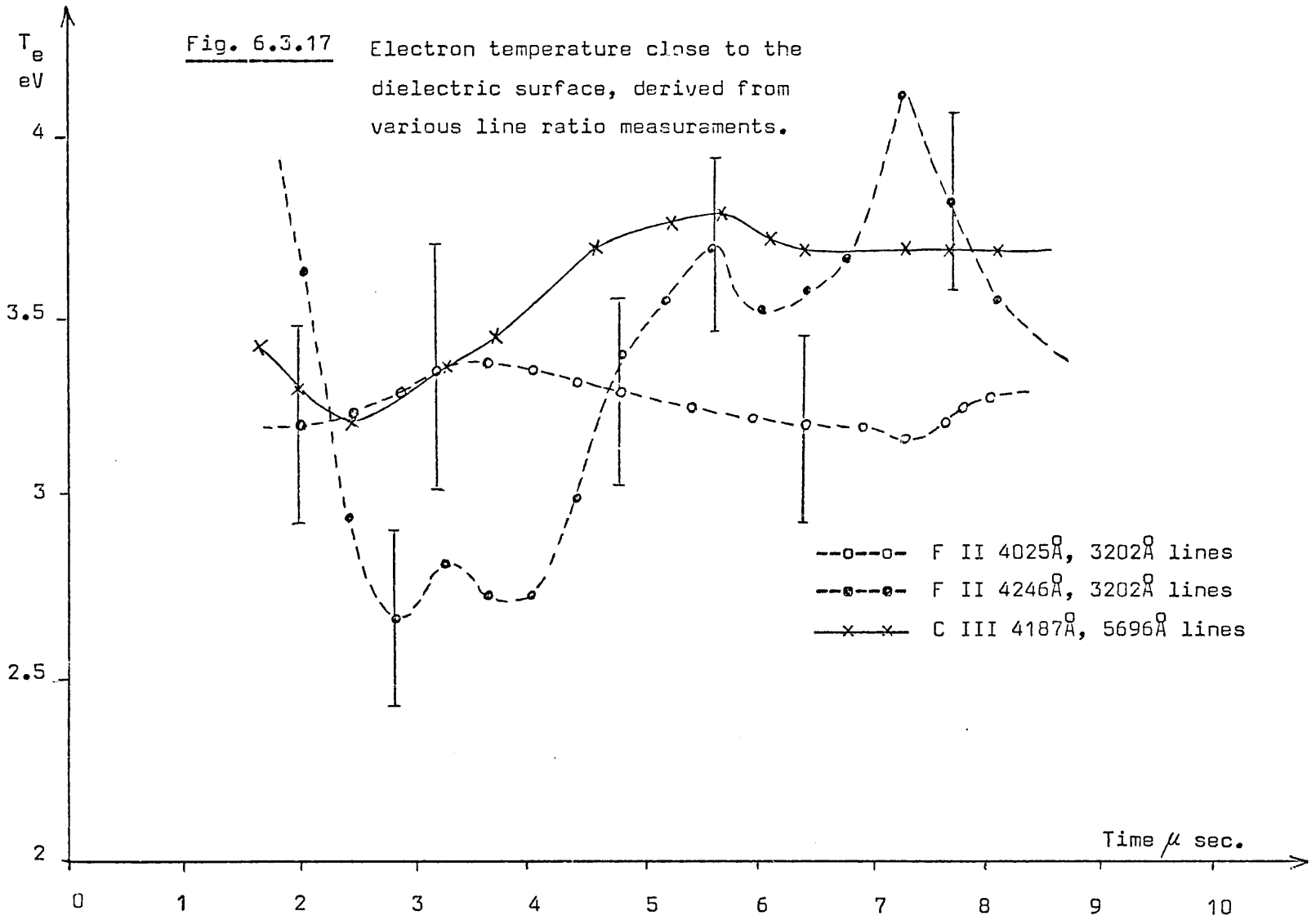

Fig. 6.3.17 Electron temperature close to the dielectric surface, derived from various line ratio measurements.

Fig. 6.3.18

Electron temperature in the plasma, determined from the intensity ratio of the C II 4267Å and C III 5696Å lines.

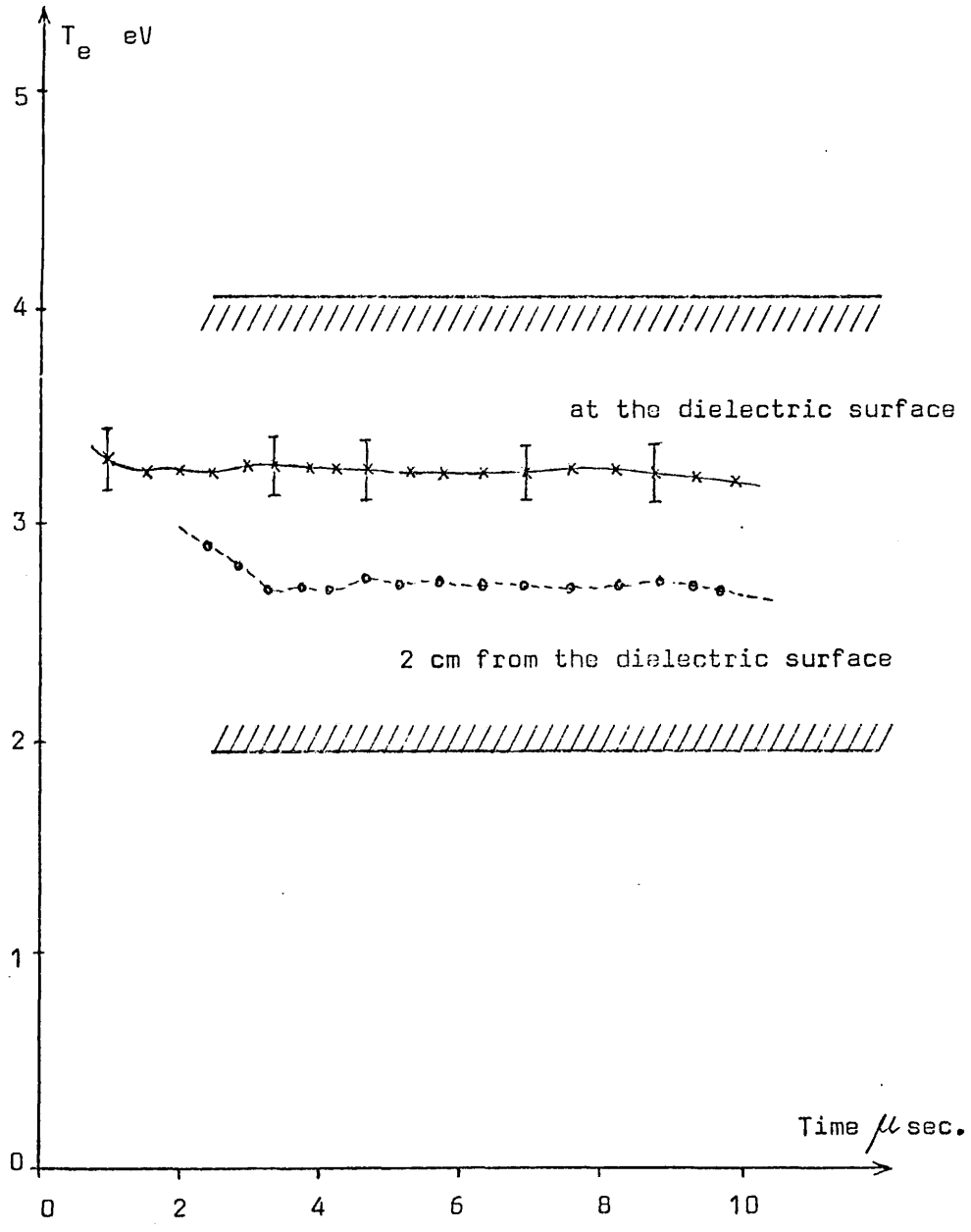

The cross-hatched lines define the range of values obtained close to the dielectric surface, using the normal line-ratio method, examples of which are shown in fig. 6.3.17.

If the ground state population density were greater than $\sim 5\times10^{15}\,cm^{-3}$ however, the 2297 Å radiation would be more than 90% absorbed and B_{12} would approach a value of unity. Equation (5.3.18) was used in the present case, so that the curves of fig. 5.3.2 could be used. Values of n_e for a PTFE-derived plasma, close to the dielectric surface are presented in fig. 6.3.19. From equation (5.3.18) with the Stark width expressed in terms of the electron density,

$$\left(\frac{I_{Tot}(2297)}{I_{Tot}(5696)}\right) = \frac{1.89\times10^{2}\; I^{*}(2297)^{2}}{I_{Tot}(5696)} \left(\frac{10^{16}}{n_e}\right)^{2} KT_e^{1/2}\, e^{\frac{5.4}{KT_e}} \qquad (6.3.7)$$

which is most sensitive to temperature if kT_e is less than $\sim$ 5 eV.

Ion densities were obtained from spectral line intensities, using the LTE-deviation parameters to find ground state populations. These parameters are tabulated in section 6.5. From equations (4.2.2) and (5.3.1),

$$n(q) = \frac{4\pi\, I(p,q)\, g_q\, e^{E_p/KT_e}}{g_p\, B_p\, h\nu(p,q)\, A(p,q)\, \delta} \qquad (6.3.8)$$

Also, from equation (4.2.2),

$$n(p) = \frac{n(q)\; B_p\, g_p\, e^{-(E_p-E_q)/KT_e}}{B_q\, g_q} \qquad (6.3.9)$$

If this sequence is truncated when $n(q)/n(q-1)$ becomes less than 0.05, say, the partition function can be estimated.

Fig. 6.3.19

Electron densities as a function of distance from the dielectric, determined from the ratio of the C III spectral lines at 2297 Å and 5696 Å .

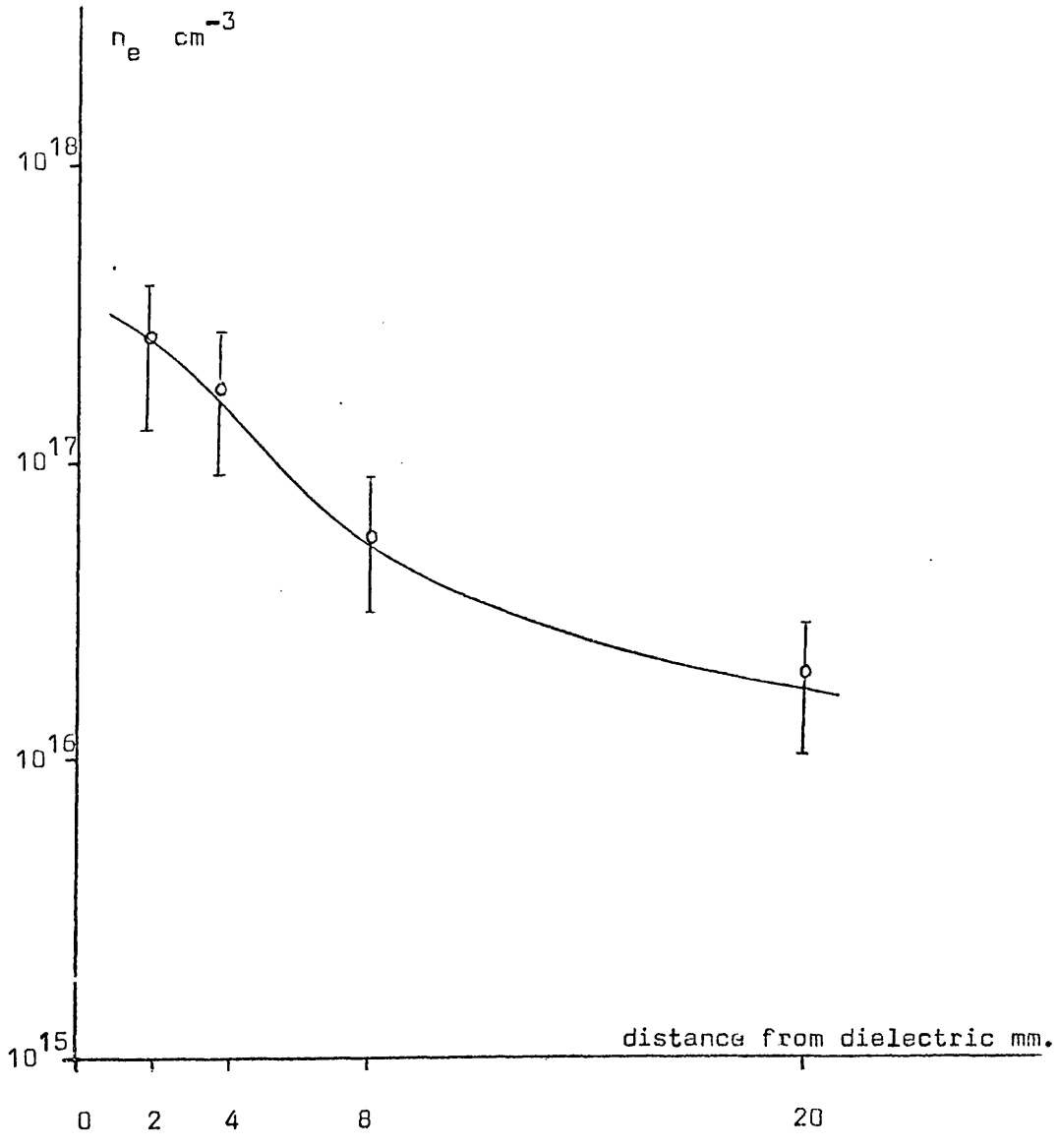

Equation (5.3.1) applies to optically thin lines. If most of the readily observable lines are strongly absorbed however, ion densities can still be determined, provided that n_e is known.

From equations (5.3.5) and (5.3.16), when $\tau_c \gg 1$ for a particular transition, then

$$\tau_o \simeq \frac{I_{Total}(\text{non-absorbed})}{I_{b.b.}} \simeq \left(\frac{\Delta\lambda}{\Delta\lambda_S}\right)^2 \qquad (6.3.10)$$

where $\Delta\lambda$ is the overall half-width including opacity broadening and $\Delta\lambda_S$ is the Stark half-width component. Thus measurement of $\Delta\lambda$ gives a direct value for τ if $\Delta\lambda_S$ is known. If only the total line intensity is known then, from equation (5.3.15),

$$\Delta\lambda \simeq I^* / 2 I_{b.b.}$$

so that

$$\tau_o \simeq \left(\frac{I^*}{2 I_{b.b.} \Delta\lambda_S}\right)^2 \qquad (6.3.11)$$

From equation (4.2.16), assuming that a Doppler profile describes the central portion of the line if it were optically thin, for a transition $p \rightarrow q$ of central wavelength λ_o ,

$$n(g) = \frac{10^{32}\, g_g \left(KT_e/\mu\right)^{1/2} e^{E_q/KT_e}}{1.61\, A(p,q)\, B_q^{**}\, \delta\, \lambda_o^3\, g_p} \left(\frac{I^*(p,q)}{2 I_{b.b.}(\lambda_c)\, \Delta\lambda_S}\right)^2 \qquad (6.3.12)$$

In some plasmas where the optical depth is a function of direction, it may be possible to measure $\Delta\lambda_S$ direct, without knowing the value of n_e .

The peak densities of C II, C III, C IV, F II, and F III ions were determined at various positions using equations (6.3.8), (6.3.9), (5.3.1) and (5.3.10). The density in the first few levels of C III was also determined using equation (6.3.12). For the transition $2p^2\ ^1D - 2s2p\ ^1P^o$, at $n_e = 2\times10^{17}$ cm^{-3}, $\Delta\lambda_S \sim 7.0\times10^{-3}$ Å from equation (5.4.1). λ_o = 2297 Å and $I(\lambda_o)_{black\text{-}body} \simeq$ 500 Watts/cm^2 Å st. if kT_e = 3.3 eV. Near the dielectric face, the value of I^* was $\sim$ 530 Watts/cm^2 Å st. so that $\tau_o \simeq 5.6\times10^3$ and the density of C III ions in the ground state at peak is $\sim 3 - 4\times10^{16}$ cm^{-3}. This agrees with the value of 4×10^{16} cm^{-3} obtained by the previous method.
Values of ion densities as a function of distance from the dielectric, together with errors, are shown in fig. 6.3.20.

From the time-of-flight measurements in fig. 6.2.7, the ratio of C III to C II ions is seen to change dramatically at $\sim$ 40 mm from the surface of the dielectric. Near to that surface the ratio is $\gtrsim$ 10, but further away the velocity of C II ions apparently increases to equal that of the C III ions. As there is no further acceleration at that point, the results suggest that significant recombination has taken place. The recombination rate for C III is greater than for C II so that, neglecting any velocity dispersion, the population density of C III ions must have dropped by a factor of $\gtrsim$ 10 by the time they have travelled 40 mm. The major part of the C II emission at that point will come from recombined C III ions. The recombination is first observed at $\sim$ 8 mm. from the surface. Expressing the decay in the form

$$n(\text{C III}) = n(\text{C III at } x=8 \text{ mm})\ e^{-n_e \alpha_{cr} t}$$

and putting n_e = a constant value of 4×10^{16} cm^{-3} (i.e. the value at 10 mm from the surface), then at d = 40 mm, after a flight time of 1.6 μ sec., $n_e \alpha_{cr} t$ is $\simeq 3$.

Fig. 6.3.20

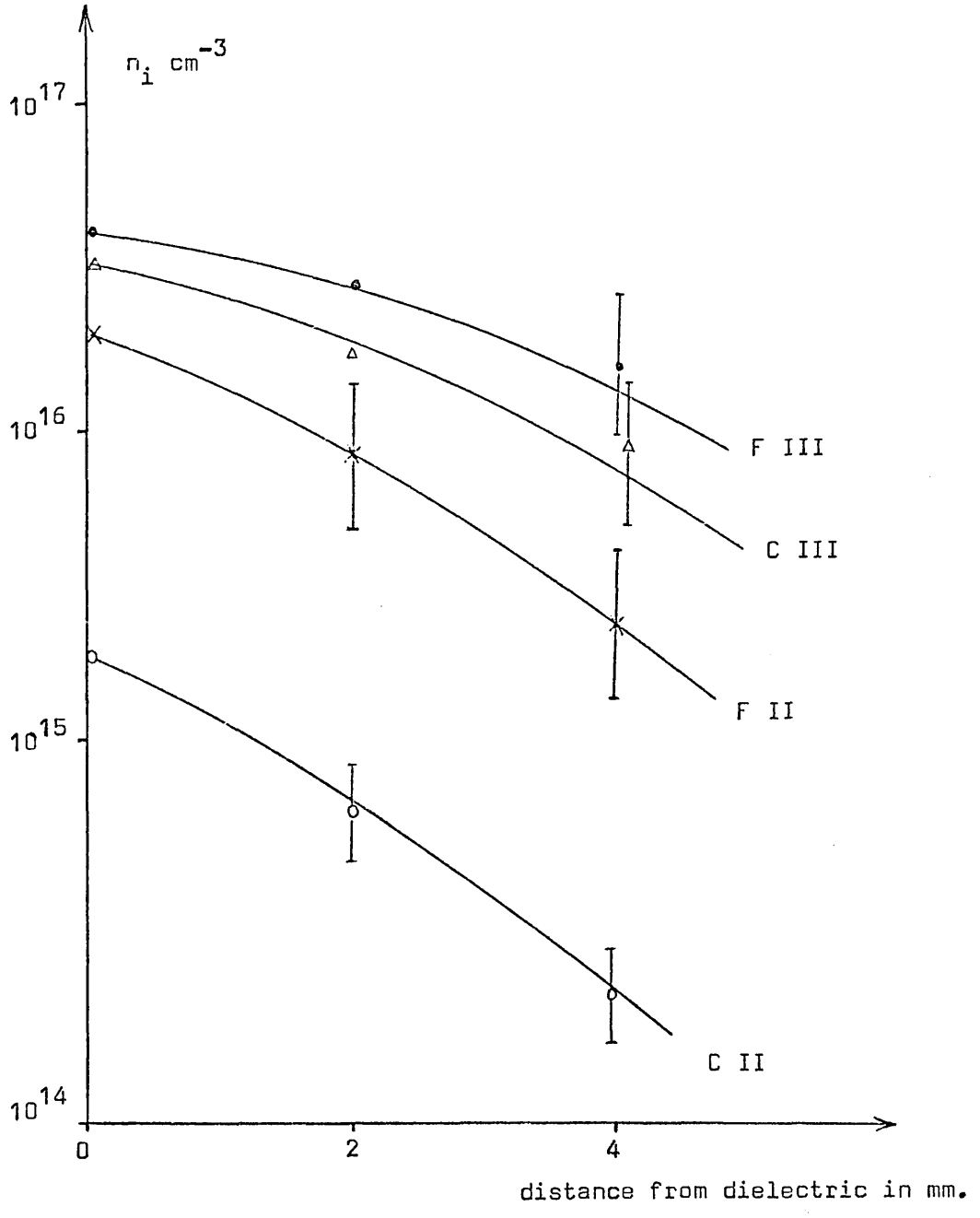
n_i cm^{-3}
10^{17}
10^{16}
10^{15}
10^{14}
F III
C III
F II
C II
0
2
4
distance from dielectric in mm.

The value of α_{CV} for recombination into doublet states of C II is $\simeq 10^{-10}$cm ^{3}sec^{-1} and, similarly, for recombination into triplet states of F II, $\alpha_{CV} \simeq 3\times10^{-11}$cm ^{3}sec^{-1}. These values are in close agreement ($\pm$50%) with the theoretical values previously discussed, which are shown in section 6.5 .

References

1. H.R.Griem,'Plasma Spectroscopy',McGraw Hill, New York, 1964

2. W.L.Wiese et.al.,Nat.Bur.Stand.Rept.no. NBS-4 vol.1,Washington,1966

3. J.T.Davies,J.M.Vaughan, Astrophys.J. , 137, p.1302, 1963

6.4 Numerical study of ablation

The production and acceleration of the ablation-derived plasma is predicted using the set of equations outlined in section 2.2 . To solve these, a mass ablation term from the dielectric is required. A numerical model for the ablation is presented here for the case when the solid is subjected to a transient energy flux from the plasma. The model incorporates literature values of bulk isothermal degradation data, and provision is also made for dealing with the problem of surface recession.
The situation is shown schematically in fig. 6.4.1.

Defining, T = temperature , ^{o}K

F = energy flux , $cal/cm^2 sec.$

G = pyrolytic pre-exponential factor , sec^{-1}

A = area of ablated surface , cm^2

α_c = thermal diffusivity of the dielectric , $cm^2/sec.$

k = thermal conductivity of the dielectric, $cal/sec\ cm\ ^{o}K$

ρ = density of the dielectric , gm/cm^3

ΔX = incremental ablating depth in the dielectric , cm.

Δt = time increment

ΔH = total heat of depolymerization and evaporation of the dielectric , kcal/mole of monomer

M = mass ablated , gm.

X = distance

t = time

E_a = pyrolysis activation energy , kcal/mole

the basic equations governing the ablation are ,

i) Conduction in the solid ,

$$\frac{\partial T(x,t)}{\partial t} = \alpha_c \frac{\partial^2 T(x,t)}{\partial x^2} \qquad (6.4.1)$$

$$\frac{\partial F(x,t)}{\partial t} = \alpha_c \frac{\partial^2 F(x,t)}{\partial x^2} \qquad (6.4.2)$$

ii) Loss of material at the surface of the dielectric

$$\frac{dM}{dt} = \rho A \Delta x \, \varsigma \, e^{-E_a/RT_s} \qquad (6.4.3)$$

iii) Transport of heat at various positions x within the dielectric

$$F(x,t) = -K \frac{\partial T(x,t)}{\partial x} + f(x,t) \qquad (6.4.4)$$

Boundary conditions prescribe,

$$\left.\begin{aligned} F(x,t) &\begin{cases} = 0 \;, & x > 0 \\ = F_c(t), & x = 0 \end{cases} \\ f(x,t) &\begin{cases} = 0 \;, & x > 0 \\ = \left(\dfrac{\Delta H \times 10^3}{\text{gramm-molec. wt.}}\right) \dfrac{dM/dt}{A} \;, & x = 0 \end{cases} \end{aligned}\right\} \qquad (6.4.5)$$

The use of equation (6.4.3) presupposes that thermal dissociation is the dominant means of degradation of the dielectric. In general cases of surface irradiation however, consideration must be given to the means of dissipation of the energy within the solid. In this plasma, temperatures range from $\sim$ 1 eV to $\sim$ 10 eV and the main wavelength region of the spectral emission is from $\sim$ 100 Å to 2000 Å , coming from optically thick resonance lines. At these wavelengths the main absorption mechanism will be photo-excitation of Carbon and Fluorine atoms within the solid. For hotter plasmas, much of the radiation will be below 100 Å, and inner-shell photo-ionization and Compton scattering will be important.

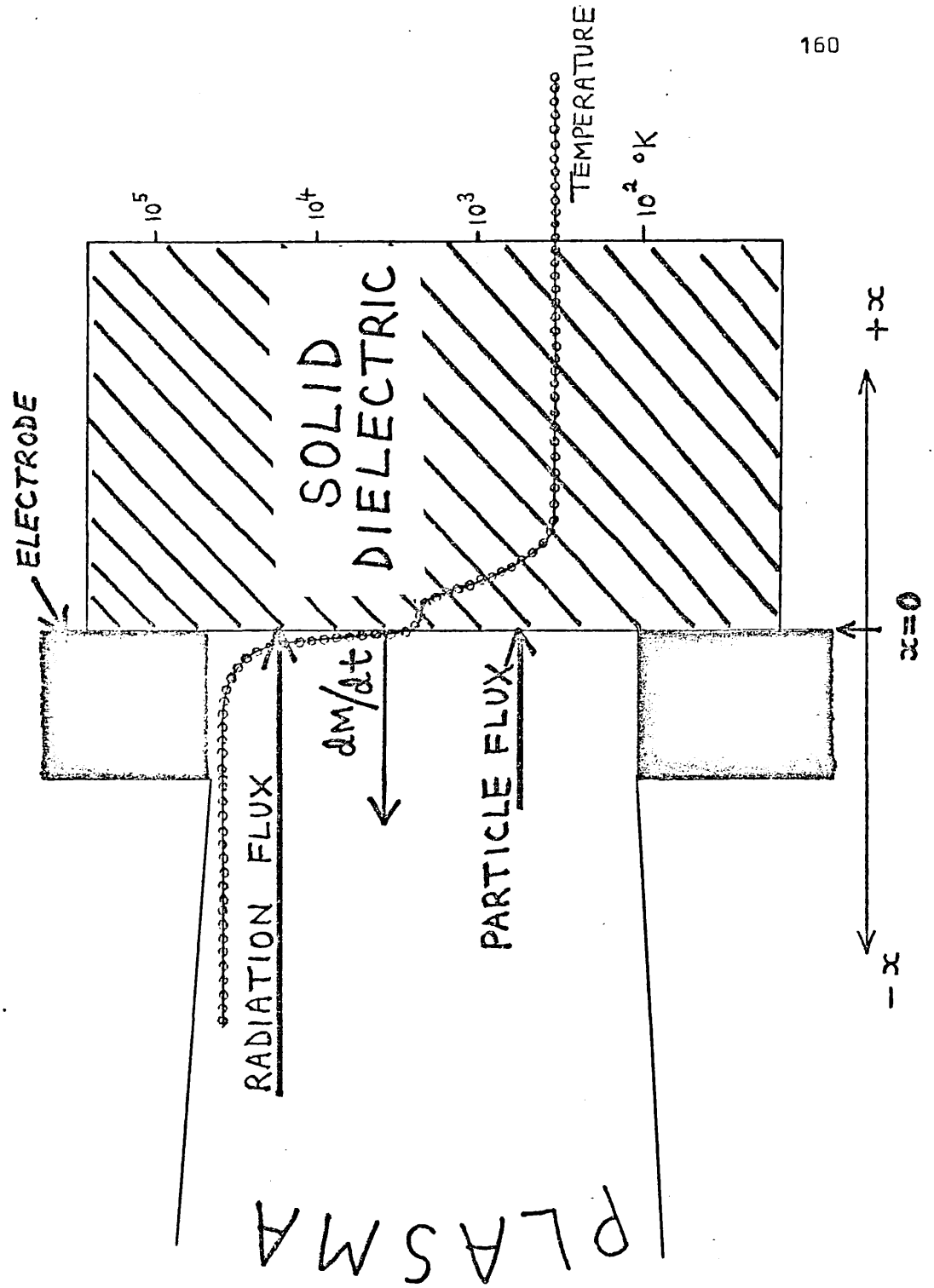
TEMPERATURE
10^5
10^4
10^3
10^2 °K
SOLID DIELECTRIC
ELECTRODE
+x
x=0
-x
dM/dt
RADIATION FLUX
PARTICLE FLUX
PLASMA

Fig. 6.4.1

Optical absorption to a depth d is almost instantaneous. The process of thermalizing the excess photon energy (up to 90% of the incident energy, after fluorescence has been accounted for) is completed in a conduction time for this distance of t^*. At low flux, in a time t^* , an amount of energy equal to A F t^* will be absorbed in the volume A d . If this energy is greater than the amount required to dissociate or ionize it all, then clearly this would have been taking place before the thermalization was completed.

Thus the condition for pyrolysis to dominate is,

$$F < \left(\frac{d\,\Delta H}{t^*} \right)$$

If the flux is large, dissociation may be direct but without direct ionization if,

$$\left(\frac{d\,\langle \chi_i \rangle}{t^*} \right) > F > \left(\frac{d\,\Delta H}{t^*} \right)$$

When $F > \left(\frac{d\langle \chi_i \rangle}{t^*} \right)$, if also $\frac{v_o \chi_i n_o d}{10\, F \lambda_{Debye}} \gtrsim 1$, where v_o is the velocity of the dissociated atoms of density n_o , both dissociation and ionization will be direct, as the probability is that a free atom will be photo-ionized before it has migrated a distance equal to about ten Debye lengths into the plasma. In that case collisional ionization would dominate. Attenuation coefficients at wavelengths around 200 Å, tabulated by Henke and Elgin[1] show that for Carbon polymers, 90% of the incident flux is lost by photo-excitation and scattering within $\sim 10^{-5}$ cm. It is expected that at least 90% of this energy is dissipated to the atoms and molecules as thermal energy. For example, in the case of Sodium Salicylate, which is an efficient fluorescent material in the vacuum-UV, it has been found[2,3] that, in the wavelength region 1 Å to 600 Å, between 70% and 95% of the

absorbed photon energy is dissipated in the solid by means of phonon interactions. This energy is distributed to all the atoms in the molecules. In order to simplify the solutions of equation (6.4.1) to (6.4.5), the following non-dimensional parameters are introduced ;

$$X' = X/L \qquad \Delta X' = \Delta X/L$$

$$t' = \alpha_c t/L^2 \qquad t' = \alpha_c \Delta t/L^2 \qquad (6.4.6)$$

$$P = T/T_o \qquad Q = F/F_o$$

where L = 1 cm. within the dielectric

A finite difference scheme is obtained from suitably truncated Taylor expansions of T(X,t) to second or third order accuracy. In difference form equation (6.4.1) becomes,

$$\frac{P(i+1,j) - 2P(i,j) + P(i-1,j)}{(\Delta X')^2} = \frac{P(i,j+1) - P(i,j)}{\Delta t'} \qquad (6.4.7)$$

where i and j define points on a space-time mesh respectively Values are chosen such that $(\Delta X')^2 = 3\,\Delta t'$, so that an explicit function for P(i,j+1) is obtained, namely

$$P(i,j+1) = \frac{P(i-1,j) + P(i,j) + P(i+1,j)}{3} \qquad (6.4.8)$$

Successive values on the space-time mesh are thus easily generated. For a time step of 10^{-7} sec., the spatial resolution on the mesh is equal to $(3\times10^{-7}\alpha_c)^{1/2}$, which is of the order 2×10^{-5} cm, for most polymer dielectrics.

A simple stability test showed this scheme to be stable toward truncation errors for all values of $\Delta X'$ and $\Delta t'$ when they are in the ratio of three to one, and the truncation error $\mathcal{E}^{o}(i,j)$ is ,

$$-\frac{(\Delta t')^2}{4}\left(\partial^2 P/\partial t'^2\right)_{i,j-1}$$

The magnitude of $\mathcal{E}^{o}(i,j)$ can be monitored by a finite difference scheme within the main program, i.e.,

$$\mathcal{E}^{o}(i,j) = \frac{P(i,j) - 2P(i,j-1) + P(i,j-2)}{4} \qquad (6.4.9)$$

and the error function $\mathcal{E}^{o}(i,j)/P(i,j)$ can be used to check if any reduction in the mesh size is necessary. Solutions for some simple analytical heating problems agreed with those obtained with this scheme to within a few percent or better.

In the case of both conduction and ablation, boundary conditions at the plasma - dielectric interface were introduced at each time step, through an iteration procedure which operated on a surface layer equal in thickness to one spatial increment of the mesh. A uniform temperature distribution was ascribed to this layer, through which equation (6.4.8) was adjusted until a balance existed between the incident energy and that lost by conduction and convection, following a partial dissociation. When, within a given time interval, the boundary of the dielectric is displaced by less than the thermal conduction depth, the iteration effectively accounts for surface recession. Temperatures within the surface layer are effectively adjusted during successive time steps, as are sub-surface temperatures. If the flux and the temperature become large, the situation is approached in which all the impacting energy is used for ablation, with a negligible amount for thermal conduction. In the present case, the validity of assuming a low - energy thermal ablation model was monitored at each time step in the program.

Values of dM/dt and $\int dM/dt \cdot dt$ are presented in figs. 6.4.2 and 6.4.3 for various values of surface energy flux equal to $kP(t)$, where $P(t)$ is the total Joule power to the plasma. With $k = 2.5\times10^{-3}$ cm^{-2}, the peak value of $kP(t)$ was equal to the maximum kinetic and ionization particle energy flux, and the ablation rate was far too small to account for the experimentally observed total ablated mass. With $k = 0.05$ cm^{-2}, a more realistic value estimated from the calculated radiation losses, the total mass ablated over the first few discharge cycles agreed with the experimental value to within 10%.

Under normal operating conditions Molybdenum was barely detectable in the plasma although it was noted in section 3.2 that, with higher electric field-strengths, the onset of electron runaway led to sputtering from the cathode. Norwood[4] has estimated the photo-electric current from a cathode of 1 cm^2 area in a plasma radiating as a black-body at a temperature of 5 eV. Assuming an efficiency for electron emission of 100%, he showed that currents of $\sim 10^7$ Amps are possible. In this plasma most of the radiation lies in the vacuum-U.V. region and is $\simeq 10^{-3}$x the black-body value at peak. Thus the major portion of the 2×10^4 Amps drawn from the cathode in this experiment could be accounted for by photo-emission.

References

1. B.L.Henke,R.L.Elgin, Advances in X-ray Analysis, 13 , p.1 , 1970

2. R.Allison,J.Burns,A.J.Tuzzolino,J.Opt.Soc.America, 54, p.747, 1964

3. E.Krokowski, Naturwiss., 45 ,p.509 , 1958

4. J.Norwood,NASA TN D-3796, NASA Washington D.C. , 1967

FIG. 6.4.2

Rate of ablation of PTFE in gm/sec for various values of surface energy flux, defined by the parameter k

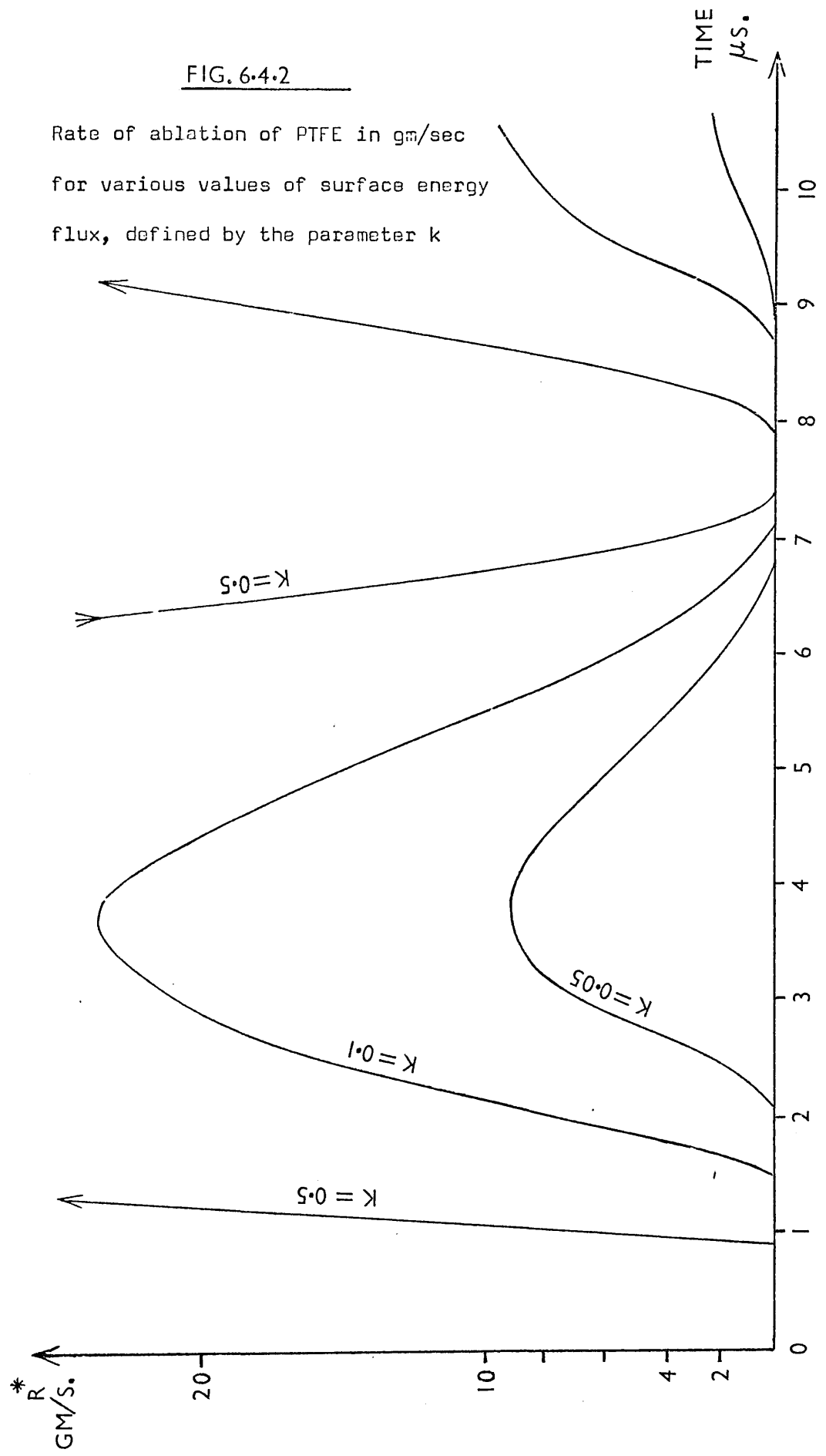

Fig. 6.4.3

Total amount of PTFE ablated, in gms, when subjected to various values of surface energy flux defined by the parameter k

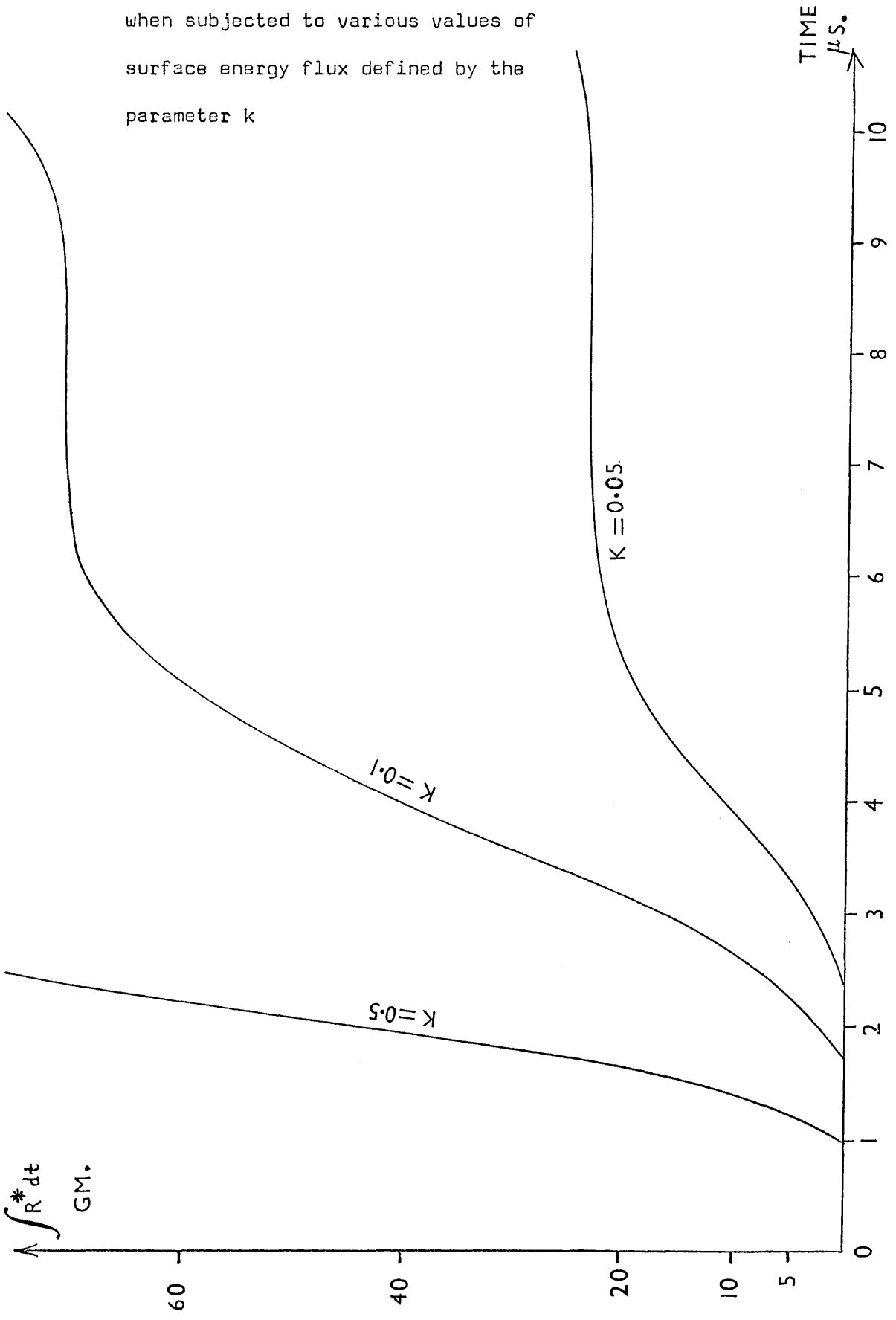

6.5 Atomic Parameters

For an isolated plasma in which stimulated emission can be neglected, the rate of population of levels p in an ion of charge i , with $p < p^*$, can be written as

$$\dot{\underline{N}} = \underline{\underline{A}}\ \underline{N}$$

where $\underline{N}$ is a column vector $= \begin{vmatrix} n_{i,1} \\ n_{i,2} \\ n_{i,3} \\ \vdots \\ n_{i,p^*} \\ n_{i+1,1} \end{vmatrix}$

and p^* is a level sufficiently high up in the term scheme of the ion that contributions to levels $p < p^*$ from levels above p^* are negligible. $\underline{\underline{A}}$ is a second-rank level-interaction tensor of order $(p^*+1) \times (p^*+1)$, consisting of collisional transition, spontaneous decay and stimulated absorption terms.

The deviation parameters obtained from the quasi-steady state solutions of equations (6.5.3) with $\left|\dot{\underline{N}}\right|_p^2 = 0$ have been obtained using the method of successive approximation outlined in chapter four. They have been derived for Carbon II, III and IV and Fluorine II for levels up to p=20, for a range of temperatures and densities covering the Coronal to LTE regimes (i.e. $n_e \sim 10^{15} - 10^{20}$ cm^{-3} , $kT_e \sim 0.5 - 20$ eV).

Under these conditions neither the depression of the ionization potential nor the pressure broadening of the levels were sufficient to affect the assumption of discrete energy states up to p=20.

The calculations were performed for plasmas both optically thin and thick to the main resonance lines by including or omitting the resonance terms for radiative decay. Values of the deviation parameters are listed in tables 6.5.1 to 6.5.6, for the most important lower levels. The intervals chosen in density and temperature were such as to allow a smooth interpolation between them and extrapolation to higher and lower values. Generally, for isolated plasmas, any of these ions will be substantially ionized when the ionization potential is of the order kT_e. The temperature range used for the calculations thus covers the situations in which these ions are most likely to be observed. The tendency towards unity in the values of B_p with increase of density can be clearly seen, as well as the tendency for B_p to stabilize as p increases. Errors are estimated at between $\sim$ 100% and $\sim$ 30% at $n_e = 10^{15}$ cm^{-3} and 2×10^{16} cm^{-3} respectively, decreasing as n_e increases. Some idea of the size of the errors is obtained by comparing the values of B_p for a given value of n_e with the value when n_e is twice that value. This simulates a 100% change in all transition rates caused by electron collisions. The results for Carbon II differed from those of Suckewer[1] by a factor less than two at $n_e = 10^{16}$ cm^{-3} and by only a few percent at $n_e = 10^{18}$ cm^{-3}. Suckewer utilised oscillator strengths listed by Allen[2] and Griem[3] whilst, in the present case, the more recent values of Wiese[4] were used. There is a difference in values for the resonance transitions of between 30% and 100% and the collisional rate coefficients also differed slightly in form from those used by Suckewer (Griem[5])

Collisional-radiative ionization and recombination coefficients covering the same density and temperature range have also been obtained, using equns. (4.2.6) and (4.2.8). The thermal levels p_T were obtained for each ion from inspection of the tables of deviation parameters.

Some values are shown in tables 6.5.7 to 6.5.10 for optically thin and thick plasmas. In the calculations a band of levels around p_T was considered and the final errors, which were governed mainly by those associated with the other parameters rather than with the method itself, were estimated as varying between $\sim$ 20% and $\sim$ 100% , being lowest when the density is low.

References

1. S.Suckewer, J.Phys.B.,3 , p.380, 1970

2. C.W.Allen,'Astrophysical Quantities',Athlone Press, London, 1963

3. H.R.Griem,'Plasma Spectroscopy',McGraw Hill, New York, 1964

4. W.L.Wiese, Nat.Bur.Stand.Rept.No. NSRDS NBS-4 ,Vol.1,Washington,1966

5. H.R.Griem,Phys.Rev. 131, p.1170, 1963

CII L.T.E. Deviation Parameters

1) Optically thin plasma

n_e cm.$^{-3}$	B_3	B_4	B_5	B_7	B_8	B_{10}	B_{11}	B_{13}	B_{18}
				T_e = 1.0 eV.					
10^{15}	8.41^{-2}	4.14^{-2}	2.77^{-2}	2.22^{-2}	3.72^{-2}	7.4^{-3}	1.41^{-2}	1.96^{-2}	1.17^{-2}
10^{16}	0.479	0.302	0.222	0.204	0.279	0.215	0.190	0.167	0.184
5×10^{16}	0.821	0.684	0.588	0.563	0.659	0.632	0.555	0.500	0.550
10^{17}	0.902	0.812	0.741	0.720	0.794	0.778	0.715	0.666	0.712
10^{18}	0.989	0.977	0.966	0.963	0.975	0.972	0.962	0.952	0.962
10^{19}	0.999	0.998	0.997	0.996	0.997	0.997	0.996	0.995	0.999
				T_e = 2.5 eV.					
10^{15}	5.49^{-2}	2.66^{-2}	1.77^{-2}	1.47^{-2}	2.38^{-2}	3.2^{-3}	8.0^{-3}	1.25^{-2}	7.2^{-3}
10^{16}	0.367	0.215	0.153	0.138	0.196	0.130	0.124	0.112	0.122
5×10^{16}	0.744	0.578	0.474	0.445	0.550	0.513	0.435	0.387	0.434
10^{17}	0.853	0.732	0.644	0.616	0.709	0.686	0.609	0.558	0.608
10^{18}	0.983	0.965	0.948	0.941	0.961	0.957	0.940	0.927	0.940
10^{19}	0.998	0.996	0.995	0.994	0.996	0.996	0.994	0.992	0.999
				T_e = 5.0 eV.					
10^{15}	3.95^{-2}	1.9^{-2}	1.26^{-2}	1.04^{-2}	1.7^{-2}	2.2^{-3}	7.2^{-3}	8.9^{-3}	5.8^{-3}
10^{16}	0.291	0.162	0.113	0.103	0.147	0.090	0.098	0.082	0.095
5×10^{16}	0.673	0.492	0.390	0.367	0.463	0.407	0.363	0.309	0.360
10^{17}	0.804	0.659	0.561	0.536	0.633	0.586	0.533	0.472	0.531
10^{18}	0.976	0.951	0.927	0.920	0.945	0.934	0.920	0.899	0.919
10^{19}	0.998	0.995	0.992	0.991	0.994	0.993	0.991	0.990	0.999

CIII L.T.E. Deviation Parameters

1) Optically thin plasma

n_e cm.$^{-3}$	B_3	B_4	B_5	B_7	B_8	B_{10}	B_{12}	B_{16}	B_{18}
				T_e = 1.0 eV.					
10^{15}	3.42^{-2}	5.66^{-2}	1.07^{-2}	6.0^{-3}	4.0^{-4}	4.8^{-3}	3.0^{-4}	3.0^{-4}	2.0^{-4}
10^{16}	0.261	0.375	0.215	0.057	0.029	0.056	0.020	0.016	0.014
5×10^{16}	0.639	0.750	0.612	0.233	0.248	0.232	0.202	0.190	0.190
10^{17}	0.780	0.857	0.763	0.378	0.437	0.377	0.386	0.376	0.375
10^{18}	0.973	0.984	0.970	0.859	0.902	0.858	0.888	0.887	0.887
10^{19}	0.997	0.998	0.997	0.984	0.989	0.984	0.988	0.988	0.988
				T_e = 4.0 eV.					
10^{15}	1.74^{-2}	2.91^{-2}	3.20^{-3}	3.0^{-3}	1.0^{-4}	2.6^{-3}	1.0^{-4}	1.0^{-4}	5.0^{-5}
10^{16}	1.5^{-1}	2.31^{-1}	1.05^{-1}	2.95^{-2}	9.0^{-3}	2.9^{-2}	7.3^{-3}	4.5^{-3}	3.7^{-3}
5×10^{16}	0.469	0.599	0.432	0.132	0.113	0.131	0.097	0.081	0.079
10^{17}	0.639	0.750	0.612	0.233	0.248	0.233	0.227	0.205	0.202
10^{18}	0.947	0.968	0.942	0.752	0.818	0.752	0.809	0.800	0.798
10^{19}	0.994	0.997	0.994	0.968	0.979	0.968	0.978	0.977	0.977
				T_e = 8.0 eV.					
10^{15}	1.24^{-2}	2.08^{-2}	4.0^{-3}	2.1^{-3}	1.0^{-4}	1.7^{-3}	1.0^{-4}	1.0^{-4}	5.0^{-5}
10^{16}	1.11^{-1}	1.75^{-1}	9.22^{-2}	2.1^{-2}	4.8^{-3}	2.05^{-2}	4.1^{-3}	3.7^{-3}	2.6^{-3}
5×10^{16}	0.385	0.515	0.370	0.097	0.071	0.097	0.059	0.056	0.053
10^{17}	0.556	0.680	0.545	0.177	0.172	0.176	0.153	0.151	0.147
10^{18}	0.926	0.955	0.924	0.682	0.758	0.682	0.747	0.746	0.745
10^{19}	0.992	0.995	0.992	0.956	0.971	0.956	0.969	0.969	0.969

CIV L.T.E. Deviation Parameters

1) Optically thin plasma

n_e cm.$^{-3}$	B_2	B_3	B_4	B_5	B_7	B_8	B_{11}	B_{12}	B_{18}
				T_e = 1.0 eV.					
2×10^{15}	2.21^{-1}	1.2^{-3}	2.2^{-3}	1.0^{-3}	6.0^{-4}	4.0^{-4}	3.0^{-4}	3.0^{-4}	2.0^{-4}
10^{16}	5.87^{-1}	1.59^{-2}	1.29^{-2}	1.26^{-2}	5.6^{-3}	5.5^{-3}	4.2^{-3}	4.2^{-3}	3.6^{-3}
5×10^{16}	0.877	0.107	0.092	0.089	0.063	0.062	0.051	0.051	0.050
10^{17}	0.934	0.203	0.186	0.181	0.148	0.147	0.130	0.130	0.129
10^{18}	0.993	0.730	0.723	0.719	0.703	0.702	0.691	0.691	0.691
10^{19}	0.999	0.965	0.964	0.963	0.961	0.961	0.960	0.960	0.960
				T_e = 4.0 eV.					
2×10^{15}	1.24^{-1}	3.0^{-4}	1.0^{-3}	3.0^{-4}	3.0^{-4}	1.0^{-4}	1.0^{-4}	1.0^{-4}	1.0^{-4}
10^{16}	4.15^{-1}	5.7^{-3}	5.7^{-3}	4.6^{-3}	1.9^{-3}	1.9^{-3}	1.4^{-3}	1.4^{-3}	1.2^{-3}
5×10^{16}	0.780	0.051	0.046	0.043	0.025	0.025	0.019	0.019	0.019
10^{17}	0.877	0.107	0.101	0.095	0.068	0.067	0.055	0.055	0.054
10^{18}	0.986	0.574	0.570	0.563	0.540	0.538	0.522	0.522	0.522
10^{19}	0.999	0.932	0.931	0.930	0.926	0.926	0.922	0.922	0.922
				T_e = 10.0 eV.					
2×10^{15}	2.12^{-1}	4.0^{-4}	7.0^{-4}	3.0^{-4}	2.0^{-4}	1.0^{-4}	1.0^{-4}	1.0^{-4}	5.0^{-5}
10^{16}	5.74^{-1}	5.0^{-3}	4.1^{-3}	3.9^{-3}	1.4^{-3}	1.4^{-3}	1.2^{-3}	1.2^{-3}	1.0^{-3}
5×10^{16}	0.871	0.037	0.031	0.030	0.015	0.015	0.013	0.013	0.012
10^{17}	0.931	0.075	0.068	0.064	0.041	0.040	0.036	0.036	0.036
10^{18}	0.993	0.465	0.459	0.452	0.422	0.421	0.415	0.415	0.415
10^{19}	0.999	0.897	0.896	0.895	0.888	0.888	0.887	0.887	0.887

FII L.T.E. Deviation Parameters

1) Optically thin plasma

n_e cm.$^{-3}$	B_4	B_6	B_7	B_8	B_{13}	B_{14}	B_{15}	B_{16}	B_{18}
				T_e = 1.0 eV.					
10^{15}	8.6^{-3}	6.2^{-3}	6.86^{-1}	4.4^{-3}	4.27^{-1}	3.1^{-3}	3.59^{-1}	8.15^{-1}	2.9^{-3}
10^{16}	7.96^{-2}	5.83^{-2}	9.56^{-1}	5.61^{-2}	9.02^{-1}	5.03^{-2}	8.76^{-1}	9.78^{-1}	5.2^{-2}
5×10^{16}	0.302	0.236	0.991	0.235	0.979	0.229	0.073	0.996	0.231
10^{17}	0.464	0.382	0.995	0.381	0.990	0.376	0.990	0.998	0.378
10^{18}	0.896	0.861	0.999	0.861	0.999	0.860	0.999	0.999	0.860
10^{19}	0.989	0.984	0.999	0.984	0.999	0.984	0.999	0.999	0.984
				T_e = 4.0 eV.					
10^{15}	4.3^{-3}	3.1^{-3}	7.66^{-1}	2.4^{-3}	5.46^{-1}	1.7^{-3}	2.72^{-1}	8.68^{-1}	1.7^{-3}
10^{16}	4.15^{-2}	3.0^{-2}	9.7^{-1}	2.92^{-2}	9.33^{-1}	2.71^{-2}	8.21^{-1}	9.86^{-1}	2.8^{-2}
5×10^{16}	0.178	0.134	0.994	0.133	0.986	0.131	0.959	0.997	0.132
10^{17}	0.302	0.236	0.997	0.236	0.993	0.234	0.979	0.999	0.234
10^{18}	0.812	0.756	0.999	0.756	0.999	0.755	0.998	0.999	0.755
10^{19}	0.977	0.969	0.999	0.969	0.999	0.969	0.999	0.999	0.969
				T_e = 8.0 eV.					
10^{15}	3.0^{-3}	2.2^{-3}	6.99^{-1}	1.6^{-3}	4.45^{-1}	1.1^{-3}	3.76^{-1}	8.23^{-1}	1.0^{-3}
10^{16}	2.97^{-2}	2.14^{-2}	9.59^{-1}	2.06^{-2}	9.07^{-1}	1.86^{-2}	8.83^{-1}	9.79^{-1}	1.9^{-2}
5×10^{16}	0.133	0.099	0.992	0.098	0.980	0.096	0.975	0.996	0.096
10^{17}	0.234	0.180	0.996	0.179	0.990	0.177	0.987	0.998	0.178
10^{18}	0.754	0.686	0.999	0.686	0.999	0.685	0.999	0.999	0.686
10^{19}	0.968	0.956	0.999	0.956	0.999	0.956	0.999	0.999	0.956

CII L.T.E. Deviation Parameters

2) Plasma optically thick towards resonance radiation

n_e cm.$^{-3}$	B_7	B_8	B_9	B_{10}	B_{11}	B_{13}	B_{16}	B_{18}
				T_e = 1.0 eV.				
10^{16}	0.985	0.279	0.925	0.583	0.944	0.167	0.936	0.937
5×10^{16}	0.997	0.659	0.984	0.875	0.988	0.500	0.987	0.987
10^{17}	0.999	0.794	0.992	0.933	0.994	0.666	0.993	0.993
10^{18}	0.999	0.975	0.999	0.993	0.999	0.952	0.999	0.999
				T_e = 4.0 eV.				
10^{16}	0.990	0.162	0.947	0.412	0.961	0.091	0.949	0.953
5×10^{16}	0.998	0.491	0.989	0.778	0.992	0.333	0.989	0.990
10^{17}	0.999	0.659	0.995	0.875	0.996	0.500	0.995	0.995
10^{18}	0.999	0.951	0.999	0.986	0.999	0.909	0.999	0.999

CIII L.T.E. Deviation Parameters

2) Plasma optically thick towards resonance radiation

	B_4	B_5	B_7	B_8	B_{10}	B_{12}	B_{16}	B_{18}
				T_e = 1.0 eV.				
10^{15}	5.66^{-2}	3.14^{-1}	6.0^{-3}	1.26^{-2}	4.8^{-3}	6.9^{-3}	2.7^{-3}	2.9^{-3}
10^{16}	0.375	0.821	0.057	0.113	0.056	0.066	0.044	0.047
10^{17}	0.857	0.979	0.378	0.560	0.377	0.490	0.477	0.479
10^{18}	0.984	0.998	0.859	0.927	0.858	0.913	0.911	0.912
				T_e = 4.0 eV.				
10^{15}	2.9^{-2}	1.87^{-1}	3.0^{-3}	6.3^{-3}	2.6^{-3}	3.4^{-3}	1.3^{-3}	1.4^{-3}
10^{16}	0.231	0.696	0.030	0.060	0.029	0.036	0.021	0.022
10^{17}	0.750	0.958	0.233	0.389	0.233	0.352	0.318	0.316
10^{18}	0.968	0.996	0.752	0.864	0.752	0.855	0.845	0.843

CIV L.T.E. Deviation Parameters

2) Plasma optically thick towards resonance radiation

n_e cm.$^{-3}$	B_3	B_4	B_5	B_7	B_8	B_{11}	B_{12}	B_{18}
				T_e = 1.0 eV.				
10^{16}	2.7^{-2}	1.67^{-2}	2.01^{-2}	8.3^{-3}	8.2^{-3}	6.7^{-3}	6.7^{-3}	5.7^{-3}
5×10^{16}	0.122	0.102	0.101	0.071	0.070	0.058	0.058	0.057
10^{17}	0.218	0.197	0.192	0.158	0.156	0.138	0.138	0.137
10^{18}	0.736	0.728	0.724	0.708	0.707	0.696	0.696	0.696
				T_e = 4.0 eV.				
10^{16}	1.37^{-2}	9.2^{-3}	1.05^{-2}	3.7^{-3}	3.7^{-3}	3.1^{-3}	3.1^{-3}	2.7^{-3}
5×10^{16}	0.065	0.057	0.054	0.032	0.031	0.024	0.024	0.023
10^{17}	0.122	0.114	0.108	0.077	0.076	0.062	0.062	0.062
10^{18}	0.582	0.577	0.571	0.547	0.546	0.529	0.529	0.529

FII L.T.E. Deviation Parameters

2) Plasma optically thick towards resonance radiation

	B_7	B_8	B_{13}	B_{14}	B_{15}	B_{16}	B_{18}
				T_e = 1.0 eV.			
10^{15}	0.687	0.714	0.428	0.224	0.359	0.814	0.333
10^{16}	0.956	0.961	0.902	0.789	0.877	0.978	0.863
10^{17}	0.996	0.996	0.989	0.975	0.987	0.998	0.985
				T_e = 4.0 eV.			
10^{15}	0.767	0.789	0.546	0.320	0.272	0.868	0.448
10^{16}	0.971	0.974	0.933	0.849	0.821	0.985	0.905
10^{17}	0.997	0.997	0.993	0.983	0.979	0.999	0.990

Fig. 6.5.7

The coefficient α_{cr} for collisional-radiative recombination into doublet states of C II for optically thin plasmas. (Values for plasmas optically thick to the first few resonance lines are shown in brackets where they differ significantly from those for optically thin plasmas)

n_e cm^{-3}	T_e= 1 eV	T_e= 2 eV	T_e= 3 eV	T_e= 10 eV
$\rightarrow$ 0	1.4×10^{-12}	1.0×10^{-12}	8.5×10^{-13}	4.7×10^{-13}
10^{15}	2.1×10^{-10}	1.5×10^{-11} (8.7×10^{-12})	5.4×10^{-12} (2.6×10^{-12})	1.1×10^{-12} (7.0×10^{-13})
10^{16}	3.7×10^{-9}	1.7×10^{-10} (7.3×10^{-11})	4.5×10^{-11} (2.0×10^{-11})	2.4×10^{-12} (1.1×10^{-12})
10^{17}	4.6×10^{-8}	1.8×10^{-9}	1.5×10^{-10}	9.0×10^{-12}
10^{18}	1.5×10^{-7}	4.4×10^{-9}	2.4×10^{-10}	1.3×10^{-11}
10^{19}	1.5×10^{-6}	4.2×10^{-8}	2.3×10^{-9}	1.3×10^{-10}
$\rightarrow\infty$	$1.5\times10^{-25}n_e$	$4.2\times10^{-27}n_e$	$2.3\times10^{-28}n_e$	$1.3\times10^{-29}n_e$

Units: cm^{3}sec^{-1}

Fig. 6.5.8

The coefficient α_{cr} for collisional-radiative recombination into singlet states of C III.

n_e cm^{-3}	T_e= 1 eV	T_e= 2 eV	T_e= 3 eV	T_e= 10 eV
$\rightarrow$ 0	2.4×10^{-12}	1.7×10^{-12}	1.4×10^{-12}	7.7×10^{-13}
10^{13}	1.3×10^{-8}	1.1×10^{-10}	2.1×10^{-11}	3.2×10^{-12}
10^{15}	1.5×10^{-6}	1.2×10^{-9}	1.2×10^{-10}	5.4×10^{-12}
10^{16}	4.7×10^{-6}	2.1×10^{-9}	1.6×10^{-10}	5.6×10^{-12}
10^{17}	3.8×10^{-5}	8.0×10^{-9}	5.8×10^{-10}	8.8×10^{-12}
10^{18}	2.8×10^{-4}	4.5×10^{-8}	3.0×10^{-9}	2.2×10^{-11}
10^{19}	2.8×10^{-3}	4.5×10^{-7}	2.9×10^{-8}	1.3×10^{-10}
$\rightarrow \infty$	$2.8\times10^{-22}n_e$	$4.5\times10^{-26}n_e$	$2.9\times10^{-27}n_e$	$1.3\times10^{-29}n_e$

Fig. 6.5.9

The coefficient α_{cr} for collisional-radiative recombination into singlet states of F II.
(Also shown in brackets are values for recombination into triplet states).

n_e cm^{-3}	T_e= 1 eV	T_e= 2 eV	T_e= 3 eV	T_e= 10 eV
$\rightarrow 0$	6.4×10^{-13} (1.3×10^{-12})	4.5×10^{-13} (9.4×10^{-13})	3.7×10^{-13} (7.7×10^{-13})	2.0×10^{-13} (4.2×10^{-13})
10^{15}	2.0×10^{-11} (3.5×10^{-11})	1.9×10^{-12} (2.0×10^{-12})	9.4×10^{-13} (1.2×10^{-12})	3.8×10^{-13} (4.4×10^{-13})
10^{16}	2.4×10^{-11} (1.1×10^{-8})	2.0×10^{-12} (2.0×10^{-11})	9.5×10^{-13} (2.9×10^{-12})	3.9×10^{-13} (4.6×10^{-13})
10^{17}	6.4×10^{-11} (3.5×10^{-8})	2.6×10^{-12} (3.2×10^{-11})	1.1×10^{-12} (3.7×10^{-12})	4.0×10^{-13} (4.8×10^{-13})
10^{18}	4.6×10^{-10} (2.7×10^{-7})	9.6×10^{-12} (1.6×10^{-10})	2.4×10^{-12} (1.1×10^{-11})	4.2×10^{-13} (5.0×10^{-13})
$\rightarrow \infty$	$4.4\times10^{-28}n_e$ ($2.6\times10^{-25}n_e$)	$7.8\times10^{-30}n_e$ ($1.4\times10^{-28}n_e$)	$1.4\times10^{-30}n_e$ ($8.4\times10^{-30}n_e$)	$3.8\times10^{-32}n_e$ ($4.1\times10^{-33}n_e$)

Fig. 6.5.10

The coefficient S_{cr} for collisional-radiative electron-impact ionization from multiplet states of various ions.

n_e cm^{-3}	C II doublets	CII quartets	C III singlets	C III triplets
$\rightarrow 0$	3.4×10^{-13}	3.0×10^{-13}	8.2×10^{-17}	3.6×10^{-17}
10^{15}	6.3×10^{-11}	2.2×10^{-11}	4.8×10^{-14}	2.3×10^{-13}
10^{16}	7.5×10^{-10}	1.6×10^{-10}	4.1×10^{-13}	5.0×10^{-13}
10^{17}	1.2×10^{-9}	8.2×10^{-10}	4.9×10^{-12}	4.2×10^{-12}
10^{18}	1.2×10^{-9}	4.5×10^{-10}	3.5×10^{-11}	3.2×10^{-11}
$\rightarrow \infty$	1.2×10^{-9}	4.5×10^{-10}	3.5×10^{-11}	3.9×10^{-11}

6.6 Energy Flux to the Propellant

The plasma loses energy to the dielectric by thermal conduction, internal ion energy transport and radiation. An expression is obtained for the instantaneous energy flux to the dielectric surface from the plasma. The fact that the temperature was observed to be almost constant during the discharge even though the input power was varying, suggested that losses were large and that some fraction of these may reach the dielectric.

In order to estimate the flux certain assumptions were made, namely

(i) each plasma constituent had an isotropic velocity distribution with current drift (v_d) and thrust (v_t) velocities superimposed.

(ii) Electrons and ions both impact onto the dielectric surface, but the net current flow to it is made zero by the establishment of a charge sheath.

(iii) The charge sheath is uniform over the whole of the dielectric surface and ion mean free paths are larger than the thickness of the sheath.

(iv) Ions are assumed to be predominantly in their ground states and to lose their ionization energy as a result of recombination after the surface impact, this energy being eventually dissipated in the solid.

(v) Differences in the mean free paths of the constituent ions do not generate any additional polarization fields at the charge sheath.

The first assumption has been verified in section 2.2 and, to a good approximation, $T_e = T_{i,j}$ with the average thermal velocities given as ,

$$v_e = (8kT_e/\pi\, m_e)^{1/2} \quad , \quad v_{i,j} = (8kT_e/\pi\, m_{i,j})^{1/2}$$

For a stationary homogeneous plasma in contact with a surface, the ion flux normal to a unit area of that surface is,

$$\int_{-\infty}^{\infty}\int_{-\infty}^{\infty}\int_{0}^{\infty} v(j,i)_x \, f_i(v) \cdot dv_x \, dv_y \, dv_z$$

For a Maxwellian distribution this becomes

$$= \sum_{j=k} \frac{n(j,i)v(j,i)H(j,i)}{4} \qquad (6.6.1)$$

The factor H(j,i) has been introduced and modifies the ion flow by taking into account the ion mean free paths λ_j. Chen[1], in dealing with probes of various shapes immersed in a plasma, has derived an expression for H(j,i) in the case of a spherical probe, namely

$$H(j,i) = \left(\frac{3\,\underline{a}^2}{4\lambda_j(\lambda_j + \underline{a})} + k' \right)^{-1} \qquad (6.6.2)$$

where k' is a factor between 1 and 1/2 which represents the solid angle blocked-off by the probe at a distance λ_j away, and $\underline{a}$ is the probe radius.

If $\lambda_j \gg \underline{a}$, the plasma is collisionless, $k' = 1$ and $H(j,i) \rightarrow 1$.

If $\lambda_j \ll \underline{a}$, H(j,i) tends towards the value $\lambda_j/\underline{a}$.

The general form of equation (6.6.2) does not depend strongly on the probe shape and in the present experiment the dielectric surface can be regarded as a rectangular probe with sides of length 2d and 2b. In this case the shadowing factor k' can be shown to be given by,

$$k' = \left(1 + \frac{4b \tan^{-1}(d/\lambda_j)}{2\pi(b^2 + \lambda_j^2)^{1/2}} \right)^{-1} \qquad (6.6.3)$$

As with the spherical case, k' lies between 1 and 1/2.

The total ion charge current to the dielectric is, from equation (6.6.1),

$$e \sum_{j=k} \frac{n(j,i)v(j,i)H(j,i)}{4} \qquad (6.6.4)$$

The electrons will hardly notice the presence of the solid surface as most of them are reflected from the charge sheath and, as they will in consequence maintain their isotropic distribution, $H_e \simeq 1$.

The electron current would be $-en_e v_e/4$ but, in accordance with assumption (ii) above, only a fraction s^* of that flux remains unrepelled by the sheath. Assuming overall charge neutrality,

$$n_e = \sum_{j=k} n(j,i)Z_j \qquad \text{and,}$$

$$s^* = \sum_{j=k} \frac{n(j,i)v(j,i)H(j,i)Z_j}{n_e v_e} = \frac{m_e^{1/2}}{n_e} \sum_{j=k} \frac{n(j,i)H(j,i)Z_j}{m(j,i)^{1/2}} \qquad (6.6.5)$$

The effect of s^* upon the thermal energy transport is similar to that discussed by Lovberg[2] when λ_j is large and $H(j,i) = 1$. By integrating the energy of those electrons that are able to penetrate the charge sheath, Lovberg has shown that the average kinetic energy of impacting electrons is

$$W_e = kT_e(\ln.\frac{1}{s^*} + 2)$$

The total average kinetic energy including the main current drift energy, which is parallel to the dielectric surface in directionality, is then

$$W_e(\text{total}) = kT_e(\ln.\frac{1}{s^*} + 2) + m_e v_{de}^2/2 \qquad (6.6.6)$$

The charge sheath represents a sink for the ions. Again following Lovberg, the average normal ion kinetic energy is kT_i , which = kT_e .
It is shown[2] that,

$$W_{j,i}(\text{total}) = 2kT_e + m(j,i)v_d(j,i)^2/2 \qquad (6.6.7)$$

The total kinetic energy flux from all particles, $F_{k.E.}$, is thus

$$F_{k.E.} = \sum_{j=k} \frac{n(j,i)v(j,i)H(j,i)}{4} \left[2kT_e + m(j,i)v_d(j,i)^2/2 \right] + \frac{n_e v_e s^*}{4} \left[kT_e(\ln.\frac{1}{s^*} + 2) + m_e v_{de}^2/2 \right] \qquad (6.6.8)$$

From equation (6.6.1) the ionization-excitation energy flux is

$$F_{I.} = \sum_{j=k} \frac{n(j,i)v(j,i)H(j,i)\Psi(j,i)}{4} \qquad (6.6.9)$$

where $\Psi(j,i)$ is the average internal and ionization energy per ion. The total energy flux to the dielectric is $F_{tot.} = F_{k.E.} + F_{I.}$ which, on rearranging equations (6.6.8) and (6.6.9) becomes,

$$F_{tot.} = \sum_{j=k} \left\{ \frac{n(j,i)kT_e^{1/2}}{(2\pi)^{1/2}} \left[\frac{H(j,i)}{m(j,i)^{1/2}} \left(2kT_e + \frac{m(j,i)v_d(j,i)^2}{2} + \Psi(j,i) \right) + \frac{Z_{j,i}\, s^*}{m_e^{1/2}} \left(kT_e(\ln.\frac{1}{s^*} + 2) + \frac{m_e v_{de}^2}{2} \right) \right] \right\} \qquad (6.6.10)$$

$F_{k.E.}$, $F_{I.}$ and $F_{tot.}$ were computed for a wide range of values of n_e and kT_e and the results are shown in fig. 6.6.1. Carbon and Fluorine were assumed to co-exist in the plasma in the ratio 2 to 1, and were assessed in terms of a single ion species of mean atomic weight equal to 15 having successive ionization potentials of 15 eV, 30 eV, 50 eV, 70 eV and 100 eV. At kT_e = 3.3 eV, the ions were assumed to be predominantly singly or doubly ionized and Ψ was put equal to $15kT_e$. This assumption should not be critical, and was supported by the experimental evidence.

The curves in fig. 6.6.1 are valid so long as the ion Larmor radii , as a result of the magnetic field, are not smaller than the mean free paths λ_j. This condition is satisfied in this device. If this had not been the case, the diffusion rate perpendicular to the field lines would be reduced , being characterized by a velocity $\sim \frac{v(\text{thermal})}{1+(\omega_e \tau_e)^2}$.

The radiated flux is computed from equation (4.4.4) as a function of n_e, $n_{j,i}$ and kT_e . Values of ϕ for the various ions are shown in fig. 6.6.2. Comparing figs. 6.6.1 and 6.6.2 and equation (4.4.5), it is seen that, for the range of parameters encountered in this device and for plasma volumes around 1 cm^3, the main contribution to the energy flux received by the dielectric is from optically thick ionic spectral lines.

References

1. F.F.Chen,'Plasma Diagnostic Techniques', (R.H.Huddlestone,Ed.),p.113, Academic Press,1965, New York.

2. R.H.Lovberg,'Plasma Diagnost. Techn.', p.69, Academic Press, 1965

Fig. 6.6.1

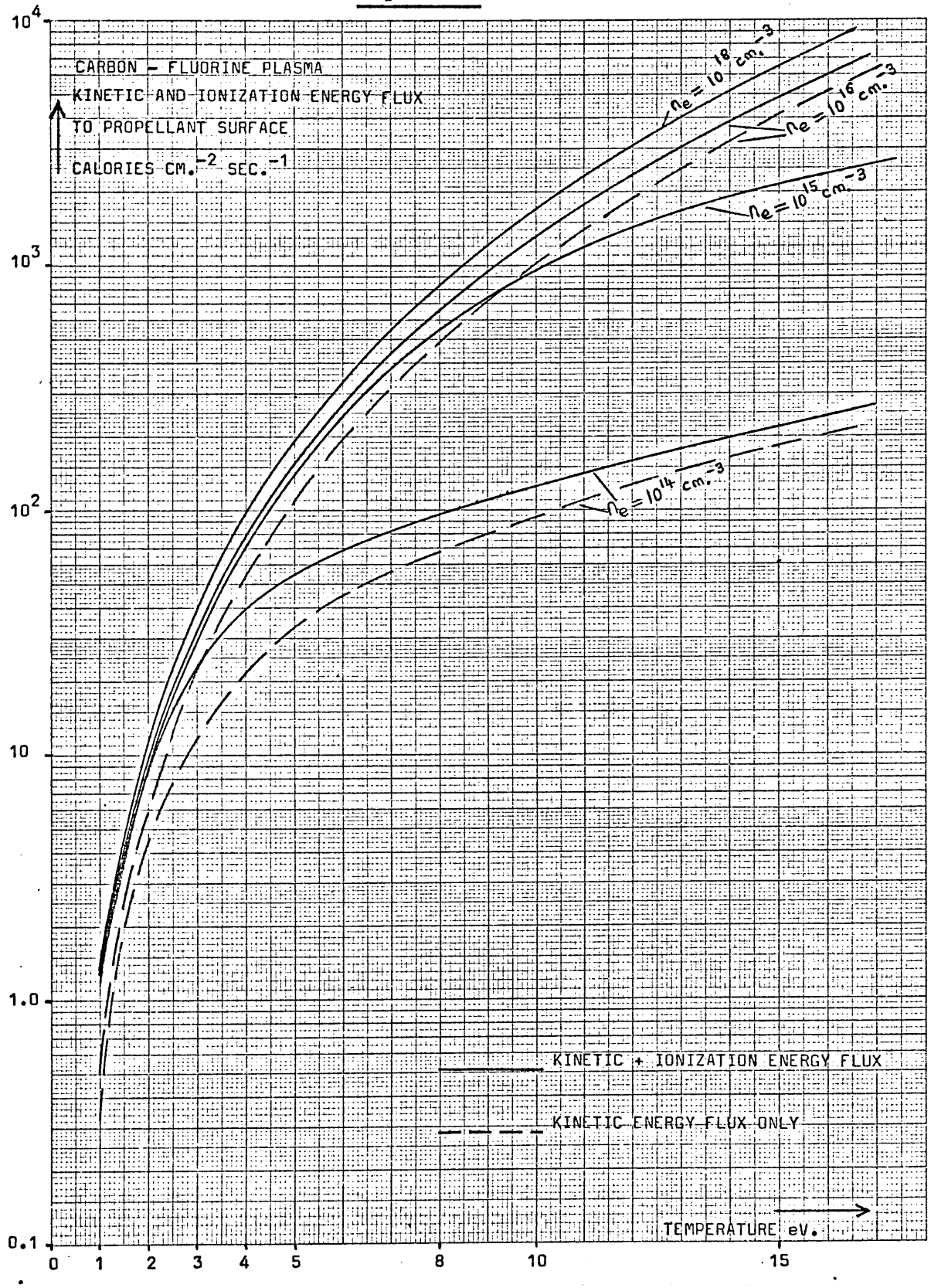
CARBON – FLUORINE PLASMA
KINETIC AND IONIZATION ENERGY FLUX
TO PROPELLANT SURFACE
CALORIES CM.-2 SEC.-1
10^4
10^3
10^2
10
1.0
0.1
$n_e = 10^{18}$ cm.-3
$n_e = 10^{16}$ cm.-3
$n_e = 10^{15}$ cm.-3
$n_e = 10^{14}$ cm.-3
KINETIC + IONIZATION ENERGY FLUX
KINETIC ENERGY FLUX ONLY
TEMPERATURE eV.
0
1
2
3
4
5
8
10
15

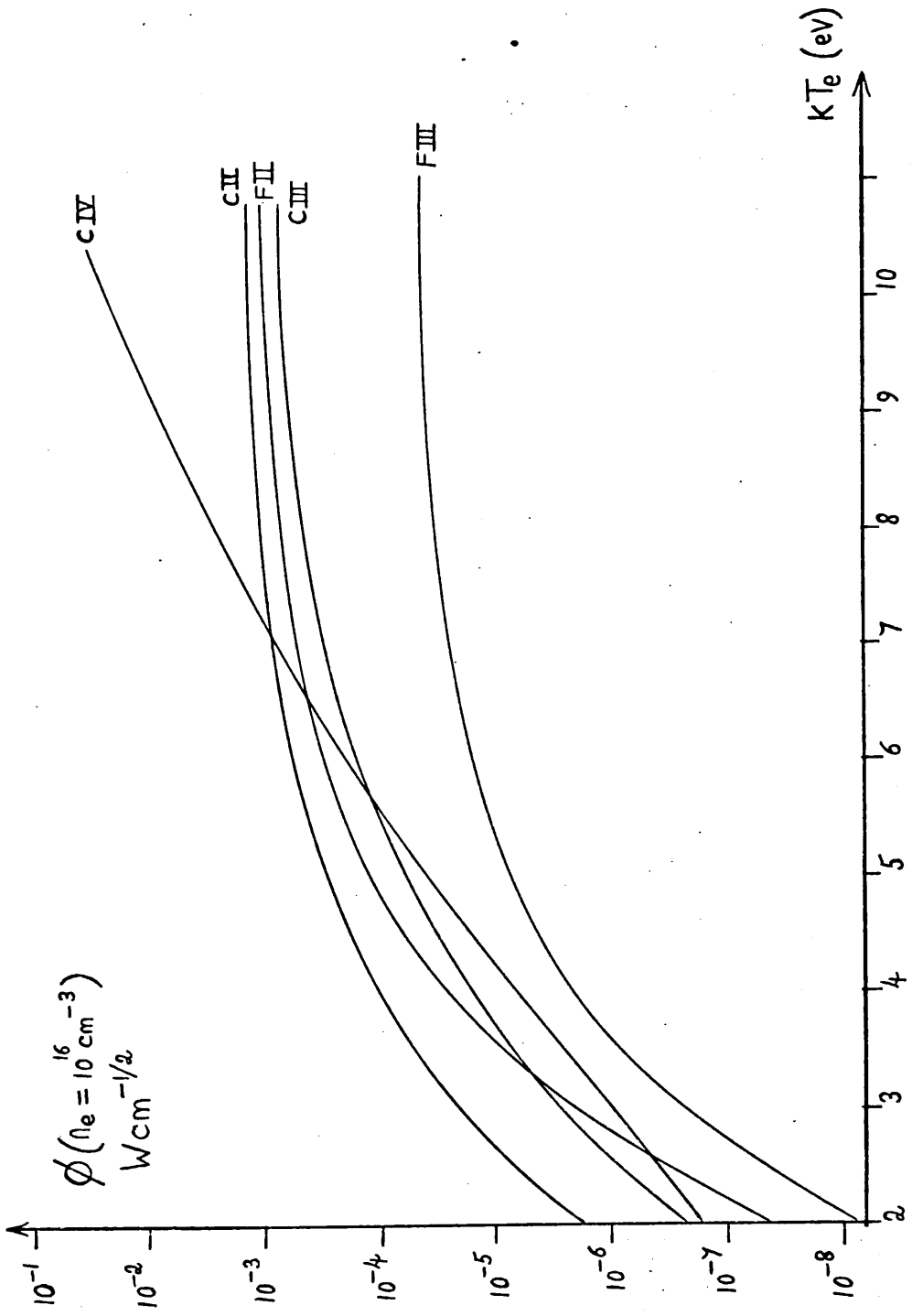
$\phi(n_e = 10^{16}\,cm^{-3})$
$W\,cm^{-1/2}$
10^{-1}
10^{-2}
10^{-3}
10^{-4}
10^{-5}
10^{-6}
10^{-7}
10^{-8}
CIV
CII
FII
CIII
FIII
KT_e (eV)
2
3
4
5
6
7
8
9
10

6.7 Numerical description of acceleration in the ablation device

In this section a simple one-dimensional numerical model is described which predicts the behaviour of the thrust device over a range of operating conditions. Results are discussed for radiation dominated plasmas when the magnetic pressure is much greater than the thermal pressure, assuming that the current distribution remains stable at all times. Equations (2.2.8) (2.2.11) and (2.2.13) are solved using the results of the ablation model described in section 6.4 .

Integrating equation (2.2.8) over volume and assuming that the density and velocity are uniform in the region between the electrodes, which experimental observations suggest, the rate of change of the plasma mass is,

$$\frac{dM}{dt} = R^* - \int \nabla\rho\, \underline{U} \cdot dV = R^* - \int \rho\, \underline{U} \cdot dA \qquad (6.7.1)$$

$\underline{U} = (U_x, 0, 0)$ is the plasma velocity.

If s is the length of the channel over which acceleration takes place, where s = the electrode thickness here, equation (6.7.1) becomes

$$\frac{dM}{dt} = R^* - M\underline{U}/s \qquad (6.7.2)$$

Integrating equation (2.2.11) over volume,

$$\frac{d(M\underline{U})}{dt} = \int \nabla(\tilde{T} + P) \cdot dV = \int (\tilde{T} + P) \cdot dA \qquad (6.7.3)$$

Using equations (2.2.10) and (3.3.1), and assuming that the current and particle temperatures and densities are uniform close to the electrodes,

$$\frac{d(MU)}{dt} = \frac{\mu_o I^2 d}{2b} + b\,d\,(n_e kT_e + \sum_i n_i kT_i) \qquad (6.7.4)$$

The assumptions are again supported by the experimental evidence of plasma uniformity and predominantly uni-directional thrust.

Integrating equation (2.2.13) and neglecting the term for the kinetic energy of the plume, which is small by comparison,

$$\frac{d}{dt}\,(3n_e kT_e/2 + 3/2 \sum_i n_i kT_i)\,b\,d = I^2 R_p - \gamma_R - R^* \bar{\chi} \qquad (6.7.5)$$

where R_p is the plasma resistance, γ_R is the radiated power and $\bar{\chi}$ is the mean ionization loss expressed as the mean ionization energy per gramme of ablated material.

Forward difference schemes were adopted for the solution of equations (6.7.2) and (6.7.4) using an Euler mesh with time steps Δt denoted by subscripts j. With a spatial mesh size greater than the Debye length and greater than or equal to the magnetic field penetration depth, the microscopic details of the acceleration process can be ignored.

The schemes are,

$$M_{j+1} = R_j^* \Delta t + M_j\,(1 - \underline{U}_j \Delta t/s)\; Z^* \qquad (6.7.6)$$

$$\underline{U}_{j+1} = \frac{\mu_o I^2 d\,\Delta t}{2b\,M_{j+1}} + \frac{M_j\,\underline{U}_j}{M_{j+1}}\,Z^* \qquad (6.7.7)$$

M is the total mass of plasma contained between the electrodes. Z^* is a factor representing the accumulation of plasma at the dielectric surface which can occur if the ablation rate is greater than that at which the material can be accelerated away.

The plasma can extend several millimetres from the surface before the current changes significantly. Z^* is then given approximately as

$$Z^* \begin{cases} = 1 \text{ if } \underline{U}_j < 2S/\Delta t \\ = 0 \text{ if } \underline{U}_j > 2S/\Delta t \end{cases}$$

Neglecting the addition of the thermal component of velocity, the maximum velocity that can be imposed by a stationary magnetic field on a plasma is the Alfvén velocity $v_A = B(\mu_0 m_i n_i)^{-1/2}$, provided that this is less than the E/B velocity, v_B, in which case the applied electric field seen by the plasma would fall to zero. Assuming a classical value for the electrical conductivity, $v_B \sim 2.7 \times 10^8 \, kT_e^{-3/2}$ cm/sec. for this device, with kT_e in eV.

A simple stability test showed that these schemes were stable towards round-off errors and it was found that, for a wide range of likely values of M, $\underline{U}$ and s, if $\Delta t \lesssim 10^{-7}$ sec., computation errors do not grow.

The ionization and excitation relaxation times and the thermal equipartition times for the ions and electrons, calculated using the results of the previous sections, are of the order $10^{-8} - 10^{-9}$ sec. for most of the duration of the discharge. If Δt is longer than these times but shorter than the times over which the current and ablation rate change appreciably, the plasma can be assumed to pass through a series of quasi-steady states, in which case

$$\frac{\partial}{\partial t} \frac{3}{2} \left(n_e kT_e + \sum_i n_i kT_i \right) \simeq 0$$

and equation (6.7.5) becomes,

$$I^2 R_p = \gamma_R + R^* \langle \chi \rangle \qquad (6.7.8)$$

In the present case equation (6.7.8) is valid if Δt is between $\sim 10^{-8}$ sec. and $\sim 10^{-6}$ sec.

In chapter four the radiative power losses per unit area were calculated for Carbon and Fluorine plasmas optically thick to the resonance lines, with densities greater than $\sim 10^{14} cm^{-3}$ and temperatures less than ~ 10 eV. The total loss from the plasmas produced in the present device can be expressed in the form

$$\gamma_R = 0.9 \times 10^{-22} n_e^{3/2} kT_e^{7/2} \qquad (6.7.9)$$

γ_R is in Watts if n_e is in cm^{-3} and kT_e in eV.

The average value of Z generally lies between 2 and 4, and $\langle X \rangle$, the average ionization energy per gramme of ablated material, is put equal to 1.7×10^5 J for PTFE and 3.8×10^5 J for Polyethylene and Polypropylene.

The resistance R_p, in Ohms, of the volume of plasma between the electrodes was given by the formula

$$R_p = 4.5 \times 10^{-2} kT_e^{-3/2} \qquad (6.7.10)$$

Assuming that at least 80% of the ablated material entering the discharge is either singly or doubly ionized,

$$n_e \simeq 3.0 \times 10^{23} M \qquad (6.7.11)$$

with n_e in cm^{-3} if M is in grammes.

A simple expression for R^* was obtained after inspection of the ablation rate curves for PTFE shown in figs. (6.4.2) and (6.4.3). From these it was found that, to an accuracy of better than 30%,

$$R^* \simeq \left(5 \times 10^{-4} F - 5\right) \qquad (6.7.12)$$

for values of the surface flux F equivalent to between 5% and 50% of the input power to the plasma.

For a PTFE -derived plasma,

$$F(\text{calories/cm}^2\text{sec.}) \simeq \gamma_R / 25 \qquad (6.7.13)$$

Equations (6.7.6) to (6.7.13) were solved using the measured values of the discharge current, although these values could have been computed in a separate sub-program. The results of the computations for a PTFE dielectric are shown in fig. 6.7.1 which depicts the growth of the temperature, density and velocity of the plasma in the inter-electrode region. Because of the simplicity of this model all values were rounded to the first decimal place during the calculations. In fig. 6.7.2 a comparison is made between the results obtained above and those obtained using two simpler models (A) and (B). In model (A) a constant fraction, namely 5%, of the input power was assumed to reach the PTFE surface throughout the course of the discharge. Model (B) was identical to model (A) except that a material other than PTFE was substituted which had an ablation rate equal to twice that of PTFE.

For polyethylene, R^* is put equal to $FA/\langle\chi\rangle$ as the bulk of the radiation loss consists of photons with insufficient energy to ionize the ablated material next to the dielectric surface. The suggestion is thus advanced that the amount of material actually entering the discharge is limited to the amount that can be ionized by the incident flux after initial melting of the solid. Fig. 6.7.3 shows the results obtained with the main model for the different materials,and for three values of the input power.

The simple model (A) was also used for PTFE to investigate the effect of changing the electrode geometry. Fig. 6.7.4 shows the values of plasma temperature, density and velocity 3μsec. after initiation of the discharge, when either the electrode width is halved or the separation is doubled. The current is maintained at the normal discharge value in each case.

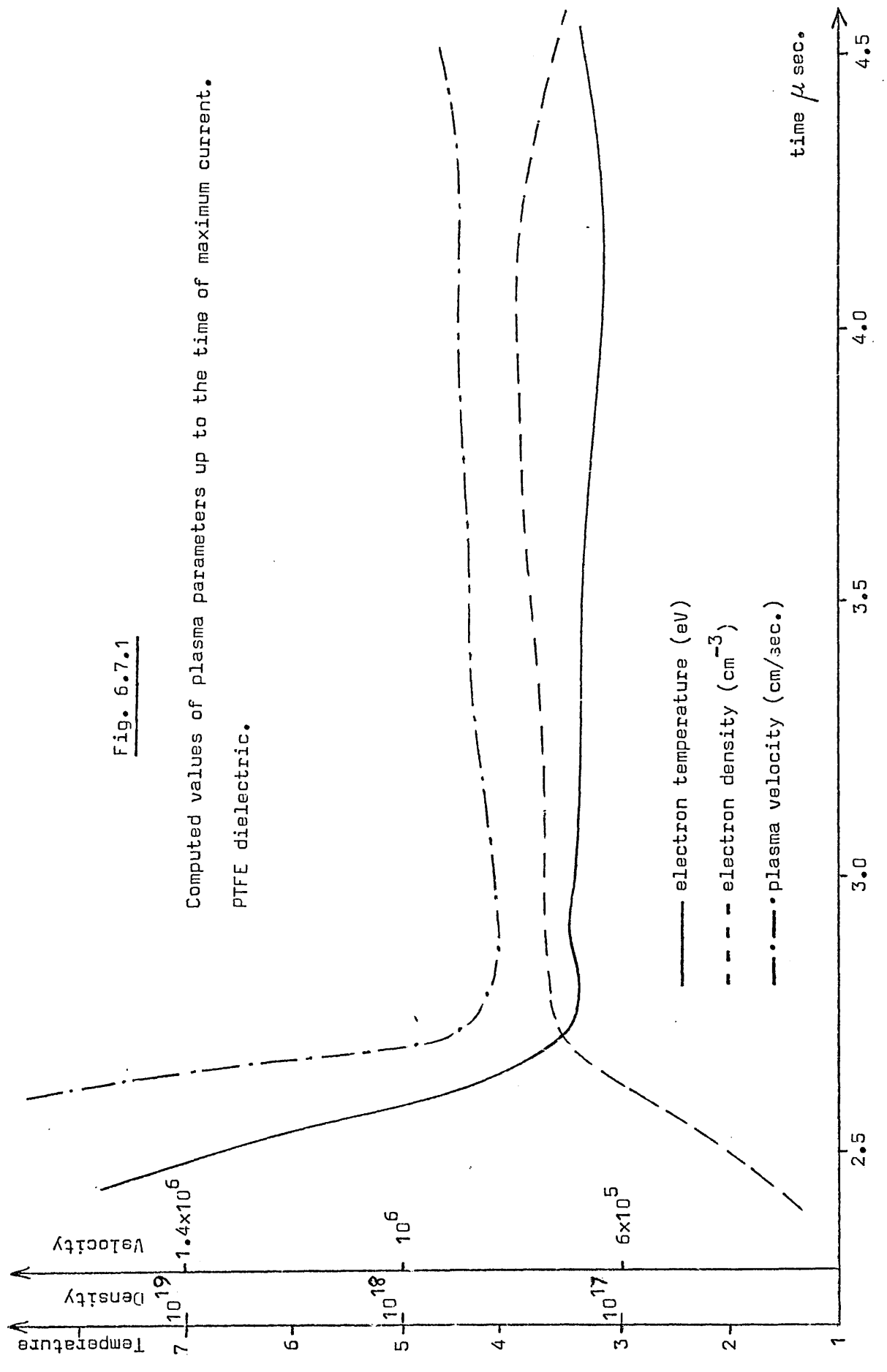

Fig. 6.7.1

Computed values of plasma parameters up to the time of maximum current.

PTFE dielectric.

Fig. 6.7.2

Computed values of plasma parameters for a PTFE-derived plasma, using various simplified models

(Units : n_e ... cm^{-3}, T_e ... eV, velocity (v) ... cm/sec.)

Time after start of discharge (μ sec.)		Model (A)	Model (B)	Main model
2.5	T_e =	5.5	3.6	6.8
	n_e =	4.0×10^{16}	8.0×10^{16}	3.0×10^{16}
	v =	3.8×10^{6}	2.0×10^{6}	5.0×10^{6}
3.0	T_e =	3.6	3.1	3.4
	n_e =	1.6×10^{17}	3.2×10^{17}	2.0×10^{17}
	v =	1.1×10^{6}	0.5×10^{6}	0.9×10^{6}
3.5	T_e =	3.4	2.8	3.3
	n_e =	2.4×10^{17}	4.7×10^{17}	2.7×10^{17}
	v =	0.8×10^{6}	0.4×10^{6}	0.7×10^{6}
4.0	T_e =	3.3	2.7	3.2
	n_e =	2.9×10^{17}	5.8×10^{17}	2.9×10^{17}
	v =	0.6×10^{6}	0.3×10^{6}	0.7×10^{6}
4.5	T_e =	3.3	2.7	3.3
	n_e =	2.6×10^{17}	5.2×10^{17}	2.1×10^{17}
	v =	0.6×10^{6}	0.3×10^{6}	0.8×10^{6}

Fig. 6.7.3

Computed average values of plasma parameters for different dielectric materials and different peak powers.

Dielectric	Peak Joule input power (MW)	Average temperature (eV)	Average density (cm^{-3})	Average velocity (cm/sec.)
PTFE	3	3.3	2.4×10^{17}	0.8×10^{6}
PTFE	6	2.5	1.2×10^{18}	0.3×10^{6}
PTFE	30	1.8 *	1.1×10^{19}	0.01×10^{6}
////////////	////////////	////////////	////////////	////////////
Polyethylene	3	4.3	3.0×10^{17}	2.0×10^{6}
Polyethylene	6	3.7	7.0×10^{17}	1.6×10^{6}
Polyethylene	30	2.8	5.0×10^{18}	1.2×10^{6}

* The plasma is assumed mainly singly ionized at this temperature, and the electromagnetic component of velocity only is shown.

Fig. 6.7.4

Values of plasma parameters 3 μ sec. after commencement of the discharge, for various values of electrode widths and separation.

	Gap separation 3 mm Electrode width 12 mm	Gap separation 3 mm Electrode width 6 mm	Gap separation 6 mm Electrode width 12 mm	Gap separation 6 mm Electrode width 6 mm
electron temperature (eV)	3.6	3.6	3.6	3.6
electron density (cm^{-3})	1.6×10^{17}	6.4×10^{17}	1.6×10^{17}	6.4×10^{17}
plasma velocity (cm/sec)	1.1×10^{6}	1.1×10^{6}	1.1×10^{6}	1.1×10^{6}

Chapter Seven

Conclusions

From the experimental results it was seen that reproducible, uniform plasmas can be produced with this device and ejection velocities greater than 10^6 cm/sec. have been obtained. Depending slightly on the type of dielectric used, electron densities around 10^{17} cm^{-3} are attainable with resistive power inputs of the order 10 MWatts, with the electron temperature below 10 eV. The electromagnetic power efficiency is approximately 20% and, at a thrust power of $\sim 10^2$ Newtons, is almost an order of magnitude greater than the gas-dynamic component. In the region between the electrodes, plasma is continuously being produced from material ablated from the dielectric and the source operates as a stationary arc, with a part of the radiative loss being utilized for the ablation. The uniformity and stability of the discharge is partly attributed to the dominance of radiation losses, as these produce a roughly uniform ablation and cause photo-emission from the cathode which reduces the possibility of sputtering.

Thrust powers ranging from ~ 30 Newtons to $\sim 10^4$ Newtons have been obtained with other, similar devices[1,2,3]. It was shown in chapter three that for a uniform acceleration and high thrust efficiency, inhomogeneities which could result in Hall current flow must be kept small, and the Hall parameter ψ must be $\lesssim 1$. This is the case in the present device for PTFE-derived plasmas, except at the beginning of each discharge cycle, i.e. at 8μ sec. and 16μ sec. after commencement, when ψ is > 1. The plasma was seen to deflect towards the anode at these times, due to the presence of a Hall current. ψ is proportional to the $\dfrac{\text{current} \times kT_e^{3/2}}{n_e}$ and in the accelerators of Balagurov et.al.[1] and Vondra et.al.[2], ψ was $\gtrsim 10$ and instabilities led to the eventual break-up of the current sheet.

In these last-mentioned devices the electrodes extended along the direction of acceleration, and it was found that only about 10% of the total mass was substantially ionized and accelerated. Returning to discussion of the present source, the performance characteristics namely, the velocity of the plasma plume, electron density, temperature and total thrust, have been determined experimentally and related to the input power, the magnetic field and the thermal properties of the dielectric. Good agreement was observed between these results and the predictions of a simple 1-Dimensional numerical model which describes both the ablation and acceleration. The main energy loss terms namely, line radiation and collisional ionization were incorporated in simple expressions such as those outlined in chapter four.

The analysis developed by Grishin et.al.[3] to describe a pulsed coaxial accelerator was simpler, and the ablation rate was expressed in terms of the measured current and the final plasma velocity. These authors pointed out, however, the need for a more detailed analysis of the ablation in order to make the model self-contained. A comparison between the various dielectric erosion sources is presented in fig. 7.1

In chapter three it was shown that for efficient operation and a mainly unidirectional thrust, inhomogeneities in the plasma should be small. Here, the acceleration length is short and the rate of mass ablation is high. As a consequence the temperature does not generally become large enough for the efficiency to exceed about 20%. However, even if inhomogeneities in temperature and density in the thrust direction are large (greater than 100%), the effect on the overall efficiency is small if the Hall current is small. Inhomogeneities of this kind are themselves unlikely to cause disruption of the current sheet. Provided that γ is less than unity, variations in plasma parameters perpendicular to the direction of thrust also have little effect on the efficiency if they are below 100% and Hall currents are negligible. However, as was shown in section 3.4 , if γ is high, density variations

of only $\sim$ 20% could more than halve the efficiency and result in current sheet distortion.

For values of ψ greater than $\sim 10^2$, the mean free paths and Larmor radii of the ions would become greater than the accelerator dimensions and the plasma would become collisionless. In that case, unless the energy transfer time between electrons and ions is less than the acceleration time, the temperature of the ions is likely to be less than that of the electrons. If the discharge current is increased, the self-field increases, and when ionization of the ions is incomplete, the internal energy of the ions is greater than their thermal energy. This means that the density will grow faster than the temperature and, unless the input power is greater than the power loss due to ionization and excitation, ablation will increase, the temperature may decrease and ψ will remain low. If for some reason the amount of ablation does not increase, ψ will grow. Such a situation could arise in several ways, e.g.,

(i) The dielectric may have a high thermal conductivity and a high melting point and be thus less easy to ablate.

(ii) The discharge may be so rapid that ionization and excitation equilibrium is not reached, thereby reducing the radiative flux. The likelihood of cathode sputtering is also greater in this case.

(iii) The dielectric may consist mainly of low-Z ions, in which case the radiative losses from the plasma will be smaller.

(iv) The electrodes may extend far out in the direction of acceleration, allowing the current sheet to move away from the ablating zone.

Using polyethylene and polypropylene as dielectrics, the temperatures obtained were higher and the densities lower, for the same input power. In each case ψ was $\gtrsim$ 5 and this could explain the fact that plasmas obtained from these materials were not so reproducible, often showing signs

of breaking-up during the first discharge cycle. Discharges with polyethylene and polypropylene could be made more stable in this device simply by increasing the current, provided that current-driven instabilities do not become important. It was seen from the results of section 3.4 that, if the current sheet remains uniform, the highest efficiency is obtained using polyethylene.

The simple model, which was set up to describe the ablation rate from a solid when subjected to a transient surface energy flux and the subsequent acceleration of the plasma produced, gave results which were in good agreement with experimental observations under the same conditions. The model was run initially for PTFE and other similar materials, where the greater part of the radiation from the plasma consists of photons with an energy greater than the first ionization potential of the neutral atoms. The results showed in this case that, as the ablation rate increases, the plasma mass increases whilst the temperature decreases. In the case of polyethylene and polypropylene however, which are both easier to ablate than PTFE, the mass of the plasma plume was found experimentally to be smaller than with PTFE, and the temperature and velocity were higher. For these materials it was noted that Hydrogen replaced Fluorine as the main atomic constituent, and the major part of the radiation loss consisted of photons with insufficient energy to ionize the neutral atoms boiling off from the dielectric surface. The thermal expansion velocity of the melted dielectric ($\lesssim 10^5$ cm/sec.) is too low for it to enter the main discharge region in the time of interest. Once it is ionized however, it begins to pick up sufficient energy from the applied field. In the case of PTFE only a small fraction of the photon flux is required to singly ionize the ablated material, but with predominantly Hydrogen-containing dielectrics a greater degree of absorption takes place at the surface, cascade excitation being important. This was incorporated into the simple model by equating the rate of entry of material into the plasma to the mean photo-flux divided by the average ionization energy of the particles.

The computed results are in rough agreement with the experimental results. At the dielectric surface the gas-dynamic expansion, though small, will be greater using polypropylene than with polyethylene as the ablation rate is greater when the temperature is high. This fact should explain why the observed temperature and velocity of the plasma plume were slightly lower using polypropylene and why the ablated mass was slightly higher.
The results of the simplified computations suggest, that the mass of the plasma is larger and the specific impulse smaller if dielectric materials containing little or no Hydrogen are used. The model is sufficiently flexible to accomodate a wide range of materials and surface energy fluxes, and could thus be used in other situations where surface deterioration is important, such as at the inside walls of thermonuclear containment devices.

During the course of this work many new values of atomic parameters for Carbon and Fluorine ions were obtained namely, eigenstate population distributions, ionization and excitation rate coefficients, recombination rate coefficients and radiative loss functions. Several new experimental diagnostic techniques were also developed for the measurement of plasma temperatures and densities.

References

1. A.Ya.Balagurov, S.D.Grishin, V.I.Levtov, L.V.Leskov, Sov.Phys.Tech.Phys. 15 , p.345, 1970

2. R.J.Vondra,K.I.Thomassen,A.Solbes, Proc. IEEE, 59, p.271, 1971

3. Yu.M.Grishin,N.P.Kozlov,V.I.Khvesyuk,Sov.Phys.Tech.Phys.,18, p.542, 1973

Fig. 7.1

Operating Characteristics of Various Ablation Accelerators

	Balagurov et.al.[1]	Vondra et.al.[2]	Grishin et.al.[3]	This device
Peak Current Amps	$\sim 2\times10^{5}$	5×10^{3}	3×10^{5}	$\sim 2\times10^{4}$
Average velocity cm/sec.	$\sim 7\times10^{6}$	$\sim 3\times10^{5}$	2×10^{6}	10^{6}
Specific Impulse sec.	$\sim 7\times10^{3}$	~ 300	$\sim 2\times10^{3}$	$\sim 10^{3}$
Average thrust Newtons	—	~ 30	$\sim 1.2\times10^{4}$	~ 100
Average Temperature eV	~ 5.0	~ 10.0	—	3.4
Average density of electrons cm^{-3}	$\sim 10^{16}$	$\sim 10^{16}$	—	2×10^{17}

Chapter 8 - Discussion

In view of the broad agreement obtained between experimental values for this device and the predictions of the simple ablation-acceleration model, an extension of this scheme to cover higher currents and different dielectric materials should provide some indication of the overall performance characteristics. In particular, it is noticed that, with increase in the Joule power delivered to the plasma, the temperature falls slightly whilst the density rises. With PTFE, densities approaching 10^{19} cm^{-3} could result if the current alone could be increased by a factor of five, with a maximum current of around 10^5 Amps. Alternatively, for a given power input, an increase in density could be obtained if the dielectric ablation rate were increased. This could be achieved either by using different materials or by surrounding the discharge with the dielectric to a greater extent than at present. For a given thrust the kinetic energy content of the plasma would be reduced in proportion to the final velocity, but the total enthalpy will increase with the mass. Thus, notwithstanding any problems of uniformity or stability, the exhaust energy efficiency could be increased either by raising or lowering the final velocity, depending upon the ratio of kinetic to internal energy.

The ablation device could also be used as a reliable and flexible light source, in view of the ease with which a uniform plasma plume, with a large spectral output in the visible to soft X-ray wavelength range, is obtained. By adding different materials to, for example, polyethylene, and by suitably controlling the discharge current, a plasma with a chosen temperature and containing ions in a particular stage of ionization could be produced. If the plasma is large, intense emission from resonance spectral lines or recombination edges of the constituent ions could be used for selective excitation in other plasmas. A resonant scattering

experiment on Hydrogen or Deuterium in a plasma containment device using the recombination radiation from As I, Se I or Ba II has been described[1]. With the range of densities possible with this device, measurements of Stark broadening[2] and population distributions among bound states of many ion species[3] could be made.

The ablation model predicts the rate of evaporation of solid materials when they are subjected to a large surface energy flux, in this device consisting predominantly of vacuum-U.V. radiation. In plasma confinement machines, operating at temperatures up to a few keV[4,5], much of the energy loss to the surrounding walls is through radiation or thermal conduction, but can also be due to relativistic runaway electrons which spill-out from the confining magnetic fields[6]. The present model could possibly be adapted for this situation, where wall interactions are known to be important[5,7]. In particular, the length of time before wall material will enter the plasma has to be kept as great as possible, although the effects of such material once in the plasma, are not fully understood. Often, in such machines, liners or limiters are made of high melting point materials such as Molybdenum or Tungsten, but the radiative losses from these materials at high stages of ionization can be severe.

High-density laser produced plasmas can lose a significant amount of energy through X-ray emission[8], and a complete study of the atomic processes within the plasma and the nature of the interaction of the radiation with solid target materials could assist in the general problem of the heating of dense plasmas with intense laser beams. Neglecting non-linear absorption processes, the plasma reflects the laser beam once the critical electron density is reached which, for a CO_2 laser is $\sim 10^{19} cm^{-3}$, and for a Nd laser is $\sim 10^{21} cm^{-3}$. To produce densities of $\sim 10^{24} cm^{-3}$, i.e. solid densities, high power lasers operating in the vacuum-U.V. region would be needed and are, at present not available. Also, the cross-section for

inverse bremsstrahlung, the principal absorption mechanism, decreases with decrease in wavelength. By using another laser produced discharge system as an effective wavelength converter[9], or with the present device operating at high density, and a Lithium-Fluoride or Calcium-Fluoride lens to focus ultraviolet radiation down to a spot a few hundred microns or less in diameter, higher density plasmas than at present could be obtained and heated, if absorption cross-sections such as inverse radiative recombination are large enough. The radiation flux from an optically thick primary layer in a laser produced plasma pellet, surrounding a central target, could be estimated using an analysis similar to that described in sections 4.4 and 5.4. Unlike thermal conduction to the core, energy transfer in this case would take place at the speed of light. Focussed powers of $\sim 10^{11} - 10^{12}$ Watts/cm^2 are feasible with the present device.

The presence within this plasma of ions from the same ionization stage having different velocities leads one to suppose that, at the leading edge of the plume as it accelerates into a vacuum, a population inversion could develop involving bound states on either side of the thermal band of levels, and could include resonance transitions, hitherto not used in laser systems. This possibility has been discussed by Norton and Wooding[10]. Laser oscillations from fast Z-pinches have been observed in Argon, Xenon and Oxygen by Likhachev et.al.[11] and Hashino et.al.[12], although the exact mechanism for their production is not clear. It has been proposed[12] that selective pumping at the time of maximum compression is achieved by means of fast ions or electrons (including runaways) which are possibly produced as a result of instabilities in the pinch. These can cause direct ionization into excited states of higher ions, although the cross-sections are small[13]. The time of emission of the laser pulses in these experiments and their directionality do not, however, rule out the possibility of velocity-induced population inversion.

References

1. B.A.Norton, Z.Naturf., 29a, p. 1937, 1974

2. H.R.Griem,'Plasma Spectroscopy', McGraw-Hill Pub.,New York, 1964

3. B.A.Norton,E.R.Wooding, J.Phys.B, to be published 1975

4. L.A.Artsimovich,A.M.Anashin, Zh.E.T.F.Letters,10, p.130, 1969

5. E.Hinnov,A.S.Bishop, Phys.Fluids, 9, p.195, 1966

6. C.W.Gowers,J.W.Long,A.A.Newton,B.A.Norton,D.C.Robinson,A.J.L.Verhage, H.A.B.Bodin, 6th European Conf. on Contr.Fus.Plasma Phys., Moscow,1973

7. R.F.Post, Ann.Rev.Nucl.Sci., 9, p.367 , 1959

8. M.Galanti,N.J.Peacock,B.A.Norton,J.Puric, 5th IAEA Conf. Plasma Phys. Contr.Nucl.Fus.Res., Tokyo,1974

9. B.A.Norton, Z.Naturf., 30a, p.263, 1975

10. B.A.Norton,E.R.Wooding, Phys.Rev.A , March 1975

11. V.M.Likhachev,M.S.Rabinovich,V.M.Sutovskii, J.E.T.P.Letters,5,p.43,1967

12. Y.Hashino,Y.Katsuyama,K.Fukuda,Jap.J.Appl.Phys., 13, p.1134, 1974

13. W.Benett, Appl.Optics.Supplement II, p.3, 1965

$A(p,q)$	Spontaneous radiative transition probability
A^*	Plasma inhomogeneity factor
B	Magnetic induction
$B(q,p)$	Einstein coefficient for stimulated transition
B_p	Boltzmann deviation parameter for energy level p
B^*	Plasma inhomogeneity factor
C	Electrical capacitance,plasma inhomogeneity factor
E	Electric field strength
E_a	Chemical kinetic activation energy
E_p	Excitation energy of level p in an atom or ion
F	Surface energy flux ,force per unit mass
F^*	Optical escape factor
G	Arrhenius pre-exponential factor
G^*	Particle density injection rate
H	Surface particle flux inhibition factor
I	Electric current
$I(\lambda),I(p,q)$	Radiation intensity
$I_{b.b.}$	Spectral intensity of black body radiation
I^*	Total intensity of an optically thick spectral line
J	Electric current density,
K	Plasma property variation factor
L	Electrical inductance
L'	Electrical inductance per unit length of accelerator
$L(\lambda),L(\gamma)$	Spectral line shape
M	Mass
M^*	Gramm molecular weight of organic dielectric monomer
P	Pressure
$\tilde{P}$	Kinetic stress tensor
p^*	Joule power input per unit volume of plasma

$Q(\lambda)$	Sensitivity of optical detection system
R	Electrical resistance
R^*	Mass injection rate of ablation products
$S(k,i)$	Collisional ionization rate coefficient
$S(\gamma)$	Radiative transfer source function
T ,kT	Particle temperature
$\tilde{T}$	Maxwell stress tensor
U	Velocity
V	Volume,voltage
W	Average kinetic energy of surface impacting particles
$X(p,q)$	Collisional transition rate coefficient
Y	Radiated power loss per unit volume
Z	Ionic charge

a	Acceleration
a_o	Bohr radius
b	Electrode width
c	Velocity of light
d	Electrode separation
e	Electronic charge
$f(v)$	Velocity distribution
$f(p,q)$	Radiative absorption oscillator strength
g_p	Statistical weight of level p
$\hat{g}$	Gaunt factor
h	Planck's constant
j	Electric current density
k	Boltzmann constant
ℓ	Acceleration length
m_e, m_i	Electron,ion mass
n_e, n_i	Electron,ion number density

p	Energy level
p'	Weight percent composition of pyrolised products
q	Energy level
r	Space coordinate
r_L	Larmor radius
s	Monochromator slit width
t	Time
t_{ee}, t_{ei}	Thermalization relaxation times
u	Velocity
v	Velocity
v_r	Random particle velocity
v_d	Electron current drift velocity
v_T	Thermal velocity
w	Frequency
w_c, w_H	Cyclotron frequency
w_p	Plasma frequency
w_s	Stark broadening parameter
x	Space coordinate
y	Space coordinate
z	Space coordinate

$\alpha(R,i)$	Radiative recombination rate cofficient
β	Three-body collisional recombination rate coefficient, Hall current index
γ	Radiative energy loss function
δ	Electrical skin depth, optical path, monochromator slit function
ϵ_o	Dielectric constant
$\mathcal{E}$	Efficiency of thrust over applied power
$\hat{\mathcal{E}}(\nu)$	Spectral emisoivity
η	Electrical resistivity, optical system sensitivity
θ_p	Saha-Boltzmann deviation parameter for energy level p

λ	Wavelength
Λ	Coulomb scattering parameter
μ_o	Permeability of free space
μ	Atomic weight
ν	Frequency
ρ	Mass density
σ	Electrical conductivity
$\sigma(p,q)$	Transition cross section
τ	Optical depth
τ^*	Boltzmann deviation parameter function
$\varnothing$	Radiative energy loss parameter
$\hat{\varkappa}(\nu)$	Radiative absorption coefficient
$\chi(p,q)$	Excitation or ionization potential
ψ	Hall parameter
ΔH	Heat of chemical transformation
$\Delta\lambda_s, \Delta\nu_s$	Stark half-width
$\Delta\lambda_D, \Delta\nu_D$	Doppler half-width
Δx	Space mesh point
Δt	time mesh point

Subscripts

Br	Bremsstrahlung	p	Plasma, energy level
Cr	Collisional-radiative	q	Energy level
e	Electron	T	Thermal
G	Gun	x	Direction
i	Ion, space step	y	Direction
j	Ion stage, time step	z	Direction
k	Ion specie		

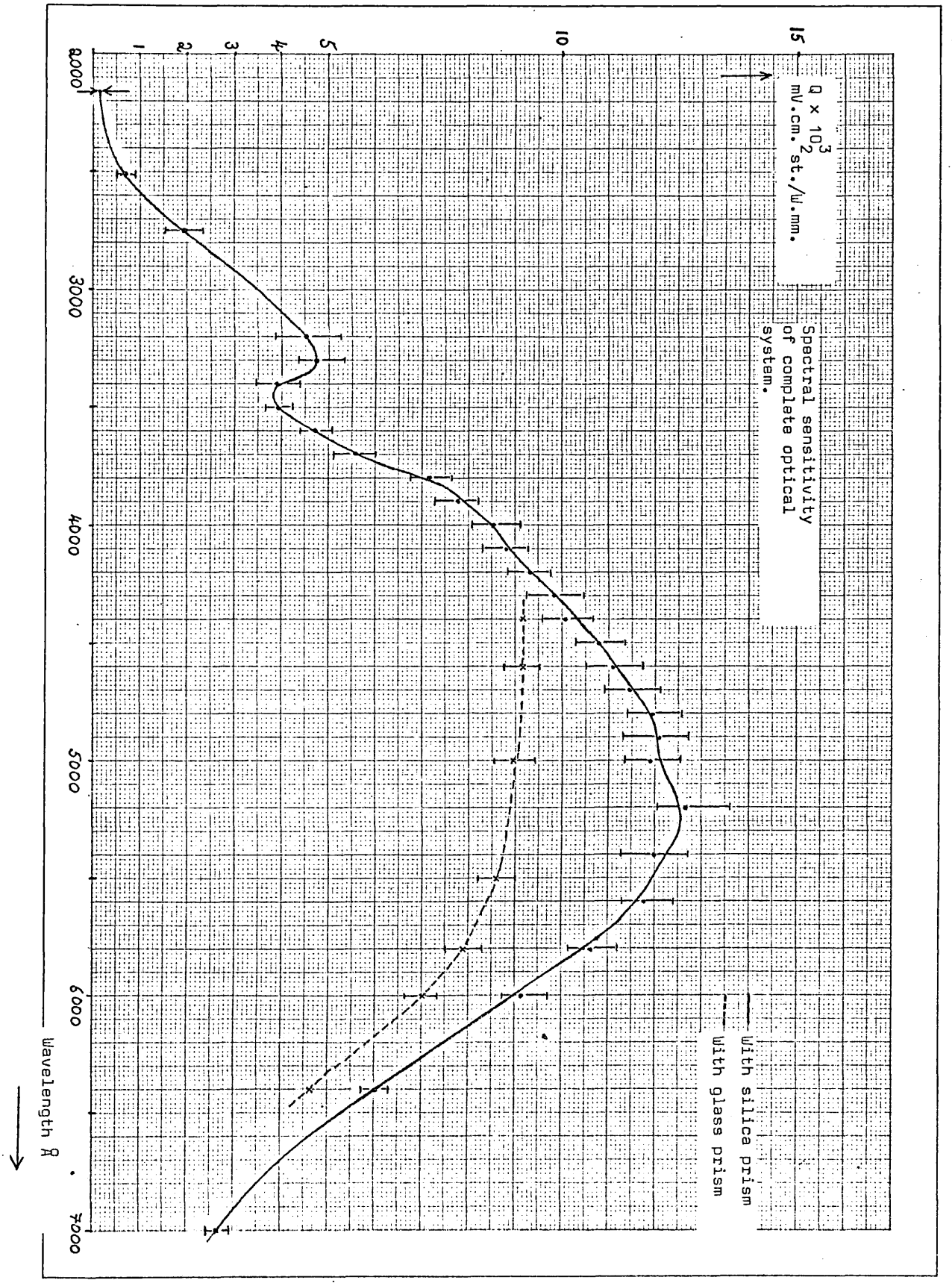
Q × 10^3
mV.cm. st./w.mm.
15
10
5
4
3
2
1
8000
3000
4000
5000
6000
7000
Wavelength Å
Spectral sensitivity
of complete optical
system.
With silica prism
With glass prism